ΕΘΝΙΚΟ ΜΕΤΣΟΒΙΟ ΠΟΛΥΤΕΧΝΕΙΟ
ΣΧΟΛΗ ΕΦΑΡΜΟΣΜΕΝΩΝ ΜΑΘΗΜΑΤΙΚΩΝ ΚΑΙ ΦΥΣΙΚΩΝ ΕΠΙΣΤΗΜΩΝ

ΑΝΑΠΤΥΞΗ ΚΑΙ ΥΛΟΠΟΙΗΣΗ ΤΕΧΝΙΚΩΝ ΕΠΙΤΟΠΙΑΣ ΦΑΣΜΑΤΟΣΚΟΠΙΑΣ-γ ΓΙΑ ΕΦΑΡΜΟΓΕΣ ΣΤΟ ΘΑΛΑΣΣΙΟ ΠΕΡΙΒΑΛΛΟΝ

ΔΙΔΑΚΤΟΡΙΚΗ ΔΙΑΤΡΙΒΗ

ΕΥΦΡΟΣΥΝΗΣ Γ. ΑΝΔΡΟΥΛΑΚΑΚΗ
Διπλωματούχου της σχολής Εφαρμοσμένων Μαθηματικών και Φυσικών Επιστημών Ε.Μ.Π.

ΕΠΙΒΛΕΠΩΝ:

Μ. ΚΟΚΚΟΡΗΣ
Αναπληρωτής Καθηγητής Ε.Μ.Π.

ΑΘΗΝΑ, Σεπτέμβριος 2016

ΕΘΝΙΚΟ ΜΕΤΣΟΒΙΟ ΠΟΛΥΤΕΧΝΕΙΟ
ΣΧΟΛΗ ΕΦΑΡΜΟΣΜΕΝΩΝ ΜΑΘΗΜΑΤΙΚΩΝ ΚΑΙ ΦΥΣΙΚΩΝ ΕΠΙΣΤΗΜΩΝ

ΑΝΑΠΤΥΞΗ ΚΑΙ ΥΛΟΠΟΙΗΣΗ ΤΕΧΝΙΚΩΝ ΕΠΙΤΟΠΙΑΣ ΦΑΣΜΑΤΟΣΚΟΠΙΑΣ - γ ΓΙΑ ΕΦΑΡΜΟΓΕΣ ΣΤΟ ΘΑΛΑΣΣΙΟ ΠΕΡΙΒΑΛΛΟΝ

ΔΙΔΑΚΤΟΡΙΚΗ ΔΙΑΤΡΙΒΗ

ΕΥΦΡΟΣΥΝΗΣ Γ. ΑΝΔΡΟΥΛΑΚΑΚΗ
Διπλωματούχου της σχολής Εφαρμοσμένων Μαθηματικών και Φυσικών Επιστημών Ε.Μ.Π.

ΤΡΙΜΕΛΗΣ ΣΥΜΒΟΥΛΕΥΤΙΚΗ ΕΠΙΤΡΟΠΗ:

1. Μ. ΚΟΚΚΟΡΗΣ, Αν. Καθ. Ε.Μ.Π. (Επιβλέπων)
2. Χ. ΤΣΑΜΠΑΡΗΣ, Ερευνητής Β ΕΛ.ΚΕ.Θ.Ε.
3. Ρ. ΒΛΑΣΤΟΥ, Καθ. Ε.Μ.Π.

ΕΠΤΑΜΕΛΗΣ ΕΞΕΤΑΣΤΙΚΗ ΕΠΙΤΡΟΠΗ:

1. Μ. ΚΟΚΚΟΡΗΣ, Αν. Καθ. Ε.Μ.Π. (Επιβλέπων)
2. Χ. ΤΣΑΜΠΑΡΗΣ, Ερευνητής Β ΕΛ.ΚΕ.Θ.Ε.
3. Ρ. ΒΛΑΣΤΟΥ, Καθ. Ε.Μ.Π.
4. Μ. ΑΝΑΓΝΩΣΤΑΚΗΣ, Αν. Καθ. Ε.Μ.Π.
5. Β. ΚΑΨΙΜΑΛΗΣ, Ερευνητής Β ΕΛ.ΚΕ.Θ.Ε.
6. I. DARBY, IAEA Physics Section Staff, Vienna
7. Z. ZHI, Ass. Prof., Tsinghua University, China

ΑΘΗΝΑ, Σεπτέμβριος 2016

Στην οικογένειά μου...

Acknowledgements

I would like to express my sincere appreciation and gratitude to my Advisory Committee, Dr. Kokkoris Michael, Associate Professor of NTUA and responsible of this PhD thesis, Dr. Christos Tsabaris, Researcher at HCMR and research supervisor, and Dr. Rosa Vlastou, Professor of NTUA, for their valuable constant guidance and support, and for the confidence they have shown me over the years, which was a source of motivation. The overall interaction I had with all the above has been a source of inspiration and encouragement throughout all these years. Moreover, I would like to express my deep appreciation to all the members of the examination committee for their constructive contributions.

I would also like to thank and express my gratitude to Dr. C. Kalfas for his valuable consulting and technical support, and all the people who contributed to this work and especially Eleftherios Skordis and Eleni Fatsea, regarding the theoretical work of this thesis and Stelios Alexakis, Filothei Pappa and Veatriki Michalopoulou-Petropoulou regarding the experimental work.

The members of the NTUA group have contributed immensely to my time at NTUA. The group is composed of eager young researchers and has been a source of friendships as well as good advice and collaboration, and for this I am deeply thankful. More particularly, I would like to especially thank my friends, with which I have worked all these years, George Eleftheriou, Dionissis Patiris, Valentina Paneta and Mary Diakaki, for the scientific and moral support.

Finally, I would like to express a special thanks to my family for their love and encouragement, and especially to Iraklis Fitsios, for his constant support in every way and for the patience he showed throughout these years.

Table of contents

ΠΕΡΙΛΗΨΗ

1. Εισαγωγή

Η παρακολούθηση των επιπέδων ραδιενέργειας στο περιβάλλον είναι απαραίτητη από πλευράς ακτινοπροστασίας λόγω των αρνητικών επιπτώσεων της ακτινοβολίας στον ανθρώπινο οργανισμό. Πηγές φυσικής ραδιενέργειας στο περιβάλλον αποτελούν οι τρεις ραδιενεργές σειρές των ^{235}U, ^{238}U, ^{232}Th με τα θυγατρικά τους στοιχεία καθώς και άλλα στοιχεία όπως το ^{40}K, που είναι κυρίαρχο στο θαλάσσιο περιβάλλον. Μέρος της φυσικής ραδιενέργειας οφείλεται επίσης στην κοσμική ακτινοβολία καθώς και σε ραδιονουκλίδια που δημιουργούνται από αλληλεπιδράσεις της κοσμικής ακτινοβολίας με τα ανώτερα στρώματα της ατμόσφαιρας (π.χ. ^{7}Be, ^{3}H). Σε πολλές περιοχές, εμφανίζονται υψηλά επίπεδα φυσικής ραδιενέργειας που αποδίδονται στην ορυκτολογία της περιοχής λόγω των υψηλών συγκεντρώσεων σε φυσικά ραδιονουκλίδια (Naturally Occurring Radioactive Materials, NORM) και σχετίζονται με τη γεωμορφολογία της περιοχής (π.χ. κοιτάσματα U). Κατά τη βιομηχανική εκμετάλλευση τέτοιων φυσικών πόρων (ορυκτά, βιομηχανική πρώτη ύλη), όπως μονάδες εξόρυξης μεταλλευμάτων και παραγωγής φωσφορικών λιπασμάτων, παράγονται προϊόντα ή παραπροϊόντα πλούσια σε φυσική ραδιενέργεια (Technologically Enhanced Naturally Occurring Radioactive Materials, TENORM). Η επαύξηση της φυσικής ραδιενέργειας στα παραγόμενα υλικά προκύπτει λόγω της εκλεκτικής εναπόθεσης ορισμένων ραδιονουκλιδίων σε αυτά, και σχετίζεται με τις διεργασίες επεξεργασίας της πρώτης ύλης. Τις τελευταίες δεκαετίες, στη συνεισφορά της ραδιενέργειας στο περιβάλλον έχουν προστεθεί και τεχνητά ραδιενεργά στοιχεία, ενδεικτικά αναφέρονται τα ^{137}Cs, ^{131}I, ^{90}Sr, ^{60}Co, που οφείλονται στην ανθρώπινη δραστηριότητα και σχετίζονται με διεργασίες όπως η σχάση σε πυρηνικούς αντιδραστήρες, η παραγωγή ραδιοφαρμάκων σε επιταχυντές και οι πυρηνικές δοκιμές. Η παρουσία τους στο περιβάλλον σχετίζεται επίσης με πυρηνικά ή άλλα ραδιολογικά ατυχήματα.

Η μέθοδος της φασματοσκοπίας ακτίνων-γ είναι μια τεχνική ευρέως διαδεδομένη που χρησιμοποιείται για την παρακολούθηση των επιπέδων ραδιενέργειας στο περιβάλλον (χερσαίο και θαλάσσιο). Η μέθοδος αυτή βρίσκει άμεση εφαρμογή στην παράκτια ζώνη σε προβλήματα που σχετίζονται με τους κανονισμούς ακτινοπροστασίας (μοντέλα υπολογισμού δόσεων/ χωρικής διασποράς ραδιονουκλιδίων) αλλά και σε ένα ευρύ πεδίο

σημαντικών ερευνητικών προβλημάτων που αφορούν διαφορετικούς επιστημονικούς κλάδους. Ενδεικτικά αναφέρονται η χρήση των ραδιοϊχνηθετών (^{137}Cs, ^{210}Pb) στον προσδιορισμό ρυθμού ιζηματογένεσης (Γεωφυσικές εφαρμογές), η χρήση ραδιονουκλιδίων (θυγατρικά του ραδονίου ^{222}Rn) στον προσδιορισμό υποθαλάσσιων πηγών γλυκού νερού (Υδρογεωλογία) και στον εντοπισμό υποθαλάσσιων ηφαιστείων (Ωκεανογραφία).

Το μεγάλο ενδιαφέρον που υπάρχει γύρω από μετρήσεις ραδιενέργειας στο θαλάσσιο περιβάλλον αναδεικνύει την ανάγκη ανάπτυξης μιας μεθόδου που να παρέχει τη δυνατότητα της χαρτογράφησης μεγάλων περιοχών σε μικρό χρονικό διάστημα. Η παραδοσιακή εργαστηριακή ανάλυση είναι μια μέθοδος χρονοβόρα και απαιτεί ειδικές εγκαταστάσεις και τεχνογνωσία για την επεξεργασία των δειγμάτων και την εξαγωγή των τελικών αποτελεσμάτων. Για το λόγο αυτό, τα τελευταία χρόνια παρατηρείται αύξηση του ενδιαφέροντος για την ανάπτυξη ανιχνευτικών συστημάτων για μετρήσεις ραδιενέργειας, μέσω της *in situ* φασματοσκοπίας ακτίνων-γ στο θαλάσσιο περιβάλλον. Χαρακτηριστικό παράδειγμα αποτελεί η εφαρμογή της για μετρήσεις των επιπέδων ραδιενέργειας σε επιβαρυμένες βιομηχανικές περιοχές με στόχο τον χαρακτηρισμό τους πριν αλλά και μετά την αποκατάσταση της περιοχής (remediation). Η *in situ* μέθοδος επιλέγεται λόγω των πλεονεκτημάτων της, τα οποία συνοψίζονται ως εξής:

1. Η άμεση ανάκτηση των αποτελεσμάτων και η δυνατότητα συνεχούς καταγραφής και παρακολούθησης συγκεντρώσεων ραδιονουκλιδίων σε επιβαρυμένες περιοχές (π.χ. πυρηνικά εργοστάσια).
2. Η μείωση του απαραίτητου χρόνου μέτρησης, σε σχέση με την χρονοβόρα εργαστηριακή μέθοδο, που επιτρέπει τη χαρτογράφηση μεγάλων περιοχών σε συγκριτικά μικρό χρονικό διάστημα. Το πλεονέκτημα αυτό βρίσκει άμεση εφαρμογή στην αποκατάσταση επιβαρυμένων βιομηχανικών περιοχών (remediation).
3. Ο γρήγορος εντοπισμός επιβαρυμένων σημείων (π.χ. εντοπισμός 'θαμμένων' πυρηνικών αποβλήτων) σε μια περιοχή, έναντι των ευρέως χρησιμοποιούμενων εργαστηριακών τεχνικών.

Η ραγδαία ανάπτυξη ανιχνευτικών συστημάτων για επιτόπιες (*in situ*) μετρήσεις στο πεδίο έχει οδηγήσει στην αύξηση των εφαρμογών της *in situ* φασματοσκοπίας ακτίνων-γ σε διαφορετικούς επιστημονικούς τομείς (Ωκεανογραφία, Γεωλογία, Υδρογεωλογία, Ακτινοπροστασία), επισημαίνοντας τη σπουδαιότητα της μεθόδου ως ένα χρήσιμο επιστημονικό εργαλείο.

Για την ποσοτικοποίηση των αποτελεσμάτων είναι απαραίτητος ο προσδιορισμός της ανιχνευτικής απόδοσης (βαθμονόμηση), του συστήματος που χρησιμοποιείται στην λήψη

φασμάτων για τη συγκεκριμένη μέτρηση. Η συνήθης διαδικασία της βαθμονόμησης περιλαμβάνει τη λήψη δεδομένων (φάσματα) από πηγές γνωστής συγκέντρωσης ραδιονουκλιδίων (πηγή αναφοράς) ίδιων χαρακτηριστικών (γεωμετρία, πυκνότητα, υλικά). Δεδομένου όμως ότι οι μετρήσεις πραγματοποιούνται στο θαλάσσιο περιβάλλον, η επιλογή αυτή θα απαιτούσε την κατασκευή βαθμονομημένης πηγής μεγάλου όγκου και άρα καθίσταται ιδιαίτερα δαπανηρή, περιπλέκεται επιπλέον από το γεγονός ότι οι μετρήσεις γίνονται στο νερό και η εξομοίωση των συνθηκών αυτών είναι δύσκολο να πραγματοποιηθεί στο εργαστήριο, ενώ εμπλέκει και πρότυπα που αφορούν στον κανονισμό ακτινοπροστασίας (πρότυπα ασφαλείας στη μεταφορά ραδιενεργών πηγών, πρότυπα διαχείρισης ραδιενεργών αποβλήτων).

Παρά λοιπόν τα ξεκάθαρα πλεονεκτήματα της *in situ* μεθόδου, η γενικευμένη εφαρμογή της περιορίζεται κυρίως από τη δυσκολία εύρεσης αξιόπιστης μεθόδου για τον προσδιορισμό της απόδοσης ενός ανιχνευτή για *in situ* μετρήσεις στο θαλάσσιο περιβάλλον, ενώ ειδικά για μετρήσεις στο θαλάσσιο ίζημα η εφαρμογή της μεθόδου είναι ακόμη πιο περιορισμένη, λόγω της μεγάλης βιβλιογραφικής έλλειψης αξιόπιστων και ολοκληρωμένων δεδομένων της επίδρασης στην απόδοση του ανιχνευτή των φυσικοχημικών χαρακτηριστικών του ιζήματος, τα οποία διαφέρουν σε κάθε περιοχή.

Ο κύριος στόχος της παρούσας διατριβής είναι η ανάπτυξη μιας μεθοδολογίας για ποσοτικές *in situ* μετρήσεις στον πυθμένα της θάλασσας, η οποία δύναται να παρέχει ακριβή αποτελέσματα όταν εφαρμόζεται σε διαφορετικά περιβάλλοντα. Ένα σημαντικό μέρος της δουλειάς επικεντρώνεται στην κατανόηση των προβλημάτων που σχετίζονται με τις *in situ* μετρήσεις στον πυθμένα της θάλασσας, όπου τα διαθέσιμα δεδομένα είναι αραιά και η ανάλυση παρεμποδίζεται από αρκετές πρόσθετες παραμέτρους (σε σύγκριση με *in situ* μετρήσεις στο υδάτινο περιβάλλον), που σχετίζονται κυρίως με τις φυσικές ιδιότητες του ιζήματος και τη γεωμορφολογία του περιβάλλοντος. Ως εκ τούτου, μια μεγάλη προσπάθεια δίνεται για τη διερεύνηση πειραματικά και θεωρητικά των παραμέτρων που οδηγούν σε αλλαγές της απόδοσης του ανιχνευτή, και προκύπτουν από τη μορφολογία του υπό μελέτη περιβάλλοντος, ή από διαφοροποιήσεις της γεωμετρίας μέτρησης. Αυτό επιτεύχθηκε μέσω προσομοιώσεων Monte Carlo (MC), εκτελώντας θεωρητικούς υπολογισμούς της απόδοσης του ανιχνευτικού συστήματος στην υπό μελέτη γεωμετρία, συμπεριλαμβάνοντας στην ρποσομοίωση λεπτομερείς πληροφορίες των φυσικών ιδιοτήτων των ιζημάτων. Επιπλέον, διεξήχθησαν συγκρίσεις με αντίστοιχα πειραματικά αποτελέσματα, σε τέσσερα διαφορετικά περιβάλλοντα, για να αξιολογηθούν οι θεωρητικοί υπολογισμοί και να επεκταθούν στο ενεργειακό εύρος ενδιαφέροντος.

2. Θεωρητικό υπόβαθρο

Ανίχνευση ακτινοβολίας-γ

Η πιο συνηθισμένη μέθοδος για μετρήσεις ραδιενέργειας στο περιβάλλον είναι η μέθοδος της φασματοσκοπίας ακτίνων-γ. Η φασματοσκοπία ακτίνων-γ στηρίζεται στην ανίχνευση των γεγονότων που εκπέμπονται από την πηγή, μέσω της αλληλεπίδρασης των ακτίνων-γ με το υλικό του ανιχνευτή, καθώς και στην αντιστοίχηση των αιχμών του φάσματος (φωτοκορυφές) με συγκεκριμένα ραδιονουκλίδια, με τελικό σκοπό την εύρεση των συγκεντρώσεων αυτών. Τεχνικές έχουν αναπτυχθεί τόσο για μετρήσεις φασματοσκοπίας-γ *in situ* αλλά πολύ περισσότερη πληροφορία βρίσκεται στη βιβλιογραφία που αφορά σε τεχνικές δειγματοληψίας και μέτρησης των δειγμάτων στο εργαστήριο.

Μετρήσεις φασματοσκοπίας ακτίνων-γ στο εργαστήριο

Η παραδοσιακή εργαστηριακή ανάλυση είναι μια μέθοδος χρονοβόρα και απαιτεί ειδικές εγκαταστάσεις και τεχνογνωσία για την επεξεργασία των δειγμάτων και την εξαγωγή των τελικών αποτελεσμάτων. Για τη λήψη των δειγμάτων χρησιμοποιείται βαρύς εξοπλισμός, ενώ πολλές φορές απαιτείται και η βοήθεια εξειδικευμένου προσωπικού (δύτες). Τα δείγματα μεταφέρονται στο εργαστήριο για μετρήσεις. Οι διεργασίες επεξεργασίας τους που απαιτούνται για τη μέτρηση φασματοσκοπίας-γ, είναι περίπλοκες ενώ ο χρόνος που μεσολαβεί μέχρι τη μέτρηση ξεπερνά τις τρεις εβδομάδες. Η μέτρηση φασματοσκοπίας-γ πραγματοποιείται συνήθως με χρήση ανιχνευτών υψηλής διακριτικής ικανότητας (HPGe). Οι ανιχνευτικές διατάξεις φασματοσκοπίας-γ που χρησιμοποιήθηκαν στην παρούσα διατριβή φαίνονται στο Σχήμα 2.1 ενώ στο Σχήμα 2.2 δίνονται μετρήσεις ραδιενέργειας υποβάθρου χρησιμοποιώντας τα δύο αυτά συστήματα. Τα δύο συστήματα είναι ήδη βαθμονομημένα ως προς την ανιχνευτική τους απόδοση για μετρήσεις σε δείγματα ιζημάτων σε διαφορετικές γεωμετρίες όπως φαίνεται στο Σχήμα 2.3.

Σχήμα 2.1: Η ανιχνευτική διάταξη μέτρησης δειγμάτων ιζήματος στο ΕΛ.ΚΕ.Θ.Ε. (πάνω) και στο Ε.Μ.Π (κάτω).

Το πρώτο βήμα που απαιτείται ώστε να είναι εφικτή η ποσοτική μέτρηση των ραδιονουκλιδίων είναι η βαθμονόμηση του συστήματος ως προς την ανιχνευτική του απόδοση. Οι διαδικασίες που υλοποιούνται για την εύρεση της ανιχνευτικής απόδοσης, αφορούν στην εύρεση της απόλυτης απόδοσης φωτοκορυφής (absolute full-energy peak efficiency) ε, στις χαρακτηριστικές ενέργειες ακτίνων-γ του ανιχνευόμενου ραδιονουκλιδίου για τον προσδιορισμό της ενεργότητάς του, A (μετρημένη σε Bq/kg ή Bq/L). Η ανιχνευτική απόδοση εξαρτάται από τις φυσικές ιδιότητες και τα γεωμετρικά χαρακτηριστικά του ανιχνευτή αλλά και της πηγής, είναι δηλαδή συγκεκριμένη για κάθε δεδομένη μέτρηση. Επιπλέον, εφόσον ενδιαφέρει η ανίχνευση πληθώρας φυσικών και τεχνητών ραδιονουκλιδίων, η ανιχνευτική απόδοση ε χρειάζεται να προσδιοριστεί σε κάθε κορυφή του φάσματος, σε μια ευρεία περιοχή ενεργειών μεταξύ 40 – 3000 keV.

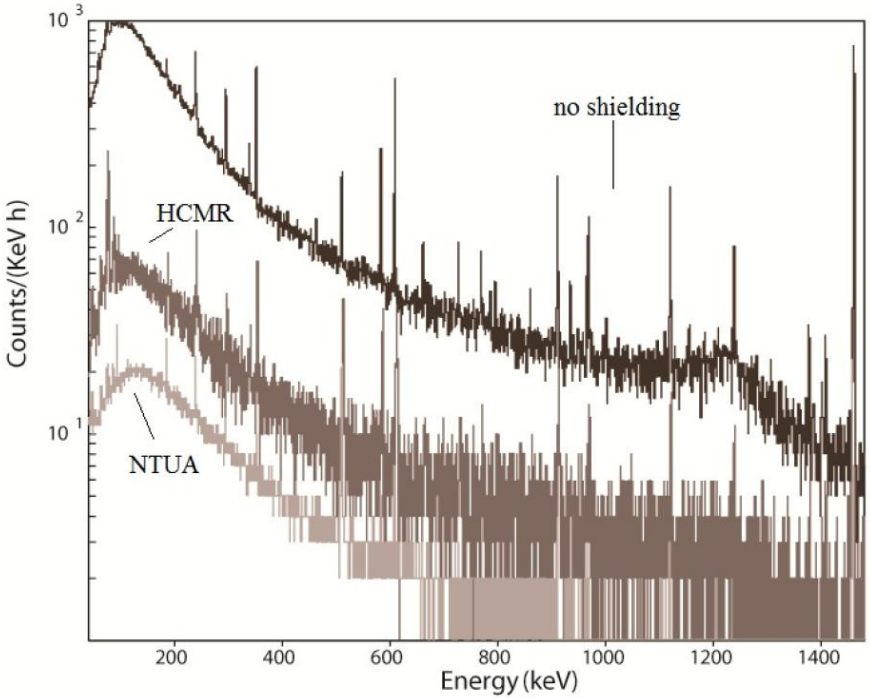

Σχήμα 2.2: Μετρήσεις ραδιενέργειας υποβάθρου χρησιμοποιώντας κατάλληλη θωράκιση στους δύο ανιχνευτές Γερμανίου (GEM-FX8530P4) στο εργαστήριο Ραδιενέργειας Περιβάλλοντος του ΕΛ.ΚΕ.Θ.Ε. και Πυρηνικής Φυσικής στον Τομέα Φυσικής του Ε.Μ.Π . και η ίδια μέτρηση χωρίς θωράκιση (Elef_15).

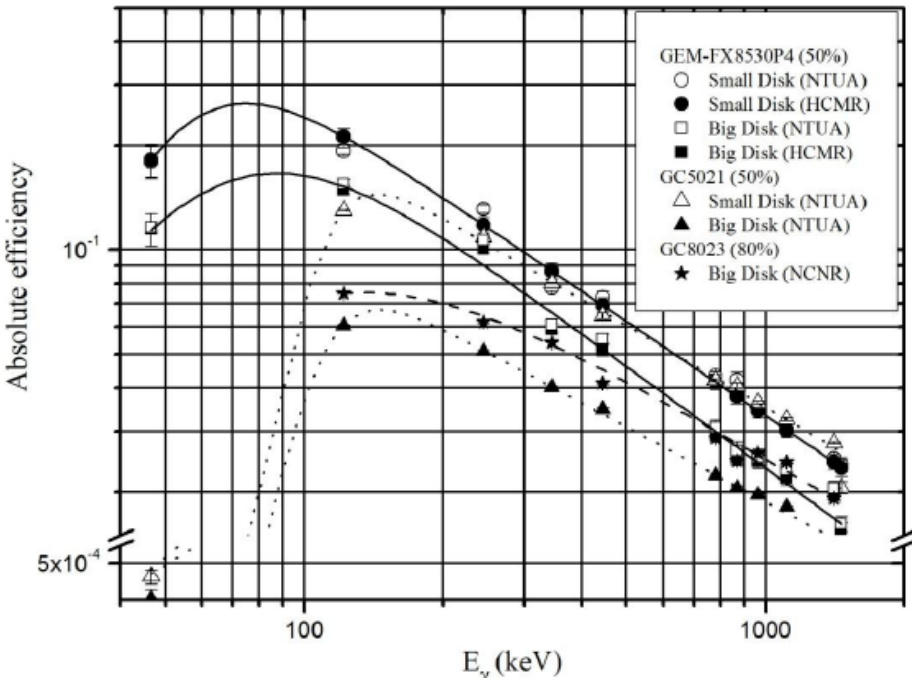

Σχήμα 2.3: Βαθμονόμηση των ανιχνευτικών συστημάτων στο ΕΛΚΕΘΕ (GEM-FX8530P4) και στο ΕΜΠ (GC5021, GEM-FX8530P4) για μετρήσεις ιζημάτων σε διαφορετικές γεωμετρίες (Elef_15).

Η πιο ευρέως διαδεδομένη μέθοδος προσδιορισμού της απόδοσης ανιχνευτή είναι η βαθμονόμηση λαμβάνοντας δεδομένα (φάσμα) από πηγές γνωστής συγκέντρωσης ραδιονουκλιδίων (πηγή αναφοράς) ίδιων χαρακτηριστικών (γεωμετρία, πυκνότητα, υλικά, ενεργειακό εύρος εκπεμπόμενων ακτίνων-γ) με το άγνωστο δείγμα και πραγματοποιείται συνήθως στο εργαστήριο. Ένας τρόπος να επιτευχθεί αυτό είναι η μέτρηση πηγής αναφοράς (π.χ. ^{152}Eu) εκτεταμένου όγκου σύμφωνα με την επιθυμητή στερεά γωνία μέτρησης (Ω). Χρησιμοποιώντας την τιμή της ενεργότητας της πηγής A (μετρημένη σε Bq/L ή Bq/kg) ως τιμή αναφοράς, η ανιχνευτική απόδοση ε (Ω, E_γ) του συστήματος σε μία φωτοκορυφή ενέργειας ακτίνων-γ (E_γ) με πιθανότητα εκπομπής (I_γ), υπολογίζεται σύμφωνα με την παρακάτω σχέση (1):

$$\varepsilon\left(\Omega, E_\gamma\right) = \frac{cps_{net} \quad (\Omega, E_\gamma)}{I_\gamma\,(E_\gamma)\cdot A} \tag{1}$$

Όπου η ποσότητα cps_{net} αναφέρεται στον συνολικό καθαρό (net) ρυθμό γεγονότων που ανιχνεύονται στη εν λόγω φωτοκορυφή και προκύπτει από την ανάλυση του φάσματος βαθμονόμησης.

***In situ* μετρήσεις φασματοσκοπίας ακτίνων-γ**

Το ανιχνευτικό σύστημα ΚΑΤΕΡΙΝΑ (Σχήμα 2.4) χρησιμοποιείται για *in situ* μετρήσεις ραδιενέργειας στο υδάτινο περιβάλλον και αποτελεί πρωτότυπο σύστημα ανίχνευσης ακτίνων-γ που αναπτύχθηκε στο ΕΛ.ΚΕ.Θ.Ε (Tsab_08), με σκοπό τη μέτρηση ραδιονουκλιδίων (φυσικών και τεχνητών) χαμηλής συγκέντρωσης στο θαλάσσιο περιβάλλον, σε εφαρμογές ωκεανογραφίας και ραδιοπροστασίας.

Το σύστημα αποτελείται από έναν 3' x 3' κρύσταλλο NaI(Tl), που συνδέεται με ένα φωτοπολλαπλασιαστή (PMT), με προενισχυτή (PRE) και παροχή ηλεκτρικού ρεύματος, μαζί με τα κατάλληλα ηλεκτρονικά για την ενίσχυση των σημάτων και την αποθήκευση δεδομένων. Η έξοδος του προενισχυτή συνδέεται με ενισχυτή (AMP) διαμόρφωσης σήματος ειδικά σχεδιασμένο για υποβρύχιες εφαρμογές. Το σήμα εξόδου του ενισχυτή εισάγεται σε πολυδιαυλικό αναλυτή (MCA) και στη συνέχεια, αφού το σήμα μετατραπεί σε ψηφιακό με κατάλληλο μετατροπέα (ADC), αποθηκεύεται σε ειδική μνήμη ενσωματωμένη στο σύστημα, ώστε να λειτουργεί αυτόνομα (χωρίς τη βοήθεια υπολογιστή).

The specifications of the detection system "KATERINA"

Sensor type	3″ × 3″ NaI(Tl)
Energy range	Adjustable maximum and minimum energy of detection (with maximum value of 3000 keV)
ADC	Successive approximation 10 bit
High voltage	Internally controlled 100–1200 V
Spectroscopy	Adjustable 256, 512 or 1024 channels
Gain amplification, pole-zero cancellation, base-line restoration	Internally controlled and adjustable
Dead time	<0.5% in aquatic operation mode
Energy resolution (140.5 keV)	10%
Energy resolution (661.6 keV)	6.5%
Operating temperature	−5 °C to +50 °C
Consumption	1.2–1.4 W
Preset time	Gross γ and γ-spectrometry
Output	Time, date, cps, spectrum, dead time.
RS232 settings	Baud rate adjustable, parity "space", flow control "none"
Enclosure	Shape "Cylinder", material "Acetal"

Σχήμα 2.4: Το ανιχνευτικό σύστημα ΚΑΤΕΡΙΝΑ.

Το περίβλημα που χρησιμοποιείται για την στεγανότητα του συστήματος αποτελείται από Ακετάλη ($C_7H_{14}O_2$). Το πολυμερές κυλινδρικού σχήματος ακτίνας 7.8 cm περιβάλλει τον κρύσταλλο, ενώ ανάμεσα στο πολυμερές και στον κρύσταλλο υπάρχει κενός χώρος (αέρας) 1.8 mm. Η επιλογή του υλικού του περιβλήματος έγινε λόγω των χαρακτηριστικών του που επιτρέπουν την ελαχιστοποίηση της απορρόφησης των ακτίνων-γ στο υλικό του περιβλήματος καθώς και λόγω της ανοχής του στις πιέσεις που δημιουργούνται σε μεγάλα βάθη. Το σύστημα δύναται να φτάσει έως και σε βάθος 400 m στη θάλασσα (ονομαστικό βάθος). Οι παράμετροι των διατάξεων στο εσωτερικό του κυλίνδρου (διάμετρος, πάχος, υλικό, ανθεκτικότητα, μέγιστη απόκλιση, κλπ.) υπολογίστηκαν σύμφωνα με το πρόγραμμα Seal Design (Apple Rubber Products Inc.), για βέλτιστη απόδοση και στεγανοποίηση (Tsab_04). Τα ηλεκτρονικά είναι κατάλληλα σχεδιασμένα ώστε να μπορούν να εγκατασταθούν μέσα στο προστατευτικό περίβλημα διαστάσεων 85 mm × 550 mm και ώστε η κατανάλωση ισχύος να είναι μικρή (~1.2-1.4 W).

Το σύστημα έχει βαθμονομηθεί ως προς την ενέργεια (energy calibration), την ενεργειακή του διακριτική ικανότητα (FWHM calibration) και την ανιχνευτική του απόδοση (full energy peak efficiency) για μετρήσεις στον αέρα στο εργαστήριο με χρήση σημειακών πηγών σε απόσταση 13.1 cm, που καλύπτουν το ενεργειακό φάσμα λειτουργίας του συστήματος (Tsab_08). Το σύστημα είναι βαθμονομημένο επίσης και για μετρήσεις στο

υδάτινο περιβάλλον (Bag_10). Το ανιχνευτικό σύστημα ΚΑΤΕΡΙΝΑ έχει χρησιμοποιηθεί επιτυχώς για μετρήσεις ραδιενέργειας στο θαλάσσιο περιβάλλον σε διάφορες εφαρμογές, ενδεικτικά αναφέρονται: Η παρακολούθηση, μέσω της συνεχούς καταγραφής, των συγκεντρώσεων των θυγατρικών ραδιονουκλιδίων του Ραδονίου, ^{222}Rn, σε υπόγεια νερά, για την παρακολούθηση των μεταβολών στις συγκεντρώσεις των ραδιονουκλιδίων αυτών και τη συσχέτιση τους με φαινόμενα μικροσεισμικότητας (Tsab_11). Η παρακολούθηση των θυγατρικών ραδιονουκλιδίων του Ραδονίου, ^{222}Rn, σε υποθαλάσσιες εκροές υπογείων υδάτων, στη Μεσόγειο (Χαλκίδα, Στούπα, Κόρφος, Cabbe) με σκοπό τον έλεγχο της ποιότητας (εύρεση επιπέδων ραδιενέργειας, ποσοτικοποίηση γλυκού νερού) της υποθαλάσσιας πηγής (Tsab_10).

Το σύστημα δεν είναι βαθμονομημένο για μετρήσεις στο θαλάσσιο ίζημα. Η ποσοτικοποίηση των *in situ* μετρήσεων σε πυθμένες θαλασσών (ίζημα), προϋποθέτει τον πειραματικό προσδιορισμό της απόδοσης του ανιχνευτή. Η εξομοίωση όμως των συνθηκών της *in situ* μέτρησης στο εργαστήριο παρουσιάζει σημαντικές δυσκολίες που συνοψίζονται παρακάτω:

1. Λόγω της σχετικά μεγάλης διεισδυτικότητας των ακτίνων-γ, κατά τις μετρήσεις στο θαλάσσιο περιβάλλον καταγράφονται γεγονότα από αποστάσεις έως και 1.6 m μακριά από τον ανιχνευτή, η καταγεγραμμένη πληροφορία δηλαδή προέρχεται από ένα μεγάλο όγκο στο υπό μελέτη περιβάλλον (πηγή). Η διαδικασία αυτή, για τους σκοπούς της εργασίας, θα απαιτούσε την κατασκευή βαθμονομημένης πηγής ιζήματος και υπερκείμενου νερού μεγάλου όγκου. Η επιλογή όμως αυτή καθίσταται ιδιαίτερα πολύπλοκη και δαπανηρή ενώ εμπλέκει και πρότυπα που αφορούν στον κανονισμό ακτινοπροστασίας (πρότυπα ασφαλείας στη μεταφορά ραδιενεργών πηγών, πρότυπα διαχείρισης ραδιενεργών αποβλήτων).

2. Πέραν των μεγάλων διαστάσεων της πηγής, η ύπαρξη δύο διαφορετικών μέσων (νερό, ίζημα) με τα οποία οι ακτίνες-γ αλληλεπιδρούν πριν ανιχνευτούν, περιπλέκει ακόμη περισσότερο την αναπαραγωγή των πραγματικών συνθηκών μέτρησης στο εργαστήριο.

3. Τα χαρακτηριστικά των θαλάσσιων πυθμένων (σύσταση, πυκνότητα, πορώδες) παρουσιάζουν μεγάλη ποικιλομορφία, και οδηγούν στην ανάγκη δημιουργίας και χρήσης πολυάριθμων πρότυπων πηγών που να περικλείουν τα χαρακτηριστικά αυτά, καθιστώντας έτσι πρακτικά αδύνατη την παρασκευή τους (σε συνδυασμό με την ανάγκη μεγάλου όγκου πηγών) και τη μέτρηση στο εργαστήριο.

Για τους λόγους αυτούς τα αποτελέσματα που λήφθηκαν στα πλαίσια της παρούσας διατριβής στηρίζονται κατά κύριο λόγο σε θεωρητικούς υπολογισμούς, κάνοντας χρήση της

μεθόδου προσομοίωσης μέσω Monte Carlo υπολογιστικών κωδίκων. Η αξιολόγηση όμως των θεωρητικών αποτελεσμάτων μέσω αντίστοιχων πειραματικών δεδομένων (validation) κρίνεται επίσης απαραίτητη. Για το σκοπό αυτό πραγματοποιήθηκαν αντίστοιχες πειραματικές μετρήσεις στο εργαστήριο αλλά και στο πεδίο, όπως συζητούνται αναλυτικά στην ενότητα 5.

3. Monte Carlo προσομοίωση

Η τεχνική Monte Carlo είναι μια στατιστική μέθοδος που χρησιμοποιεί ακολουθίες τυχαίων αριθμών για να προσομοιώσει τα πιθανά γεγονότα μιας διαδικασίας. Η αλληλεπίδραση της ακτινοβολίας-γ με την ύλη είναι μια στατιστική διαδικασία και η προσομοίωσή της με την τεχνική αυτή είναι εφικτή. Κάθε γεγονός θεωρείται ως μια ξεχωριστή ιστορία που παρακολουθείται σε κάθε στάδιο της πορείας του ως την πλήρη απορρόφησή του. Η πορεία της κάθε ιστορίας καθορίζεται από κατανομές πιθανότητας που επιλέγονται με τυχαίο τρόπο χρησιμοποιώντας δεδομένα που λαμβάνονται από βιβλιοθήκες. Το πιο κρίσιμο βήμα στους υπολογισμούς αυτούς αποτελεί η λεπτομερής περιγραφή στον κώδικα α) των παραμέτρων της πραγματικής μέτρησης που επηρεάζουν το αποτέλεσμα (απόδοση του ανιχνευτή), και β) της υποκείμενης φυσικής του προβλήματος. Η τελευταία απαίτηση είναι το κύριο κριτήριο στην επιλογή του κατάλληλου κώδικα Monte Carlo καθώς υπάρχουν πολλοί αξιόπιστοι κώδικες με διαφορετική όμως εξειδικευμένη χρήση. Η μέθοδος προσομοίωσης με τη χρήση υπολογιστικών κωδίκων (γενικοί και εξειδικευμένοι κώδικες) αποτελεί μια γρήγορη και ευέλικτη μέθοδο που παρέχει αξιόπιστα αποτελέσματα.

Η επιλογή του κατάλληλου κώδικα MC βασίζεται στον στόχο της εκάστοτε εφαρμογής, καθώς κάθε κώδικας MC παρέχει διαφορετικές δυνατότητες στους τελικούς χρήστες. Στην παρούσα εργασία οι κωδικοί MCNP5, MCNP-CP και FLUKA χρησιμοποιήθηκαν για την εκτίμηση της απόδοσης φωτοκορυφής του συστήματος ΚΑΤΕΡΙΝΑ στο θαλάσσιο περιβάλλον.

Ο κώδικας MCNP5 μεταφοράς νετρονίων και φωτονίων χρησιμοποιείται για τη διάδοση-μεταφορά νετρονίων, ηλεκτρονίων, φωτονίων ή τη μεταφορά συνδυασμένων

φωτονίων/ νετρονίων /ηλεκτρονίων. Τα πλεονεκτήματά του έναντι άλλων διαθέσιμων κωδίκων είναι η δυνατότητα δημιουργίας περίπλοκης γεωμετρίας αποτελούμενης από πολλά γεωμετρικά στοιχεία όπως συναντάται συνήθως σε ένα πραγματικό πείραμα, η ευκολία στη χρήση του με την παροχή έτοιμων συναρτήσεων υπολογισμού, και η ευρεία συλλογή βιβλιοθηκών με ενεργές διατομές και άλλα χρήσιμα δεδομένα. Ο κώδικας παρέχει τη δυνατότητα προσομοίωσης της μεταφοράς σωματιδίων με ενέργειες από 1 keV μέχρι 100 MeV σε υλικά των οποίων οι παράμετροι όπως επιφάνεια, γεωμετρική έκταση, πυκνότητα, θέση καθορίζονται από τον χρήστη. Έτσι ο χρήστης καθορίζει τα δεδομένα του προβλήματος καθώς και όλα τα στοιχεία της φυσικής που σχετίζονται με το εκάστοτε πρόβλημα. Στην περίπτωση που μελετάται η μεταφορά φωτονίων ο κώδικας λαμβάνει υπόψη τη σύμφωνη σκέδαση Rayleigh, τη σκέδαση Compton, τη φωτοηλεκτρική απορρόφηση και το φαινόμενο της δίδυμης γένεσης.

Ο κώδικας χρησιμοποιεί έτοιμες συναρτήσεις όπως είναι οι εικονικοί ανιχνευτές ύψους παλμών (F8 tally), μετρητές μήκους διαδρομής F6, F4 τους οποίους χρησιμοποιεί για να υπολογίσει την ποσότητα που ζητήθηκε από τον χρήστη πχ. ρεύμα σε μια επιφάνεια, ροή σωματιδίων αποτιθέμενη ενέργεια, επαγόμενη θερμότητα σε μια περιοχή και άλλα. Το αποτέλεσμα του MCNP5 συνοδεύεται από μια ποσότητα σ που αποτελεί το σχετικό σφάλμα της μέτρησης, δx/x, αφού το αποτέλεσμα υποβληθεί σε στατιστικούς ελέγχους. Η μείωση της ποσότητας σ επιτυγχάνεται με την αύξηση των γεγονότων N που δημιουργούνται και παρακολουθούνται στον κώδικα.

Ο κώδικας MCNP-CP αποτελεί μια αναβαθμισμένη έκδοση του κώδικα MCNP. Παρέχει στον χρήστη τη δυνατότητα περισσότερων υπολογισμών και χρησιμοποιεί επιπλέον βιβλιοθήκες που στοχεύουν στην αύξηση της αξιοπιστίας των υπολογισμών. Οι δύο κύριες προσθήκες του κώδικα αυτού όσον αφορά στην παρακολούθηση φωτονίων που χρησιμοποιήθηκαν στην παρούσα διατριβή είναι α) η δυνατότητα ταυτόχρονης παρακολούθησης περισσότερων του ενός σωματιδίου, και β) η λήψη δεδομένων αποδιέγερσης από κατάλληλες βιβλιοθήκες για την ταυτόχρονη αναπαραγωγή και παρακολούθηση όλων των ακτίνων-γ που εκπέμπονται από κάθε ραδιονουκλίδιο λαμβάνοντας υπόψη τις αντίστοιχες πιθανότητες αποδιέγερσης.

Ο κώδικας FLUKA παρέχει τις ίδιες δυνατότητες με τον κώδικα MCNP-CP στην παρακολούθηση φωτονίων και επιπλέον αποτελεί πολύτιμη εναλλακτική λύση για περιβαλλοντικές εφαρμογές, λόγω των ωφέλιμων χαρακτηριστικών του. Αυτά είναι α) η ικανότητα να ενσωματώνει στους υπολογισμούς εξωτερικές ρουτίνες (ρουτίνες που καθορίζονται από το χρήστη), β) το κέρδος σε υπολογιστικό χρόνο, τόσο στη σχεδίαση του

μοντέλου MC όσο και στην εκτέλεση των προσομοιώσεων, χρησιμοποιώντας το γραφικό περιβάλλον Flair, από το οποίο όλα τα βήματα της προσομοίωσης μπορούν να ελεγχθούν αποτελεσματικά, και γ) ο κώδικας FLUKA διανέμεται δωρεάν στην επιστημονική και ακαδημαϊκή κοινότητα.

Οι παραπάνω κώδικες MC εφαρμόστηκαν για την εκτίμηση της απόδοσης του συστήματος ΚΑΤΕΡΙΝΑ για μετρήσεις στο υδάτινο περιβάλλον και στο θαλάσσιο ίζημα. Η αξιοπιστία των θεωρητικών υπολογισμών εξαρτάται πρωταρχικά από την λεπτομερή περιγραφή στον κώδικα της πειραματικής μέτρησης. Για μετρήσεις στο θαλάσσιο περιβάλλον αυτό επιτυγχάνεται αναπαράγοντας με τον κώδικα την πειραματική μέτρηση περιγράφοντας λεπτομερώς όλες τις παραμέτρους που μπορεί να επηρεάζουν το θεωρητικό αποτέλεσμα (πηγή, ανιχνευτικό σύστημα, περιβάλλοντας χώρος). Η ολοκληρωμένη περιγραφή της πειραματικής μέτρησης περιλαμβάνει την εισαγωγή στον κώδικα των κύριων στοιχείων από τα οποία αποτελείται κάθε παράμετρος (επιφάνειες, γεωμετρική έκταση, πυκνότητα, σύσταση).

Με σκοπό την ανάπτυξη του μοντέλου ανιχνευτή για το σύστημα ΚΑΤΕΡΙΝΑ, εισάγονται στον κώδικα, ο κρύσταλλος NaI(Tl), ο ανακλαστήρας Al_2O_3, οι δυο μηχανισμοί στήριξης και προστασίας της διάταξης, το παράθυρο αλουμινίου Al γύρω από τον κρύσταλλο και το υλικό στεγανοποίησης (housing) από Ακετάλη $C_7H_{14}O_2$ (acetal). Τα μέρη της ανιχνευτικής διάταξης που αναπαραστάθηκαν στο MC μοντέλο, παρουσιάζονται στο Σχήμα 3.1 καθώς και οι διαστάσεις και οι πυκνότητες των επιμέρους στοιχείων. Για την αναπαραγωγή των υλικών και των διαστάσεων του συστήματος εισάγονται στον κώδικα τα στοιχεία όπως δίνονται από τον κατασκευαστή.

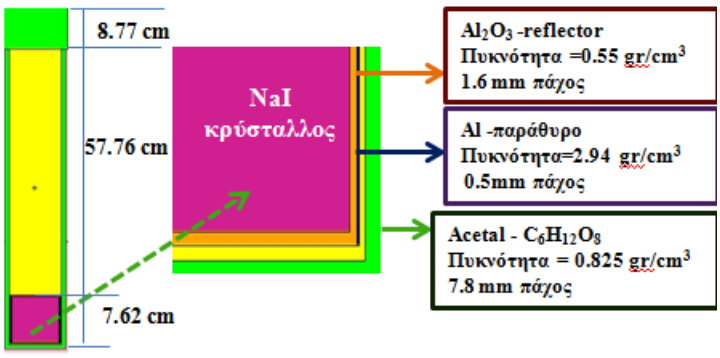

Σχήμα 3.1: Το μοντέλο του ανιχνευτικού συστήματος ΚΑΤΕΡΙΝΑ στον κώδικα MCNP5.

Η σωστή περιγραφή της πηγής έγκειται στην εύρεση της απόστασης από την οποία δύναται να φτάσουν στον ανιχνευτή γεγονότα. Η απόσταση που μπορεί να διανύσει μία ακτίνα-γ

ενέργειας E_γ μέσα στο ίζημα έως ότου απορροφηθεί πλήρως ονομάζεται ενεργός ακτίνα (effective radius x_{eff}) και καθορίζεται μέσω της σχέσης 2, συναρτήσει του ολικού γραμμικού συντελεστή εξασθένησης μ (Z,E) για ένα συγκεκριμένο υλικό :

$$x_{eff} = \ln(10000)/\mu = 9.21/\mu. \quad (2)$$

Έτσι για τον υπολογισμό της απόδοσης $\boldsymbol{\varepsilon_V}$ του *in situ* συστήματος σε μετρήσεις στο θαλάσσιο περιβάλλον, απαιτείται να μελετηθεί η ενδο-απορρόφηση της ακτινοβολίας-γ στο υλικό της πηγής (νερό, ίζημα) συναρτήσει του όγκου. Στον κώδικα δηλώνονται επίσης ως παράμετροι η ενέργεια του σωματιδίου και η χημική σύσταση του μέσου αλληλεπίδρασης. Για κάθε διαφορετική ενέργεια φωτονίου που μελετάται, γεννιούνται στον κώδικα MCNP5 γεγονότα σε τυχαίες θέσεις μέσα στον όγκο ο οποίος υπολογίζεται κατάλληλα, από τις τιμές συντελεστών εξασθένησης. Με αυτόν τον τρόπο υπολογίζεται θεωρητικά ο ενεργός όγκος ανίχνευσης δηλαδή, ο όγκος από τον οποίο εάν εκπεμφθούν ακτίνες-γ έχουν μη μηδενική πιθανότητα να αλληλεπιδράσουν με τον κρύσταλλο του ανιχνευτή προτού απορροφηθούν πλήρως. Εφόσον τα αρχικά φωτόνια παράγονται ισοτροπικά στον κώδικα μπορεί να υποτεθεί ότι η απόσταση αυτή θα είναι η ίδια σε όλες τις κατευθύνσεις (σφαιρική συμμετρία) για μια συγκεκριμένη ενέργεια φωτονίου, και θα αλλάζει μόνο με την ενέργεια και το μέσο διάδοσης λόγω των διαφορετικών αλληλεπιδράσεων που θα λαμβάνουν χώρα στα διάφορα μέσα μέχρι να απορροφηθεί. Για το λόγο αυτό η πηγή περιγράφεται στον κώδικα ως ένας σφαιρικός όγκος γύρω από τον ανιχνευτή στην προσομοίωση των μετρήσεων στο θαλασσινό νερό (Σχήμα 3.2), και ως ένας ημισφαιρικός όγκος σε επαφή με τον ανιχνευτή στην προσομοίωση των μετρήσεων στο ίζημα (Σχήμα 3.3). Η ενεργός ακτίνα, που ορίζεται ως η απόσταση από την οποία καταφθάνουν γεγονότα στον κρύσταλλο, προσδιορίζεται με τη βοήθεια του προγράμματος X-COM (Berg_10) που υπολογίζει τον ολικό μαζικό συντελεστή εξασθένησης (total mass attenuation coefficient) μ σε μονάδες cm^2/gr για τα χαρακτηριστικά της εκάστοτε πηγής.

Οι δύο κώδικες MCNP-CP και FLUKA χρησιμοποιήθηκαν για την εύρεση της απόδοσης του συστήματος ΚΑΤΕΡΙΝΑ για μετρήσεις στο υδάτινο περιβάλλον. Το μοντέλο προσομοίωσης που αναπτύχθηκε για τους υπολογισμούς περιλαμβάνει τον ανιχνευτή, μια σφαιρική πηγή γύρω από τον ανιχνευτή στην οποία δημιουργούνται τα προς παρακολούθηση σωματίδια καθώς και ένα πεπερασμένο γεωμετρικό χώρο έξω από τη σφαίρα αυτή, που καθορίζει χωρικά τα όρια της προσομοίωσης. Η σύγκριση των αποτελεσμάτων των δύο κωδίκων δίνεται στο Σχήμα 3.4 χρησιμοποιώντας πηγή ^{208}Tl, ^{214}Bi και ^{60}Co. Τα αναλυτικά αποτελέσματα παρουσιάζονται στον Πίνακα 3.1. Για την εκτίμηση

της απόδοσης του συστήματος ΚΑΤΕΡΙΝΑ σε μετρήσεις στο θαλάσσιο ίζημα χρησιμοποιήθηκε ο κώδικας MCNP5.

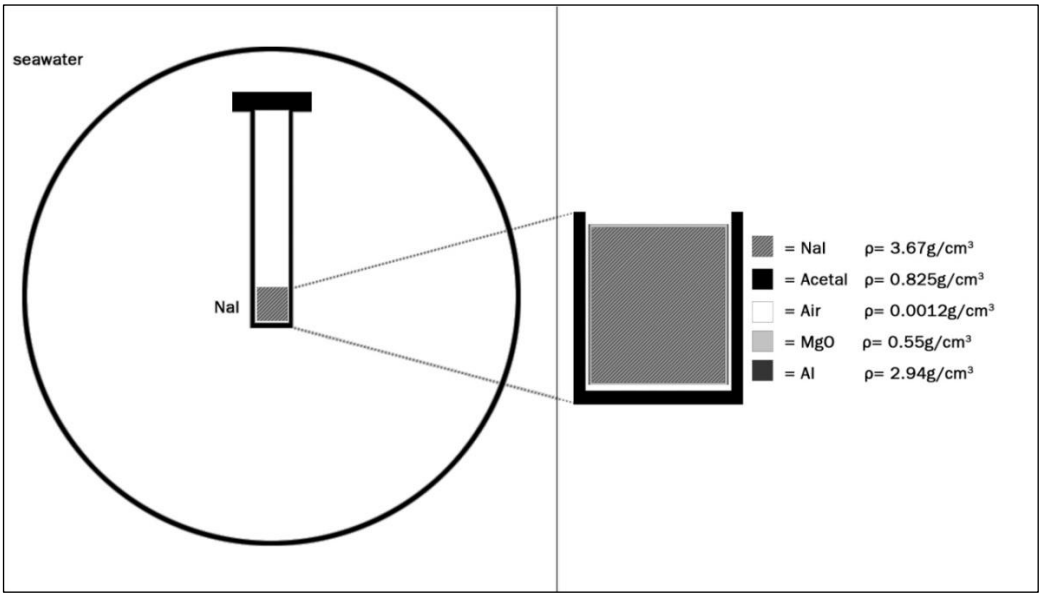

Σχήμα 3.2: Αναπαράσταση του μοντέλου προσομοίωσης για την εύρεση της απόδοσης του ανιχνευτικού συστήματος ΚΑΤΕΡΙΝΑ για μετρήσεις στο υδάτινο περιβάλλον.

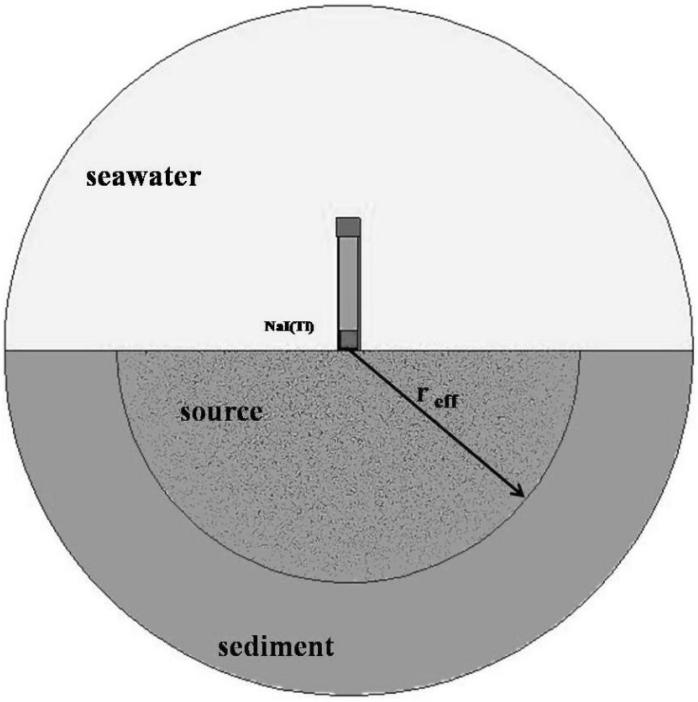

Σχήμα 3.3: Αναπαράσταση του μοντέλου προσομοίωσης για την εύρεση της απόδοσης του ανιχνευτικού συστήματος ΚΑΤΕΡΙΝΑ για μετρήσεις στο ίζημα.

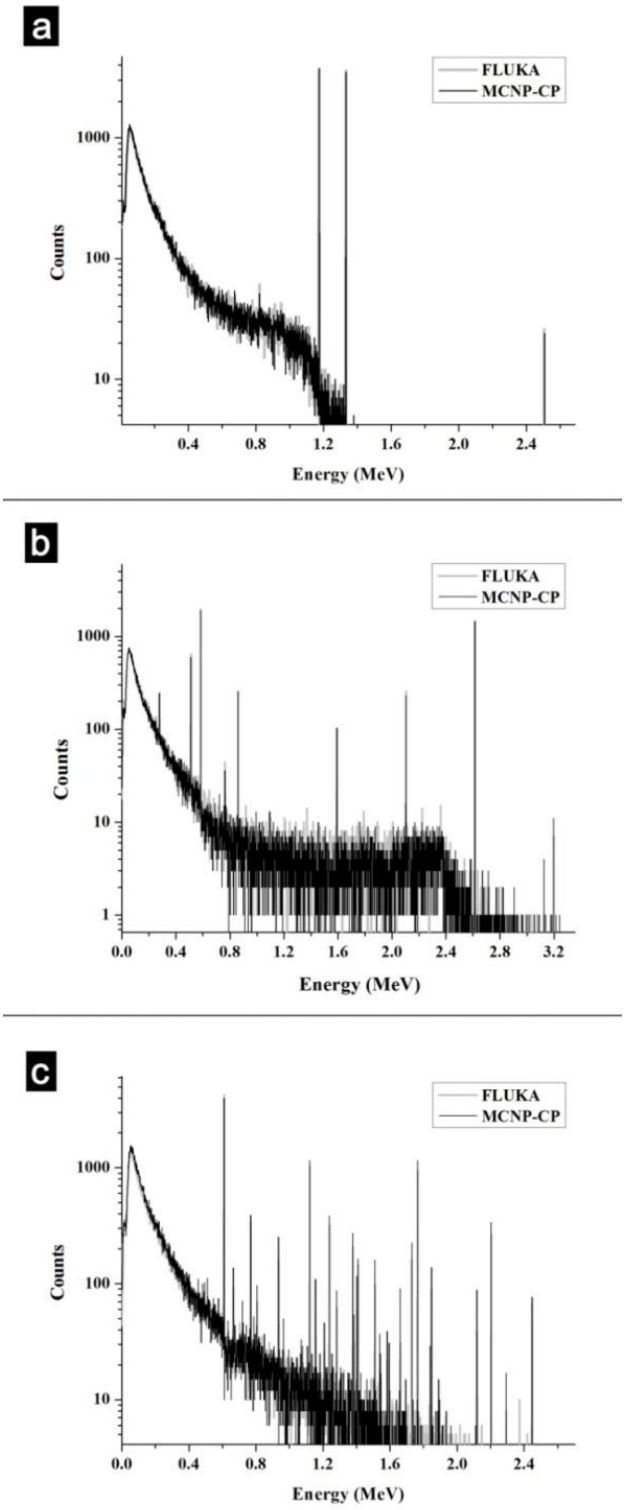

Σχήμα 3.4: Αναπαράσταση των αποτελεσμάτων των δύο κωδίκων FLUKA και MCNP-CP για μετρήσεις στο υδάτινο περιβάλλον χρησιμοποιώντας πηγές ^{60}Co (a.), ^{208}Tl (b.) και ^{214}Bi (c.)

Πίνακας 3.1: Σύγκριση των αποτελεσμάτων των γεγονότων (Counts) που καταγράφονται στις κύριες φωτοκορυφές των ^{60}Co , ^{208}Tl και ^{214}Bi για μετρήσεις στο υδάτινο περιβάλλον, όπως προέκυψαν χρησιμοποιώντας τους κώδικες FLUKA και MCNP-CP.

Πηγή	Ενέργεια keV	Ένταση I_γ%	Γεγονότα FLUKA	Γεγονότα MCNP-CP	R	
^{60}Co	1173.24	99.97	3744 (2)	3754 (2)	1.00	0.03
	1332.5	99.99	3638 (2)	3482 (2)	0.96	0.03
^{208}Tl	277.35	6.3	241 (7)	248 (6)	1.03	0.09
	510.77	22.6	644 (4)	600 (4)	0.93	0.05
	583.19	84.5	1963 (2)	1928 (2)	0.98	0.03
	763.13	1.8	44 (16)	36 (16)	0.82	0.18
	860.56	12.4	256 (6)	255 (6)	1.00	0.09
	2614.53	99.0	1434 (3)	1465 (3)	1.02	0.04
^{214}Bi	609.32	46.1	4243 (2)	3973 (2)	0.94	0.02
	768.36	4.94	337 (5)	390 (5)	1.16	0.06
	1120.29	15.1	1017 (3)	1155 (3)	1.14	0.05
	1238.11	5.79	317 (6)	384 (5)	1.21	0.09
	1764.49	15.4	916 (3)	882 (3)	0.96	0.04
	2204.21	5.08	255 (6)	233 (7)	0.91	0.06

Στις ενότητες που ακολουθούν περιγράφονται αναλυτικά, η εφαρμογή του μοντέλου για τη βαθμονόμηση του *in situ* συστήματος στο νερό, και η μεθοδολογία για την εφαρμογή του μοντέλου στην εκτίμηση της ε_V, που αφορά σε μετρήσεις ραδιενέργειας σε θαλάσσιο ίζημα.

4. Φασματοσκοπία-γ χρησιμοποιώντας την τεχνική Full Spectrum Analysis

Για την ανάλυση των φασμάτων, στην πράξη χρησιμοποιούνται δύο μέθοδοι: η ανάλυση φωτοκορυφών ή ενεργειακών παραθύρων (peak or window analysis) και η τεχνική Full Spectrum Analysis (FSA). Με την πρώτη μέθοδο προσδιορίζεται η συγκέντρωση των ραδιονουκλιδίων εκείνων που εμφανίζονται σε επιλεγμένα ενεργειακά παράθυρα γύρω από μεμονωμένες κορυφές. Στη δεύτερη μέθοδο το σχήμα καθώς και τα καταγεγραμμένα γεγονότα του συνολικού φάσματος λαμβάνονται υπόψη στην ανάλυση. Οι

δύο μέθοδοι διαφέρουν με την έννοια ότι με τη μέθοδο των windows μόνο μια περιοχή ενδιαφέροντος του φάσματος μελετάται. Συνήθως επιλέγονται τρεις περιοχές γύρω από τις πιο εξέχουσες κορυφές του φάσματος και αντιστοιχούν στα ραδιονουκλίδια ^{208}Tl, ^{40}K και ^{214}Bi. Αντίθετα, η τεχνική FSA καλύπτει σχεδόν πλήρως το ενεργειακό φάσμα. Επιπλέον, στην μέθοδο των windows, μόνο ο καθαρός αριθμός γεγονότων κάτω από τα επιλεγμένα παράθυρα συμμετέχει στην ανάλυση, ενώ με την τεχνική FSA περιλαμβάνονται στην ανάλυση του φάσματος όχι μόνο τα καταγεγραμμένα γεγονότα στις εμφανιζόμενες κορυφές αλλά ολόκληρη η μορφή με όλα τα χαρακτηριστικά του φάσματος και ο ολικός αριθμός καταγεγραμμένων γεγονότων.

Η πιο διαδεδομένη τεχνική για την ανάλυση των φασμάτων *in situ* μετρήσεων είναι η window analysis. Ωστόσο, υπάρχουν ορισμένα κρίσιμα μειονεκτήματα που σχετίζονται με αυτήν την τεχνική, και η ανάλυση παρεμποδίζεται από τρεις παράγοντες: α) την ύπαρξη αλληλεπικαλυπτόμενων κορυφών που αντιστοιχούν σε διαφορετικά ραδιονουκλίδια εντός των ενεργειακών παραθύρων (windows), β) την αξιοποίηση περιορισμένης μόνο φασματικής πληροφορίας και γ) τη συστηματική αβεβαιότητα που απορρέει από την αφαίρεση του υποβάθρου (Compton continuum). Το πιο σημαντικό μειονέκτημα είναι η αδυναμία της μεθόδου για την ανίχνευση/αναγνώριση απρόσμενων ραδιονουκλιδίων (Cac_12) που μπορεί να συμβάλουν στον μετρημένο αριθμό γεγονότων στο επιλεγμένο ενεργειακό παράθυρο και δεν συνυπολογίζονται στην ανάλυση. Κατά συνέπεια, αυτή η τεχνική αντικαταθίσταται σταδιακά από την ανταγωνιστική τεχνική FSA με την οποία πραγματοποιείται η πλήρης ανάλυση του φάσματος (FSA). Την τελευταία δεκαετία, υλοποιήθηκαν ευρέως τεχνικές βασισμένες στην FSA, για διαφορετικά ανιχνευτικά συστήματα και σε διαφορετικές εφαρμογές (Mahm_13; Cac_12; Graaf_11; Kovler_13; Mauč_04; Guil_01; Hendr_01; Minty_92).

Η FSA τεχνική βασίζεται στην παραγωγή πρότυπων φασμάτων για όλα τα ραδιονουκλίδια ενδιαφέροντος, που λαμβάνονται είτε πειραματικά, πραγματοποιώντας μετρήσεις βαθμονόμησης (Cac_12; Hendr_01), ή θεωρητικά, πραγματοποιώντας MC προσομοιώσεις (Graaf_11; Vlastou_06; Mauč_04), συμπεριλαμβάνοντας και στις δύο περιπτώσεις την ακριβή γεωμετρία και τα λεπτομερή χαρακτηριστικά της υπό μελέτης *in situ* μέτρησης. Η τεχνική βασίζεται στην προσαρμογή των πρότυπων φασμάτων, χρησιμοποιώντας κατάλληλες ελεύθερες παραμέτρους, στα πειραματικά δεδομένα και την ελαχιστοποίηση των διαφορών μεταξύ του θεωρητικού και του πειραματικού φάσματος μέσω του στατιστικού κριτηρίου χ^2. Η υπό μελέτη μέτρηση (πειραματικό φάσμα) αντιπροσωπεύεται από ένα γραμμικό συνδυασμό των πρότυπων φασμάτων όπου κάθε

πρότυπο φάσμα πολλαπλασιάζεται με τις διαθέσιμες ελεύθερες παραμέτρους που με την ολοκλήρωση της διαδικασίας λαμβάνουν κατάλληλες τιμές τέτοιες ώστε να μεγιστοποιείται η σύγκλιση μεταξύ των δύο φασμάτων, του θεωρητικού (FSA) και του πειραματικού (exp.). Οι βέλτιστες τιμές των ελεύθερων παραμέτρων λαμβάνονται χρησιμοποιώντας διαφορετικές αριθμητικές μεθόδους για την εκτέλεση της διαδικασίας ελαχιστοποίησης και την επίτευξη της σύγκλισης. Οι αντίστοιχες τιμές της συγκέντρωσης κάθε ραδιονουκλιδίου υπολογίζονται μετά από τις παραμέτρους αυτές.

Τα οφέλη από την εφαρμογή της τεχνικής FSA είναι α) η μείωση του χρόνου απόκτησης απαιτείται για την επίτευξη επαρκούς ακρίβειας (Hendr_01), β) η αξιοποίηση της πλήρης έκτασης του φάσματος που προσφέρει, τη δυνατότητα ποσοτικοποίησης περισσότερων ραδιονουκλιδίων και τη δυνατότητα της επαλήθευσης των αποτελεσμάτων από διάφορες κορυφές του ίδιου ραδιονουκλιδίου στο φάσμα, γ) ο εντοπισμός ανωμαλιών στο πειραματικό φάσμα (π.χ. αναγνώριση της παρουσίας επιπλέον ραδιονουκλιδίων που δεν συμπεριλήφθηκαν στην ανάλυση) και δ) η γρήγορη διεξαγωγή των μετρήσεων, που αποτελεί πλεονέκτημα εξέχουσας σημασίας ειδικά σε περιπτώσεις όπου άμεσες αποφάσεις πρέπει να ληφθούν (π.χ. πυρηνικά ατυχήματα).

Στα πλαίσια της παρούσας διατριβής αναπτύχθηκε μεθοδολογία ανάλυσης των φασμάτων που λαμβάνονται με την πόντιση του ανιχνευτικού συστήματος ΚΑΤΕΡΙΝΑ στο υδάτινο περιβάλλον, που βασίζεται στην τεχνική FSA. Οι κύριες διαφορές στην μεθοδολογία που αναπτύχθηκε σε σχέση με άλλες μεθοδολογίες που βασίζονται στην τεχνική FSA και έχουν χρησιμοποιηθεί στο παρελθόν είναι: α) η παραγωγή των πρότυπων φασμάτων χρησιμοποιώντας τον κώδικα MCNP-CP ο οποίος αναπαράγει αυτόματα όλες τις εκπεμπόμενες ακτίνες-γ από κάθε ραδιονουκλίδιο, σταθμισμένες ως προς την πιθανότητα εκπομπής τους, χρησιμοποιώντας τα αντίστοιχα δεδομένα από κατάλληλες βιβλιοθήκες και παρακολουθεί όλα τα γεγονότα έως την πλήρη απορρόφησή τους λαμβάνοντας επιπλέον υπόψη φαινόμενα πραγματικής σύμπτωσης (True Coincidence Summing), β) η ενσωμάτωση στον υπολογισμό των κυρίαρχων φυσικών ραδιονουκλιδίων που απαντώνται στο περιβάλλον (σύνολο 10 διαφορετικών ραδιονουκλιδίων από τη σειρά ^{238}U και ^{232}Th και το κυρίαρχο στο θαλάσσιο περιβάλλον ^{40}K), των οποίων οι συγκεντρώσεις θεωρούνται εντελώς ανεξάρτητες (δε λαμβάνεται υπόψη a priori η ύπαρξη ραδιενεργού ισορροπίας μεταξύ των ραδιονουκλιδίων της ίδιας σειράς) και γ) η διαδικασία της προσαρμογής του θεωρητικού φάσματος στα πειραματικά δεδομένα μέσω της ελαχιστοποίησης των μεταξύ τους διαφορών, γίνεται προοδευτικά σε διαφορετικά βήματα που καθορίζονται από τον χρήστη (επιλεγμένα ενεργειακά παράθυρα που καλύπτουν όλο το

ενεργειακό εύρος του πειραματικού φάσματος), με αποτέλεσμα τη μεγιστοποίηση της σύγκλισης μεταξύ των δύο φασμάτων ακόμη και σε περιοχές με χαμηλή στατιστική. Τα βήματα της μεθοδολογίας FSA που αναπτύχθηκε συνοψίζονται στο Σχήμα 4.1.

.

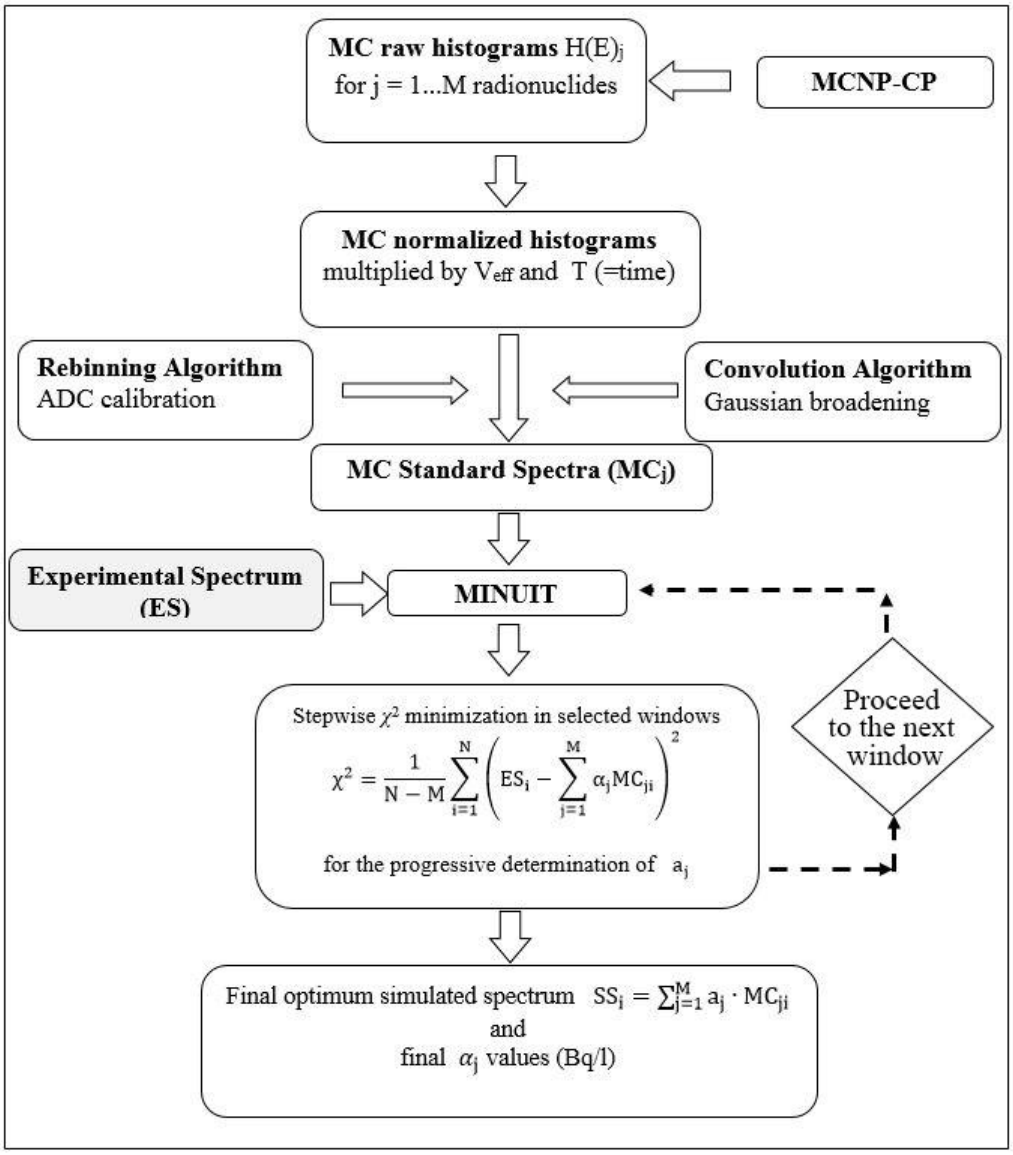

Σχήμα 4.1: Αναπαράσταση των βημάτων της τεχνικής FSA.

Τα θεωρητικά φάσματα που προκύπτουν από την εκτέλεση του κώδικα MCNP5 για κάθε ραδιονουκλίδιο, προσαρμόζονται στις ρυθμίσεις του πειραματικού φάσματος (χρόνος μέτρησης T, ενεργειακή βαθμονόμηση (Rebinning), βαθμονόμηση διακριτικής ικανότητας (Gaussian broad.)). Τα πρότυπα αυτά φάσματα εισάγονται μαζί με το αντίστοιχο πειραματικό στο πακέτο MINUIT όπου πραγματοποιείται η ελαχιστοποίηση των διαφορών μεταξύ του θεωρητικού και του πειραματικού φάσματος μέσω του στατιστικού κριτηρίου χ^2. Η ελαχιστοποίηση εκτελείται σε συγκεκριμένες ενεργειακές περιοχές του πειραματικού

φάσματος (windows) σε ξεχωριστά βήματα χρησιμοποιώντας μια επαναληπτική διαδικασία όπως περιγράφεται στο Σχήμα 4.1. Ο αριθμός των καναλιών του παραθύρου στο οποίο πραγματοποιείται κάθε φορά ο υπολογισμός, επιλέγεται από τον χρήστη. Σε κάθε βήμα (παράθυρο), προσδιορίζεται η συγκέντρωση a_j του αντίστοιχου ραδιονουκλιδίου. Στο Σχήμα 4.2 φαίνονται τα 10 πρότυπα φάσματα που χρησιμοποιήθηκαν στους υπολογισμούς και περιλαμβάνουν φάσματα πηγών φυσικών ραδιονουκλιδίων και συγκεκριμένα τα ^{214}Bi, ^{214}Pb, ^{234}Pa, ^{226}Ra και ^{222}Rn σειράς του ^{238}U, τα ^{208}Tl, ^{228}Ac, ^{212}Bi και ^{212}Pb της σειράς του ^{232}Th και το ^{40}K. Στο ίδιο σχήμα αποτυπώνονται και τα ενεργειακά παράθυρα που επιλέγονται για να γίνει η προσαρμογή χ^2 κατά την εκτέλεση του πακέτου MINUIT.

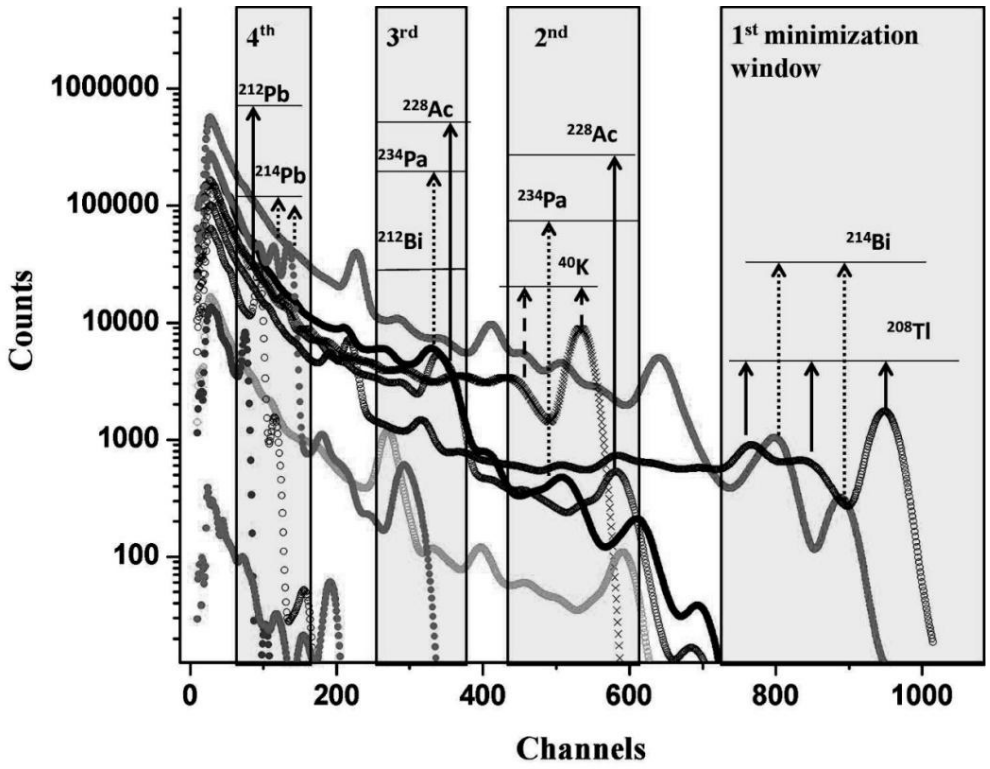

Σχήμα 4.2: Απεικόνιση των 10 θεωρητικών φασμάτων (1 Bq/L) που χρησιμοποιήθηκαν στην τεχνική FSA και των ενεργειακών παραθύρων στα οποία πραγματοποιείται η ελαχιστοποίηση των διαφορών μεταξύ του θεωρητικού και του πειραματικού φάσματος μέσω του στατιστικού κριτηρίου χ^2.

Στην προτεινόμενη μεθοδολογία, η διαδικασία ελαχιστοποίησης ξεκινά από τις κορυφές υψηλής ενέργειας του φάσματος και ολοκληρώνεται όταν και η τελευταία κορυφή του θεωρητικού φάσματος (δηλαδή, η αιχμή με τη χαμηλότερη ενέργεια) προσαρμοστεί στα πειραματικά δεδομένα.

Στο Σχήμα 4.3c παρουσιάζεται η εφαρμογή της τεχνικής, βήμα προς βήμα, στα επιλεγμένα

ενεργειακά παράθυρα για ένα τυπικό φάσμα στο θαλάσσιο περιβάλλον. Το σημείο εκκίνησης της διαδικασίας (δηλαδή το πρώτο ενεργειακό παράθυρο) βρίσκεται στην περιοχή του φάσματος υψηλών ενεργειών και επιλέγεται να είναι το διάστημα μεταξύ των δύο πρώτων κορυφών που εμφανίζονται στην υψηλή ενεργειακή περιοχή του φάσματος (από το κανάλι περίπου 650 σε 990).

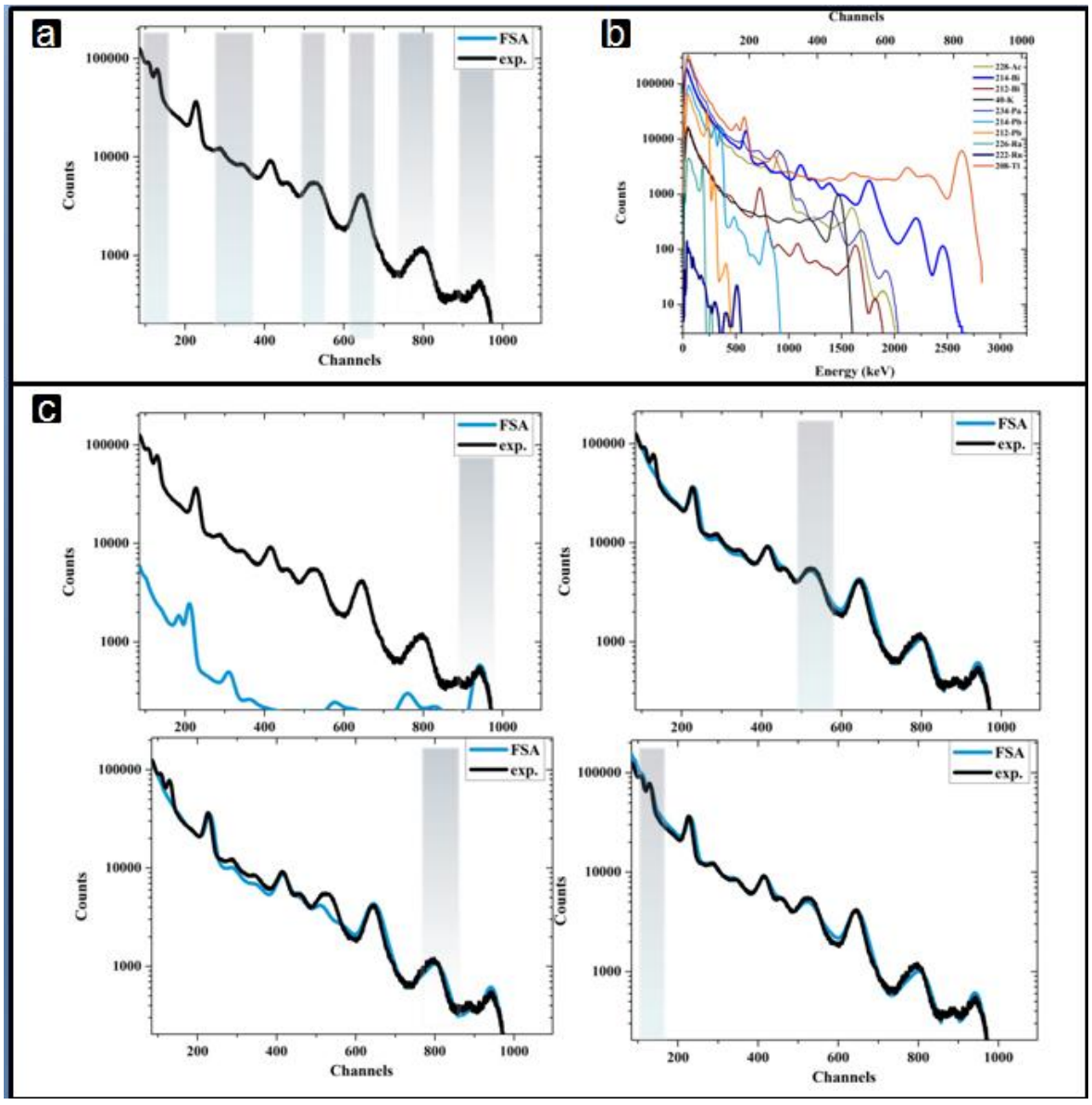

Σχήμα 4.3: Απεικόνηση a) ενός τυπικού πειραματικού φάσματος (exp), b) των πρότυπων φασμάτων που χρησιμοποιούνται στην τεχνική FSA και c) της σταδιακής προσαρμογής σε βήματα (ενεργειακά παράθυρα) του θεωρητικού φάσματος (γραμμικός συνδυασμός των πρότυπων φασμάτων) στο αντίστοιχο πειραματικό μέσω του πακέτου MINUIT.

Η όλη διαδικασία είναι γρήγορη και η σύγκλιση επιτυγχάνεται μέσα σε λίγα λεπτά,

ανάλογα με τον αριθμό των παραμέτρων α_j και των παραθύρων (βημάτων) ελαχιστοποίησης. Οι τιμές της συγκέντρωσης κάθε ραδιονουκλιδίου τυπώνονται αυτόματα στην οθόνη σε κάθε βήμα. Το τελικό αποτέλεσμα της διαδικασίας είναι το θεωρητικό φάσμα που απαρτίζεται από την άθροιση των πρότυπων φασμάτων με τις βέλτιστες συγκεντρώσεις ραδιονουκλιδίων όπως αυτές προέκυψαν μέσα από τη διαδικασία που περιγράφηκε.

Η μεθοδολογία FSA εφαρμόστηκε για την ανάλυση φασμάτων στο θαλασσινό νερό τα οποία πάρθηκαν ποντίζοντας το σύστημα ΚΑΤΕΡΙΝΑ σε τρεις διαφορετικές περιοχές της Μεσογείου, συγκεκριμένα στο λιμάνι Βασιλικού στην Κύπρο (site 1), στο λιμάνι της Ιερισσού στη Χαλκιδική (site 2) και Στούπα Μεσσηνίας στην Πελοπόννησο (site 3). Η περιοχή της Στούπας, στη νοτιοδυτική Πελοπόννησο χαρακτηρίζεται από την παρουσία πολυάριθμων υποθαλάσσιων πηγών ανάβλυσης γλυκού νερού (Submarine Groundwater Discharges, SGD). Σε αυτή τη μέτρηση το ανιχνευτικό σύστημα ήταν τοποθετημένο σε κοντινή απόσταση από μια τέτοια πηγή. Η μεθοδολογία που συζητήθηκε παραπάνω εφαρμόστηκε σε όλες τις περιπτώσεις.

Στο Σχήμα 4.4 δίνεται η σύγκριση μεταξύ θεωρητικού (FSA) και πειραματικού φάσματος (exp) για την περιοχή μελέτης site 1. Στο Σχήμα 4.5 παρουσιάζονται τα αντίστοιχα αποτελέσματα για την περιοχή μελέτης site 2. Όπως φαίνεται η συμφωνία μεταξύ των θεωρητικών και των πειραματικών δεδομένων είναι ικανοποιητική σε όλο το εύρος ενεργειών του φάσματος, στις δύο περιοχές μελέτης. Στον Πίνακα 4.1 συγκρίνονται τα θεωρητικά αποτελέσματα των συγκεντρώσεων των ραδιονουκλιδίων που προέκυψαν από την προσαρμογή του θεωρητικού φάσματος στα πειραματικά δεδομένα, με τις αντίστοιχες συγκεντρώσεις που προέκυψαν από την ανάλυση των φασμάτων με χρήση του λογισμικού SPECTRW (Kalf_16), στις δύο αυτές περιοχές μελέτης. Σε όλες τις περιπτώσεις οι αποκλίσεις βρέθηκαν μικρότερες από 10%.

Η ίδια μεθοδολογία εφαρμόστηκε και στην περιοχή μελέτης site 3, σε συνδυασμό με μια επιπλέον εκτέλεση της τεχνικής FSA, υποθέτοντας στην περίπτωση αυτή ύπαρξη ραδιενεργού ισορροπίας μεταξύ των ραδιονουκλιδίων της ίδιας σειράς. Για την συγκεκριμένη εκτέλεση της FSA μεθοδολογίας, χρησιμοποιήθηκαν μόνο τρία πρότυπα φάσματα, συγκεκριμένα του ^{40}K και δύο ακόμη φάσματα των σειρών του ^{238}U και ^{232}Th συμπεριλαμβάνοντας όλα τα στοιχεία κάθε σειράς (^{214}Bi, ^{214}Pb, ^{234}Pa, ^{226}Ra και ^{222}Rn και ^{208}Tl, ^{228}Ac, ^{212}Bi και ^{212}Pb), υποθέτοντας ίσες συγκεντρώσεις για όλα τα στοιχεία της ίδιας σειράς (υπόθεση ραδιενεργού ισορροπίας).

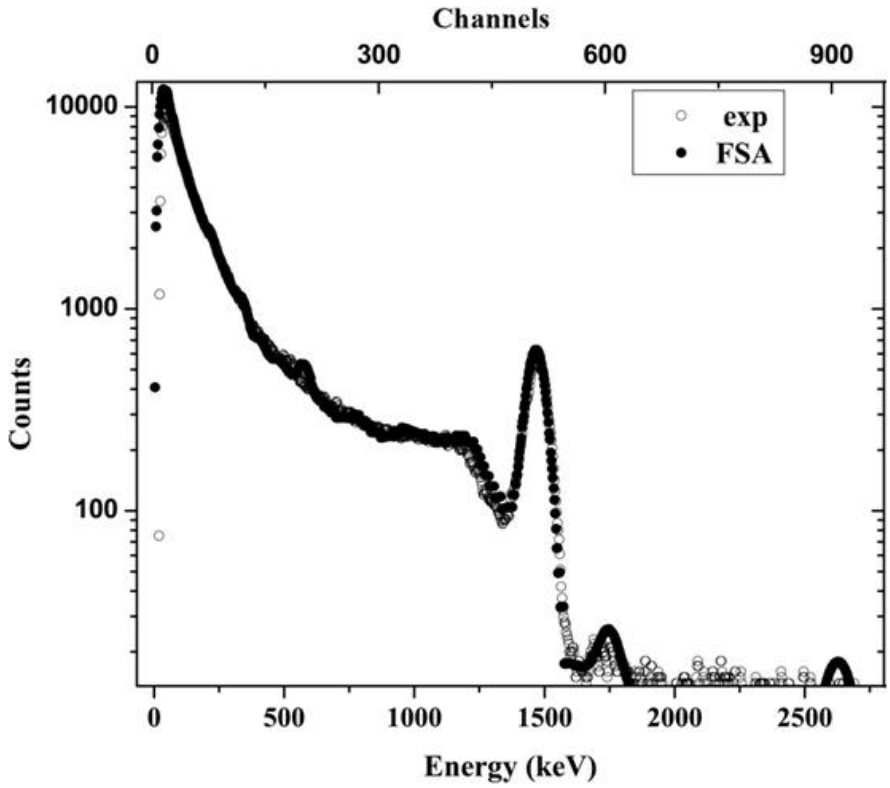

Σχήμα 4.4: Σύγκριση μεταξύ θεωρητικού (FSA) και πειραματικού φάσματος (exp) για την περιοχή μελέτης site 1 (Λιμάνι Βασιλικού, Κύπρος).

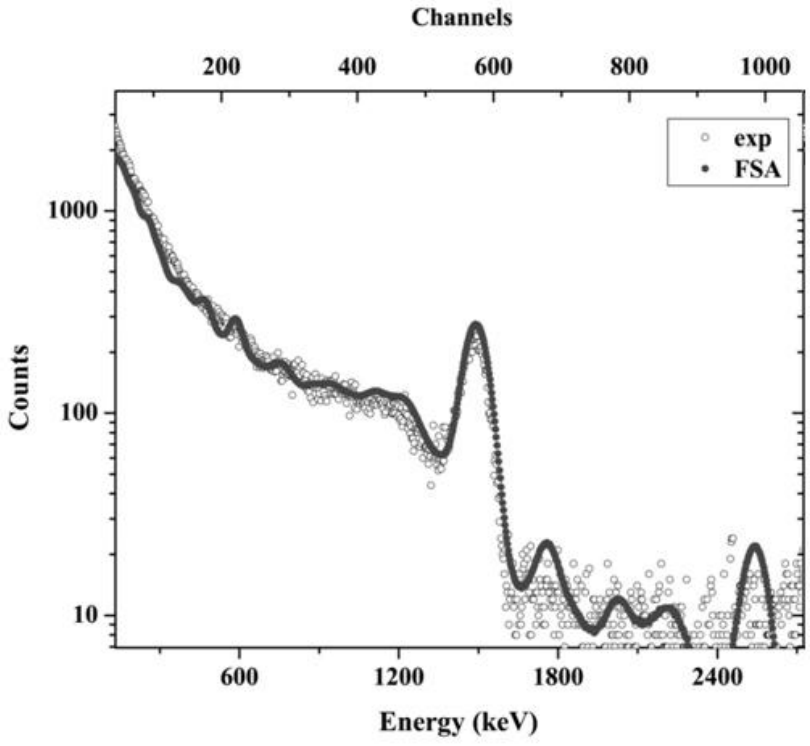

Σχήμα 4.5: Σύγκριση μεταξύ θεωρητικού (FSA) και πειραματικού (exp) φάσματος για την περιοχή μελέτης site 2 (Ιερισσός Χαλκιδικής).

Πίνακας 4.1: Σύγκριση μεταξύ πειραματικών (*in situ*) και θεωρητικών (*FSA*) αποτελεσμάτων συγκεντρώσεων ραδιονουκλιδίων (Bq/L) στις δύο περιοχές (site 1, 2).

sites	1			2		
Nuclides	*In situ*	*FSA*	%	*In situ*	*FSA*	%
	(Bq/L)	(Bq/L)		(Bq/L)	(Bq/L)	
^{40}K	18.10 (6%)	16.80	8	15.06 (8%)	13.85	9
^{214}Bi	0.26 (21%)	0.24	8	0.34 (19%)	0.31	10

Στο Σχήμα 4.6 δίνεται η σύγκριση των φασμάτων (θεωρητική, πειραματική), για τις δύο διαφορετικές εκτελέσεις της FSA μεθοδολογίας, όπως εφαρμόστηκε υποθέτοντας ραδιενεργό ισορροπία μεταξύ των ραδιονουκλιδίων της ίδιας σειράς (1st run), και στη δεύτερη εκτέλεση (2nd run) όπου ακολουθήθηκε η μεθοδολογία που εφαρμόστηκε στις δύο άλλες περιοχές μελέτης. Στον Πίνακα 4.2 συγκρίνονται τα αντίστοιχα αποτελέσματα των συγκεντρώσεων των ραδιονουκλιδίων που προέκυψαν από τις δύο εκτελέσεις της FSA μεθοδολογίας μεταξύ τους, αλλά και με τα αντίστοιχα αποτελέσματα που προέκυψαν από την ανάλυση των φασμάτων με χρήση του λογισμικού SPECTRW (Kalf_16). Στην πρώτη εκτέλεση (ύπαρξη ραδιενεργούς ισορροπίας) της FSA τεχνικής, η προσαρμογή στο πειραματικό φάσμα δεν είναι ικανοποιητική, εφόσον παρατηρούνται σημαντικές διαφορές σε διάφορες ενεργειακές περιοχές του φάσματος. Αυτό ήταν αναμενόμενο, καθώς είναι γνωστό ότι η υπόθεση ραδιενεργούς ισορροπίας συχνά δεν ικανοποιείται σε δυναμικά συστήματα και ιδιαίτερα στο θαλάσσιο περιβάλλον. Οι διαφορές μεταξύ των δύο φασμάτων οφείλονται κυρίως στην υπερεκτίμηση της συγκέντρωσης του ^{234}Pa (κορυφή γύρω από κανάλια 260-328) και του ^{208}Tl, ενώ ταυτόχρονα παρατηρείται υποεκτίμηση της συγκέντρωσης του ^{214}Bi. Τα θεωρητικά αποτέλεσμα των συγκεντρώσεων παρουσιάζουν μεγάλες αποκλίσεις, από τα αντίστοιχα δεδομένα που προέκυψαν από την απλή ανάλυση του φάσματος, ειδικά στην περίπτωση του ^{40}K (αλληλοεπικαλυπτόμενες φωτοκορυφές των ραδιονουκλιδίων ^{214}Bi, ^{234}Pa, ^{228}Ac, ^{40}K), όπως φαίνεται στον Πίνακα 4.2 (1st run). Οι τιμές των συγκεντρώσεων στην δεύτερη εκτέλεση (υπόθεση μη a priori ύπαρξης ισορροπίας) βρέθηκαν σε πολύ καλή συμφωνία με τα πειραματικά δεδομένα για όλα τα ανιχνευόμενα ραδιονουκλίδια, όπως φαίνεται από τις τιμές του Πίνακα 4.2.

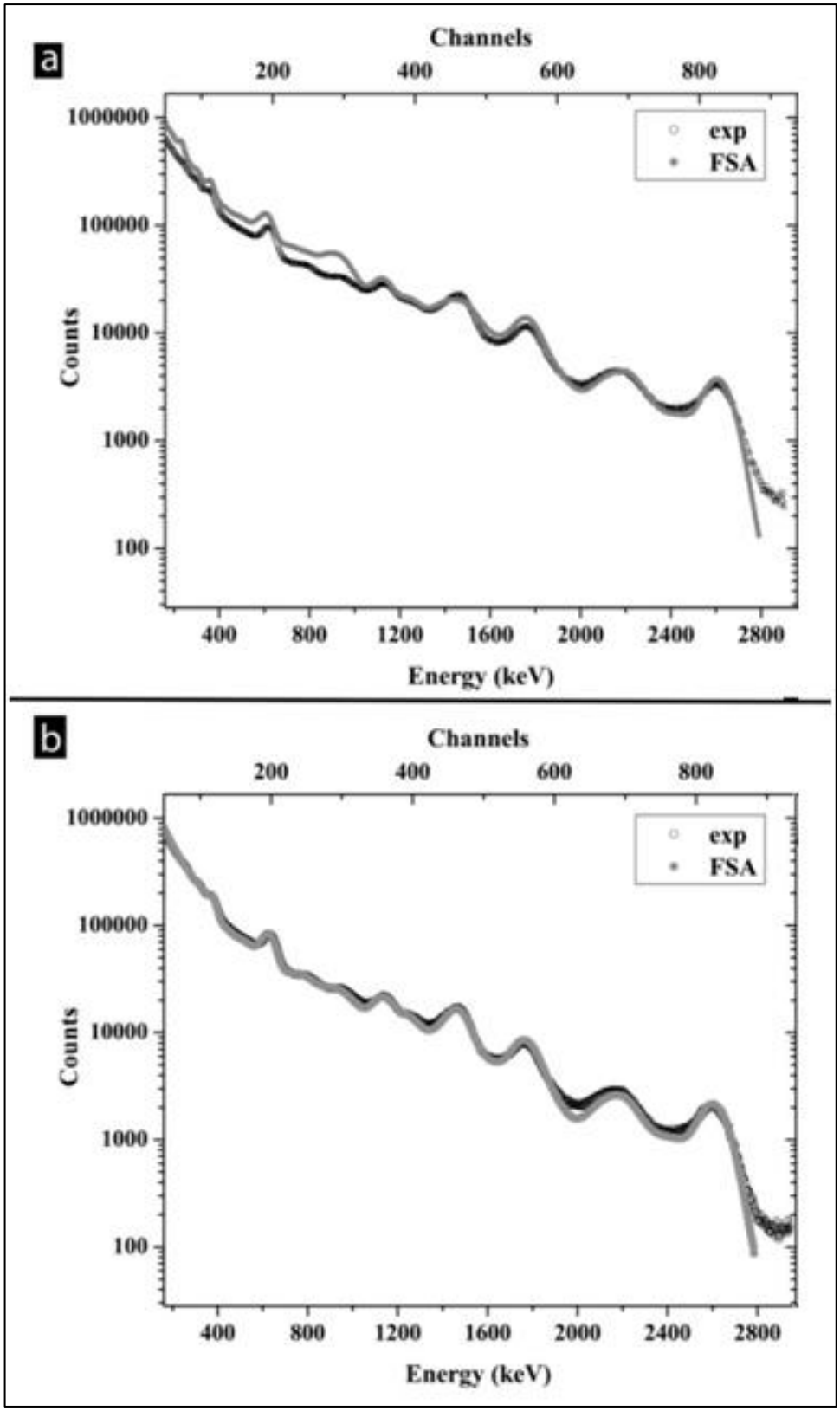

Σχήμα 4.6: Σύγκριση μεταξύ θεωρητικού (FSA) και πειραματικού (exp) φάσματος για την περιοχή μελέτης site3 (Στούπα Μεσσηνίας), υποθέτωντας ραδιενεργό ισορροπία μεταξύ των ραδιονουκλιδίων της ίδιας σειράς (a) και χρησιμοποιώντας τα 10 θεωρητικά ανεξάρτητα φάσματα (b).

Πίνακας 4.2: Σύγκριση θεωρητικών (FSA) αποτελεσμάτων των συγκεντρώσεων ραδιονουκλιδίων (Bq/L), για την περιοχή μελέτης site 3 (Στούπα Μεσσηνίας), υποθέτωντας αρχικά ραδιενεργό ισορροπία μεταξύ των ραδιονουκλιδίων της ίδιας σειράς (1^{st} run), και χρησιμοποιώντας τα 10 πρότυπα φάσματα (2^{nd} run).

		1^{st} run		2^{nd} run	
Radionuclides	*In situ*	*FSA*	%	*FSA*	%
	(Bq/L)	(Bq/L)		(Bq/L)	
^{40}K	6.40 (6%)	10.38	62	7.02	10
^{214}Pb	3.27 (9%)	3.35	2	3.39	4
^{214}Bi	4.20 (5%)	3.35	20	4.30	2
^{208}Tl	0.30 (13%)	0.35	18	0.32	7
^{228}Ac	1.05 (10%)	1.06	1	1.20	14

Η στατιστική αβεβαιότητα τυπικών μετρήσεων στο θαλασσινό νερό κυμαίνεται συνήθως από 6% έως 20%, ανάλογα με τα επίπεδα ραδιενέργειας στην υπό μελέτη περιοχή, τον χρόνο λήψης δεδομένων και την απόδοση του ανιχνευτικού συστήματος σε κάθε ενέργεια ακτίνων-γ. Όσον αφορά τις προσομοιώσεις MC η στατιστική αβεβαιότητα κρατήθηκε κάτω από 5% στις ενεργειακές περιοχές γύρω από τις φωτοκορυφές σε όλες τις εκτελέσεις του κώδικα. Έτσι η συνολική στατιστική αβεβαιότητα διέπεται κυρίως από τη στατιστική των γεγονότων που καταγράφονται στην πειραματική μέτρηση. Η ελαχιστοποίηση της συστηματικής αβεβαιότητας που εισέρχεται στους υπολογισμούς έγκειται στη λεπτομερή και αξιόπιστη περιγραφή της πειραματικής μέτρησης καθώς και στη σωστή περιγραφή της ενεργειακής βαθμονόμησης του συστήματος στο μοντέλο προσομοίωσης. Η αξιοπιστία των αποτελεσμάτων εξαρτάται σε μεγάλο βαθμό τον αριθμό των χρησιμοποιούμενων παραμέτρων και των παραθύρων ελαχιστοποίησης. Η χρήση πολλών παραμέτρων α_j και επαρκών παραθύρων, σε κατάλληλα επιλεγμένες περιοχές του φάσματος, με τη χρήση των οποίων η προσαρμογή των πρότυπων φασμάτων επιτυγχάνεται σε βήματα, σταθεροποιώντας σε κάθε βήμα, τις βέλτιστες τιμές συγκεντρώσεων των αντίστοιχων ραδιονουκλιδίων, αυξάνουν την αξιοπιστία των θεωρητικών (FSA) αποτελεσμάτων.

5. Μετρήσεις στο ίζημα με το σύστημα ΚΑΤΕΡΙΝΑ

5.1 Περιγραφή πειραματικής διάταξης και μεθοδολογίας για *in situ* μετρήσεις σε πυθμένες θαλασσών χρησιμοποιώντας το ανιχνευτικό σύστημα ΚΑΤΕΡΙΝΑ

Η τοποθέτηση του συστήματος εντός του ιζήματος σε βάθος τέτοιο, ώστε το υπερκείμενο ίζημα να απορροφά πλήρως τις ακτίνες-γ που εκπέμπονται από ραδιονουκλίδια στο νερό, θα ήταν η ιδανική γεωμετρία μέτρησης στον πυθμένα. Με τον τρόπο αυτό το σύστημα θα μετρούσε εντός του ιζήματος γεγονότα που θα προέρχονται αποκλειστικά από την αποδιέγερση ραδιονουκλιδίων που βρίσκονται στον όγκο του ιζήματος, στη βέλτιστη γεωμετρία μέτρησης, από πλευρά αύξησης της στατιστικής. Ωστόσο, μια τέτοια γεωμετρία απαιτεί πολύπλοκες τεχνικά διαδικασίες και ειδικό προσωπικό για την πόντιση και την τοποθέτηση του συστήματος κάτω από την επιφάνεια του πυθμένα. Επιπρόσθετα, τα γεωμορφολογικά χαρακτηριστικά πυθμένων (σκληρό υπόστρωμα) θα καθιστούσαν μια τέτοια προσπάθεια ακόμα πιο πολύπλοκη και δαπανηρή. Για τον λόγο αυτό επιλέχθηκε η κατακόρυφη τοποθέτηση του συστήματος με τέτοιο τρόπο ώστε το ανιχνευτικό σύστημα να ακουμπά στο ίζημα χωρίς να εισχωρεί σε αυτό (γεωμετρία επαφής). Η σταθεροποίηση του ανιχνευτή στη θέση αυτή και η ακριβής απόστασή του από τον πυθμένα επιτυγχάνεται χρησιμοποιώντας κατάλληλο πλαίσιο στήριξης στο οποίο προσαρμόζεται και το σύστημα παροχής τάσης του ανιχνευτικού συστήματος. Η υιοθέτηση μιας τέτοιας γεωμετρίας δεν απαιτεί πολύπλοκες τεχνικές πόντισης ωστόσο, το σύστημα κατά τη διάρκεια της μέτρησης ανιχνεύει ακτίνες-γ προερχόμενες από ένα όγκο ιζήματος υπό μια ημισφαιρική γεωμετρία αλλά και ακτίνες-γ προερχόμενες από το υπερκείμενο νερό σε μια εξίσου ημισφαιρική γεωμετρία (Σχήμα 5.1a).

Είναι λοιπόν αναγκαία η εύρεση των γεγονότων που προέρχονται από ραδιονουκλίδια στο νερό, με σκοπό την αφαίρεσή τους από τη μέτρηση στο ίζημα. Αυτό πραγματοποιείται λαμβάνοντας επιπλέον ένα φάσμα και στο νερό (Σχήμα 5.1b). Για τη μέτρηση στο υπερκείμενο νερό το σύστημα τοποθετείται σε μεγάλη απόσταση από τον πυθμένα (~ 1.5 m). Στην επιλεγμένη γεωμετρία έτσι η συλλογή γεγονότων γίνεται αποκλειστικά από ραδιονουκλίδια που βρίσκονται στη στήλη νερού σε έναν όγκο νερού που περιβάλλει τον ανιχνευτή υπό μια σφαιρική γεωμετρία.

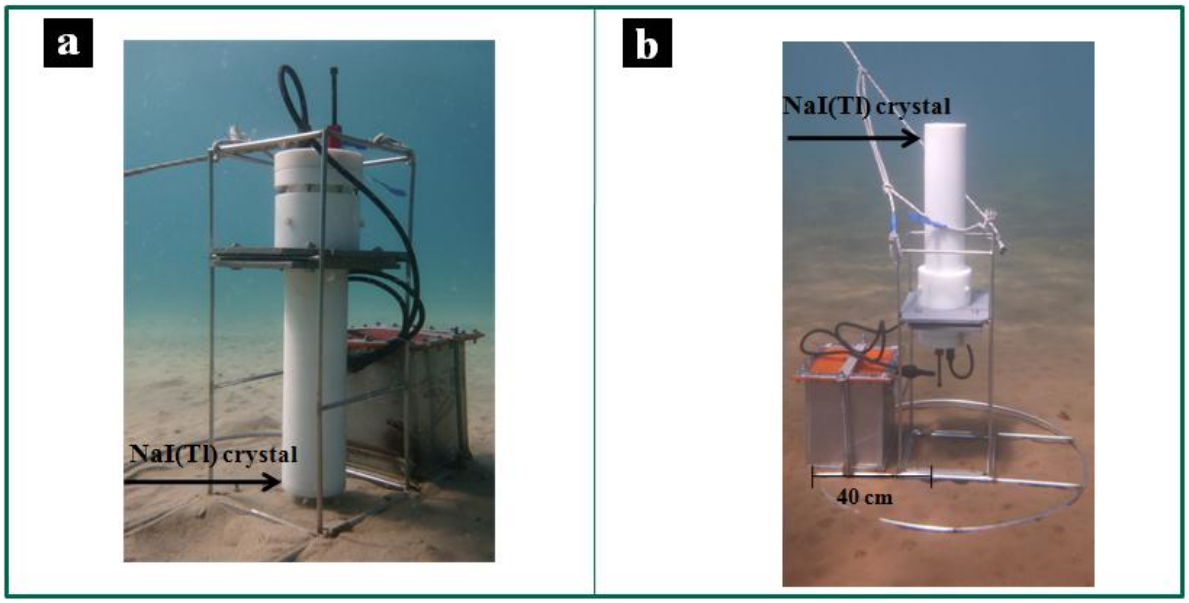

Σχήμα 5.1: Φωτογραφίες από τις ποντίσεις του συστήματος ΚΑΤΕΡΙΝΑ για μετρήσεις στο θαλάσσιο ίζημα (a) και στο θαλασσινό νερό (b).

Καθώς, ο συνολικός μαζικός συντελεστής εξασθένησης μ_{tot} στα δυο υλικά (νερό και ίζημα) διαφέρει, η απόσταση που μια ακτίνα-γ διανύει σε κάθε ένα υλικό μέχρι να απορροφηθεί πλήρως (r_{eff}) αλλάζει. Ως αποτέλεσμα οι όγκοι νερού και ιζήματος από τους οποίους συλλέγονται ακτίνες-γ από το σύστημα διαφέρουν λόγω των διαφορετικών χαρακτηριστικών των δυο υλικών. Τα χαρακτηριστικά αυτά αφορούν στην πυκνότητα και στη σύσταση του νερού και του ιζήματος. Η σχηματική αναπαράσταση της πειραματικής διάταξης των δύο μετρήσεων στο νερό και στο ίζημα δίνονται στο Σχήμα 5.2.

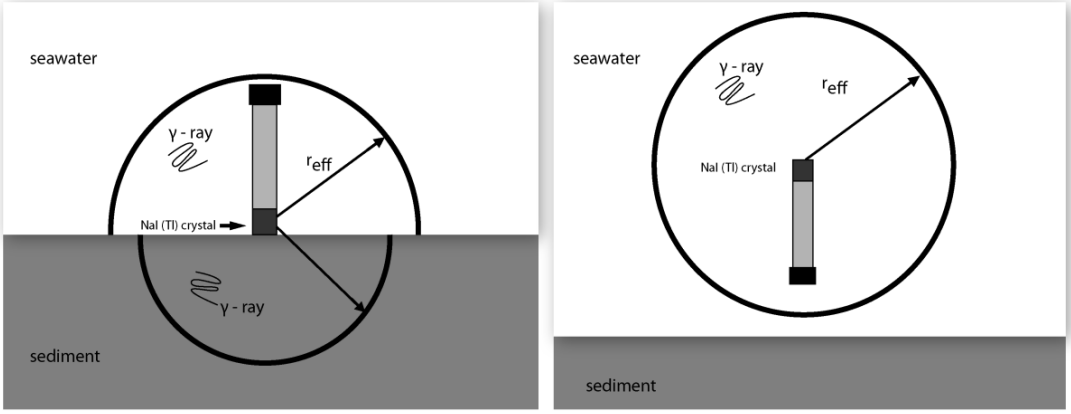

Σχήμα 5.2: Αναπαράσταση της πειραματικής διάταξης των δύο μετρήσεων στο νερό (δεξιά) και στο ίζημα (αριστερά).

5.2 Μελέτη ευαισθησίας της απόδοσης του συστήματος ΚΑΤΕΡΙΝΑ για μετρήσεις σε πυθμένες θαλασσών μέσω Monte Carlo προσομοίωσης

Η απόδοση ενός συστήματος φασματοσκοπίας ακτίνων-γ εξαρτάται α) από την ενέργεια των εκπεμπόμενων ακτίνων β) από τις φυσικές ιδιότητες τόσο των υλικών που απαρτίζουν το ανιχνευτικό σύστημα όσο και της πηγής (περίπτωση πηγών με πεπερασμένες διαστάσεις) και γ) από τη στερεά γωνία μέτρησης. Το πρόβλημα που δημιουργείται λοιπόν στην ανάπτυξη κατάλληλης μεθοδολογίας για την εύρεση της απόδοσης (βαθμονόμηση) ενός *in situ* ανιχνευτικού συστήματος, είναι ότι η ποσότητα αυτή, εξαρτάται από τα χαρακτηριστικά του ιζήματος, τα οποία παρουσιάζουν μεγάλη ποικιλομορφία και διακυμάνσεις ακόμη και στην ίδια περιοχή. Για τον λόγο αυτό, πριν την εφαρμογή της μεθοδολογίας που αναπτύχθηκε στα πλαίσια της παρούσας διατριβής για *in situ* ποσοτικές μετρήσεις σε πυθμένες θαλασσών, πραγματοποιήθηκε μια εκτεταμένη και συστηματική μελέτη των παραγόντων που ενδέχεται να επηρεάζουν την απόδοση του συστήματος και προσδιορίστηκε ο βαθμός της επίδρασης καθενός από αυτούς. Οι παράγοντες που μελετήθηκαν αφορούν α) στα φυσικά χαρακτηριστικά των ιζημάτων και β) σε αλλαγές στη γεωμετρία μέτρησης (στερεά γωνία). Η μελέτη αυτή βασίστηκε αποκλειστικά σε προσομοιώσεις Monte Carlo χρησιμοποιώντας τον κώδικα MCNP5 σύμφωνα με τη μεθοδολογία που παρουσιάστηκε στην ενότητα 3. Συγκεκριμένα μελετήθηκαν:

Α) Η επίδραση στην απόδοση του συστήματος σε αλλαγές της σύστασης των κυρίων στοιχείων από τα οποία αποτελείται το ίζημα.

Β) Η επίδραση στην απόδοση του συστήματος σε αλλαγές της πυκνότητας (υγρή) στο ίζημα.

Γ) Η επίδραση στην απόδοση του συστήματος σε αλλαγές της περιεκτικότητας σε νερό (ποσόστωση νερού w/w) στο θαλάσσιο ίζημα.

Δ) Η επίδραση στην απόδοση του συστήματος σε αλλαγές της απόστασης (0-6.5 cm) μεταξύ της επιφάνειας του πυθμένα και της θέσης του παραθύρου του ανιχνευτή (αποκλίσεις από τη γεωμετρία επαφής).

Ε) Η επίδραση στην απόδοση του συστήματος στην περίπτωση κεκλιμένου βυθού (αποκλίσεις από την κάθετη τοποθέτηση του συστήματος) λαμβάνοντας υπόψη κλίση του πυθμένα που αντιστοιχεί σε γωνίες μεταξύ των δύο επιφανειών έως και 5^{o}.

Οι προσομοιώσεις πραγματοποιήθηκαν για ένα μεγάλο εύρος ενεργειών (238-2614 keV) και τιμών για κάθε παράμετρο, στο οποίο περιλαμβάνονται οι πιθανές τιμές που συναντώνται στο θαλάσσιο περιβάλλον. Η επιπλέον παράμετρος που μεταβάλλεται σε κάθε

εκτέλεση του κώδικα είναι η ενεργός ακτίνα της πηγής, καθώς η τιμή αυτής εξαρτάται από το γραμμικό συντελεστή εξασθένησης και επομένως από την ενέργεια της εκπεμπόμενης ακτίνας-γ και τα φυσικά χαρακτηριστικά του ιζήματος (σύσταση, πυκνότητα). Τα μοντέλα προσομοίωσης που χρησιμοποιήθηκαν στην εκτίμηση της απόδοσης του ανιχνευτή σε κάθε περίπτωση παρουσιάζονται στο Σχήμα 5.3. Στον Πίνακα 5.1 συγκεντρώνονται τα δεδομένα της σύστασης κύριων στοιχείων του ιζήματος που χρησιμοποιήθηκαν για την περιγραφή της πηγής ιζήματος στο μοντέλο προσομοίωσης. Τα συγκεντρωτικά αποτελέσματα των προσομοιώσεων παρουσιάζονται στα Σχήματα 5.4-5.7 και 5.9-5.10 καθώς και στον Πίνακα 5.2. Τα αποτελέσματα της μελέτης έδειξαν ότι οι δύο παράμετροι που αλλάζουν δραστικά τις τιμές της απόδοσης του ανιχνευτικού συστήματος σε όλο το εύρος ενεργειών, είναι η αύξηση της απόστασης μεταξύ πυθμένα και παραθύρου του ανιχνευτή, όπου παρατηρήθηκε μείωση της απόδοσης μέχρι και ενός παράγοντα 3 και η αλλαγές στην πυκνότητα του ιζήματος οι οποίες επιφέρουν αλλαγή στην απόδοση που ισοδυναμεί με το ποσοστό μεταβολής της πυκνότητας. Η αύξηση της κλίσης του πυθμένα επιφέρει μείωση της απόδοσης έως και 10%, ενώ αύξηση της ποσόστωσης νερού του ιζήματος επιφέρει μείωση της απόδοσης μικρότερη από 8%. Η αλλαγή στη σύσταση του ιζήματος φαίνεται να επηρεάζει πιο έντονα την απόδοση του συστήματος στις χαμηλές ενέργειες (ως 300 keV). Η αλλαγές στην παράμετρο αυτή φαίνονται να επιφέρουν αποκλίσεις στην απόδοση του ανιχνευτή που κυμαίνονται μεταξύ 5 και 30% στις χαμηλές ενέργειες, ενώ δεν ξεπερνούν το 10% στο ενεργειακό εύρος 500 – 1000 keV.

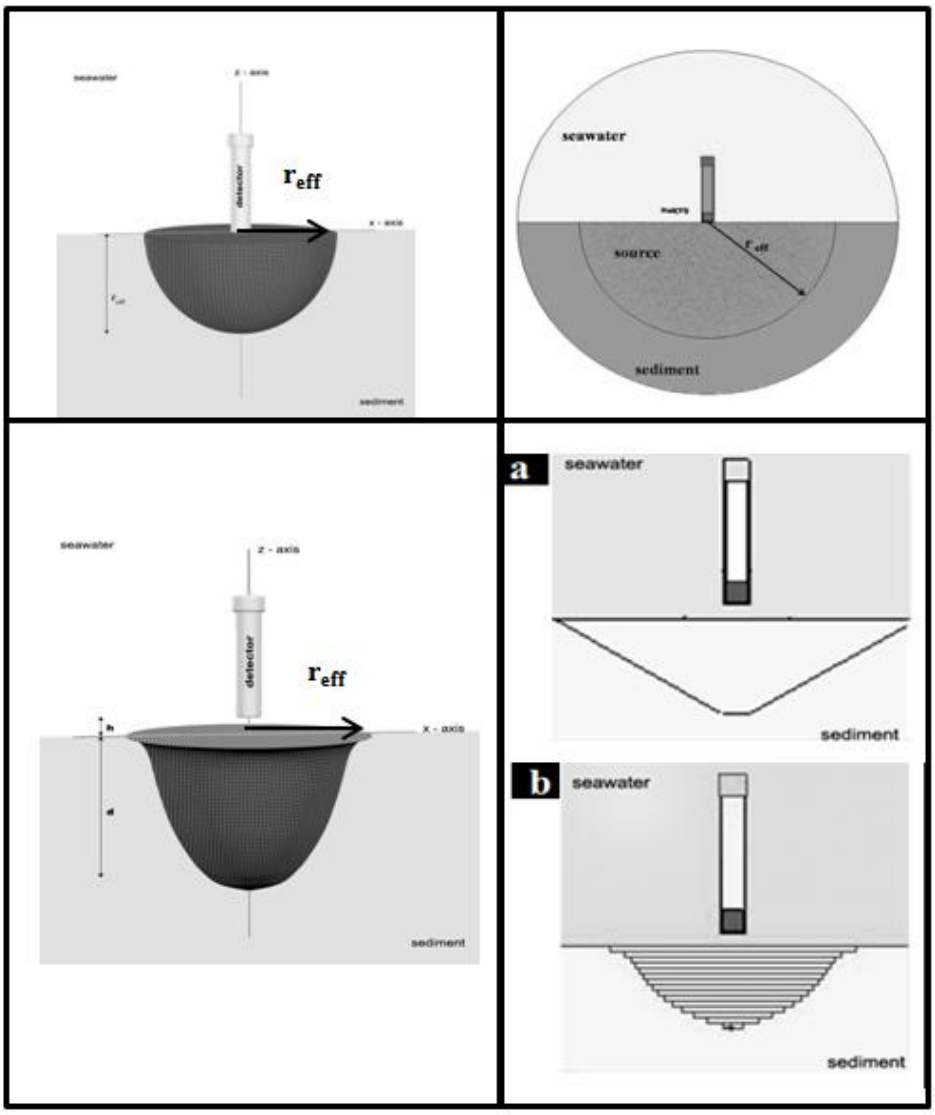

Σχήμα 5.3: Αναπαράσταση των μοντέλων προσομοίωσης για την εύρεση της απόδοσης του ανιχνευτικού συστήματος ΚΑΤΕΡΙΝΑ για μετρήσεις στο ίζημα στις περιπτώσεις όπου το σύστημα τοποθετείται σε γεωμετρία επαφής (πάνω) και σε απόσταση 2 cm από τον πυθμένα της θάλασσας (κάτω) χρησιμοποιώντας για την περιγραφή της πηγής (a) κώλουρο κώνο και (b) την ακριβή γεωμετρία.

Πίνακας 5.1: Σύσταση ιζημάτων (κύρια στοιχεία και ποσόστωση νερού w.c.) που χρησιμοποιήθηκε στη μελέτη επίδρασης των χαρακτηριστικών του ιζήματος στην απόδοση του συστήματος ΚΑΤΕΡΙΝΑ.

	Major elements (wt. %)											**w.c. (%)**
	Al_2O_3	**SiO_2**	**P_2O_5**	**K_2O**	**CaO**	**TiO_2**	**Fe_2O_3**	**Na_2O**	**MgO**	**SO_3**	**MnO**	**H_2O**
sed 1	2.6	55.3	0.1	0.6	8.5	0.3	8.4	1.2	2.6	5.1	0.5	15.0
sed 2	8.5	14.5	0.1	2.4	34.0	0.3	17.0	1.2	2.6	4.0	0.5	15.0
sed 3	8.5	8.5	0.1	2.6	26.4	0.8	31.5	1.2	2.6	1.7	1.2	15.0
sed 4	6.5	43.2	0.04	0.3	13.9	0.5	9.4	0.8	6.7	3.5	0.1	15.0

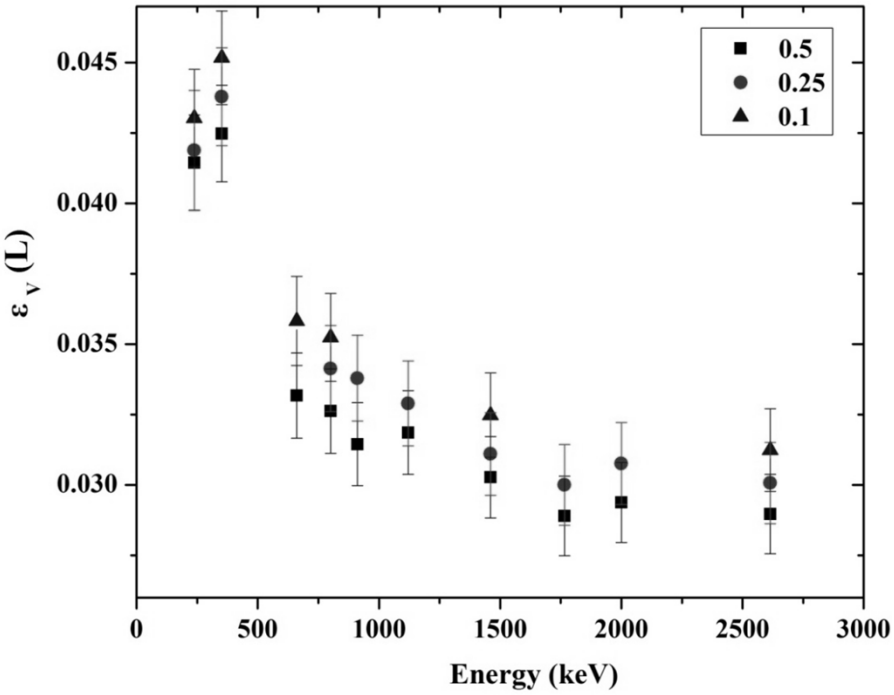

Σχήμα 5.4: Αποτελέσματα προσομοίωσης της απόδοσης του ανιχνευτικού συστήματος ΚΑΤΕΡΙΝΑ (ε_v (L)) συναρτήσει της ενέργειας, λαμβάνοντας υπόψη διαφορετικές ποσοστώσεις νερού του ιζήματος, συγκεκριμένα 0.1, 0.25 και 0.5 w/w.

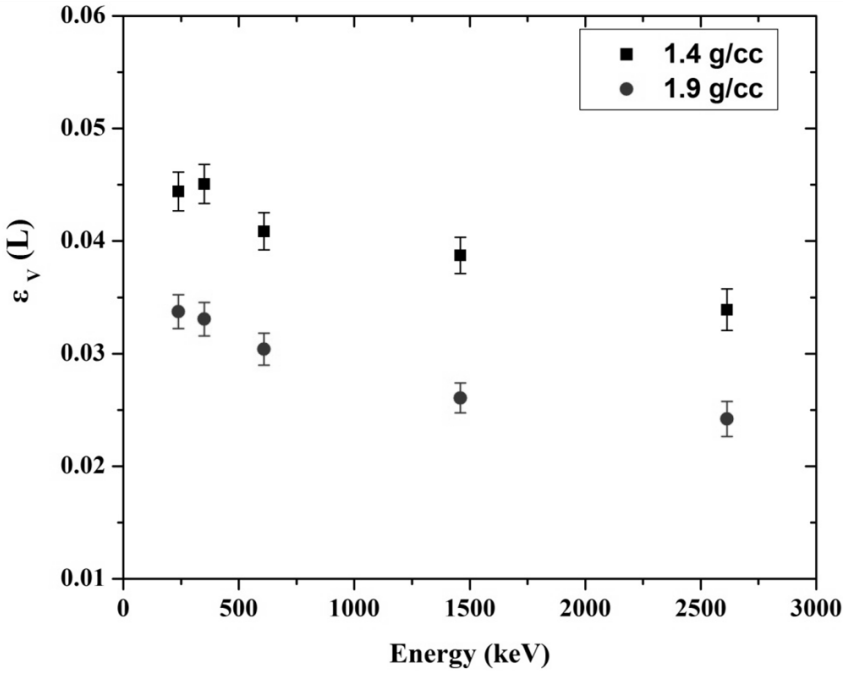

Σχήμα 5.5: Αποτελέσματα προσομοίωσης της απόδοσης του ανιχνευτικού συστήματος ΚΑΤΕΡΙΝΑ (ε_v (L)) συναρτήσει της ενέργειας, λαμβάνοντας υπόψη δύο διαφορετικές τιμές υγρής πυκνότητας του ιζήματος (d), συγκεκριμένα d=1.4 g/cc και d=1.9 g/cc, όταν το σύστημα τοποθετείται 2 cm από τον πυθμένα της θάλασσας.

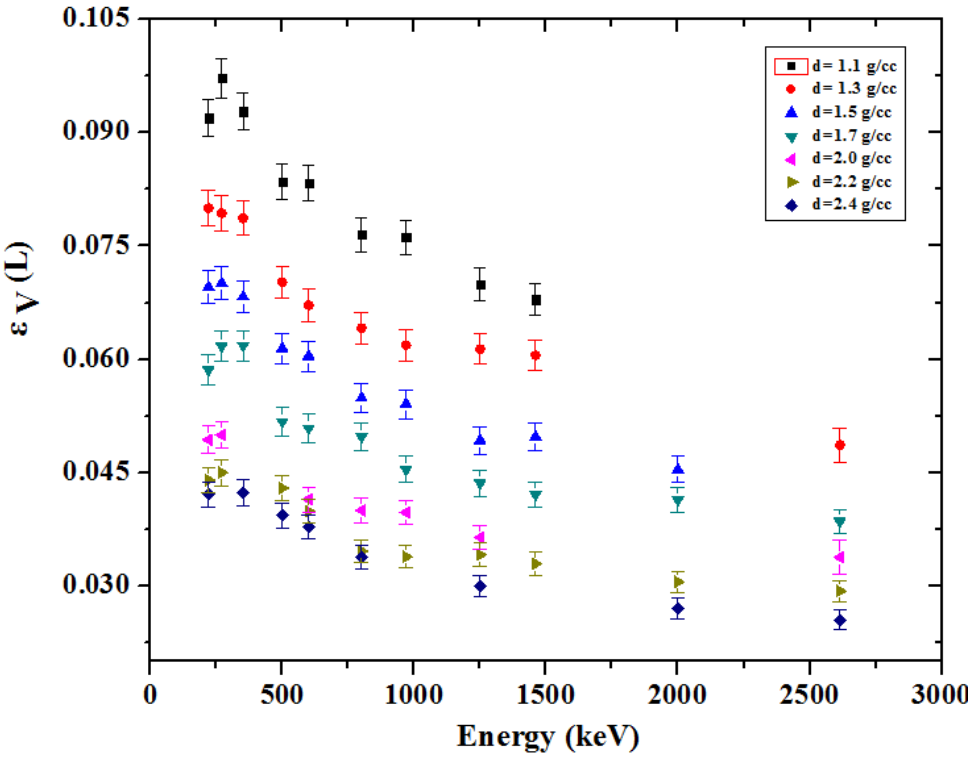

Σχήμα 5.6: Αποτελέσματα προσομοίωσης της απόδοσης του ανιχνευτικού συστήματος ΚΑΤΕΡΙΝΑ (ε_v (L)) συναρτήσει της ενέργειας, για διαφορετικές τιμές υγρής πυκνότητας του ιζήματος (d), στο διάστημα 1.1 - 2.4 g/cc, σε γεωμετρία επαφής.

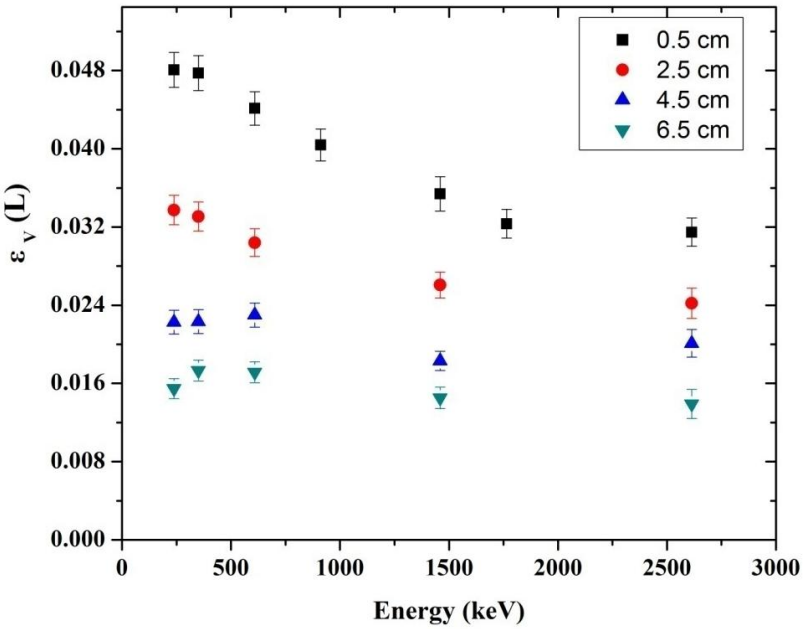

Σχήμα 5.7: Αποτελέσματα προσομοίωσης της απόδοσης του ανιχνευτικού συστήματος ΚΑΤΕΡΙΝΑ (ε_v (L)) συναρτήσει της ενέργειας, για διαφορετικές αποστάσεις μεταξύ του συστήματος και της επιφάνειας του πυθμένα, συγκεκριμένα 0.5 cm, 2.5 cm, 4.5 cm και 6.5 cm πάνω από την επιφάνεια του πυθμένα.

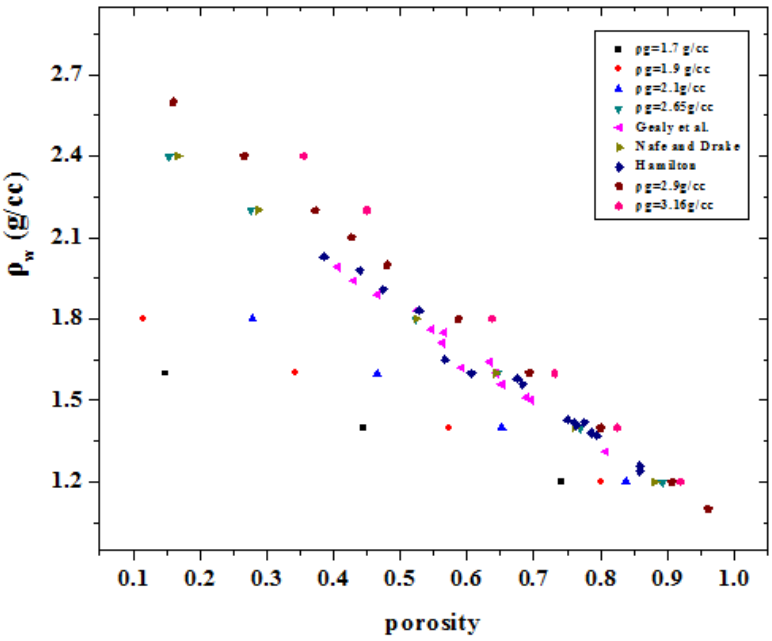

Σχήμα 5.8: Αναπαράσταση της γραμμικής εξάρτησης της υγρής πυκνότητας του ιζήματος (ρ_w) από το πορώδες (porosity) αυτού για διαφορετικές συνήθεις τιμές πυκνότητας ρ_g ιζημάτων (ρ_g =1.7 -3.16 g/cc).

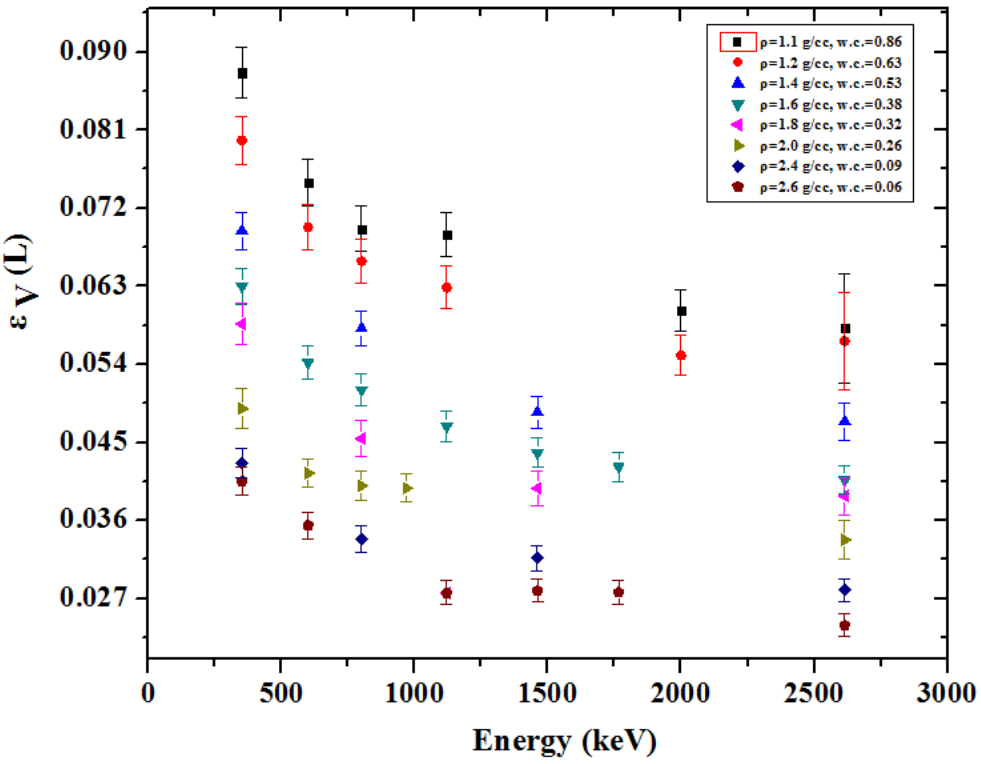

Σχήμα 5.9: Αποτελέσματα προσομοίωσης της απόδοσης του ανιχνευτικού συστήματος ΚΑΤΕΡΙΝΑ (ε_v (L)) συναρτήσει της ενέργειας, για διαφορετικά χαρακτηριστικά ιζήματος (υγρής πυκνότητας του ιζήματος (ρ) και ποσόστωσης νερού (w.c.), λαμβάνοντας υπόψη τα δεδομένα του σχήματος 5.8, σε γεωμετρία επαφής.

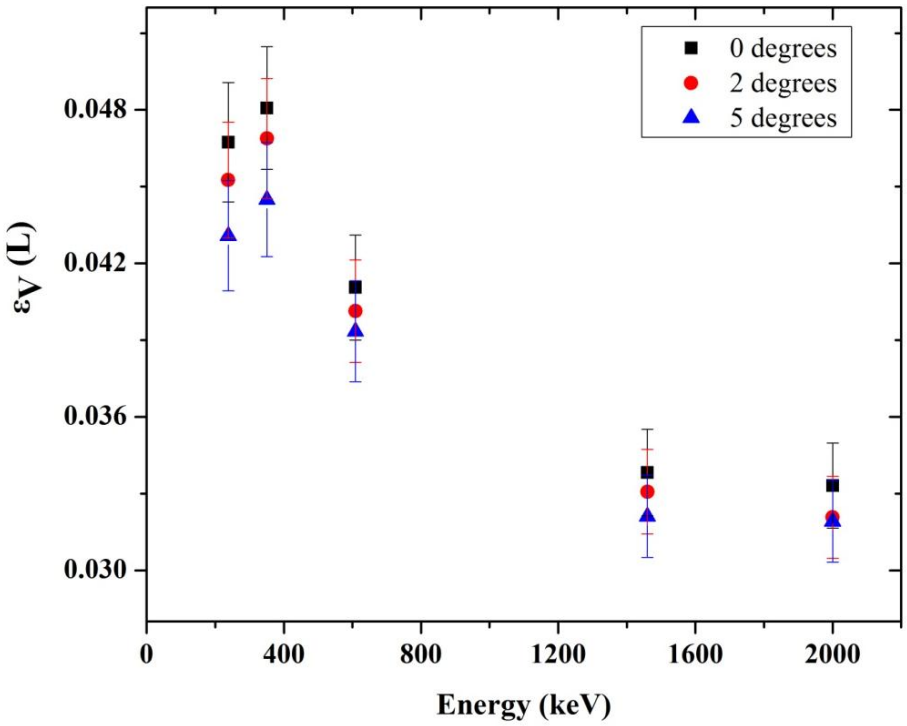

Σχήμα 5.10: Αποτελέσματα προσομοίωσης της απόδοσης του ανιχνευτικού συστήματος ΚΑΤΕΡΙΝΑ (ε_v (L)) συναρτήσει της ενέργειας, σε περιπτώσεις ύπαρξης αποκλίσεων (σε γωνίες 0^o, 2^o και 5^o) από την κάθετη τοποθέτηση του συστήματος στην επιφάνεια του πυθμένα όταν αυτός τοποθετείται σε γεωμετρία επαφής.

Πίνακας 5.2: Θεωρητικά αποτελέσματα της απόδοσης του συστήματος ΚΑΤΕΡΙΝΑ συναρτήσει της ενέργειας, για ένα μεγάλο εύρος διαφορετικών χαρακτηριστικών ιζημάτων που απαντώνται στο θαλάσσιο περιβάλλον.

Energy (keV)	**MC detection efficiency ε_V (L)**							
	ρ= 1.1g/cc w.c.= 0.86	***ρ= 1.2g/cc w.c.= 0.63***	***ρ= 1.4g/cc w.c.= 0.53***	***ρ= 1.6g/cc w.c.= 0.38***	***ρ= 1.8g/cc w.c.= 0.32***	***ρ= 2.0g/cc w.c.= 0.26***	***ρ= 2.4g/cc w.c.= 0.09***	***ρ= 2.6g/cc w.c.= 0.06***
351	0.0876 (3)	0.0798 (3)	0.0694 (2)	0.0630 (2)	0.0587 (2)	0.0489 (2)	0.0426 (2)	0.0405 (2)
600	0.0750 (3)	0.0698 (3)	-	0.0542 (2)	-	0.0415(2)	-	0.0355 (2)
800	0.0696 (3)	-	0.0581(2)	0.0511(2)	0.0454 (2)	0.0400 (2)	0.0339 (2)	-
1120	0.0690 (3)	0.0659 (3)	-	0.0469 (2)	0.0277(2)	-	-	-
969	-	-	-	-	-	0.0397 (2)	-	-
1460.8	-	0.0629 (3)	0.0485 (2)	0.0438 (2)	0.0397(2)	-	0.0317 (2)	0.0277 (2)
1765	0.0602 (3)	-	-	0.0422 (2)	-	-	-	0.0279 (2)
2000	0.0582 (3)	0.0551 (3)	-	0.0407 (2)	-	-	-	0.0277 (2)
2614	-	0.0567 (3)	0.0474 (2)	0.0407 (2)	0.0388 (2)	0.0338 (2)	0.0280 (2)	0.0239 (2)

5.3 Πειραματική επιβεβαίωση των θεωρητικών υπολογισμών της απόδοσης του συστήματος ΚΑΤΕΡΙΝΑ για μετρήσεις σε πυθμένες θαλασσών

Στο Σχήμα 5.11 φαίνονται οι περιοχές μελέτης και σημειώνονται τα σημεία όπου πραγματοποιήθηκαν οι *in situ* μετρήσεις στο ίζημα. Συγκεκριμένα πραγματοποιήθηκαν ποντίσεις σε 4 διαφορετικές περιοχές, στην παραλία Οξυγόνου στο Λαύριο (site 1), στις περιοχές Ιερισσός (site 2) και Στρατώνι (site 3) Χαλκιδικής και στο Costinesti της Ρουμανίας (site 4). Σε όλες τις περιοχές, εκτός της μέτρησης στο ίζημα έγινε και συλλογή φάσματος στο θαλασσινό νερό στο ίδιο σημείο. Οι *in situ* μετρήσεις στο ίζημα στα επιλεγμένα σημεία, πραγματοποιήθηκαν ποντίζοντας το σύστημα ΚΑΤΕΡΙΝΑ στον πυθμένα σε διαφορετικές αποστάσεις από αυτόν, εξετάζοντας με τον τρόπο αυτό πειραματικά την επίδραση της αύξησης της απόστασης μεταξύ συστήματος και πυθμένα στην απόδοση του συστήματος. Οι αποστάσεις που τηρήθηκαν ήταν 2.5 cm, 2.9 cm και 6.0 cm στις περιοχές site 1, site 2, 3 και site 4 αντίστοιχα.

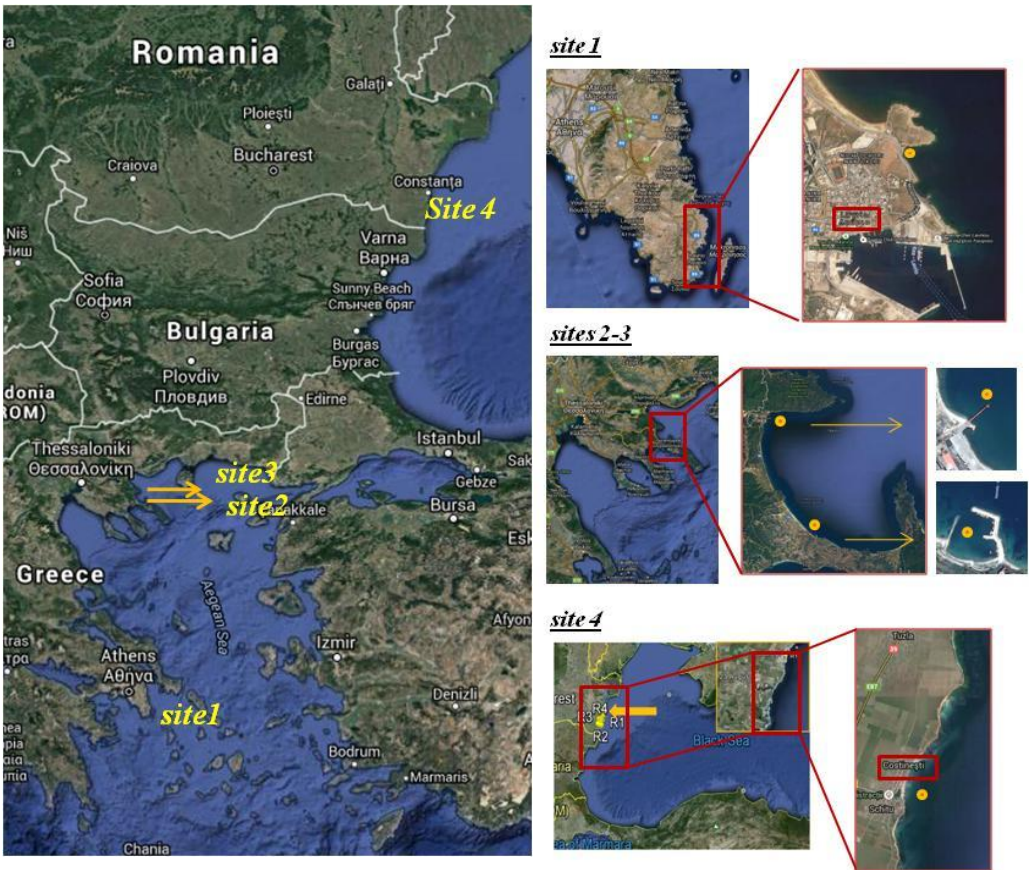

Σχήμα 5.11: Χάρτης περιοχών μετρήσεων βαθμονόμησης για το σύστημα ΚΑΤΕΡΙΝΑ.

Στα σχήματα 5.12 ως 5.15 συγκεντρώνονται τα φάσματα όπως μετρήθηκαν στο νερό και στο ίζημα χρησιμοποιώντας το σύστημα ΚΑΤΕΡΙΝΑ στις υπό μελέτη περιοχές.

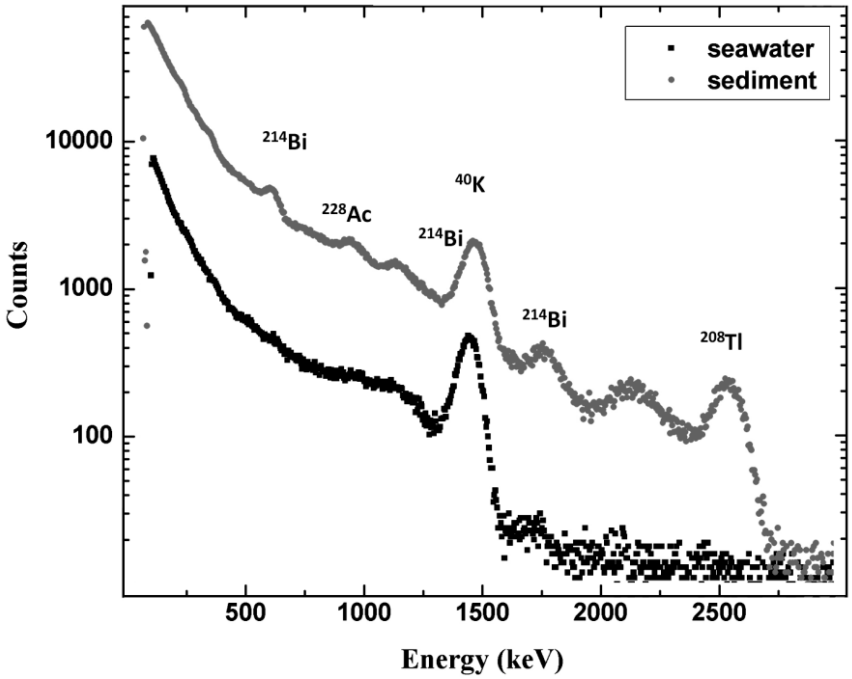

Σχήμα 5.12: Απεικόνιση φασμάτων ιζήματος και νερού όπως μετρήθηκαν με το σύστημα ΚΑΤΕΡΙΝΑ κανονικοποιημένα στον ίδιο χρόνο (61517 sec), στην περιοχή μελέτης site 1 (παραλία Οξυγόνου, Λαύριο).

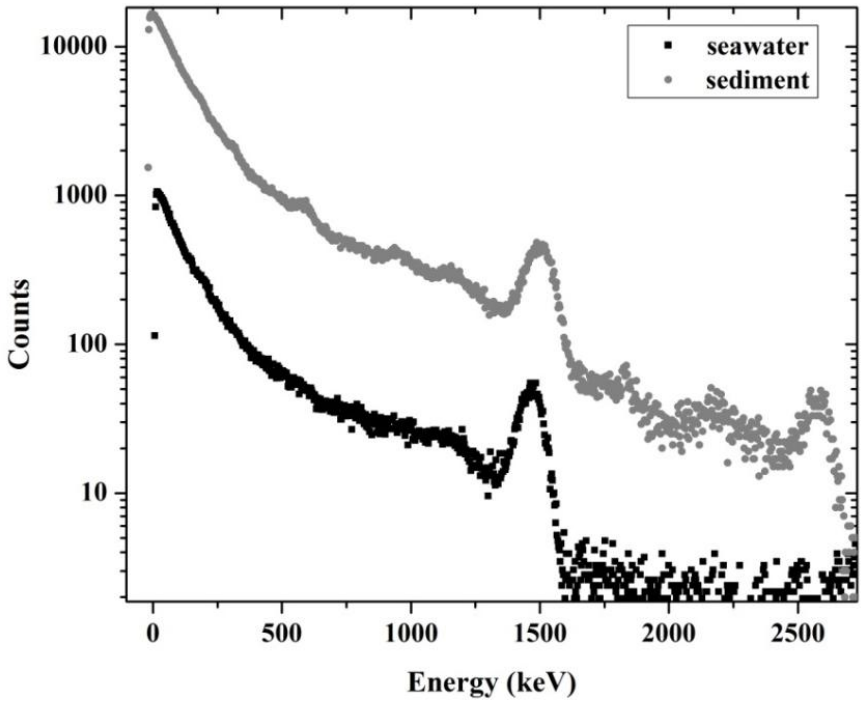

Σχήμα 5.13: Απεικόνιση φασμάτων ιζήματος και νερού όπως μετρήθηκαν με το σύστημα ΚΑΤΕΡΙΝΑ κανονικοποιημένα στον ίδιο χρόνο (7200 sec), στην περιοχή μελέτης site 2 (Ιερισσός Χαλκιδικής).

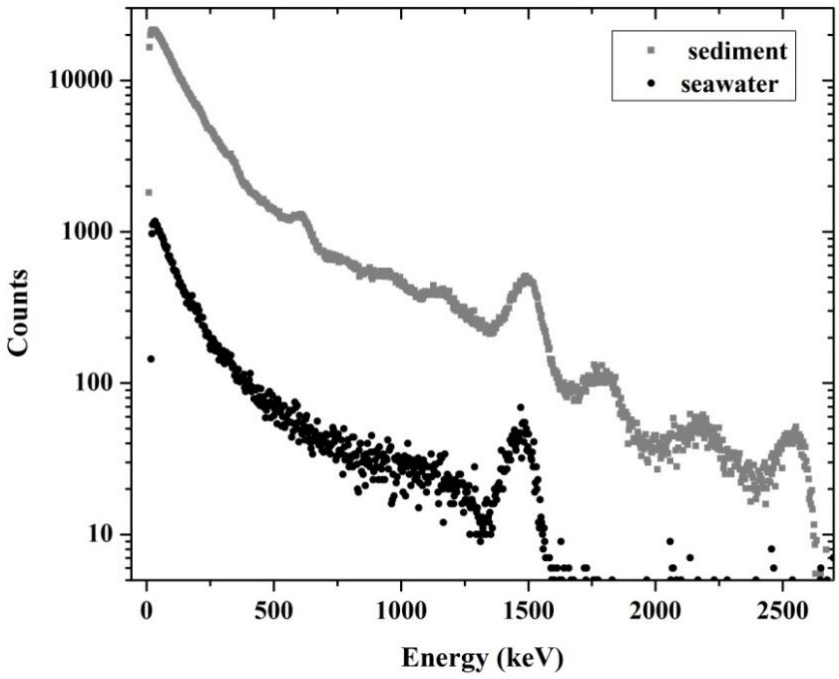

Σχήμα 5.14: Απεικόνιση φασμάτων ιζήματος και νερού όπως μετρήθηκαν με το σύστημα ΚΑΤΕΡΙΝΑ κανονικοποιημένα στον ίδιο χρόνο (6587 sec), στην περιοχή μελέτης site 3 (Στρατώνι Χαλκιδικής).

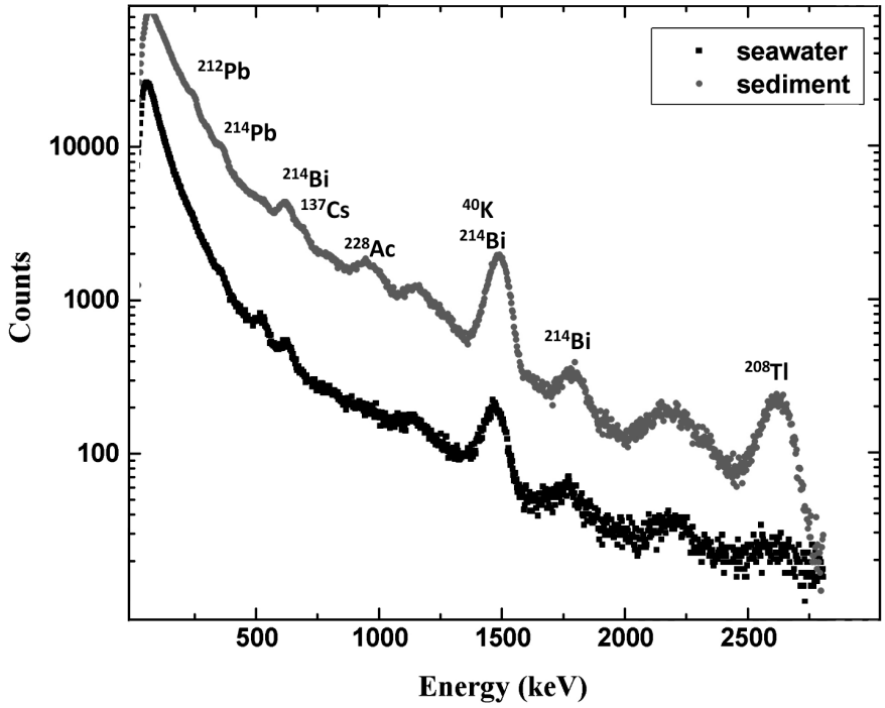

Σχήμα 5.15: Απεικόνιση φασμάτων ιζήματος και νερού όπως μετρήθηκαν με το σύστημα ΚΑΤΕΡΙΝΑ κανονικοποιημένα στον ίδιο χρόνο (57585sec), στην περιοχή μελέτης site 4 (Costinesti, Ρουμανία).

Εκτός από τις *in situ* μετρήσεις στο πεδίο, συλλέχθηκαν δείγματα ιζήματος σε όλα τα σημεία χρησιμοποιώντας κατάλληλους 'δειγματολήπτες αρπαγής' (sites 2, 4) ή πυρηνολήπτες για τη συλλογή δείγματος ιζήματος από ένα βάθος ως 60 cm μέσα στον πυθμένα (sites 1,3). Στα δείγματα αυτά πραγματοποιήθηκαν μετρήσεις φασματοσκοπίας ακτίνων-γ στο εργαστήριο σε βαθμονομημένο ανιχνευτή HPGe και προσδιορίστηκαν τα χαρακτηριστικά του πυθμένα σε κάθε περιοχή μετρώντας στο εργαστήριο τη σύσταση σε κύρια στοιχεία, την υγρή πυκνότητα και την ποσόστωση νερού των δειγμάτων ιζήματος. Τα αποτελέσματα των μετρήσεων συγκεντρώνονται στον Πίνακα 5.3 και Πίνακα 5.4 για τον προσδιορισμό των χαρακτηριστικών του ιζήματος και των συγκεντρώσεων ραδιονουκλιδίων αντίστοιχα. Η δειγματοποίηση των πυρήνων ιζήματος έγινε ανά 2 cm και ανά 1 cm στις περιοχές site 1 και site 3 αντίστοιχα (Σχήμα 5.16). Τα αποτελέσματα των μετρήσεων φασματοσκοπίας ακτίνων-γ συγκεντρώνονται στα Σχήματα 5.17 και 5.18. Στον υπολογισμό της απόδοσης του συστήματος για μετρήσεις στο ίζημα χρησιμοποιήθηκαν οι μέσες τιμές των μετρήσεων αυτών. Ομοίως τα δεδομένα των χαρακτηριστικών του ιζήματος (σύσταση κύριων στοιχείων, υγρή πυκνότητα και ποσόστωση νερού του ιζήματος) που εισήχθησαν στους θεωρητικούς υπολογισμούς, μέσω Monte Carlo προσομοίωσης, για την θεωρητική εκτίμηση της απόδοσης του συστήματος αποτελούν τις μέσες τιμές που υπολογίστηκαν από την ανάλυση όλων των δειγμάτων του πυρήνα ιζήματος ξεχωριστά.

Πίνακας 5.3: Αποτελέσματα των χαρακτηριστικών των υπό μελέτη ιζημάτων, συγκεκριμένα η σύσταση κύριων στοιχείων (major elements), η υγρή/στεγνή πυκνότητα (ρ_d, ρ_w) και η ποσόστωση νερού (w.c.), όπως αυτά μετρήθηκαν στο εργαστήριο, στις 4 περιοχές μελέτης (sites 1-4).

				Major elements (wt. %)									
	w.c. %	**ρ_w** g/cc	**ρ_d** g/cc	**Al_2O_3**	**SiO_2**	**P_2O_5**	**K_2O**	**CaO**	**TiO_2**	**Fe_2O_3**	**Na_2O**	**MgO**	**SO_3**
site 1*	0.26	1.88 (4)	1.57 (4)	3.49	28.34	0.1	0.69	19.91	0.3	14.55	1.12	1.96	11.34
site 2	0.21	2.2 (3)	1.74 (3)	9.68	65.04	0.09	2.16	8.65	0.28	1.01	2.89	1.25	0.07
site 3*	0.35	1.71 (5)	1.26 (3)	10.78	48.31	0.16	2.93	9.96	0.35	13.39	1.88	3.52	7.73
site 4	0.6	1.78 (6)	1.12 (3)	12.17	60.83	0.23	2.11	5.86	0.83	4.38	1.69	1.97	0.82

**μέσες τιμές από τον πυρήνα ιζήματος*

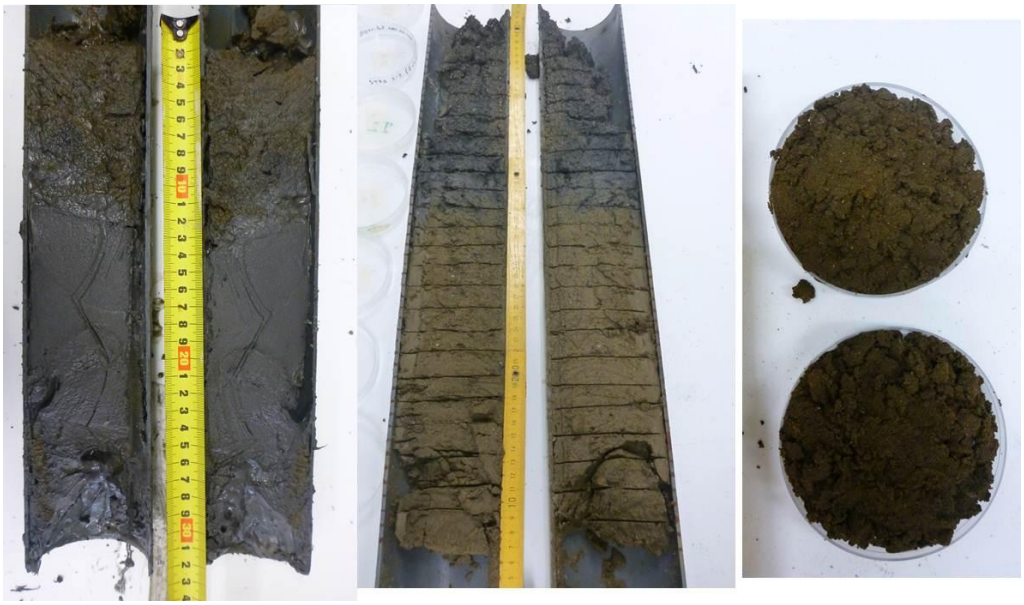

Σχήμα 5.16: Δειγματοποίηση των πυρήνων ιζήματος που συλλέχθηκαν στις περιοχές site 1 (δεξιά) και site 3 (αριστερά).

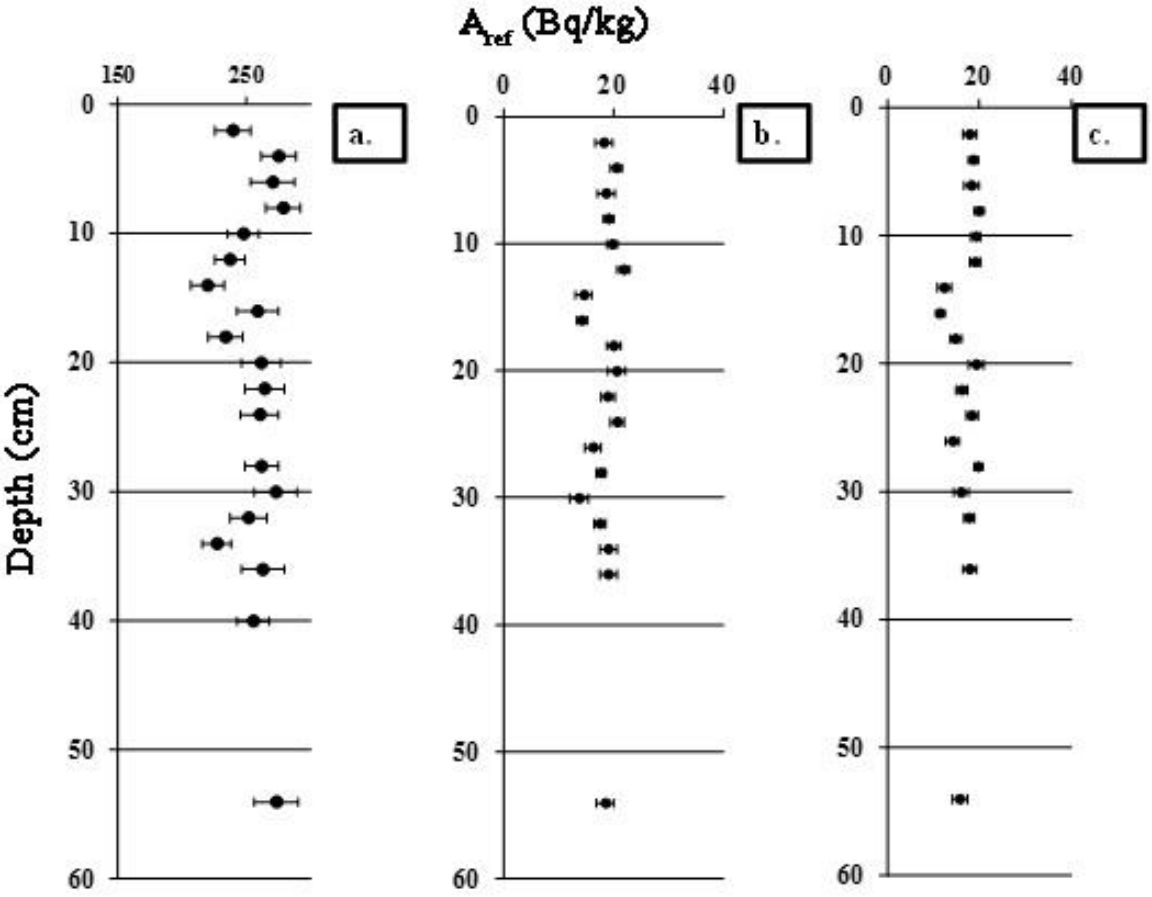

Σχήμα 5.17: Κατανομή συγκέντρωσης ραδιονουκλιδίων A_{ref} (Bq/kg) για το ^{40}K (a) και τις δύο φυσικές ραδιενεργές σειρές ^{238}U (b) και ^{232}Th (c) συναρτήσει του βάθους (Depth) του πυθμένα, όπως μετρήθηκαν στο εργαστήριο λαμβάνοντας πυρήνα ιζήματος από το σημείο πόντισης του συστήματος ΚΑΤΕΡΙΝΑ στην περιοχή μελέτης site 1 (Andr_16a).

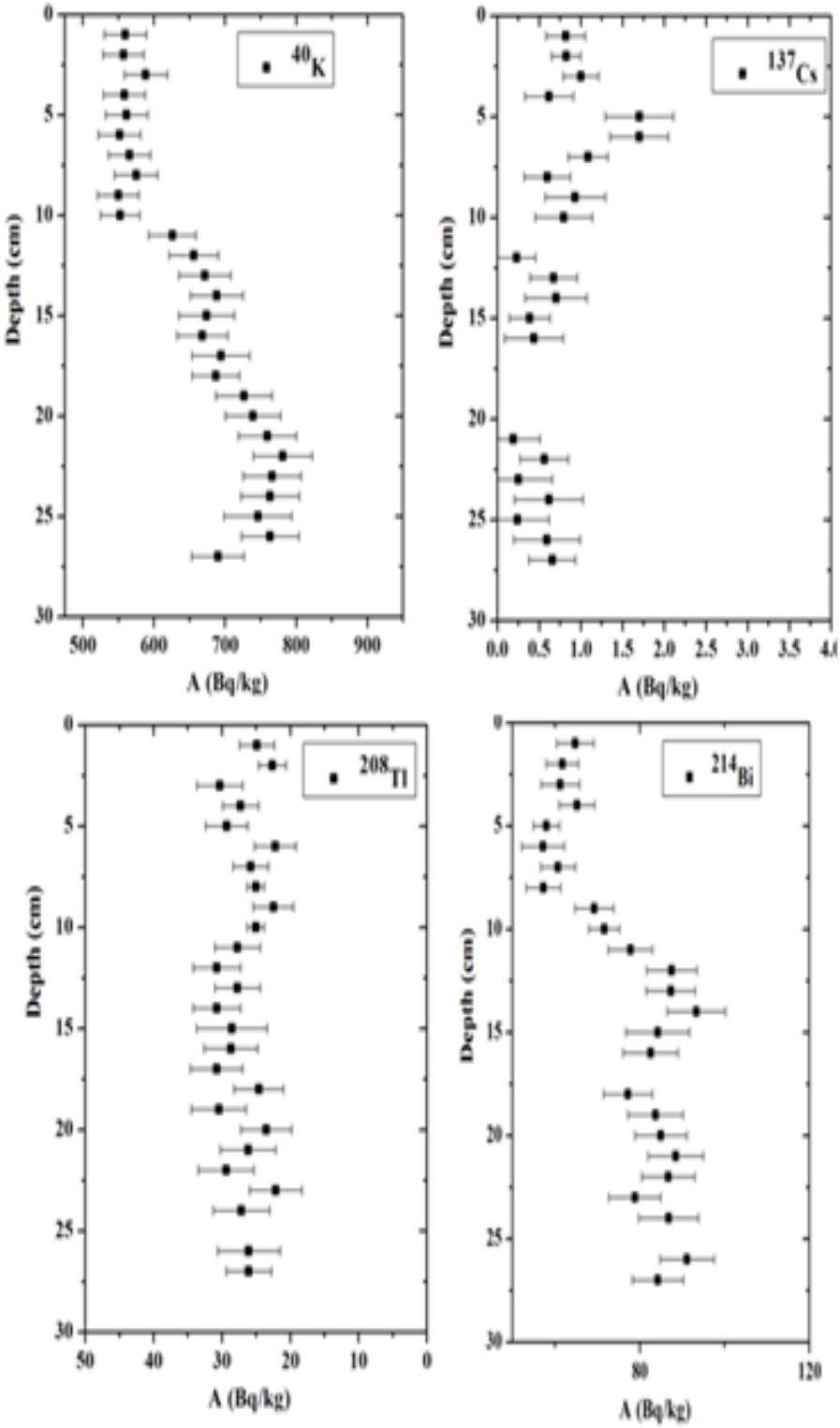

Σχήμα 5.18: Κατανομή συγκέντρωσης ραδιονουκλιδίων A_{ref} (Bq/kg) για τα ^{40}K, ^{214}Bi, ^{208}Tl, και ^{137}Cs, συναρτήσει του βάθους (Depth) του πυθμένα, όπως μετρήθηκαν στο εργαστήριο λαμβάνοντας πυρήνα ιζήματος από το σημείο πόντισης του συστήματος ΚΑΤΕΡΙΝΑ στην περιοχή μελέτης site 3.

Πίνακας 5.4: Αποτελέσματα συγκέντρωσης ραδιονουκλιδίων A_{ref} (Bq/kg), όπως μετρήθηκαν στο εργαστήριο λαμβάνοντας δείγματα ιζήματος από το σημείο πόντισης του συστήματος ΚΑΤΕΡΙΝΑ, στις περιοχές μελέτης site 2 (Ιερισσός) και site 4 (Costinesti).

Sites		**Site 2**			**Site 4**	
Series		Energy (keV)	A_{ref} (Bq/kg)	± %	A_{ref} (Bq/kg)	± %
^{238}U	^{210}Pb *	46.5	-	-	60	20
	^{214}Bi	1764.5	18	10	22	7
	^{214}Pb	351.9	19	6	21	6
^{232}Th	^{228}Ac	911.2	15	9	39	8
	^{208}Tl	583.2	15	8	34	5
	^{212}Bi	727.3	20	18	33	21
	^{212}Pb	238.6	19	6	40	6
-	^{40}K	1460.8	509	5	561	6
-	^{137}Cs	661.7	0.62	26	24	6

* *ανιχνευτικό σύστημα (Ortec GEM-FX8530P4)*

Όλα τα παραπάνω αποτελέσματα χρησιμοποιήθηκαν για την πειραματική βαθμονόμηση του συστήματος ΚΑΤΕΡΙΝΑ στις υπό μελέτη περιοχές. Τα δύο βασικά μεγέθη (cps, A_{ref}) που χρειάζονται στους υπολογισμούς της ανιχνευτικής απόδοσης στο ίζημα προσδιορίστηκαν από μετρήσεις στο πεδίο και στο εργαστήριο και περιλαμβάνουν :

Α.) Τον υπολογισμό του ρυθμού γεγονότων (cps) όπως ανιχνεύονται στα *in situ* φάσματα των μετρήσεων στο νερό (cps_w) και στο ίζημα (cps_s) σε μία συγκεκριμένη κορυφή και οφείλονται στην εκπομπή ακτίνων –γ ενός ραδιονουκλιδίου.

Β.) Την εύρεση των συγκεντρώσεων των ραδιονουκλιδίων (A_{ref}) στο δείγμα ιζήματος, που συλλέγεται στο σημείο βαθμονόμησης του *in situ* συστήματος, οι οποίες αποτελούν τιμές αναφοράς.

Ο πειραματικός προσδιορισμός της απόδοσης του ανιχνευτικού συστήματος ΚΑΤΕΡΙΝΑ για τα χαρακτηριστικά του ιζήματος που βρέθηκαν σε κάθε υπό μελέτη περιοχή και τη γεωμετρία μέτρησης που επιλέχθηκε σε κάθε σημείο, πραγματοποιήθηκε μέσω των παρακάτω σχέσεων:

$$\boldsymbol{\varepsilon_V = \frac{Netcps_s^{E,i}}{I_\gamma^{E,i} \cdot A_{ref}^{\,i}}} \quad (3)$$

$$\boldsymbol{Netcps_s = Ncps_s - (1 + cont._{u.l.}) \cdot \left(^1/_2 \cdot Ncps_w\right)} \quad (4)$$

Όπου:

$\boldsymbol{\varepsilon_V}$: Η ανιχνευτική απόδοση στο ίζημα στην ενέργεια που αντιστοιχεί στην υπό ανάλυση κορυφή.

$\boldsymbol{I_\gamma}$: Η πιθανότητα εκπομπής της ακτίνας-γ του ραδιονουκλιδίου i το οποίο συμμετέχει στον σχηματισμό της κορυφής.

$\boldsymbol{Ncps_s}$: Τα γεγονότα (νερό και ίζημα) ανά μονάδα χρόνου στην κορυφή **στο φάσμα του ιζήματος,** που οφείλονται αποκλειστικά στην εκπομπή ακτίνων-γ από την αποδιέγερδη του ραδιονουκλιδίου i.

$\boldsymbol{Ncps_w}$: Τα γεγονότα (νερό) ανά μονάδα χρόνου στην κορυφή (1460) **στο φάσμα του νερού,** που οφείλονται αποκλειστικά στην εκπομπή ακτίνων-γ από την αποδιέγερδη του ραδιονουκλιδίου i.

$\boldsymbol{A_{ref}}$: Η συγκέντρωση ραδιονουκλιδίων σε μονάδες Bq/L, όπως προσδιορίστηκε στο εργαστήριο στα δείγματα ιζήματος .

$\boldsymbol{Netcps_s}$: Τα καθαρά γεγονότα (ίζημα) ανά μονάδα χρόνου στην κορυφή **στο φάσμα του ιζήματος**, που οφείλονται αποκλειστικά στην εκπομπή ακτίνων-γ από την αποδιέγερδη του ραδιονουκλιδίου i και υπολογίζονται με την κατάλληλη αφαίρεση της συνεισφοράς του φάσματος υποβάθρου (φάσμα στο νερό).

$\boldsymbol{cont._{u.l.}}$: Επιπρόσθετος όρος της συνεισφοράς του φάσματος υποβάθρου όταν το ανιχνευτικό σύστημα τοποθετείται σε απόσταση μεγαλύτερη του 0 cm από τον πυθμένα ($cont._{u.l.}$=0 σε γεωμετρία επαφής).

Η εκτίμηση της απόδοσης του ανιχνευτικού συστήματος ΚΑΤΕΡΙΝΑ μέσω MC προσομοίωσης, για τα χαρακτηριστικά του ιζήματος που βρέθηκαν σε κάθε υπό μελέτη περιοχή και τη γεωμετρία μέτρησης που επιλέχθηκε σε κάθε σημείο, πραγματοποιήθηκε χρησιμοποιώντας τον κώδικα MCNP5, σύμφωνα με τη μεθοδολογία που παρουσιάστηκε στην ενότητα 3.

Τα αποτελέσματα των προσομοιώσεων παρουσιάζονται στα σχήματα 5.19 ως 5.22 όπου σημειώνονται και οι πειραματικές τιμές (exp.) με τα αντίστοιχα σφάλματα. Όπως φαίνεται στα σχήματα αυτά, οι θεωρητικοί υπολογισμοί MC συγκλίνουν με τα αντίστοιχα πειραματικά αποτελέσματα εντός των ορίων των σφαλμάτων, σε όλο το εύρος ενεργειών. Τα μεγάλα πειραματικά σφάλματα οφείλονται στη χαμηλή στατιστική των μετρήσεων στο εργαστήριο.

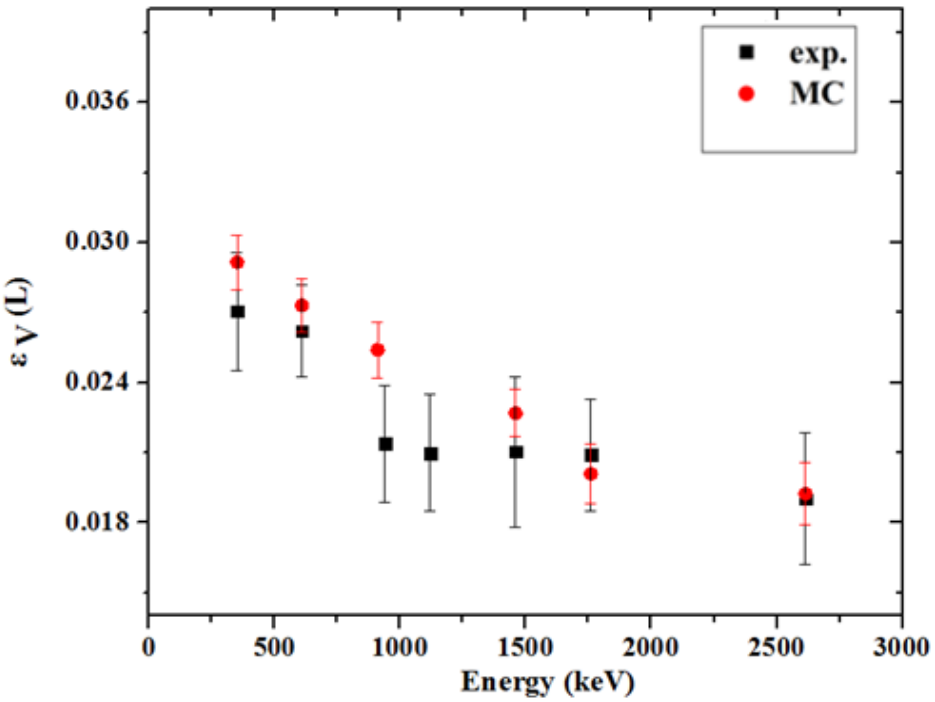

Σχήμα 5.19: Σύγκριση πειραματικής (exp.) - θεωρητικής (MC) καμπύλης ανιχνευτικής απόδοσης (ε_v) του συστήματος ΚΑΤΕΡΙΝΑ για τη μέτρηση στο ίζημα στην περιοχή site 1 (περιοχή Λαυρίου).

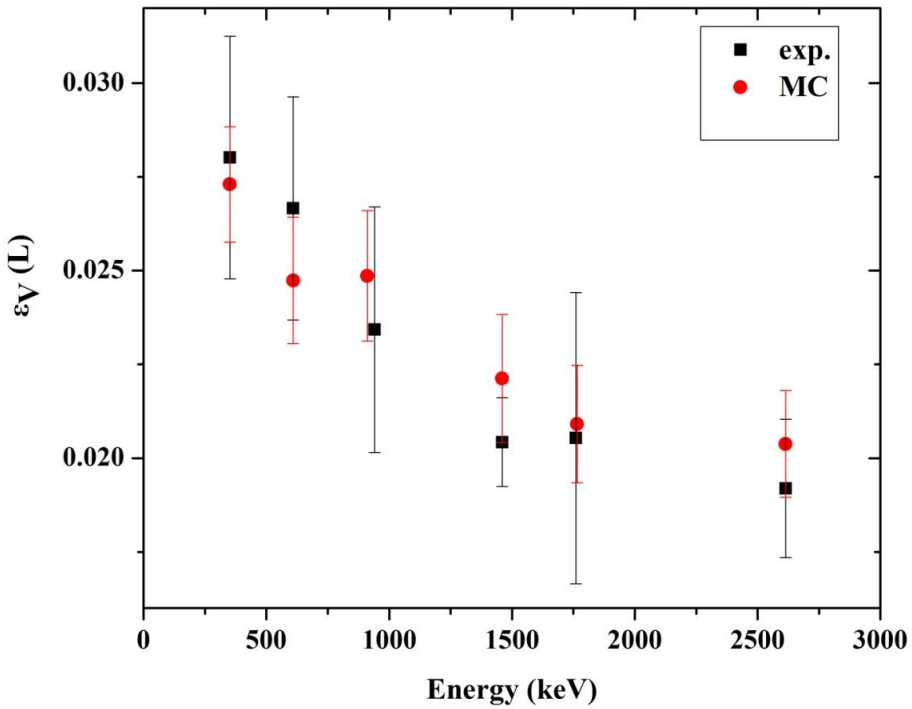

Σχήμα 5.20: Σύγκριση πειραματικής (exp.) - θεωρητικής (MC) καμπύλης ανιχνευτικής απόδοσης (ε_v) του συστήματος ΚΑΤΕΡΙΝΑ για τη μέτρηση στο ίζημα στην περιοχή site 2 (Ιερισσός Χαλκιδικής).

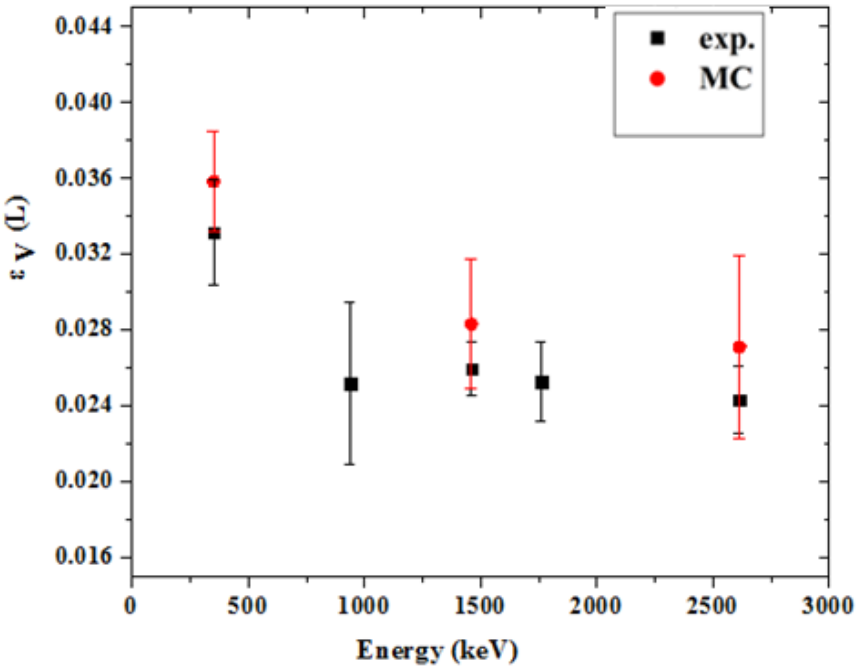

Σχήμα 5.21: Σύγκριση πειραματικής (exp.) - θεωρητικής (MC) καμπύλης ανιχνευτικής απόδοσης (ε_v) του συστήματος ΚΑΤΕΡΙΝΑ για τη μέτρηση στο ίζημα στην περιοχή site 3 (Στρατώνι Χαλκιδικής).

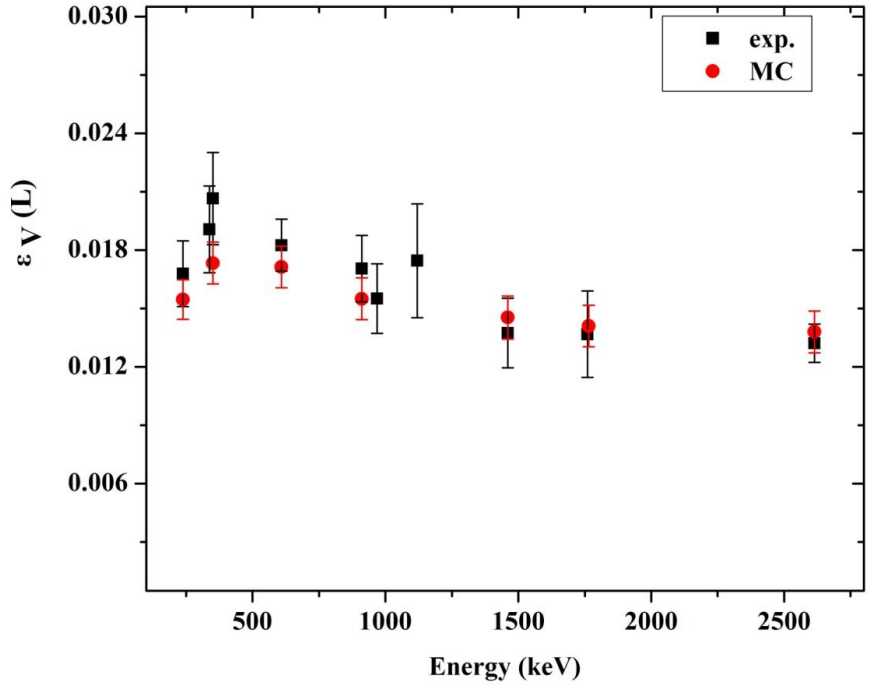

Σχήμα 5.22: Σύγκριση πειραματικής (exp.) - θεωρητικής (MC) καμπύλης ανιχνευτικής απόδοσης (ε_v) του συστήματος ΚΑΤΕΡΙΝΑ για τη μέτρηση στο ίζημα στην περιοχή site 4 (Costinesti, Ρουμανία).

6. Συμπεράσματα - Προοπτικές

Η μεθοδολογία Full Spectrum Analysis που αναπτύχθηκε στα πλαίσια της παρούσας διατριβής και βασίζεται σε προσομοιώσεις Monte Carlo χρησιμοποιώντας τον κώδικα MCNP-CP, αξιολογήθηκε χρησιμοποιώντας τόσο πειραματικά όσο και αντίστοιχα θεωρητικά δεδομένα χρησιμοποιώντας τον MC κώδικα FLUKA. Στη συνέχεια εφαρμόστηκε σε μετρήσεις στο θαλάσσιο περιβάλλον, παρέχοντας ικανοποιητική συμφωνία με τα αντίστοιχα πειραματικά αποτελέσματα σε όλες τις περιπτώσεις.

Ο κώδικας FLUKA αποδείχθηκε πολύτιμη εναλλακτική λύση για περιβαλλοντικές εφαρμογές, λόγω των πλεονεκτικών του χαρακτηριστικών, τα οποία είναι (α) την ικανότητα να ενσωματώνει στους υπολογισμούς ρουτίνες που καθορίζονται από το χρήστη, (β) το κέρδος του χρόνου, στον σχεδιασμό του μοντέλου MC, χρησιμοποιώντας το φιλικό προς το χρήστη γραφικό περιβάλλον Flair, μέσω του οποίου όλα τα βήματα της προσομοίωσης (μοντέλο MC, λάθη στη γεωμετρία, εκτέλεση του κώδικα) μπορούν να ελεγχθούν αποτελεσματικά, και (γ) η δωρεάν διάθεσή του στην επιστημονική και ακαδημαϊκή κοινότητα.

Τα πλεονεκτήματα της τεχνικής FSA σε σύγκριση με τις συμβατικές τεχνικές μπορούν να αξιοποιηθούν σε μια πληθώρα εφαρμογών. Η προτεινόμενη μεθοδολογία FSA θα δοκιμαστεί περαιτέρω σε βραχυπρόθεσμες και μακροπρόθεσμες εφαρμογές για τον εντοπισμό και τη χρονική μελέτη διαφορετικών ωκεανογραφικών φαινομένων που παρατηρούνται σε δυναμικά περιβάλλοντα (SGD, pockmarks, cold seeps, mud volcanoes, faults).

Αναφορικά με τις *in situ* μετρήσεις στον πυθμένα της θάλασσας (θαλάσσιο ίζημα), η διαδικασία ποσοτικού προσδιορισμού των ραδιονουκλιδίων προϋποθέτει τη γνώση της απόδοσης του συστήματος, η οποία εξαρτάται από τα χαρακτηριστικά του ιζήματος (που μπορεί να ποικίλουν σε μεγάλο βαθμό ακόμη και στην ίδια περιοχή μελέτης). Στο πλαίσιο της παρούσας διατριβής μελετήθηκαν οι βασικές παράμετροι που επηρεάζουν την ανιχνευτική απόδοση του συστήματος ΚΑΤΕΡΙΝΑ. Η μελέτη βασίστηκε αποκλειστικά στο MC προσομοιώσεις, λαμβάνοντας υπόψη τις φυσικές ιδιότητες των ιζημάτων (χημική σύσταση, υγρή πυκνότητα, περιεκτικότητα σε νερό) και διαφορετικές γεωμετρίες μέτρησης.

Η μεθοδολογία που αναπτύχθηκε για *in situ* μετρήσεις στον πυθμένα της θάλασσας με τη χρήση του συστήματος ΚΑΤΕΡΙΝΑ, επιτρέπει την ανίχνευση πολλαπλών

ραδιονουκλιδίων και τον ταυτόχρονο προσδιορισμό των συγκεντρώσεων τους, χρησιμοποιώντας όλες τις κορυφές του φάσματος. Επιπλέον, παρέχει μια οικονομικά αποδοτική λύση, εξαλείφοντας τις χρονοβόρες διαδικασίες δειγματοληψίας και εργαστηριακής ανάλυσης. Τα αποτελέσματα της διατριβής, καθιστούν δυνατή την υλοποίηση *in situ* μετρήσεων στον πυθμένα της θάλασσας σε μια μεγάλη ποικιλία εφαρμογών.

Αναλυτικότερα, τα βασικά συμπεράσματα της διατριβής σχετικά με την *in situ* φασματοσκοπία ακτίνων-γ σε πυθμένες θαλασσών συνοψίζονται παρακάτω:

• Επιτεύχθηκε η βαθμονόμηση της ανιχνευτικής απόδοσης του συστήματος ΚΑΤΕΡΙΝΑ για μετρήσεις σε θαλάσσια ιζήματα. Η μελέτη της επίδρασης των διακυμάνσεων των χαρακτηριστικών του ιζήματος στην απόδοση του συστήματος ανέδειξε την υγρή πυκνότητα του ιζήματος ως την πιο σημαντική παράμετρο που ενδέχεται να επηρεάσει τα αποτελέσματα, καθιστώντας έτσι τη γνώση της ποσότητας αυτής (υγρή πυκνότητα) απαραίτητη πριν από κάθε μέτρηση. Η απόδοση του συστήματος επηρεάζεται πολύ λιγότερο από μεταβολές στις τιμές του πορώδους των ιζημάτων (ποσόστωση νερού). Αυτές οι ποσότητες (υγρή πυκνότητα, η περιεκτικότητα σε νερό) μπορούν να προσδιοριστούν εύκολα στο πεδίο, αποφεύγοντας έτσι τις χρονοβόρες διαδικασίες δειγματοληψίας ιζημάτων και της εργαστηριακής ανάλυσης αυτών. Ως αποτέλεσμα, οι συγκεντρώσεις των ραδιονουκλιδίων, χρησιμοποιώντας την *in situ* μέθοδο, μπορούν να προσδιοριστούν σε δραστικά μειωμένο χρόνο. Η λήψη φασμάτων χρονικής περιόδου 2-3 ωρών οδηγεί συνήθως σε επαρκή στατιστική των μετρήσεων.

• Όσον αφορά την επίδραση της ύπαρξης ανομοιογενειών στο προφίλ των συγκεντρώσεων των ραδιονουκλιδίων συναρτήσει του βάθους του πυθμένα, απαιτείται μια πιο συστηματική μελέτη.

• Η προτεινόμενη πειραματική διάταξη για τις μετρήσεις στο ίζημα:

α) Εξασφαλίζει την γνώση της ακριβούς απόστασης του παραθύρου ανιχνευτή από την επιφάνεια πυθμένα της θάλασσας πριν από τη μέτρηση.

β) Παρέχει μια πρακτική και γρήγορη μετάβαση μεταξύ των δύο μετρήσεων στο θαλασσινό νερό και στο θαλάσσιο ίζημα.

Όσον αφορά το θαλάσσιο περιβάλλον, οι μεθοδολογίες που αναπτύχθηκαν αποτελούν ένα πολύτιμο εργαλείο για μια ποικιλία εφαρμογών που σχετίζονται με την παρακολούθηση των επιπέδων ραδιενέργειας, και παρέχουν τη δυνατότητα δημιουργίας μεγάλης βάσης δεδομένων σχετικά με περιβαλλοντικές μελέτες, που αφορούν:

• Στην εκτίμηση ρυθμού δόσης

• Στην χρήση των δεδομένων σε μοντέλα διασποράς των ραδιονουκλιδίων

• Σε γεωλογικές μελέτες (SGD, pockmarks, mud volcanoes, faults) που βασίζονται στη χρήση ραδιοϊχνηθετών.

• Στην παρακολούθηση των επιπέδων ραδιενέργειας σε περιοχές στις οποίες λειτουργούν πυρηνικοί αντιδραστήρες ή/και άλλες βιομηχανίες.

• Στον έλεγχο των ραδιενεργών αποβλήτων που απελευθερώνονται στο θαλάσσιο περιβάλλον και στον χαρακτηρισμό των πηγών αυτών. Η *in situ* μέθοδος αποτελεί τη μοναδική λύση όταν απαιτείται άμεση δράση, ενώ ταυτόχρονα διασφαλίζει την ελαχιστοποίηση των δόσεων που λαμβάνει το επιστημονικό προσωπικό.

Οι MC προσομοιώσεις που υλοποιήθηκαν για *in situ* μετρήσεις στον πυθμένα της θάλασσας, μπορούν να επεκταθούν ώστε να καταστεί δυνατός ο προσδιορισμός των συγκεντρώσεων ραδιονουκλιδίων σε περιπτώσεις πρόσφατων εναποθέσεων (π.χ. εκλύσεις ^{137}Cs από πυρηνικά ατυχήματα). Επιπλέον, και οι δύο μεθοδολογίες που αναπτύχθηκαν μπορούν να υλοποιηθούν σε διαφορετικά συστήματα ανίχνευσης (π.χ. κρυστάλλους $CeBr_3$), αυξάνοντας έτσι ακόμη περισσότερο η εφαρμογή της *in situ* μεθόδου, δεδομένου ότι οι κρύσταλλοι αυτού του τύπου αποτελούν το πλέον ανταγωνιστικό εργαλείο για *in situ* μετρήσεις σε περιβαλλοντικές εφαρμογές.

Λόγω των πλεονεκτημάτων της τεχνικής FSA, η μεθοδολογία που αναπτύχθηκε θα αξιοποιηθεί επίσης για *in situ* μετρήσεις σε πυθμένες θαλασσών (ίζημα), πραγματοποιώντας εκτεταμένες προσομοιώσεις MC. Για το σκοπό αυτό ο κώδικας FLUKA θα χρησιμοποιηθεί για την προσομοίωση της ακριβής γεωμετρίας της πηγής ιζήματος (με χρήση εξειδικευμένων ρουτίνων που καθορίζονται από το χρήστη), λαμβάνοντας υπόψη στην προσομοίωση όλες τις λεπτομέρειες της πειραματικής μέτρησης (φυσικές ιδιότητες των ιζημάτων, γεωμετρία μέτρησης). Η επέκταση της τεχνικής FSA για *in situ* μετρήσεις στον πυθμένα της θάλασσας, αναμένεται να αυξήσει περαιτέρω την αξιοπιστία των αποτελεσμάτων και κατά συνέπεια να διευρύνει το ήδη υπάρχον πεδίο εφαρμογών.

CHAPTER I:
Introduction

1.1 Motivation and objectives

1.1.1. Sources of marine radioactivity

Ionization radiation sources can be divided into two main categories, the natural sources and the sources arising from anthropogenic activities. The first category includes naturally occurring radionuclides either present on the earth's crust (primordial or terrestrial) or produced in the upper atmosphere due to the interaction with cosmic rays (cosmogenic). Cosmic radiation is an important contribution of the natural radiation background and is a collection of many different types of radiation from charged particles or sub-atomic particles to heavier nuclei and photons. Some of the most abundant cosmogenic radionuclides are ^{3}H, ^{14}C, $^{36/38}Ar$, $^{7/10}Be$ ^{26}Al and ^{22}Na. Primordial radionuclides exist since the time of the formation of the earth and are still present due to their very long half-lives or due to the constant production in decay chains from progenies with long half-life. The main components in this category in terms of contribution to human exposure, are the decay series of ^{238}U and ^{232}Th, the radionuclide ^{40}K and to a lesser extend the radionuclides associated with the decay series of ^{235}U (approximately 0.72% of the natural U) and the singly occurring ^{87}Rb.

The second category includes both natural radionuclides as Technologically Enhanced Natural Occurring Radioactive Materials (TENORM) and artificial ones. TENORM can be associated with some involved activities of different industries during the processing of the raw material, such as coal industries during mining and combustion (Karst_07; Landa_07; Rouni_01), oil and gas (Nab_16; Landa_07), metal mining (Landa_04; Sal_95; Heat_95), fertilizer (Bol_95) and recycling industries (Bah_07; Mas_06). In all the above cases the processing of the raw material leads to large quantities of by-products that may contain enhanced levels of certain radionuclides, depending on the raw material composition and the process involved. These by-products are stored in open plants either in solid (e.g. fly-ash tailings) or in soluble form (e.g. phosphogypsum stacks).

The expansion of industrial activities near coastal areas poses the risk of direct leakage of these material into the sea (either by underground paths or weathering) thus affecting the involved ecosystems.

In addition to the natural radiation sources, large amounts of anthropogenic radionuclides have been added to the environment. Some of these elements are radioactive isotopes of H, C, Cl, I, Te, Xe, Cs, Sr, Am, Pu. The artificial radionuclides present in the marine environment can be associated with various human activities (IAEA_91):

- The explosion of nuclear weapons either in the atmosphere or during underwater testing, from which several radionuclides such as ^{90}Sr, $^{239,240}Pu$, ^{137}Cs, ^{241}Am, ^{3}H and ^{14}C are still present in measurable quantities.
- The controlled release of low level radioactive materials from nuclear power plants, reprocessing plants, industries, hospitals, scientific research centers and nuclear weapons facilities.
- The disposal of radioactive wastes directly into the ocean.
- Accidents occurring directly at sea, involving potential releases of radioactive materials into the marine environment, (e.g. the loss of a vessel of a nuclear powered submarine, or losses of submarines carrying nuclear fuel or nuclear weapons, or the re-entry of a satellite containing nuclear materials).

The three main sources of anthropogenic radionuclides (observed in the ocean) are, nuclear weapons testing in the atmosphere, the power plants' accidents (i.e. Chernobyl, Fukushima) and water-borne discharges from nuclear reprocessing plants, notably Sellafield in the UK and Cap de la Hague in France. Other sources contribute orders of magnitude less to the contamination of the world ocean than the three major sources (IAEA_05a). The oceans may receive radioactive fallout directly from the atmosphere, or by discharges into the ocean as liquid waste or from dumped solid wastes, and indirectly as runoff from rivers (IAEA_05a). Some radionuclides stay in the water in soluble form, whereas others are insoluble or adhere to particles and thus, are transferred to marine sediments. Due to variations in the source inputs and subsequent path (dispersion, mixing and transport) in the world's oceans, one region differs from another according to the predominant source and transport path. Although the ocean contains most of the anthropogenic radionuclides released into the environment, the radiological impact of this contamination is still low compared to radiation doses from naturally occurring radionuclides in the marine environment (e.g. ^{210}Po), that are on the average two orders of magnitude higher (IAEA_05a).

In particular, the Mediterranean Sea exchanges water with the Sea of Marmara (through the Dardanelles Strait) the Black sea (through the Bosporus Strait) and the North Atlantic Ocean (through the Strait of Gibraltar). The majority of anthropogenic radioactive releases in the Mediterranean Sea have originated from the Chernobyl accident and nuclear weapon tests. Nevertheless, to a small extent, part of the overall output has originated from nuclear plants operating in other European countries. Nuclear facilities in the Mediterranean basin are mainly located along rivers and therefore the potential radioactive releases are subjected to riverine geochemical processes that delay the discharge to the sea. Nowadays, two nuclear plants are planned to be commissioned close to coastal areas in Turkey at Sinop (construction start is planned for 2017 and operation from 2023) and at Akkuyu (construction is expected to begin at the end of 2017). In addition to the anthropogenic radionuclides, releases from oil transportation accidents and industrial solid wastes (consisting of slag from coal mining, coal processing and steel making, sludge from the processing of ores, dust or combustion ashes, mine tailings) end up in the Mediterranean Sea, since a large number of industries is located along the coast and at the catchment basins of rivers.

As nuclear and industrial activities continuously grow and accidents still occur (a recent example is the accident at the Fukushima Daiichi nuclear power plant (Stein_14), the environmental radioactivity monitoring has been practiced for many decades now. Moreover, in recent years the original focus of monitoring the environment for artificial radioactivity has shifted into the control monitoring of releases from nuclear installations and has extended to naturally occurring radionuclides (Engel_08). The radioactivity monitoring program for the marine environment varies according to the purpose, the source of radioactivity and the studied environment. A first classification among the different categories may distinguish between monitoring in emergency conditions and under normal operating conditions. In general, the monitoring planning addresses in three different situations, routine monitoring, emergency readiness and emergency monitoring (Engel_12). While sporadic measurements of high accuracy are sufficient in the first case, continuously monitoring, even with a compromise in the precision, is necessary in emergency monitoring for rapid assessments in order to quickly inform the involved authorities but also to verify the effectiveness of the actions taken (Engel_12). On the other hand, the strategy followed regarding emergency readiness requires continuous measurements in order to detect an emergent event but also temporal measurements of many different parameters (radionuclides concentration, temperature, salinity values, distribution coefficient K_d) in

order to determine the environmental impact of the event. Nowadays, the continuous monitoring programs in the marine environment consist of *in situ* observations, satellite data for key oceanographic parameters (including ^{137}Cs) and sophisticated numerical models (Harms_03). Concerning numerical models, there are two types: a) hydrodynamic circulation models (HD) that give estimates on the three-dimensional flow field and (b) transport models able to estimate the dispersion of a radioactive contaminant in the aquatic systems. These models can be used separately, however frequently the transport models use the results of the HD models to extrapolate the event in space and time.

To evaluate the environmental impact of the radioactive release to the oceans, activity concentration measurements are required both in the seawater column and on the seabed either as reference data, e.g. for the execution and/or validation of numerical models, the characterization of a radiological incident/accident or for clear radiation protection purposes, e.g. dose estimations. One of the most widely used techniques for the determination of the activity concentrations is γ-ray spectroscopy, which is also utilized in this work.

1.1.2. Radio-tracers and applications

Despite the hazardous effects of radiation to the human health, the wealthy presence and the diversity of non-stable elements in the environment offers the possibility to use them to study a great variety of dynamic physical, chemical and biological processes in soils, air, freshwater and oceans. Moreover, radionuclides have been extensively used as tracers in industrial activities (IAEA_04) and nuclear medicine. The selection of a certain radionuclide as a radiotracer depends primarily on the chemical association of the tracer to the elements involved in the studied process and the radionuclide's half-life that should be in relevant time-scale with the studied process. Some of the most extensively applied radionuclides in environmental studies and the corresponding processes are summarized in the work of Santschi and Honeyman (1989), Lal (1999) and Santos et al. (2008). The most extensively used radionuclides of cosmogenic or anthropogenic origin in environmental studies, are ^{14}C, ^{3}H, $^{7/10}$Be, ^{90}Sr and Cs ($^{134/137}$Cs), I and Pu ($^{238\text{-}242}$Pu) isotopes (Lind_10; Pov_10). In addition, a great variety of naturally occurring radionuclides mainly from the ^{238}U and ^{232}Th series complements the large list of the available radiotracers for environmental applications. In this section a brief discussion on the available radiotracers and its association to various processes is made, focusing on the applications in the marine

environment.

^{7}Be has been widely applied in studies of atmospheric circulation (Loz_12; Garc_12). Moreover, it is also used in sediment studies (Tayl_13) but the data are derived for much shorter time periods due to the very short half-life (53.3 days) (Chop_13). ^{14}C has been used for archeological, geological, and biological dating. The first application of ^{14}C as a tracer was to estimate the age of deep-sea sediment cores was performed in 1951 (Arrhe_51) while archeological dating has been reported in literature since 1949 (Libby_49). Furthermore, the concentration ratio of certain radionuclides has been used for dating geologic materials (Brö_93, 04, 05), such as ^{40}K/^{40}Ar for igneous (plutonic) rocks and ^{87}Rb/^{87}Sr for metamorphic and sedimentary rocks (Chop_13).

Several anthropogenic radionuclides have been applied for soil erosion and sediments aging, deposition and accumulation rates (lakes, marine sediments, stream sediments). However, most studies have been focused on the use of ^{137}Cs (Pap_13; Mab_13; Tsab_15) which has originated primarily from nuclear weapons testing and nuclear accidents (fallout was first detected in the early 1950s, reached a peak in the early 1960s and rapidly declined to low levels till 1986 where significant inputs were received in several European countries as a result of the Chernobyl accident). This time-variable input of ^{137}Cs can be traced in soils and sediments through depth profiling. In the depth (vertical) profile, at least one or more regions containing high ^{137}Cs concentrations (peaks) are formed that can be directly associated with the fallout of nuclear weapon tests and the Chernobyl accident. By attributing the peaks present in the vertical profiles to the dates of these incidents, the chronology of sediment deposits and thereby the estimation of sedimentation rates is possible.

Increasing usage of alternative radionuclides for soil and sediment aging and rate studies, particularly ^{210}Pb and ^{7}Be, has led to the improvement of the quality and accuracy of the results when multiple radiotracers are used (Mar_10). For instance, ^{210}Pb profile measurements are frequently used complementary to ^{137}Cs ones in many applications, while in other studies, the profile of the anthropogenic radionuclide ^{241}Am, is also included (Smith_97; Beks_00). ^{210}Pb has been widely applied in studies concerning rates and patterns of soil redistribution and sediment deposit dating (Abril_92; He_97; Mab_14).

Concerning the marine environment, radionuclides have been widely used as tracers in different applications, providing basic insight into a variety of oceanic processes (IAEA_05a). Moreover, radiotracers have been increasingly used in studies in aquatic reservoirs associated with oceans, such as rivers, lakes or groundwater sources, in order to

investigate different processes and their space scales (e.g. flow rates, transfer, settling or mixing rates, residence times or reservoir age and size, pathways of transfer). The first implementation of a radionuclide as a tracer in oceanic investigations was the application of ^{226}Ra to study the vertical diffusion in the water column (Koc_58) and the renewal time of water masses in oceans (Koc_62). Different Ra isotopes (^{226}Ra, ^{228}Ra, ^{224}Ra, and ^{223}Ra) have been used independently or in correlation to determine water age and mixing (Pov_05).

Another example of great interest is the utilization of ^{14}C and tritium in studies on the rates of ocean mixing. ^{14}C is particularly useful since, due to the slow radioactive decay (half-life of approximately 5.700 y) and the slow mixing and ventilation of deep-ocean waters, it can provide information about the source and age of deep water masses and validate global ocean circulation models. On the other hand, ^{3}H is a tracer for modern groundwater (due to the relatively short half-life 12.32 y) studies and it has been widely used for estimating residence time distributions of groundwater and surface water (Viss_16).

Anthropogenic radionuclides have been widely applied as tracers in oceanographic studies. For instance, Pu isotopes have been used to study water mass transport (advection and convection), particle fluxes and scavenging, and are used for validating purposes in various global circulation and biogeochemical ocean models (Lind_10). Plutonium isotopes and ^{129}I have been utilized as historical indicators for the transport of seawater, contaminated with radioactive waste from nuclear fuel reprocessing plants (Yam_12; Coop_01; Yiou_94). ^{90}Sr, ^{137}Cs, ^{3}H and other fission products have been utilized as tracers of water movements from land via lakes and rivers into the sea, as well as for exchange between surface and deep waters studies in the oceans (Tsab_14; Del_14; Miró_12; Schlo_91).

A different application of Ra isotopes and its progenies is found in studies of freshwater discharges into the oceans through underground paths. Subsurface discharge of water from coastal aquifers, called submarine groundwater discharge (SGD), has been recognized as an important component of the hydrological cycle. SGD is an important factor in the understanding and sustainable management of coastal fresh water aquifers, especially in highly populated areas of the world. In addition, SGD is a significant pathway for material transfer between the land and the sea (Char_08). As a noble gas, ^{222}Rn can diffuse out of soils and sediments and thus has been extensively used for determining exchange rates across both air-sea and sediment-water interfaces as well as in studies

related to SDGs into the coastal zone. ^{222}Rn and its progenies have been widely used for tracing possible location of SGD sources or determining SGD fluxes or freshwater/saltwater mixtures (Tsab_12; Burn_06; Pov_06a,b). Continuous monitoring of the ^{222}Rn progenies has been also utilized in pre-earthquake studies (Plast_10; Das_06).

Another application of great importance is the utilization of radiotracers for studying the accumulation of toxic or radioactive substances entering the marine environment and tracking the flux and fate of both dissolved and particulate matter (Bues_90). Radioactive isotopes of Th have been used for studying the removal behavior of potential pollutants as they present a similar chemical behavior with Fe, Po, Pb, Am, Cr (III) and Hg (Sants_80). ^{234}Th has been used as a particle scavenging tracer to determine particle residence time and transformation rates in seawater (Gust_98; Sants_89). The export rate of particulate organic carbon (POC) has been determined from the export flux of Th using the ^{234}Th/^{238}U disequilibrium (Bues_92).

Different elements and measurement types and techniques are used depending on the studied process, the radiotracer abundance and the emission type (alpha, beta, γ-rays). The benefit of exploiting the γ-ray emission of a radiotracer is that γ-rays are highly penetrating and therefore can be easily detected, in many applications even without pretreatment of the samples that is oftentimes mandatory in techniques using alpha or beta spectroscopy. Therefore, an advantage of using γ-ray spectroscopy is that the measurements can be held directly on site (depending on the studied process), giving a better representation of the studied environment. Moreover, γ-ray spectroscopy provides the possibility of continuous monitoring that is required in many applications (e.g. characterization of an SGD, seismicity studies). More importantly, a significant part of the available radiotracers, including the extensively studied ^{137}Cs and many naturally occurring radionuclides, can be detected through their γ-ray emission.

1.1.3. *In situ* and laboratory based γ-ray spectroscopy techniques

As mentioned above, the most widely applied method for radioactivity measurements in the environment is the γ-ray spectroscopy. Measurements have been performed either on laboratory or directly in the field (*in situ* measurements). Different techniques have been developed for both *in-situ* and laboratory measurements but much more information is found in the literature related to the latter. There are some applications in which laboratory measurements are irreplaceable (e.g. applications of ultra-low activity concentrations) and

others, in which one technique has been implemented complementary to the other. For instance, laboratory measurements have been implemented in order to experimentally perform calibrations of detectors used for *in situ* measurements (Mauč_04; Bag_10). On the opposite side, *in situ* measurements are often used for optimization and focusing in the sampling procedure that is required for laboratory measurements (Osv_99). Nevertheless, there is an extended field of applications in which the exclusive utilization of one method or the other is possible, and in such cases the appropriate method is selected according to its beneficial characteristics. In general, laboratory-based measurements are preferable when high-precision measurements are essential, nevertheless in many applications the *in situ* method is the only option, as in cases where mapping of large areas or measurements on a continuous basis are required.

Laboratory measurements are performed in stationary high resolution detectors mounted with the necessary electronics for signal processing. Traditional laboratory analysis is a time- consuming technique that involves many different processing procedures before obtaining the results. The overall procedure includes several steps, starting with the collection of the samples and their transportation to the laboratory, where they are stored under controlled conditions. The samples in many applications (soil, sediment samples) have to be further processed before performing the measurement. This procedure involves moisture removal by oven or freeze-drying, sieving and pulverization of the samples in order to be homogenized and shielding in air-tight containers prior to the measurement. In other applications, even more time-consuming pre-concentration procedures are required (e.g. ^{137}Cs measurements in water samples).

Although the laboratory technique can provide high-accuracy measurements and can simultaneously identify many radionuclides (usually laboratory facilities are supplied with high-resolution detectors), it suffers from many disadvantages. Starting with the sampling procedure, this is a time-consuming operation sometimes involving expensive and heavy equipment for sampling, especially for applications in the marine environment, or difficulties in accessing the samples (unreachable sites for divers), while the collected samples may not be representative for covering large areas. An additional drawback is the loss of radioactive gasses during the sample transport and preparation (Benk_00). Another important disadvantage is the increased acquisition time that is necessary to obtain spectra with adequate statistics (typical time is ~24h). It has been reported that the laboratory counting time must be increased by 20 times in order to give a similar statistical accuracy to the one obtained using the *in situ* method (Finck_76). The enhanced counting time can be

associated with the smaller quantities involved, since laboratory measurements are performed on small samples while the information is collected over a wide surface or volume using the *in situ* method. It has also been reported that the minimum detectable activity can thus be reduced by approximately 6 times (Finck_76) or more (Elef_13) in a field measurement.

On the contrary, the *in situ* method is a two-step procedure, thus reducing the requirements for sampling expeditions and laboratory-based analytical work (Hamil_94; Pov_97). The detection system is deployed directly on the field in the studied area and the results are obtained in a considerably reduced time. The prompt availability of the results is a significant advantage that can be exploited in many different applications. An additional advantage over laboratory-based measurements is that the measurements are performed in large volume samples and additional depth information is obtained, while minor inhomogeneities are averaged out (Allys_94). Therefore, the *in situ* method is more sensitive and provides more representative data since the measurements are performed directly in the studied environment.

Nevertheless, for *in situ* γ-ray spectroscopy applications in soils or sediments, the separate knowledge of the activity distribution with depth, as well as the density, water content and the chemical composition are required in order to perform accurate measurements (Beck_72), since variations (lateral or vertical) of these parameters may affect the detector response (Beck_72; Tyler_94). Moreover, a re-calibration procedure is mandatory each time the physical characteristics of the studied environment or the measurement geometry change. These are the most important disadvantages that limit the applicability of the *in situ* method.

Despite these drawbacks, *in situ* gamma-ray spectroscopy has clear advantages over conventional laboratory measurements when applied in the aquatic environment for a number of applications (Pov_08) that are summarized below:

- It allows time-efficient mapping of the levels and distributions of natural and/or anthropogenic radionuclides, in large areas like rivers, lakes and on the seabed used in many applications, such as in geological mapping, mineral exploration and contamination assessment studies.
- When used in conjunction with a sampling campaign, it provides an efficient and cost-effective method to guide sampling in order to achieve a more representative sampling from the studied area, especially in cases where hot spots are present.
- It can offer real-time information on large scale (spatial and temporal) about the

presence and levels of radionuclides, thus replacing the time-consuming laboratory measurements

- It offers the unique ability of providing information on the presence and nature of radioactive material contained in sunken or dumped radioactive wastes. Using underwater monitoring systems, potential releases can be under surveillance and control **(**Harms_99**)**.
- It can operate on a continuous base, monitoring gamma-ray emitters in seawater and fresh water. This operational mode can provide early warning at nuclear facilities with authorized discharges to the aquatic environment (e.g., nuclear reprocessing plants, nuclear power plants), at underwater nuclear waste dumpsites or in cases of accidental releases to the marine environment.
- It can provide rapid information of contaminated areas in emergency situations related to accidental releases from nuclear facilities, by estimating possible increases in the radionuclide levels both on seabed sediments and on water columns as well as the evolution in time and space) of the pollutant.
- The continuous monitoring of natural radionuclides is essential in many tracing applications, such as the investigations of ^{222}Rn progenies in groundwater, pre-earthquake studies and submarine groundwater discharge studies or the use of ^{40}K and Ra isotopes to study various marine and coastal processes.

1.2 Scope of the thesis

Due to the great variety of applications of radionuclides and their relation to human welfare either through radiological and environmental science surveys or industrial exploitation, γ-ray spectroscopy on the laboratory basis has been practiced for nearly a century now and is a well-established technique. However, soon after the first nuclear weapon tests, the need of field measurements led to the development of the *in situ* γ-ray spectroscopy.

The main reasons that have led to the increasing interest for *in situ* measurements can be attributed to some advantages that are crucial in radiological surveys, such as:

- The ability of continuous monitoring, that serves as an alarm system in large industrial facilities.
- The benefit of rapid assessments that is essential for a) quantifying accidental releases and routine emissions from nuclear power plants, b) site characterization

applications in cases of remediation and decommissioning of nuclear and other industrial facilities.

- The ability to obtain large scale (temporal and spatially) data which are crucial for hydrodynamic and dispersion models.

Nowadays, the implementation of *in situ* measurements is continuously growing, in an extended field of applications, as it is a cost-effective technique, able to provide immediate results or long-term observations (Pov_08). Moreover, the unique ability to provide real-time information, under real conditions, leads to a better representation of the studied environment.

During the last decades, several *in situ* systems consisting of different types of detectors have been widely employed for studies in air (Allys_98; Tyler_08; Casan_14) or soils (Beck_72; Boson_08; Gonz_12). A review of the development and implementation in the environment of *in situ* and airborne γ-ray spectroscopy techniques can be found in literature (Tyler_08; Jones_01; Hendr_01). While analytical techniques are available and high accuracy results can be obtained using *in situ* or aerial techniques for soil measurements there are still some unresolved issues. The prior knowledge of the vertical activity distribution and - to a lesser extend - the moisture content, density and chemical composition of the soil (Tyler_99; Tyler_96; Beck_72) are important parameters affecting the accuracy of the analysis when the *in situ* method is implemented for quantitative measurements in soils. The main parameter affecting the accuracy of the results using aerial techniques is the complexity of the geometry of the measurements (buildings, trees, rocks). In many cases, the surroundings can add to the total detected photon flux (buildup due to surrounding materials, background radiation) or act as a shield, screening the radiation (Boson_08).

Regarding the marine environment, there is an increased interest for radioactivity monitoring that can be associated with the expansion of industrial activities and nuclear power plants near coastal zones. In addition, the development and application of models for the dispersion of radionuclides proved the necessity of large scale radionuclides concentration measurements in order to validate these models. Despite the clear advantages of the implementation of an *in situ* method instead of laboratory-based measurements for radiological surveys, relatively few applications concerning *in situ* measurements in the marine environment are reported in literature. Among them only a small number is addressed in applications in marine sediments including mapping surveys for:

a.) Anthropogenic radionuclides **(**Miller_82; Noakes_99; Osv_99; Kob_99; Osv_01) as well

as for natural radionuclides (Hendr_01; Graaf_07; Andr_15).

b.) Investigation of ^{137}Cs-containing radioactive particles offshore (Mauč_04).

c.) Radiological investigation at dump sites (Hamil_94; Pov_97).

d.) Continuous distributions of ^{137}Cs and ^{134}Cs released from the Fukushima Daiichi Nuclear Power Plant (Thorn_13a).

In the water column, studies related to monitoring of anthropogenic and natural radionuclides in the seawater column have been performed (Aak_95; Wedek_99; Pov_01; Meij_02; Put_04; Osv_05; Sart_11; Zhang_15), while a substantial part is focused on monitoring natural radionuclides for applications of SGD characterization (Pov_06a; Pov_06b; Tsab_08; Tsab_10; Tsab_12).

The sparse reported data can be associated with the rise of complexity when performing measurements in the marine environment both due to the requirement of special equipment (water-tight mounting, low power consumption, stand-alone operation) and due to the introduced implications related to the detector response, especially for seabed applications, which are discussed below. The aim of the thesis is to investigate problems associated with underwater γ-ray spectroscopy and provide solutions for accurate measurements both on the seabed and in the seawater column. Regarding the aquatic environment, γ-ray spectroscopy has reached a high level of analytical performance (Tsab_11; Bag_10; Pov_08; Tsab_05; Jones_01). The most commonly used approach, is to monitor broad spectral windows that include the photopeaks of the radionuclides of interest. Nevertheless, there are some important drawbacks inherent in the window analysis technique, starting from the fact that only limited spectral information is exploited and sometimes large uncertainties may occur due to the existence of convoluted peaks, since the majority of the available *in situ* systems consist of low resolution crystals (e.g. BGO, NaI). An additional crucial drawback is the inability of the technique to identify unexpected radionuclides (Cac_12). The presence of additional unexpected features in the spectra, would lead to erroneous results in the activity concentration measurements (Guil_01). The window analysis has been gradually substituted by more promising techniques that exploit the whole spectral information and can overcome the aforementioned disadvantages.

A widely implemented technique is the full-energy peak analysis over the whole spectrum. Using this technique, a calibration performance over a wide range of energies is required (Bag_10; Zhang_15) in order to derive the activity concentrations. Recently, a Full Spectrum Analysis (FSA) technique that utilizes the full spectral shape (full-energy peaks, Compton Continuum) has been employed and applied in soils (Cac_12), sediments

(Mauč_04) and airborne studies (Guil_01; Hendr_01; Minty_92). This technique requires reference spectra, which exactly match the properties of the measurement (materials, geometry setup) and can be experimentally obtained or via theoretical simulations (Monte-Carlo codes). Therefore, the spectrum of the actual measurement is represented by a theoretical spectrum formed by a linear combination of these reference spectra. Using this technique, the optimal activity concentrations are derived by fitting the theoretical spectrum to the measured one via χ^2 minimization calculations in a straightforward manner. The great benefit of this technique is that the time-consuming analysis is substituted by the convergence of the utilized code, which is usually reached within a few minutes.

Nevertheless, the currently developed FSA techniques take into account only a minimum number of radionuclides and additionally assume that the secular equilibrium is ensured for the natural radionuclides of the same decay series. The main purpose of this work regarding *in situ* measurements on the aquatic environment was to develop a time-efficient method using the FSA technique, able to provide accurate quantitative results, regardless of the existence of any type of equilibrium. The steps in developing the proposed FSA technique included the implementation of general purpose Monte Carlo codes (Chapter III) to perform a theoretical calibration of the detector, the evaluation of the theoretical results (using both experimental and data obtained using a different MC code) and the application of the technique in the marine environment in several different test cases. The proposed technique and the obtained results are discussed in detail in Chapter IV.

Regarding measurements on the seabed, additional factors hinder the quantification procedure in addition to the large volumes and complex geometry setup measurements that are always related to *in situ* γ-ray spectroscopy measurements. A first implication is that events arriving from radionuclides present both in the seawater and the sediment are recorded during the measurement. The contribution of the recorded events attributed to radionuclides present in the seawater column constitutes a source of background radiation that should be properly subtracted. Moreover, photons are highly attenuated both in the seawater and in the sediment and thus, the selection of a close source to detector measuring setup is mandatory. This selection leads to the detection of radionuclides present at deep sediment layers lying well beneath the detector. Therefore, the understanding of the radionuclide concentration vertical distribution, the attenuation properties of photons on the source and surrounding materials, the sediment physical properties as well as the effect of these parameters to the detector response (detection efficiency) is crucial in order to perform accurate measurements. A major drawback to the difficult task of quantification is

the fact that the aforementioned parameters can change from one environment to another or even within the same environment. The unknown distribution of the radionuclides in the sediment matrix prior to the measurement remains a problem up to date, since extreme inhomogeneous profiles can drastically affect the results, however partial solutions have been proposed by implementing different approaches (Feng_12; Tyler_08; Korun_91; Korun_94). However, this problem concerns only a few cases, while the distribution of natural radionuclides in the sediment in undisturbed environments is rather homogeneous.

A major drawback of global range, that remains a challenging problem, is the lack of a generalized calibration procedure able to provide accurate quantitative results in different environments. The influence of the sediment physical characteristics to the response (detection efficiency) of the detector (Groot _09; Graaf _07) renders the calibration site-specific, related to the sediment characteristics. Therefore, the influence of the sediment geophysical characteristics to the detection efficiency should be thoroughly studied in order to obtain accurate results. As a consequence, the need for independent recalibration procedures occurs which limits the applicability of the *in situ* spectroscopy as an absolute method (Tyler_96).

The main objective of this thesis was thus also to develop a methodology for quantitative *in situ* measurements on the seabed able to provide accurate results when applied in different environments. The description of the adopted methodology and the obtained results are discussed in Chapter V. A substantial part of the analytical work is focused on understanding the problems associated with *in situ* measurements on the seabed, where the available data are sparse and the analysis is impeded by several additional parameters (compared to *in situ* measurements in the aquatic environment), related mostly to the physical properties of the sediment and the geomorphology of the environment. Therefore, a lot of effort is given to investigate experimentally and theoretically a wide range of associated problems that lead to corrections of detector responses and calibrations, arising both from the morphology and the physical properties of the studied environment as well as from the implementation of different geometry setups. This was accomplished via Monte Carlo simulations, by performing theoretical calculations of the transport of photons in the studied geometries including detailed information of the sediment physical properties. In addition, comparisons with experimental results were performed to evaluate the theoretical work, by deploying the detector in four different environments.

As a result, a calibration approach for *in situ* γ-ray measurements on the seabed is presented, in full spectral range (instead of window analysis) exploiting the advantage of

the simultaneous detection of more than one radionuclides (calibration in full spectral range). The parameters affecting the detection efficiency were determined, and their effect on the detector calibration was systematically studied, via MC simulations. Moreover, an alternative approach of conducting an experimental calibration was accomplished by performing *in situ* γ-ray measurements on the seabed along with complementary laboratory measurements. The advantages and disadvantages of the two methods are thoroughly discussed. The aspects of the optimization of the proposed techniques as well as future applications are discussed in Chapter VI along with the main conclusions of this thesis.

CHAPTER II:
Theoretical aspects of γ-ray spectroscopy in the marine environment

2.1. Introduction

In the following sections a description of the properties of sediment and seawater, related to radionuclide concentration measurements is given. Moreover, the instrumentation utilized for γ-ray spectroscopy measurements is discussed along with the arising implications in the determination of the activity concentrations when dealing with voluminous environmental samples.

2.2. Sediment and water properties

2.2.1. Properties of marine sediments and the ocean

The ocean covers 71% of the surface of earth. The seawater is composed of a mixture of water with salts (mostly constituents of chlorine, sodium and sulfate, as well as magnesium, sulfur, calcium, and potassium) and smaller amounts of other substances, including dissolved inorganic/organic materials, nutrients (e.g. silica, phosphate, and nitrogen compounds), as well as a great variety of dissolved mineral solids and a few gases originating from the Earth's crust or extraterrestrial activity (Ste_08; Tall_11). In general, seawater follows the properties of pure water; however it exhibits some distinct properties mainly attributed to the salt content. The ocean circulation is influenced by the Coriolis force, the atmospheric circulation (prevailing winds), but also by the morphology of the sea bottom (e.g. ridge, trench Continental shelf and slope). The current patterns and hydrodynamic properties of the ocean affect the transport and mixing processes in the water column which in turn, tend to homogenize the physical properties and the chemical

composition of the seawater.

The most important physical characteristics are the salinity, temperature, conductivity and density. Due to the salt content of seawater, its density is slightly different from the density of pure water 1.0 g/cc at 0^{o}C and at atmospheric pressure, but it is rather homogeneous, exhibiting only slight variations with a mean seawater density value of 1.024 g/cc. The seawater density depends on the salinity, pressure and temperature properties. Density increases with depth due to compression in the water column and can vary from 1.021-1.07 g/cc in the open ocean; while pressure values exhibit variations up to 2%. Due to various oceanographic processes, temperature, salinity and pressure vary with depth according to different types of water masses, while seasonal variations are also observed. Several physical phenomena (evaporation, precipitation, river inflow, phase change) influence the distribution of temperature and salinity at the ocean's surface. Lateral differences in surface waters salinity may result from evaporation and dilution by freshwater (e.g. rain, river runoff, and groundwater). The temperature values found in the ocean basins vary approximately from -1.7 ^{0}C to 30 ^{0}C. Salinity values, derived from conductivity and temperature measurements, typically vary from 33 to 37‰.The determination of the aforementioned properties in the aquatic environment, combined with the radio-tracing methods that involve key radionuclides, provide a valuable insight on a great variety in oceanic processes.

The marine sediment is formed by weathering (air, water, ice) and erosion of the continents, or volcanic eruptions, by chemical processes within the oceanic crust (groundwater, mud volcanoes, turbidity), by biological activity (accumulation of shells of dead organisms) and by extraterrestrial (cosmic dust, meteors) deposits. The sediment generation processes and their distance ranges depend on the primary shape, size, and weight of particles as well as the velocity of the transporting medium (Cruz_13). The ocean constitutes the end path of the transport, through precipitation, river flow and underground paths, of a large list of substances and is responsible for their redistribution within the seawater column and the seabed. A schematic illustration of several different paths resulting in the sediment generation is depicted in Fig. 2.1.

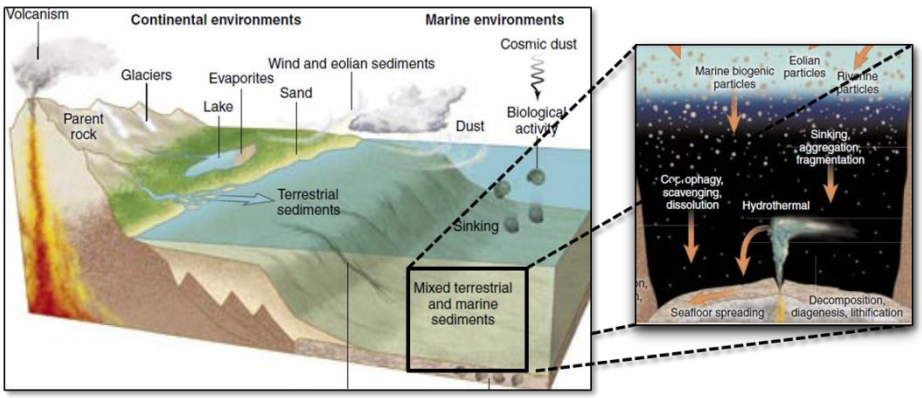

Fig. 2.1: Schematics of different paths leading to the generation of the marine sediment.

The sediment structure and properties, therefore, depend on the transport distance, the ocean fertility and the conditions of the depositional environment conditions (depth, temperature, and dissolved gas, calcium carbonate, and silica concentrations) (Ten_14). The great variety and complexity of the processes involved in the creation of sediments, leads to their diversity; therefore sediments consist of mixtures of different mineral, clastic and fossil particles, and the relative proportions can greatly vary both laterally and with sediment depth. The sediment diversity leads to variations in its physical and geochemical properties. Different classifications of sediments have been established. Sediments can be subdivided according to the particle size (grain size) from which they are composed and the origin (mode of formation) of the sediment. An additional classification based on location can distinguish between neritic (near continental margins and islands) and pelagic (deep-sea) sediments which usually exhibit different characteristics.

The classification according to the particle size distinguishes the sediment grains in different ranges, defined by the grain diameter assuming a close to sphere geometry for all the grains. The different classes include gravel, sand, silt and clay, as well as mixtures of the above, since marine sediments are usually composed of mixed types of grain sizes (especially coastal sediments). The characterization of the sediment type according to the grain diameter (Wentworth Scale), is presented in Fig. 2.2 along with the logarithmic phi (φ) scale ($\varphi=\ln(d)$, d in millimeters). The transport distances according to the sediment grain size and transport mean velocity are depicted in Fig. 2.3.

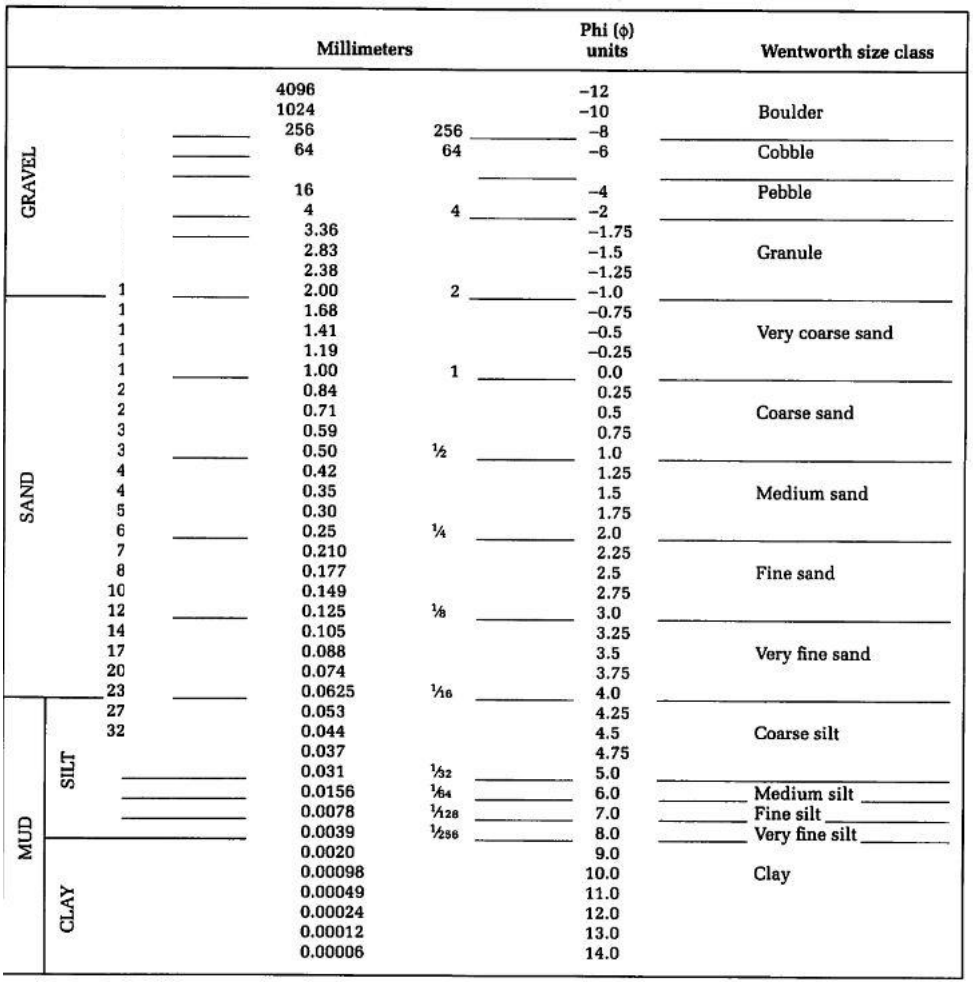

Fig.2.2: The sediment classification according to grain size (Wentworth Scale).

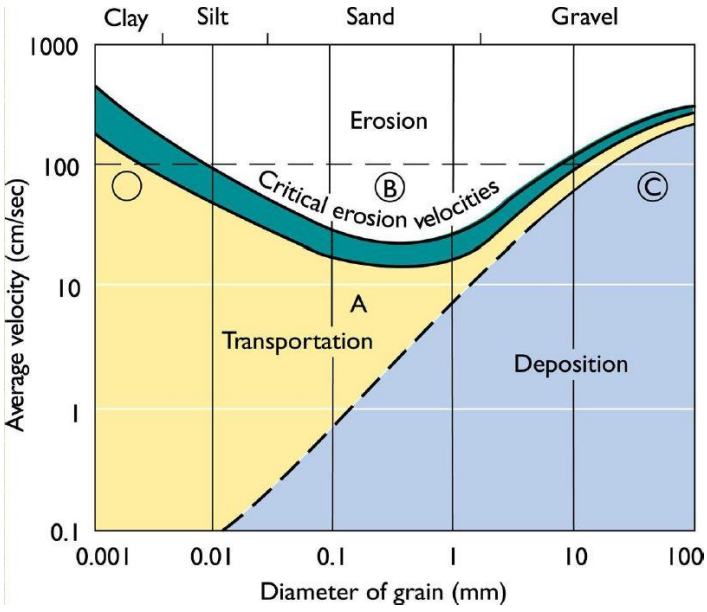

Fig. 2.3: Different sedimentation processes defined by the sediment grain size and transport medium velocities (Hjulstrom's diagram).

Clays are typically less than 2 μm in diameter and are formed by the chemical weathering of primary minerals, while clay minerals larger than 2 μm and clays consisting of various minerals can also be found, as well as particles (colloidal fraction of clays) smaller than 0.1 μm (Grab_11). Silt consists of intermediate size grains (2 μm to 63 μm), while mixed silt and clay particles (mud) are frequently found. Sands are mainly composed of mineral quartz ranging from 63 μm to 2 mm.

The grain distribution in marine sediments is described by sorting; large variations in grain diameters indicate poorly sorted sediment and reflect the multiplicity of transport processes, while well-sorted sediments are composed by slightly varying grains (Fig. 2.4). Sorting occurs due to differences in settling and pick up of grains composed of different size, density and shape and depends on variations in local hydrodynamic conditions, such as currents, waves and/or wind that tend to concentrate certain sediment types at specific locations (Koom_01). Fine particles (small diameter) are transported in suspension in longer distances from the coast compared to coarser particles and a decrease in sediment grain size with the increasing coastal distance is observed (Grab_11).

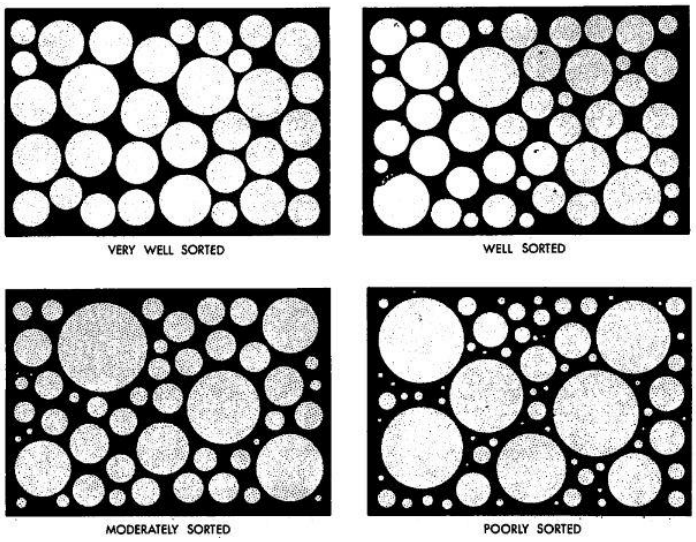

Fig. 2.4: Representation of the differences in sediment sorting (Anst_74).

Several classification schemes have been adopted to describe approximate relations between the different size fractions. In Figs. 2.5 and 2.6 the classification by Folk (Folk_54) and by Shepard (Shep_54) are presented.

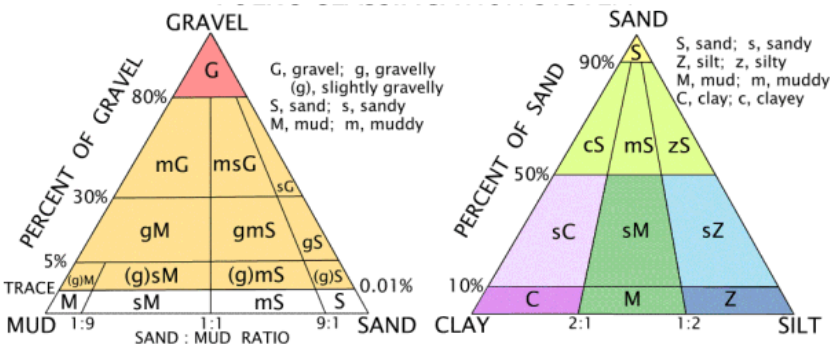

Fig. 2.5: Representation of the Folk's classification system.

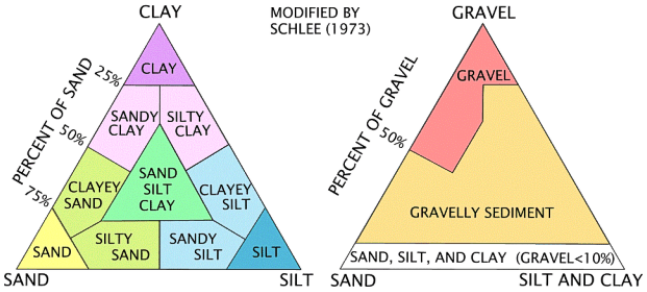

Fig. 2.6: Representation of the Shepard's classification system.

From the grain size distribution (granulometric analysis), the average grain size can be estimated, which reflects the energy of the depositional environment according to the Hjulstrom's Diagram (Fig. 2.3). Sorting can reflect both the sediment source and the way of transport. Aeolian transported sediments are well sorted, while glacial sediments lie among the most poorly sorted (Encyc_16).

Origin classification divides sediment into five distinct categories, which are:

- **Terrigenous (or lithogenous) sediments**: They consist of particles transported from land (continents, volcanoes, islands) by water, wind, or ice.
- **Biogenic sediments:** Substances originating from the biological activity of marine organisms.
- **Authigenic (or hydrogenous) sediments:** They include mainly pyrites and non-biogenous carbonates which are produced by chemical processes in seawater (e.g. submarine gas hydrate, submarine eruptions).
- **Volcanogenic sediments:** Pyroclastic sediments that are formed as the primary or secondary result of volcanic activity and are transported like terrigenous sediments but aeolian transport prevails.

- **Cosmogenic sediments:** Cosmic dust, micrometeorites and tektites. Cosmogenous sediments consitute a minor component of ocean sediments.

Nevertheless, marine sediments consist always of different mixtures of the above categories, due to the multiplicity of the sedimentation properties, thus they are classified using the 30% rule (when there is more than 30% of any type of component in the sediment it will be classified as such). In Fig. 2.7 the four major sediment types according to their origin are presented along with a description of the various processes involved in the sediment generation.

Type	Composition		Sources		Main locations found
Lithogenous	Continental margin	Rock fragments Quartz sand Quartz silt Clay	Rivers; coastal erosion; landslides		Continental shelf
			Glaciers		Continental shelf in high latitudes
			Turbidity currents		Continental slope and rise; ocean basin margins
	Oceanic	Quartz silt Clay	Wind-blown dust; rivers		Abyssal plains and other regions of the deep-ocean basins
		Volcanic ash	Volcanic eruptions		
Biogenous	Calcium carbonate ($CaCO_3$)	Calcareous ooze (microscopic)	Warm surface waters	Coccolithophores (algae) Foraminifers (protozoans)	Low-latitude regions; sea floor above CCD; along mid-ocean ridges and the tops of volcanic peaks
		Shells and coral fragments (macroscopic)		Macroscopic shell-producing organisms	Continental shelf; beaches
				Coral reefs	Shallow low-latitude regions
	Silica ($SiO_2 \cdot nH_2O$)	Siliceous ooze	Cold surface waters	Diatoms (algae) Radiolarians (protozoans)	High-latitude regions; sea floor below CCD; upwelling areas where cold, deep water rises to the surface, especially that caused by surface current divergence near the equator
Hydrogenous	Manganese nodules (manganese, iron, copper, nickel, cobalt)		Precipitation of dissolved materials directly from seawater due to chemical reactions		Abyssal plain
	Phosphorite (phosphorous)				Continental shelf
	Oolites ($CaCO_3$)				Shallow shelf in low-latitude regions
	Metal sulfides (iron, nickel, copper, zinc, silver)				Hydrothermal vents at mid-ocean ridges
	Evaporites (gypsum, halite, other salts)				Shallow restricted basins where evaporation is high in low-latitude regions
Cosmogenous	Iron–nickel spherules Tektites (silica glass)		Space dust		In very small proportions mixed with all types of sediment and in all marine environments
	Iron–nickel meteorites		Meteors		Localized near meteor impact structures

Fig. 2.7: Sediment classification according to the sediment origin (Truj_14).

Despite their diversity, as marine sediments are formed by greatly varying physical mixtures, only a few lithological end-members are found in sediments, each exhibiting a relatively restricted chemical composition range (Plank_98). Therefore, a further classification according to the different sediment mixtures can be made based on their different mineral composition (lithology) to determine the sediment type. There are five marine sediment lithologies constituting the most distinctive sediment types which are:

- **Calcareous ooze:** These are biogenic sediments composed of calcareous nanofossils and/or foraminifers, while they also contain a SiO_2 component greater than 30%.They cover~50% of the ocean floor.
- **Siliceous ooze:** These are biogenic sediments composed of diatoms, radiolarians, sponge spicules, and/or silicoflagellates, while they also contain a $CaCO_3$ component greater than 30%.They cover~15% of the ocean floor.
- **Red clays:** These are very fine terrigenous sediments that often contain siliceous microfossils, fish teeth, Mn-Fe micronodules, and/or volcanic glass.
- **Terrigenous sediment:** These are substances originating from the weathering of continents or volcanic islands.
- **Glaciomarine sediment:** Sediment containing terrigenous sand, pebbles, or cobbles transported to the sea by ice melting.

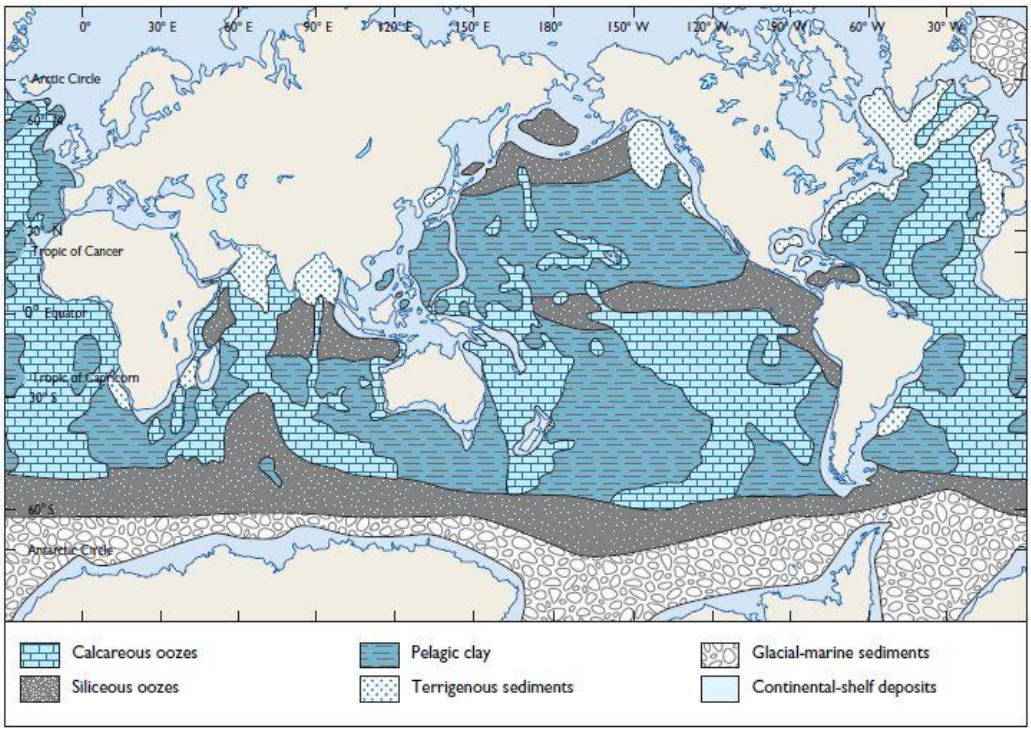

Fig. 2.8: Distribution of sediments in the deep-sea (Davi_76).

In any type of the above marine sediment types, volcanic ash may also form a minor lithology, more pronounced in biogenic oozes and deep-sea red clay. These sediment types are again found in mixtures of different components and are therefore classified using the 30% rule. The distribution of these lithologies in the different compartments of the ocean (deep sea) is depicted in Fig. 2.8. Apart from lateral variations, these lithologies can also

change within a sediment core (abrupt or gradual changes from one to another reflecting different sedimentation processes).

There are several physical characteristics of marine sediments, significant for the majority of environmental applications. These are the sediment **water content, porosity, dry** and **wet bulk densities, grain density** and **mineral composition** (major and trace elements). The mineral composition and physical characteristics of marine sediments are the result of a complex interaction among geological, oceanographic, and biological processes (Ten_14). Therefore, these quantities exhibit large variations; however they are correlated and, to some extent, relationships among them have been extracted as well as between physical and textural parameters (Casas_04, 06; Komi_11; Weber_97).

Porosity

In marine sediments a large portion of the pore space is occupied by saline water while a small fraction within grains (void pore) may not be filled by water (Breit_06). The porosity (p) in a water-saturated sediment is defined as the ratio between the water pore volume, V_w, and the total volume, V_s of an undisturbed sediment sample expressed as a percentage (%) and is calculated using the following equation:

$$\boldsymbol{p = 100 \cdot \frac{V_w}{V_s}} \tag{2.1}$$

In the above equation, a correction to the water volume V_w, for the mass and volume of the salt precipitated from the pore water during drying must additionally be applied (Gealy_07; Encyc_16). Instead of calculating directly the different volumes (pycnometer method), an alternative calculation is based on the knowledge of water content and water density (Blum_97a, b). Nevertheless, in marine sediments the assumption that the whole void pore space is filled with water is quite often insufficient, and in such cases the void volume should also be calculated. The marine sediment's porosity can vary from below 0.2 (20%) to 0.95 (95%) (the porosity values range between 0 and 1). The sediment's porosity is the result of a number of complex, interrelated factors; among them the size, shape distribution, mineralogy and packing of the sediment grains are the most important (Hamil_70). The porosity generally varies as a function of depth, lithology (grain size and composition), diagenesis, and local conditions (Komi_11). Dependence of porosity on lithology is related to the size of the pore space and the amount of water adsorbed onto particles. Trends of increasing porosity with increasing sorting and decreasing grain size are well-established

for marine sediments (Hamil_74; Bryant_81). A diagram of the porosity dependence on the sediment grain size and sorting is presented in Fig. 2.9.

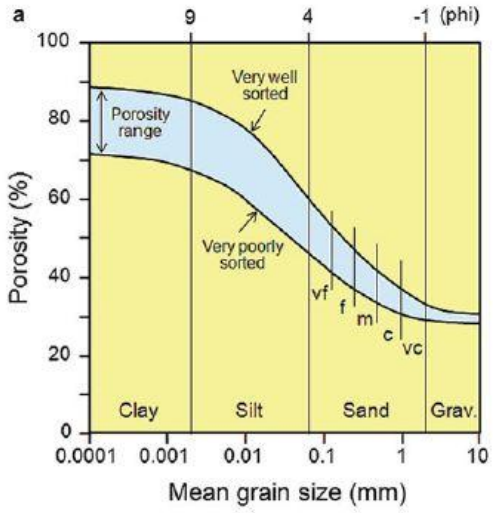

Fig. 2.9: Dependence of porosity on grain sizes and their distribution (Ency_16).

Finer grains in a sediment matrix of mixed components are more affected by compaction than the coarser ones (e.g., Scherer_87; Pittman_91). Porosity increases with increasing abundance of clay-sized particles because i) their high specific surface (surface area per unit mass) results in greater adsorption of water on particle surfaces and ii) they tend to be arranged in open structures, while both these characteristics depend on the composition of the clay fraction (Prell_91). Therefore, clays, silts and sediments rich in organic carbon (Carbon mixtures originating from marine organisms) contain substantial amounts of water at the time of deposition (Encyc_16). Organic matter abundance affects porosity through the formation of clay-organic aggregates (Pusch_73; Reime_82) and adsorption of water on its surface (Pusch_73).

Surface sediments up to a 10–20 cm depth may contain large and variable amounts of water up to 95% (IAEA_03). A general trend of an exponential decrease of porosity with respect to sediment depth (mostly for high depths, above 10 m) has been observed in many different studies, while the exponential correlation of porosity with depth is well established for great depths. Nevertheless, different exponential curves apply in different sediment cores, rendering the relation site-specific. Recently, a study that correlates the depth profile of the porosity with different sediment types was conducted providing different exponential trends for different lithologies (Komi_11). The decrease of the sediment porosity with depth can also be related to the increased compaction of sediments with depth (Encyc_16). Compaction is the decrease in the sediment volume, resulting primarily from an expulsion

of water due to the sediment accumulation after its deposition and the compression of the overlying sediment (Encyc_16).

Wet bulk density

The wet bulk density $\boldsymbol{\rho_s}$ is defined from the mass of a water saturated sediment sample (M_s) divided by the volume of the sample (V_s):

$$\boldsymbol{\rho_s = \frac{M_s}{V_s}} \tag{2.2}$$

Although Eq. 2.2 offers a direct calculation of the wet bulk density, other formulas have been additionally used relating the wet bulk density to the dry bulk density or water content (Encyc_16). The wet bulk density, however, can also be calculated on the basis of various assumptions concerning the physical properties of sediment and seawater. The wet bulk density (ρ_s), porosity (p) and grain density of minerals (ρ_g), in a gas-free system, are linked through the following equation (marine science2):

$$\boldsymbol{\rho_s = \rho_w \cdot p + \rho_g \cdot (1 - p)} \tag{2.3}$$

where

$\boldsymbol{\rho_w}$: is the density of seawater

$\boldsymbol{\rho_g}$: is the average grain density of the minerals composing the sediment

$\boldsymbol{p}$: is the fractional porosity (volume of pore space / total volume), assuming a water-saturated (pore space filled with water) sediment.

Wet-bulk density varies as a function of porosity and grain density, while both of these parameters vary with sediment lithology (Prell_91). Despite the dependence of bulk density upon the particle grain density (Nafe_57), porosity and wet bulk density are strongly inversely related (Ve_01) and in fact they are related through a linear regression equation, as it can be derived from Eq. 2.3. In many cases, the porosity and wet density data can be fitted with fixed values, theoretically determined by the estimation of the mean grain density and the known seawater, only slightly varying, density values. Therefore in the work of Nafe and Drake (1957) a single linear regression equation, assuming a mean grain density and seawater density of 2.68 g/cc and 1.0 g/cc respectively, was utilized to fit a large list of data (porosity, wet bulk density) arising from different sediment lithologies resulting in an excellent correlation. This was attributed to the small variations in the mean

grain densities, since a large variety of minerals with different textures (soil, sand, sandstone, limestone, clay and shale) fall within the same grain density (Ahre_95). The linear dependence of the wet bulk density to porosity is a well established relation, nevertheless, the constant values vary, from 1.0-1.04 g/cc for the seawater density and 2.1-2.9 g/cc for the mean grain density in different studies (Gealy_07; Komi_11) rendering the correlation site-specific. Moreover, in several sediment cases, deviations from the straight line could be observed due to the presence of minerals, which exhibit a large deviation, from the mean grain density of 2.6 g/cc, within the sediment matrix.

Bulk densities of water saturated sediments range approximately between 0.8 g/cc (when gases are also present within matrix) and 2.8 g/cc. The lateral density distribution depends primarily on the mineral composition and transportation distance (general equations). A general pattern of decreasing wet bulk density of surface sediments with increasing ocean depth has been established. This trend may be attributed to the following issue: Coarse particles (gravels and sands) form mostly near-shore deposits, while the grain size typically decreases offshore with clays occupying the deep-ocean basins, since lighter and fine particles are transported at longer distances. The wet bulk density may also vary within the sediment depth (sediment core) and a general trend of increased density values with higher depths is observed for large distances (0-2 km) inside the seabed as shown in Fig. 2.10, that could be related to the opposing inverse porosity pattern (see Fig. 2.10).

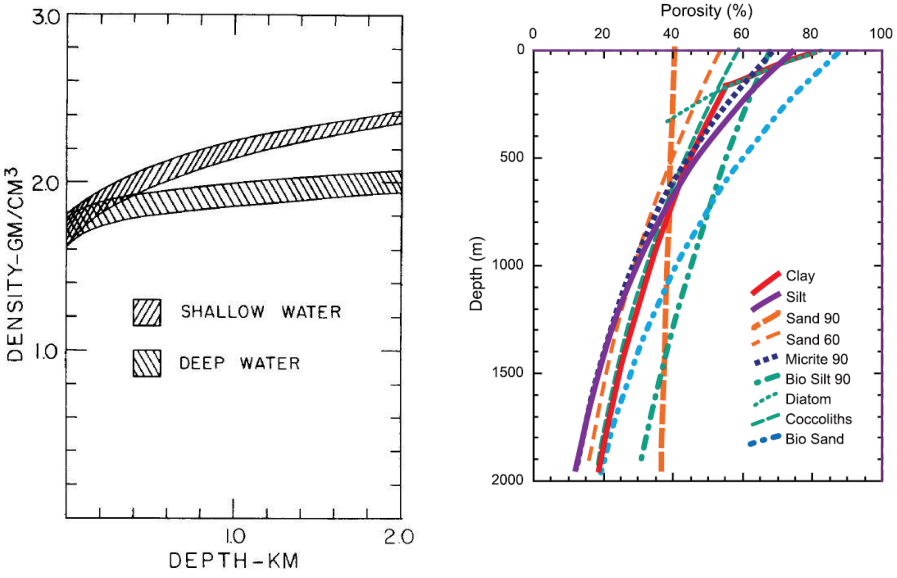

Fig. 2.10: Depth profile of marine sediment wet bulk densities (left) and porosities (right) for different lithologies (Komi_11).

.

Grain density

The grain density is defined as the average density of the minerals forming the sediment, excluding the density of the pores. Grain density values depend on the mineral composition and thus vary with sediment lithology (Prell_91). Quartz and Calcite exhibit grain density values of 2.65 and 2.71 g/cc, respectively. The grain density of biogenic silica has been determined to be in the range of 1.70-2.05 g/cc (Hurd_77). For terrigenous clays these values may vary from 1.8-2.2 g/cc. Some biogenous sediments exhibit lower grain density values due to the presence of large quantities of organic matter, with values ranging from 2.41 to 2.51 g/cc, while even small amounts of such components can significantly reduce the bulk density. Grain density values for the minerals that constitute the prominent components in the marine sediment, present smaller deviations (with some exceptions) as compared to wet bulk densities. Moreover, unlike the wet bulk density, which increases with depth, the grain density has a rather homogenous vertical profile (the mean grain density varies between 2.4-2.7 g/cc in common lithologies).

Table 2.1: Grain densities (g/cc) of different minerals.

Sediment type	Minerals	Chemical composition	ρ_g (g/cc)
Terrigenous	Potassium Feldspar	$KAl_2SiO_5(OH)_4$	2.54-2.6
	Plagioclase Feldspar	(Na,Ca)(Si,Al)4O8	2.6-2.8
	Biotite Mica	$KMg_3AlSi_3O_{10}(OH)_2$	2.7-3.1
	Quartz	SiO_2	2.65
	Dolomite	$CaMg(CO_3)_2$	2.87
	Kaolinite	$Al_2Si_2O_5(OH)_4$	2.63
	Illite	$(K,H_3O)(Al,Mg,Fe)_2(Si,Al)_4O_{10}$	2.64-2.69
Biogenous	Opal	$SiO_2 \cdot {}_n(H2O)$	1.9-2.3
	Calcite / Aragonite	$CaCO_3$	2.71 / 2.9-3
	Barite	$BaSO_4$	4.5
	Apatite	$Ca_5(PO_4)_3(F,OH,Cl)$	3.16–3.22
Authigenous	Gupsum / Anhydrite	$CaSO_4(H_2O)_n$, $CaSO_4$	2.32 / 2.94
	Pyrite	FeS_2	5.0
	Zeolites	Hydrous alumino-silicates	2.1-2.2
	Halite	NaCl	2.1-2.6
	Arsenopyrite	(Fe,Co)AsS	5.5-6

A parameter that tends to increase the grain density values to a value higher than 2.7 g/cc is the presence of iron sulphates. In Table 2.1, the grain density values for several different minerals found in marine sediments are presented.

Water content

The absolute water content refers to the amount of interstitial fluid contained in a unit mass of water-saturated sediment and is defined as the mass of water relative to the mass of the water-saturated sediment (Encyc_16). It is usually expressed as a percentage value (weight %) and is mathematically formulated as :

$$\boldsymbol{W.C.} = \mathbf{100} \cdot \frac{\boldsymbol{M_w}}{\boldsymbol{M_s}} = \mathbf{100} \cdot \frac{(\boldsymbol{M_s} - \boldsymbol{M_d})}{\boldsymbol{M_s}} \tag{2.4}$$

where

W.C. : is the absolute water content (weight %),

$\mathbf{M_w}$: is the mass of the pore water, defined by drying the water-saturated sediment sample and the subtracting of the obtained mass before and after drying the sediment sample, corrected for the mass added by the precipitated salt.

$\mathbf{M_s}$: the total mass of the water-saturated sediment sample

$\mathbf{M_d}$: the total mass of the dried saturated sediment sample

These values can vary from 0% to 100%. The water content concerns the mass of water, while porosity concerns the volume of water within the sediment. As a result, these two quantities are related and one can be defined from the other.

Dry bulk density

The dry bulk density ρ_d, is defined from the mass of dry solids of a water saturated sediment sample (M_d) divided by the total volume (V_s) of the sample, as shown in the following equation:

$$\boldsymbol{\rho_d} = \frac{\boldsymbol{M_d}}{\boldsymbol{V_s}} \tag{2.5}$$

In saline environments, a correction for the salt content in the pore water has to be implemented. Again, different relations can be applied for the dry density calculation. The dry bulk densities can be calculated from the wet bulk ones, and vice versa (Flem_00). The dry and wet bulk densities can be indirectly calculated solely from the water content value, due to the high correlation between the bulk densities (both wet and dry) and the water content for typical terrigenous sediments (mean grain density of 2.65 g/cc), while these calculations have a universal character for such sediments (Flem_00).

Major elements

The major element composition of marine sediments is ruled by the fractions of the different minerals forming the sediment matrix. The major elements that constitute the sediment matrix are usually given in the form of oxide percentages and are determined by X-Ray fluorescence spectrometry (XRF). Among the most prominent detected elements are Si, Al, Fe, Ca, Mg, K, P, Na, P, Ti, Mn and Ba.

Although the majority of the physical sediment parameters are traditionally determined in the laboratory, on-board or shore-labs based measurements have also been conducted. Moreover, several sensors have been developed which enable the *in situ* measurements of several parameters. For instance, bulk-density measurements can be obtained *in situ* by using geochemical methods or multi-sensor core loggers (Weber_97; Jacob_09; Fortin_13).

2.2.2. Disequilibrium in the radioactive decay series

There are three naturally occurring radioactive decay series; each one starts with an actinide radionuclide, namely ^{238}U, ^{235}U and ^{232}Th, each one exhibiting a long half-life ($t_{1/2}$> 0.7 Gy). All these elements decay (by alpha or beta emission) to a different radioactive element which in turn decays to another, forming this way a large series of radioactive nuclides, with half-lifes ranging from μs to 10^9 y, which is terminated with the production of a stable isotope of Pb at the end of each series (Fig. 2.11). In this way, each element in the series (progenies) is constantly formed by the previous one in the series (referred to as the parent nuclide) while at the same time it continuously decays to the next element in the series. The state in which the activity of a progeny has become equal to the one of its parent is known as ‘secular equilibrium’ and this is realized under the condition that the half life of the parent nuclide is greater than the one of its decay product. This depends on the progeny formation and the parent decay rate and the time after which equilibrium is reached can be defined through Bateman equations (Bate_10). In many undisturbed natural environments, which are referred to as closed-systems, the activities between products of radioactive nuclei have reached secular equilibrium (i.e. the ratio of the activities (A.R.) between the parent and progeny radionuclides is unity). In practice, this can be accomplished, if in a material the decay chain remains undisturbed for a period of approximately 6 times the longest half-life, intermediate radionuclide in the chain

(Bourd_03). Nevertheless, for reasons that are described below, in the majority of natural environments deviations from secular equilibrium are observed among several radionuclides in the same series.

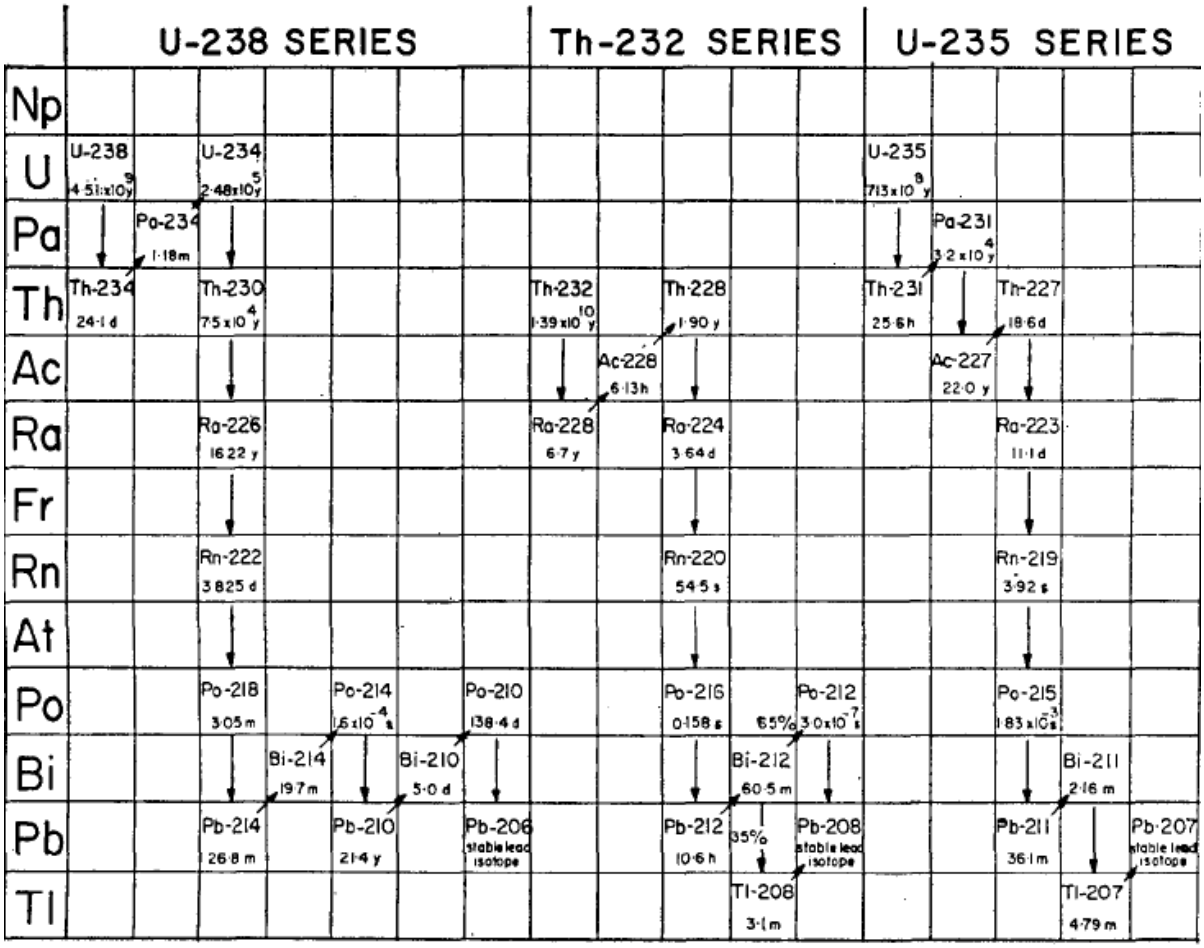

Fig. 2.11: Representation of the naturally occurring radioactive decay series.

The U- and Th- decay series contain different radioactive elements as well as different isotopes of these elements. These elements exhibit quite distinct physical properties and chemical behaviors and thus, the degree to which these elements participate in physical, chemical and biogeochemical processes on the Earth greatly varies (Krish_08). The different geochemical properties of these elements, lead to fractionation among the members within the same decay chain, in different geological environments. The isolation of a radionuclide from its parent renders the particular nuclide the head of the decay chain and thus, results in the sequential appearance of radioactive disequilibrium among the radionuclides of a series. This means that the activity of the parent radionuclide is no longer equal to the one of its progeny. In fact, the ratio of the two activity values can range from

values of several orders of magnitude below unity to several orders of magnitude above unity. This is a non-steady state condition; however, the return to equilibrium can greatly vary in time and it is mostly controlled by the half-life of the daughter nuclide.

Fractionation among the radionuclides of the same series is attributed to two different correlated mechanisms; the first associated with the weathering and more general water-rock interactions and the second with the decay properties. Fractionation can happen during processes that discriminate according to the chemical behavior, such as degassing, oxidation/reduction, partial melting, crystallization, partitioning, desorption, adsorption, and surface complexation (Porc_08; Chab_08). For instance, a pair of radionuclides exhibiting disequilibrium due to the different solubility fractions is the case of $^{234}U/^{238}U$; although the decay mechanism, discussed below, is also significant in this case. In waters, especially in oxidizing environments (such as surface waters) ^{234}U atoms are leached into solution faster than ^{238}U ones due to the different oxidation states of the two isotopes and therefore waters are more enriched in ^{234}U compared to ^{238}U (Bor_14). Especially in the marine environment, deviations of activity concentrations due to disequilibrium processes are large (Bor_14). Excesses in ^{234}U over ^{238}U are observed also (Nu_15; Coc_86) in some sediments (e.g. sediments with high organic matter contents), nevertheless deficits in ^{234}U compared to ^{238}U concentrations from loss of uranium with preferential ^{234}U-leaching are expected in soils or sediments (Bor_14; Ivan_94). In Fig. 2.12 the different transport processes causing fractionation and variations in the $^{234}U/^{238}U$ ratio are depicted.

In contrast to U, Th isotopes are mobilized mostly by particulate transport in ground and surface water systems (Ivan_94). In the marine environment, highly reactive particles in seawater (e.g., Th, Pa, and Pb), which are produced by the decay of relatively soluble parent radionuclides (e.g., U, Ra, and Ac) can cause a daughter/parent disequilibrium in several different compartments (Pov_12; Loeff_99; Coc_84; Krish_08). ^{234}Th produced in seawater from decay of dissolved ^{238}U, is rapidly scavenged onto particles and removed to bottom sediments (Coc_05). The residence time of Th ranges from extremely rapid values in shallow coastal environments to days-weeks offshore (Kauf_81).

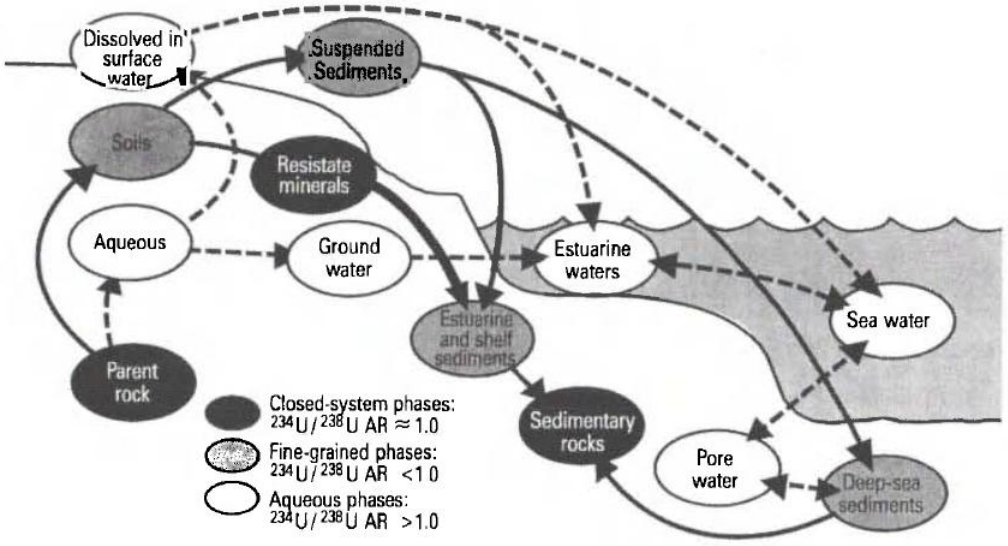

Fig. 2.12: Different transport processes causing fractionation and variations in the $^{234}U/^{238}U$ ratio (Ivan_94).

The removal of Th from the water column is governed by particle concentration and flux (Sants_80), as well by particle size and type (Sants_89; Quigley_02). Moreover, the different Th isotopes exhibit large variations in their residence time in water (scarce solubility of Th in water). In seawater, long-lived Th isotopes, such as ^{230}Th and ^{232}Th, are deposited on the bottom, while short lived ones, such as ^{234}Th, prefer to decay while they are still in the water column. In groundwater, adsorption and precipitation tend to reduce the concentrations of ^{230}Th and ^{232}Th more than those of shorter-lived ^{234}Th and ^{228}Th. Thus, along the major flow pathways, higher $^{234}Th/^{230}Th$ and $^{228}Th/^{232}Th$ ratios are found in fresh groundwater, due to its more intense interaction with rocks (Luo_00).

Pa isotopes are insoluble and are affected by surface complexation from hydroxide complexes or polymers similar to Th. Nevertheless, Pa has strong affinities for organic complex ligands and can be more soluble in natural waters (Bourd_03). For instance, $^{231}Pa/^{230}Th$ disequilibrium has been observed in the oceans and it is attributed to the longer residence time of ^{231}Pa in seawater (Hend_03) and to the lower reactivity of ^{231}Pa (10 times approximately), that allows it to be transported laterally over larger distances than ^{230}Th before being scavenged (Loeff_01).

An example of disequilibrium due to fractionation by melting procedures and subsequent crystallization is the case of $^{230}Th/^{238}U$ and $^{226}Ra/^{238}U$ disequilibria after volcanic episodes (Sant_02). The same applies to $^{231}Pa/^{235}U$ disequilibrium (Peate_05). $^{226}Ra/^{210}Pb$ disequilibrium has been reported in the deep sea since 1970, attributed to the

rapid scavenging of the latter by organisms from the sea surface to deeper waters. In marine sediments, the migratory behavior of ^{226}Ra, as well as ^{222}Rn, from sediments to seawater (via pore water exchange and diffusion) due to their high mobility, leads to Pb excess (Pb_{ex}) activities in surface sediments, while a similar behavior has also been reported in soils. Furthermore, ^{222}Rn/^{210}Pb disequilibrium can be found due to the ^{222}Rn loss from the system by degassing or due to the preferential removal of the insoluble ^{210}Pb in aqueous systems (Bourd_03). ^{210}Po/ ^{210}Pb disequilibrium can be found in the seawater due to the different isotopic biogeochemical behavior, although both radionuclides are particle reactive (Lin_14). ^{210}Po (the immediate product of the ^{210}Pb decay) has a strong affinity for organic materials and cytoplasm and thus, high ^{210}Po /^{210}Pb activity ratios can be found ranging from 3 in phytoplankton, to 12 in zooplankton due to the bioaccumulation of ^{210}Po (Loeff_01).

^{224}Ra is continuously produced from the alpha decay of ^{228}Th, which in marine environments, is strongly bound to sediments. During mixing with seawater, ^{224}Ra actively migrates across the sediment–water interface into the overlying seawater and disequilibrium between ^{224}Ra and ^{228}Th in near-surface sediments is anticipated (Cai_12). Moreover, in freshwater, ^{224}Ra is strongly bound onto particle surfaces; however, whereas increases during mixing with seawater (estuarine environments, SGDs), desorption occurs and ^{224}Ra is released in the seawater (Swarz_03).

Fractionation can also take place as a result of a radioactive decay. The recoil effect occurs as a consequence of momentum conservation during radioactive decay, and the effect is especially important for alpha decay (Chab_08; Porc_03; Coc_92; Hend_03). The released energy from the decay is distributed between the emitted a-particle and the produced (daughter) nuclide. This causes the daughter nuclide to be displaced from its original site and to be found in distances far from the crystal lattice (in a solid) where the parent nuclide is positioned. Therefore, the daughter nuclide is less related to the structure of minerals and can easily diffuse to the surface of mineral grains and through the cracks (Bor_14). The extent of this displacement is a function of the decay energy and the density of the solid phase and in common mineral phases, the recoil range can vary from 40 to 70 nm. (Chab_08). In water saturated materials the disequilibrium caused by the recoil effect is even more pronounced, as in the case of ^{234}U/^{238}U disequilibrium. In water-saturated materials the displacement of ^{234}U (produced from the ^{238}U decay) in the water porous between grains is highly possible (depending on the grain sizes and density) from where it can diffuse, as it is easily leached in solutions. This mechanism is referred to as the recoil-

induced vulnerability to leaching (Ivan_94). Other radionuclides subject to the recoil effect in natural systems (Coc_08) are ^{234}Th (produced from ^{238}U), Ra isotopes ^{226} Ra, ^{228} Ra, ^{223} Ra, ^{224} Ra (produced from ^{230}Th, ^{232}Th, ^{227}Ac and ^{228}Th, respectively) and ^{222}Rn (produced from ^{226}Ra).

Among the different environments, in oceans, marine groundwater sources and hydrothermal fluids compose environments with prominent disequilibria characteristics. Within hydrothermal fluids and groundwater, ^{222}Rn activities are enriched by three orders of magnitude (or more) and disequilibrium is observed with its distant parent and progeny radionuclides (^{226}Ra, ^{210}Pb), mostly due to the recoil effect during rock-water interaction (Coc_08; Burn_03). ^{210}Pb/^{226}Ra, ^{228}Th/^{228}Ra, ^{228}Ra/^{232}Th and ^{230}Th/^{234}U disequilibria have been observed in sulfide- and barite-containing hydrothermal deposits on the seafloor. In submarine groundwater discharges, high disequilibria have been reported among different pairs, such as ^{234}U/^{238}U, ^{214}Pb/^{222}Rn (~0.2-0.3) and ^{214}Pb/^{210}Pb (~10^{3}), as well as extremely low, such as ^{230}Th/^{234}U (~10^{-2}), ^{210}Pb/^{222}Rn (~10^{-5}-10^{-3}) and ^{228}Th/^{224}Ra (~10^{-2}) (Luo_14; Luo _00; Porc_08; Coc_08).

The disequilibrium among the U- and Th-series radionuclides is the basis for the utilization of a great variety of the naturally occurring nuclides as tracers for applications in earth sciences (Krish_08). The extent of disequilibrium between different parent–daughter pairs and the time needed to return to equilibrium provide valuable information about the transport and reaction of several geological and oceanographic processes, as well as about their time-scales, in ranges from days to 10^{5} years (Pov_12; Krish_08; Bourd_03). Such processes involve the determination of water mass circulation, particle fluxes (^{234}Th/^{238}U, ^{210}Po/^{210}Pb, ^{210}Pb/^{226}Ra and ^{228}Th/^{228}Ra disequilibrium), residence time and the estimation of sediment accumulation rates (^{230}Th/^{234}U, Pb_{ex}) (Pov_12), as well as, the age estimation of geological and biological materials (^{230}Th/^{234}U, ^{231}Pa/^{235}U, ^{230}Th/^{238}U and ^{226}Ra/^{238}U) (Stirl_09; Schul_04; Sant_02).

Disequilibrium between U- and Th-series radionuclides found in the environment can also be related to anthropogenic activities. For instance, large disequilibria appear in by-products of various industries during the different steps of the ore material processing. Large quantities of such materials are produced and can be redistributed in soils and in the marine environment by different paths.

2.2.3. Photon interaction theory

Photons interact with matter by elastic scattering and inelastic processes. In all the involved processes the interaction leads to the attenuation of the photon, while the latter also include energy absorption. The three dominant interactions between photons and matter, in the energy range from 50 to 3000 keV, which is interesting for environmental applications, are the photoelectric absorption, the Compton scattering and the pair production. These are all inelastic processes in which the photon loses part or all of its energy. Elastic scattering also occurs, but these effects are significant only for low photon energies. The interaction of the photon through Rayleigh and Thomson scattering causes an alteration in the direction in which the photon is transmitted, but the energy remains unchanged (elastic processes). Thomson scattering usually involves an interaction with loosely bound electrons and is independent of the photon primary energy, nevertheless it is a process occurring only when the photon energy is considerably less than the rest mass on the electron. Rayleigh scattering is an interaction of the photon with the atom as a whole (coherent interaction with all the electrons of the atom) and becomes significant only at very low photon energies, typically below a few hundred keV (Kn_00). The probability of this interaction depends on the photon primary energy and the atomic number of the interacting material. The probability increases with heavier materials (large atomic number Z) and the deflection angle decreases with increasing energy.

The photoelectric absorption is an interaction of the photon with one of the bound electrons in an atom. The necessary condition for the realization of this interaction is that the primary photon energy is larger than the binding energy of a shell. The energy of the photon is transferred to the ejected electron as kinetic energy, reduced by its binding energy to the shell from which it is ejected. Usually the e^- is ejected from the K shell, but if the photon energy is not sufficient, an L or M electron is ejected instead. With the removal of the bound electron, the atom is left in an excited state. To counterbalance the excess of energy and reach an equilibrium state again, two phenomena prevail, namely the X-ray fluorescence and the Auger emission. The vacancy caused by the interaction of the γ-ray with the atom, may be filled by a higher level electron followed by a characteristic X-ray emission (X-ray fluorescence**)**. The characteristic X-ray may travel some distance before it is reabsorbed by further photoelectric interactions emitting characteristic X-rays, until, ultimately, all of the excess energy is absorbed. Alternatively, the excess energy caused by the vacancy can be redistributed between the electrons in the atom. In this process, the

excess energy, after the vacancy substitution with a higher level electron, can be transferred to another bound one that has enough kinetic energy to be ejected from the atom (Auger electron). In the photoelectric absorption, the secondary produced high-energy electrons have a total electron kinetic energy that equals the incident gamma-ray energy and are quickly reabsorbed inside the material. The basis of the detection of γ-rays, is the deposition of all their energy inside the detector, so that the deposited energy can be directly associated with a certain radionuclide. Therefore the photoelectric absorption is a significant process regarding γ-ray spectroscopy. The probability of a photon interaction through photoelectric absorption depends on the primary photon energy and the atomic number Z of the medium and mainly occurs for low-energy photons and high-Z materials.

The prominent photon interaction in a wide energy range (50-5000 keV) for relatively low-Z materials is the incoherent Compton scattering. This interaction occurs at photon energies greater than the electron rest-mass energy and therefore concerns less tightly bound electrons. In this interaction, the photon gives up a part of its energy that is transferred to the electron and undergoes scattering, moving in a different direction. Photons may be scattered in any direction, however forward scattering prevails at energies higher than 100keV (Klein-Nishina differential cross-section). The photon energy left after the interaction $\mathbf{E}_{\gamma}'$, depends on the photon energy $\mathbf{E}_{\gamma}$, the angle of impact as described in the following formula:

$$E'_{\gamma} = \frac{E_{\gamma}}{1+\left(E_{\gamma}/mc^2\right)\cdot(1-cos\theta)} \tag{2.6}$$

The probability of Compton scattering at a given primary photon energy is linearly dependent of the atomic number Z. For a given material the probability reduces as the incidence photon energy rises.

The pair production is a process that occurs in the field of a nucleus of the interacting medium and corresponds to the creation of an electron-positron pair simultaneously with the disappearance of the incident gamma ray photon (Gilm_08). A minimum energy of 1.024 MeV is required to make the process energetically possible since the primary photon energy must be 2 times the electron rest energy to create the electron-positron pair. Usually, when pair production occurs, the primary photon energy exceeds this value and the excess energy appears in the form of kinetic energy shared by the electron-positron pair. The positron, as a positively charged particle, will quickly interact with an electron resulting in their mutual annihilation and the simultaneous emission of two photons

with an energy that equals the electron rest mass (511 keV) in opposite directions (annihilation photons). The annihilation can be regarded as instantaneous with the pair production event due to the very short time of the process (~1ns). Pair production is the dominant mechanism of interaction at energies greater than 10MeV (Gilm_08). A different mechanism of photon interactions with matter involves photonuclear processes, but such interactions are insignificant for photons exhibiting energies of less than 5 MeV.

The relative importance of the three dominant interactions between photons and matter described above for different absorber materials and gamma-ray energies is illustrated in Fig. 2.13 (Evans_55). The two lines represent the equal probability of the photoelectric absorption and Compton effect (left line) and the Compton effect and pair production (left line), at a given energy as a function of the interacting material atomic number.

2.2.4. Photon attenuation in the seawater and sediment matrix

When photons pass through matter they interact via the aforementioned processes until they are fully-absorbed. Considering a narrow beam of photons passing through a material, the degree of the attenuation follows an exponential law (Beer-Lambert law):

$$\boldsymbol{I = I_o \cdot e^{-\sum \mu_i \cdot x_i}} \tag{2.7}$$

Where:

$\mathbf{I_o}$: is the incident beam intensity, **I** is the intensity transmitted after passing through the thickness $\mathbf{x_i}$ of the i material (absorber) and $\boldsymbol{\mu_i}$ are the attenuation coefficients that give the probability of each interaction. The attenuation coefficients μ_i are given in units consistent with the thickness x, in cm^{-1} (linear attenuation coefficients) or in cm^2/g (mass attenuation coefficients), when the thickness is given in units of mass/area. The linear attenuation coefficients vary with density and thus, the mass attenuation coefficients is more widely available. From this data the linear attenuation coefficients can be calculated by dividing with the corresponding density value. For real geometry problems, scattering in the surrounding materials should also be taken into account and therefore, an additional multiplication parameter should be added to the above equation, which is called the build-up factor, B (Singh_14; ANSI_91).

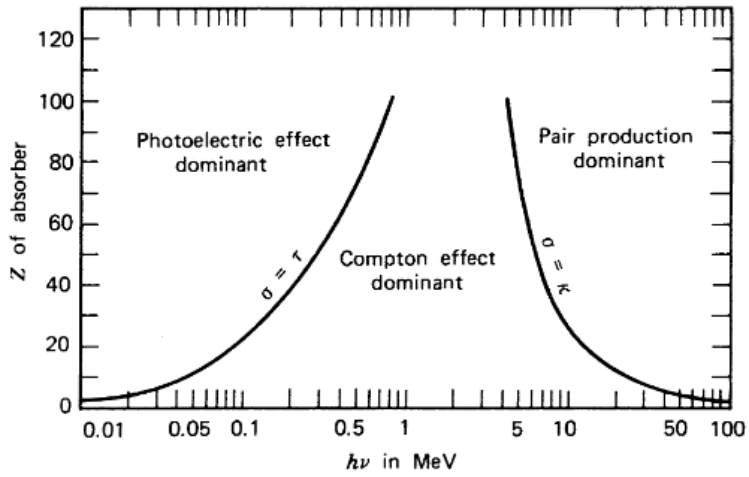

Fig. 2.13: The relative importance of the three dominant photon interactions.

Both the attenuation coefficients and the build-up factor can be calculated using analytical formulas. Nevertheless, for complicated geometries, accurate calculations require the implementation of Monte Carlo simulations, since such codes are able to track and calculate the interactions in different materials in each step, from the generation till the full absorption of a particle or photon. Moreover, different software programs have been developed, based on analytical calculations and a large library of reference data, able to provide accurate estimations of the mass attenuation coefficients in cases of simple transportation of a narrow photon beam for different materials (elements, mixtures or compounds)over a wide range of γ-ray energies (Oku_07; Now_98; Ber_87). Among the available codes, a web program called XCOM (Berg_10), can provide the cross sections and attenuation coefficients for elements, compounds and mixtures as needed, at energies between 1 and 100 GeV. The program provides total cross sections and attenuation coefficients, as well as partial cross sections for the following processes: incoherent scattering (Com), coherent scattering (Ray), photoelectric absorption (photo) and pair production in the field of the atomic nucleus (pair_n) and atomic electrons (pair_e). In Figs. 2.14 and 2.15 the mass attenuation coefficients for the different interactions are presented as a function of energy for two different elements, namely water (H_2O compound as the main constituent of seawater) and quartz (SiO_2 compound as the key constituent of sediment).

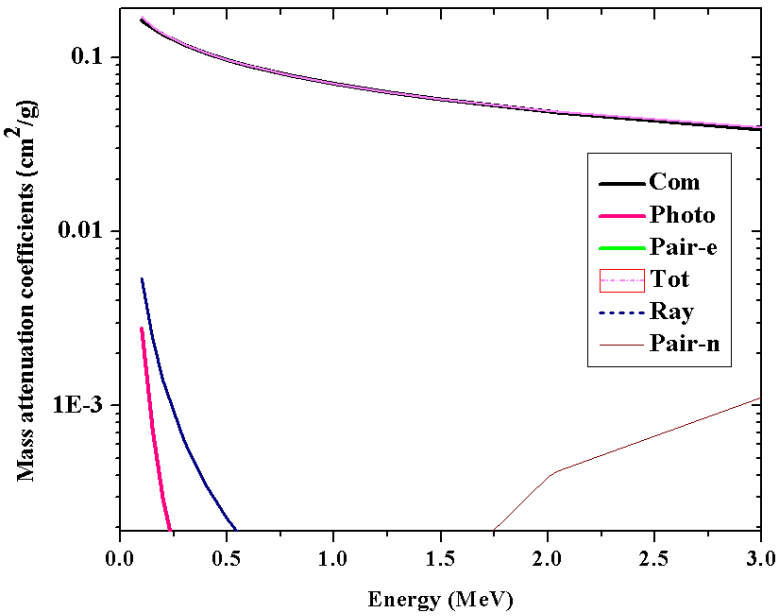

Fig. 2.14: Mass attenuation coefficients (cm^2/g) for H_2O calculated using the X-COM software.

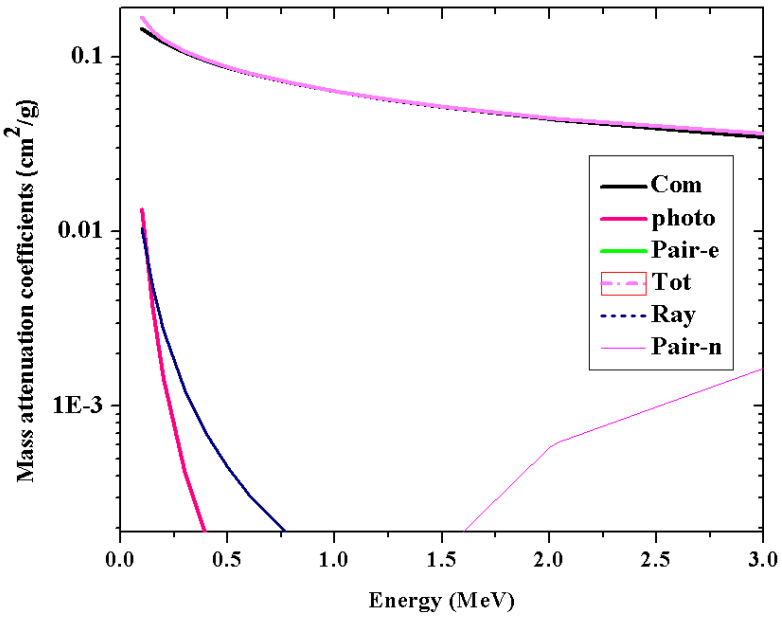

Fig. 2.15: Mass attenuation coefficients (cm^2/g) for SiO_2 calculated using the X-COM software.

As it can be seen from the graphs, the dominant interaction is the incoherent scattering (Compton Effect) which equals the total attenuation coefficient (sum of all processes) over a wide energy range. The differences in the incoherent scattering were small regarding the incoherent scattering probabilities, even for large variations in the Z_{eff} value (maximum difference of 45% for H_2O (Z_{eff} =7.2) and sed_0 (Z_{eff}=13.3) among the absorbers. The different SiO_2 absorbers exhibited reduced incoherent scattering coefficients compared to

the H_2O absorber. The maximum differences (more than one order of magnitude) were observed for the photoelectric absorption coefficients (high Z dependence), again between H_2O and sed_0. From the two graphs, the low probability of pair production for both materials can be seen, while again it is higher for the sed_0 absorber by approximately comparing factor of two compared to the H_2O absorber. In Fig. 2.16 the total mass attenuation coefficients for the different interactions are presented as a function of energy for 4 different elements, namely water (H_2O compound), quartz (SiO_2 compound), a typical sediment matrix (mixture of Al_2O_3 (4.66), SiO_2 (37.79), P_2O_5 (0.079), K_2O (0.623), CaO (31.28), TiO_2 (0.18), Fe_2O_3 (0.895), Na_2O (0.94), MgO (1.17), SO_3 (0.26), MnO (0.036)) and of a water-saturated sediment (water content 50% w/w) with the same matrix, respectively.

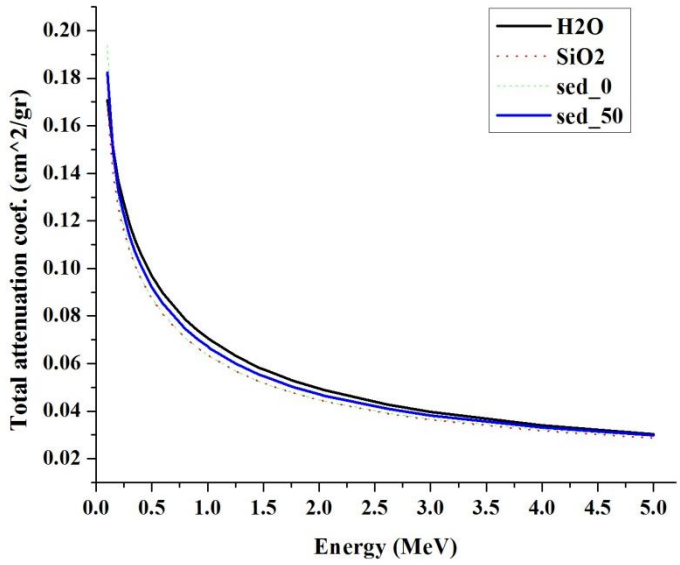

Fig. 2.16: Total mass attenuation coefficients (cm^2/g) for H_2O calculated using the X-COM software, for 4 different absorbers, namely water (H_2O), quartz (SiO_2), a typical sediment matrix (sed_0) and a water saturated sediment matrix (sed_50).

The maximum relative differences (mean value of 10%) of the total mass attenuation coefficients were found between the H_2O and SiO_2 absorbers in the studied energy range. The maximum relative differences between the sediment (sed_0) and the SiO_2 absorber was found to be ~3% around 200 keV and quickly dropped to 1% above 400 keV. The water saturated absorber exhibited values lying below the ones of H_2O and above SiO_2 as expected, due to the addition of a high attenuation material (H_2O) in the matrix.

In Fig. 2.17 the total linear attenuation coefficients are presented as a function of

energy for the 3 different absorbers, namely, water (Z_{eff}=7.22, ρ=1.026 g/cc), SiO_2 (Z_{eff}=10.8, ρ=2.65 g/cc) and the water-saturated (water content of 50% w/w) sediment matrix (Z_{eff}=10.25, ρ=1.4 g/cc). In Figs. 2.18 and 2.19 the photoelectric absorption and the pair production linear attenuation coefficients are presented as a function of energy for the same 3 absorbers.

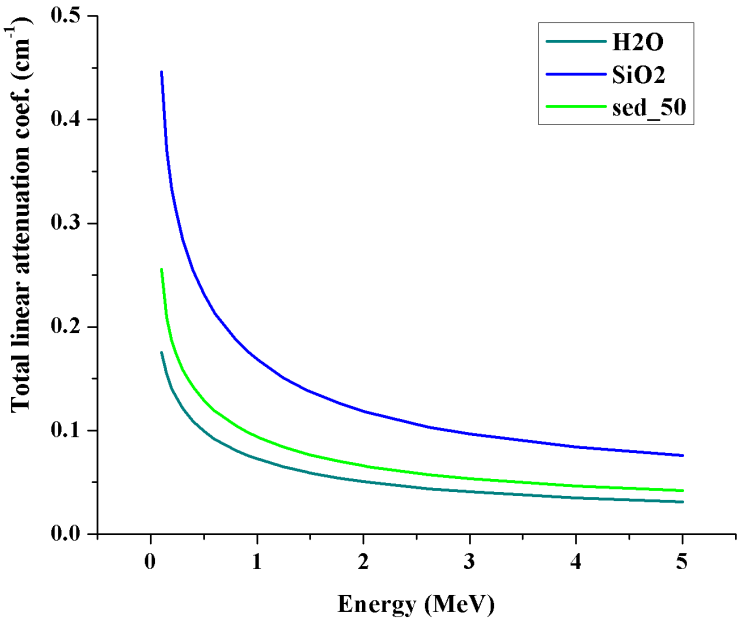

Fig. 2.17: The total linear attenuation coefficients are presented as a function of energy for the 3 different absorbers.

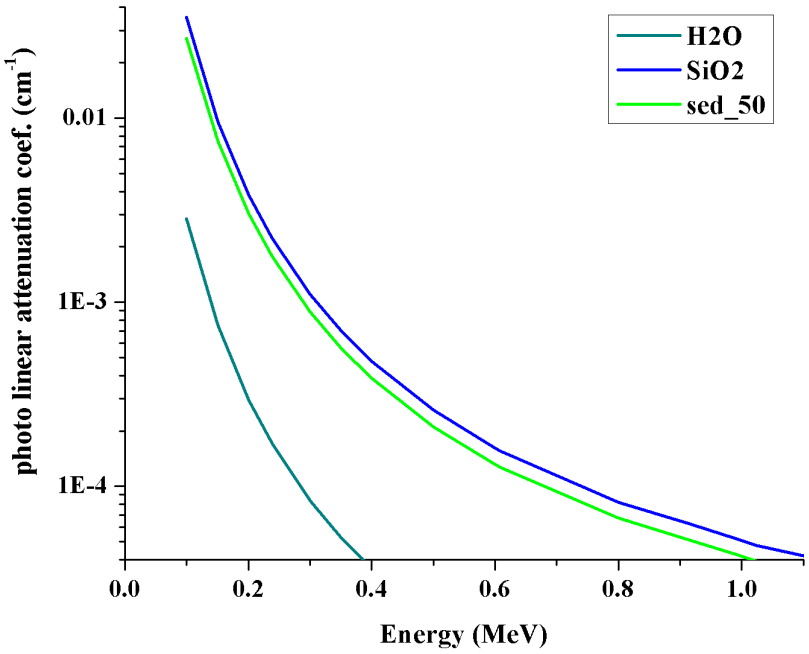

Fig. 2.18: The linear attenuation coefficients (cm^{-1}) for photoelectric absorption are presented as a function of γ-ray energy for the 3 different absorbers.

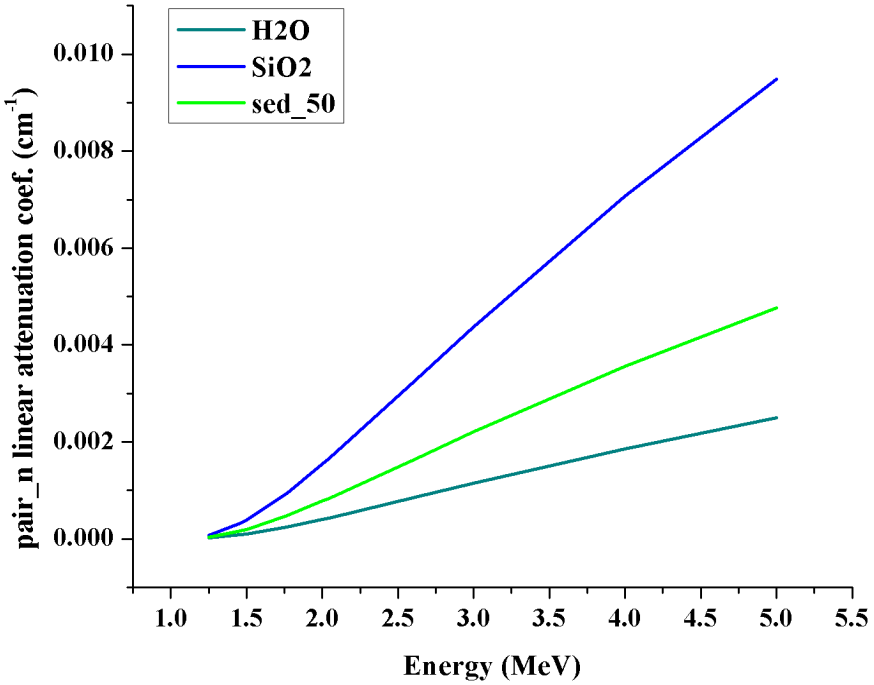

Fig. 2.19: The linear attenuation coefficients (cm^{-1}) for pair production (pair_n) are presented as a function of γ-ray energy for the 3 different absorbers.

The linear attenuation coefficients take into account the density of the absorber and therefore the differences are expanded and actually the H_2O absorber exhibits the lower values in every interaction process. As it can be seen in Fig. 2.17, the density of the material plays a defining role, compared to the Z_{eff} differences, regarding Compton scattering, as the similar behavior of water saturated sediment to H_2O can be attributed to their density values proximity (ρ=1.026, 1.4 g/cc). On the contrary, the photoelectric effect is governed by the Z-dependence as shown in Fig. 2.18. The same pattern, to a lesser extend however, applies also to the pair production (Fig. 2.19).

2.3. Utilized detectors for γ-ray spectrometry applications

The detection of γ-rays relies on the transfer of their energy to electrons and the subsequent measurement of the ionization created as the high-energy electrons move through matter. Therefore, a detection system is designed according to the interaction processes of γ-rays with matter in the energy range of interest (Eber_08). Thus, materials of high atomic number (Z) and density, as well as adequate dimensions, to ensure the deposition of energy inside the detector and the restriction of radiation escape are preferable. Different types and sizes of detectors have been used in γ-ray spectroscopy.

There are principally two detector types most widely utilized in γ-ray spectroscopy: i) inorganic scintillators, and ii) solid state semiconductors. Their beneficial characteristics in γ-ray spectroscopy differ and depend primarily on differences in their properties and the process of the ionization collection.

2.3.1. Semiconductor detectors

Semiconductors have some interesting properties that are beneficial for γ-ray detection. Crystals of adequate dimensions for γ-ray spectroscopy are commercially available and a large variety of semiconductors exhibit moderate to high-Z and density values. Different semiconductors have been tested so far, such as Si, Ge, GaAs, CdTe, CdZnTe, TlBr and HgI_2. Generally, the principle of operation of a semiconductor detector is based on the collection of the charges (electrons and holes), created by the primary photon interactions in the crystal active volume which is the depletion region. This is a region stripped of free charge carriers created by adding proper impurities in the crystal and applying reverse high voltage bias. For γ-ray spectroscopy applications, the active volume of the detector needs to be maximized and therefore a high voltage bias is applied. Through the application of the external electric field the electrons and holes, created by the primary photon interactions, move in opposite directions towards the electrodes (anode and cathode for electrons and holes, respectively). The movement of the electrons and holes causes a variation of induced charge on the electrodes and therefore a direct electrical signal. The signal created from the collected electron–hole pairs is directly related to the absorbed γ-ray energy. Semiconductors exhibit a small energy band gap between the conduction and valence band zones and therefore the energy of just a few eV suffices to create an electron–hole pair. This property of semiconductors constitutes their great advantage for γ-ray spectrometry, since the small energy band gap leads to an efficient collection of the primary radiation. Moreover, the small energy band gap leads to nicely separated pulses with respect to the primary γ-ray energy and therefore, to a high ability of distinguishing neighboring peaks (i.e. high energy resolution).

From the available materials, Ge crystals have a superior energy resolution due to their small band gap (~0.67 eV). Nevertheless, the small band gap of Ge favors the thermal excitation of electrons and therefore the production of electronic noise. This process can only be sufficiently suppressed by cooling to low temperatures (approximately around -196.15^{o} C). Liquid nitrogen is the most common medium used for cooling the Ge crystal,

however, recent advances in electrical cooling systems have made electrically refrigerated cryostats a viable alternative for many detector applications (Canber_14). Despite this implication of cooling, Ge crystals are still favorable compared to the other semiconductors, especially for laboratory-based measurements, due to their superior resolution and their high efficiency over a wide γ-ray energy range. Nevertheless the necessity of cooling complicates the use of Ge detectors and in some cases limits their application, especially when measurements are held directly in the field. The electrical cooling requires high power consumption and thus continuous measurements for long time intervals are not possible.

GaAs, CdTe, CdZnTe and HgI_2 present a medium to high Z matrix, which promises a good peak-to-total ratio. In addition, the band gap is large enough to operate the detectors at room temperature; however the energy resolution is again significantly improved when cooling is performed. The aforementioned detector crystals are not well-suited for high quality γ-ray spectroscopy due to their limited efficiency (small crystal sizes) and energy resolution, which is about a factor of three worse than the one of a Ge detector (Eber_08).

2.3.2. Scintillation detectors

Scintillators rely on the conversion of the absorbed energy, caused by the interaction of incident rays with the crystal, to optical photons. The incident γ-rays interact with the crystal material producing a secondary emission of high energy electrons which subsequently interact with the less bound electrons in the atoms causing ionizations and excitations in the crystal. The de-excitation in such materials is accomplished with a simultaneous emission (10^{-8} sec) of optical photons (scintillation). The scintillation mechanism depends on the structure of the crystal lattice which forms the available energy states. In many cases, small amounts of impurities (activators) are added to the crystal in order to cause changes in the energy states, thus permitting the de-excitation. The emission of scintillation light is isotropic in all directions. Therefore, a reflector is mounted around the crystal to assure that a larger fraction of light is collected. The output from a scintillation crystal can be converted into an electrical signal by different pieces of instrumentation, while the most common technique is the use of a photomultiplier tube (PMT). Again, a high voltage bias is applied for the electrical signal collection, however a much lower voltage supply is required compared to semiconductor detectors. The PMT

consists of a photosensitive cathode which converts the visible photons into photoelectrons and a set of dynodes, in which the electrons are repeatedly multiplied. The produced photons inside the crystal are collected in the window of the PMT. The photons strike the photocathode, thus producing electrons by the photoelectric effect. These produced photoelectrons are accelerated towards the first dynode by applying a positive potential with respect to the photocathode. The electrons are sufficiently energetic to cause secondary electron emissions, which are accelerated towards the next dynodes by increasing in each dynode the bias voltage, where a similar process occurs, and eventually, an amplified signal is produced in the anode. The resulting signal is proportional to the incident γ-ray energy. The resolution of scintillation detectors is relatively worse compared to that of semiconductor detectors, owing to the combined effects of scintillation efficiency, light loss, and in the statistical spread in the number of photoelectrons produced at the photocathode.

The most widely utilized scintillation detectors are NaI(Tl), CsI (pure or doped with Tl or Na), and $Bi_4Ge_3O_{12}$(BGO), due to their high efficiency (high Z materials) and tolerable resolution. Among them BGO detectors exhibit higher efficiency (due to the higher density, 7.13 g/cc) but much lower resolution, while CsI detectors have again larger density (4.51 g/cc) compared with NaI(Tl) detectors but are rather slow (thus they are avoided for high count-rate applications) and exhibit lower resolution values. Scintillation detectors are mostly used for *in situ* γ-ray spectrometry applications due to their compatible sizes, lower cost and high detection efficiency. Lately, Lanthanum ($LaBr_3$(Ce), $LaCl_3$(Ce)) and Cerium ($CeBr_3$) based crystals are also commercially available. These are very promising scintillating materials for γ-ray spectroscopy due to their superior resolution and efficiency properties. Nevertheless, their use for environmental applications is still limited due to their high intrinsic activity, especially in the case of La detectors (Quar_13), where a high intrinsic count-rate (compared to measured environmental count-rates) within the crystal is always present (from the ^{138}La radioactive decay). However, $CeBr_3$ detectors with a very low intrinsic activity are also commercially available and constitute a competitive alternative for environmental applications using the *in situ*γ-ray spectrometry.

2.3.3. Detectors in underwater γ-ray spectrometry

Several detection systems have been developed from different research groups and have been deployed in the sea for *in situ*γ–ray spectrometry. These instruments consist of

different types of scintillators, such as BGO (Jones_01; Graaf_07), a variety of different size NaI (Osv_01; IAEA_99; Tsab_08, Tsab_12; Cine_16; Zhang_15), fluorides (e.g., CsF and BaF2), CsI or semiconductor detectors which do not require external cooling (e.g., CdTe, CdZnTe, HgI2, and GaAs). Nevertheless, such systems have not yet become competitive to NaI(Tl) and HPGe detectors for applications in the marine environment (Pov_12), mainly due to their lower efficiency or resolution properties in the energy interval 30-3000 keV. HPGe systems have been applied (Pov_96; IAEA_99; Sokolov_99) in the marine environment, nevertheless small acquisition times (autonomous operation) were achieved, ranging from 20min, to 24h, due to the necessity of electrical cooling. On the contrary, NaI systems can operate continuously for 3 months without maintenance and their power consumption is relatively low (1.0 – 2.0W) (IAEA_10b).

2.4. Signal processing, calibrations and implications

2.4.1. Signal processing

Apart from the detector, there are several units needed for the signal amplification and processing in order to obtain the final pulse-height spectrum. Such units include the high voltage bias supply necessary for the operation of the detector, a preamplifier (which is attached to the crystal and is usually provided by the manufacturer) and an amplifier, a Multi-Channel Analyzer (MCA) unit and a PC unit, in which appropriate software for the display, analysis and storage of the spectrum is incorporated. A simplified diagram of a typical electronic set-up for γ- spectrometry is depicted in Fig. 2.20. The preamplifier is responsible for producing a pulse with amplitude proportional to the collected charge and converting the initial signal (collected charge) in appropriate units so that it can be recognized by the pulse shaping amplifier. The preamplifier is placed in close contact with the detector to maximize the signal to noise ratio. The pulse exiting the preamplifier is driven to the amplifier input gate. Shaping is the primary function of the amplifier, while it also magnifies the amplitude (coarse and fine gain) of the output preamplifier pulse, so that the maximum voltage output of the amplifier matches the MCA voltage range (Gilm_08). Moreover, additional features are incorporated within the amplifier to provide pole-zero cancellation, baseline restoration and pile-up rejection (Gilm_08). Adjusting the optimal shaping is vital to the production of high-quality spectra, as it is responsible for the optimization of the energy resolution and the minimization of overlaps between the pulses.

The Multi-Channel Analyzer MCA consists of an analog-to-digital converter (ADC), a control logic, a memory and a display. The ADC is located at the MCA input and is responsible for the conversion of the voltage pulse coming from the amplifier to a binary number that is proportional to the amplitude of the input pulse. The accepted pulses are controlled by the lower and upper discriminator levels. Each produced number is addressed to a memory location, and one count is added to the contents of that memory location. MCA collects and sorts the pulses coming from the amplifier into a large number of contiguous, equal-width, user-defined bins (channels). The number of available channels varies from 256 to 16384 in different MCA units.

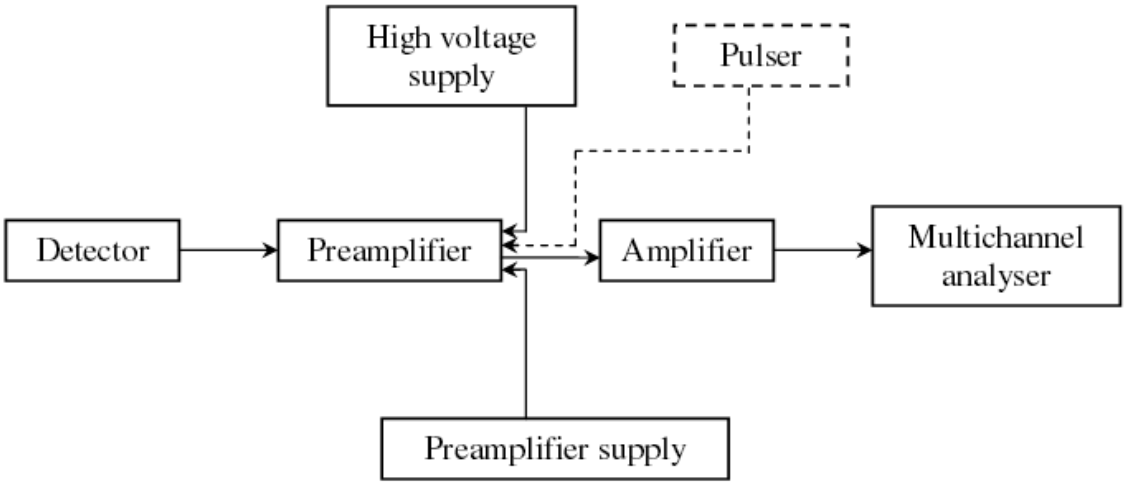

Fig. 2.20: A simplified diagram of a typical electronic set-up for gamma-ray spectrometry.

After collecting data for some period of time, the memory contains a list of numbers corresponding to the number of pulses at each discrete voltage. The MCA collects pulses in all voltage ranges at once and displays this information in real time. The memory is accessed by a host computer, equipped with appropriate software for the control of the MCA and the display of the final representation of the pulse-height spectrum.

Although the procedure of producing a pulse-height spectrum is common in both semiconductor and scintillation detectors, the electronic units (high voltage units, preamplifiers, amplifiers) utilized in each case exhibit different characteristics. Moreover, digital electronics are progressively used nowadays; nevertheless, the above discussion was limited to analog electronics which were utilized in the present work.

2.4.2. Calibration procedures

Prior to performing a measurement, several steps are required concerning the calibration of the detector and electronics in order to obtain reliable results. As a first step, the electronic setup is fixed in a way to achieve the best signal to noise ratio and assure that the detection is performed in the desired energy range. After the electronic setup performance, an energy calibration is required, so that each radionuclide present in the sample can be recognized from its corresponding full energy peak (photopeak) in the spectrum. The energy calibration is the determination of the slope (keV/channel) and offset (keV) calibration constants. It is usually performed using standard (calibrated or not) sources covering the whole energy range of interest. The next step is to perform the resolution calibration which can again be performed using standard sources. The charge collection efficiency is a crucial property of a radiation detector that strongly affects the energy resolution. High charge collection efficiency ensures a good energy resolution. Generally, the energy resolution of a radiation detector is mainly influenced by the statistics of the charge carrier generation (Fano factor), the electronic noise and the charge collection process. A measure of the energy resolution is given by the full width at half maximum (FWHM) of the amplitude of the photopeak and can be quoted in terms of energy or by the full width at half maximum (FWHM) divided by the peak centroid energy and given as a percentage. The resolution of the system provides a measure of how well two neighboring peaks can be distinguished. Therefore, the performance of the resolution calibration enables us to detect hidden features in the spectrum. For instance, resolution values larger than the expected ones could indicate the presence of convoluted peaks in the spectrum or artifacts attributed to electronics.

The determination of the activity concentrations requires a prior knowledge of the detector efficiency. Therefore, the most important calibration procedure, which enables the determination of the activity concentrations, is the absolute photopeak (or full energy peak) efficiency calibration, also referred to as ‘detection efficiency’. This is a measure of the detector sensitivity to an incident γ-ray according to its energy. The absolute photopeak efficiency , ε, is calculated by the ratio of the counts detected in a photopeak to the expected emitted counts in a certain solid angle as shown in the following equation:

$$\varepsilon = \frac{number\ of\ Net\ Counts\ detected}{number\ of\ Counts\ emitted}\ |d\Omega \tag{2.8}$$

Different methods that rely either on relative measurements, or analytical calculations, both absolute and semi-empirical, have been applied for the detection efficiency calibration (IAEA_10b). Originally, relative measurements constituted the first and only technique that could provide quantitative results for quite a long time (IAEA_10b), and still constitute the most widely applied technique for laboratory-based measurements. The detection efficiency values are derived from a measurement of a source with a known activity concentration (calibrated source) which exhibits the same geometrical and physical characteristics with the sample under study and contains radionuclides with multiple γ-rays emissions in the energy range of interest. By analyzing the obtained spectrum, the detected counts under a photopeak are calculated. An additional blank measurement is required to quantify the contribution of the ambient background in the photopeak and subtract the corresponding counts. By this subtraction the detected net counts are calculated. The efficiency values are derived using Eq. 2.8, where **ε**, is the only unknown quantity, since the emitted counts can be derived from the activity concentrations. The measurement therefore results in discrete efficiency values, which correspond to γ-ray energies emitted from the radionuclides present in the calibrated source. In order to expand the experimental results in a wide range of energies, the experimental data is fitted with an appropriate function. Different polynomial or exponential functions have been used, while the most commonly used among them is the one proposed by Debertin and Helmer (1988).

This technique that relies on a relative calibration is indeed the most accurate, but is also inflexible. This is because a variety of samples are required for its implementation, exhibiting different geometrical and physical characteristics, depending on the measurement. Moreover, any calibration source should contain γ-rays emitted in a wide range of energies covering the available detection range. In addition to the problem that such sources are not widely available, a recalibration performance is required each time the measurement geometry (solid angle according to different measuring geometries e.g. Marinelli beaker or petri, or distance from the detector) or the physical characteristics of the source (density, chemical composition) change. In fact, in order to achieve accurate activity concentration results the calibration source should ideally exhibit characteristics that exactly match the properties of the real sample. Nevertheless, the problem of

heterogeneities among the samples and calibrated sources is easily resolved, as corrections can be applied to account for differences in the physical characteristic between the calibrated source and the samples through efficiency transfer techniques. Despite the aforementioned difficulties, the technique based on relative measurements assures accurate results, thus limiting the probability of systematic errors and thus constitutes the most widely applied technique for laboratory-based measurements.

On the contrary, this technique is not well suited for *in situ* spectrometry for various reasons. First of all, it is not easy to produce realistic calibration sources (IAEA_10b) due to the complex geometries, as well as the implications of real conditions involved when measuring in the field. In addition, large amounts of a powder radioactive material are required with known activity concentrations (calibration source), ideally exhibiting similar characteristics to the studied environment and such sources are not widely available. Even if such sources were available, the calibration procedure would lead to large quantities of radioactive waste. Moreover, while the calibration would be valid only for the physical characteristics (e.g. density, composition) of the material utilized, the need for independent recalibration procedures would arise. This is a serious drawback limiting the application of this technique for *in situ* spectrometry (Tyler_96). Nevertheless, there are some reported works in the literature that have performed relative measurements for the efficiency calibration using complementary laboratory measurements.

An absolute calibration via Monte Carlo (MC) simulations is better suited for *in situ* measurements, since a better representation of the actual conditions is possible (IAEA_10b). MC simulations have been widely applied to reproduce experimental results, even in very complex geometries, both for *in situ* and laboratory-based measurements (Elef_13, Mauč_09; Askri_08; Róden_07; Hendr_02). The excellent reproduction of the detection efficiency experimental data for a wide range of different applications using γ-ray spectrometry rendered the MC simulations a robust and reliable technique. Nevertheless, it requires the precise knowledge of the measurement details (detector, source and intercepting layers geometry characteristics, as well as, chemical and physical data).

Codes using semi-empirical methods for the efficiency calibration are also available, combining advantages and minimizing drawbacks of the two previous calibrations. These methods can be accommodated in a great variety of measurement situations and are broadly applicable. More details on the available codes are given in sections 2.4.3 and 2.4.4. The aforementioned calibration procedures need to be periodically repeated for an individual detector and geometry set-up, since, drifts in the detector active volumes along with long-

term changes in the charge collection efficiency and in the electronic set-up, can lead to variations in the results, affecting the activity concentration calculations (especially in the case of the detector efficiency calibration).

2.4.3. Coincidence summing effects

Coincidence summing effects occur when two or more γ-rays interact with the detector and deposit all of their energy within a time that is short compared to the response time of the detector or the resolving time of the associated electronics. As a result, the events cannot be distinguished and are recorded as a result of a single interaction. This means that the energy transferred to the detector and finally recorded in the spectrum is the sum of the energy arising from all the individual interactions. There are two types of coincidence summing effects, random coincidence summing or pile-up and True Coincidence Summing (TCS).

Pile-up concerns events that originate from more than one decaying nucleus and is ruled by the statistical probability of simultaneously detecting two or more incident γ-rays as a single event. Its occurrence is therefore dependent on the available number of nuclei and therefore, the activity of the source. If pile-up is present, it can be observed in the spectrum through the appearance of a peak with an energy that equals two times the energy of the photopeak. Moreover, a large continuum of sum events will also occur at lower amplitudes (between the sum peak and the photopeak) due to the summation of partial energy loss interactions. Random coincidence summing is related to high count-rates and is usually not present in environmental sample measurements (low count rate). Pile-up effects can be reduced by limiting the source activity (Pb shielding, increase of the distance between the source and the detector). In cases where it is not possible to reduce the counting rate, a correction for the lost events should be applied.

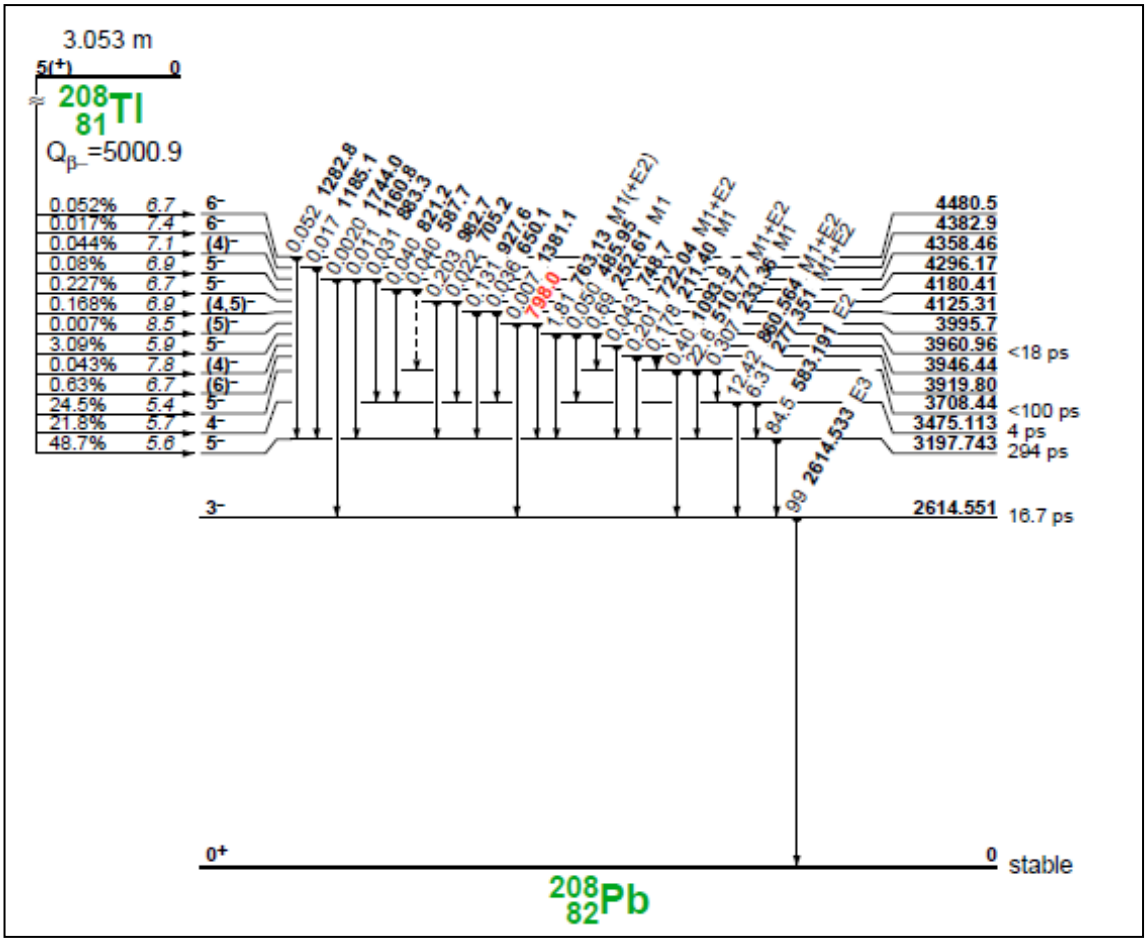

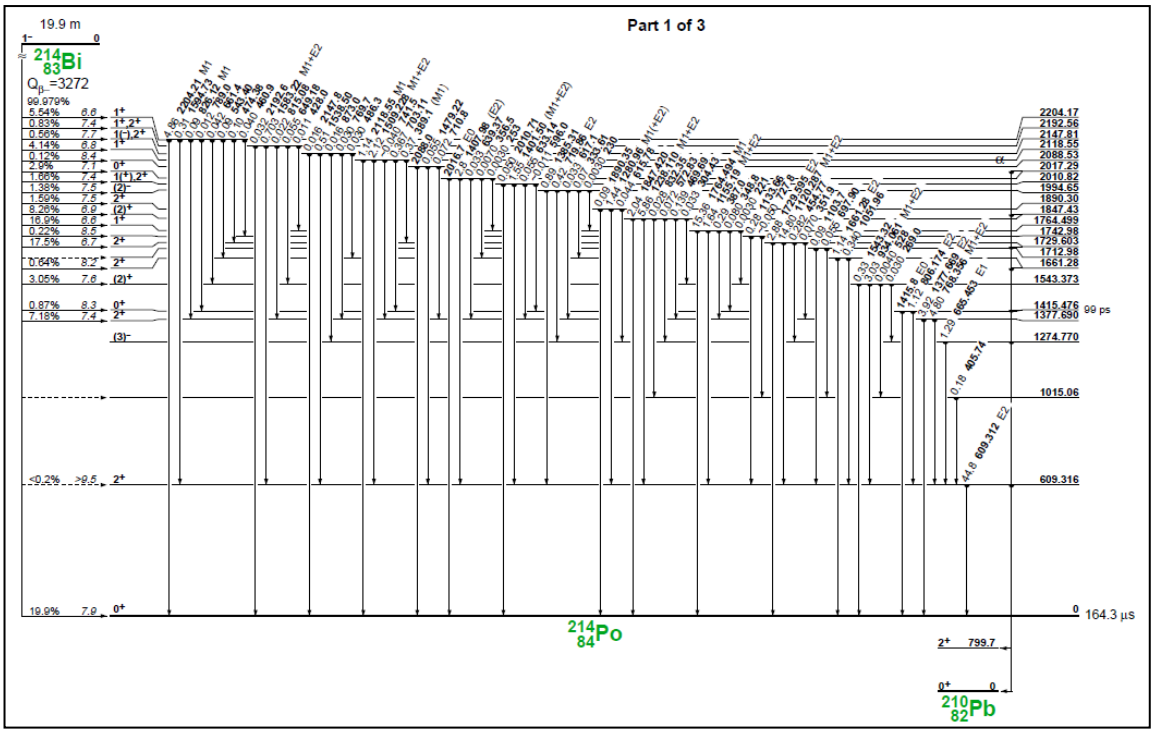

Fig. 2.21: Diagrams of the cascade decay schemes of ^{208}Tl (up) and ^{214}Bi (down).

TCS concerns events arising from the emission of multiple photons or X-rays within a single decay of an unstable nucleus (cascade nuclides). ^{208}Tl and ^{214}Bi exhibit a rather simple and much more complicated cascade decay scheme, respectively, as shown in Fig. 2.21. True Coincidence Summing or 'cascade effect' is realized when the lifetime of the intermediate state is generally so short, that the events (γ-, X-rays) are emitted in coincidence, meaning that a single output pulse will be generated as the charge collection time is much greater than the corresponding nuclear lifetimes. Therefore, cascade summing occurs for nuclides which emit two or more γ-rays in coincidence, or X-rays in coincidence with the emitted γ-rays within the solid angle subtended by a γ-ray detector. The result of the TCS effect is an output signal from the detector that equals the sum of the energy of the emitted γ- and X-rays. These events will therefore be interpreted as a full energy peak (sum peak) in the spectrum at an energy that equals the sum of the cascade photons, followed by the loss of counts in the full energy peak for the γ-rays participating in the sum peak as well as an increase in counts in the spectrum background at higher amplitudes than those of the full energy peaks (again due to the summation of partial energy loss interactions). The aforementioned description of the loss of counts in the full energy peak is known as the 'summing out' effect (Bri_14). Nevertheless, a process with opposite results in the full energy peak may also occur. This means that the sum peak coincides with one of the photopeaks present in the spectrum. This leads to an 'artificial' increase of counts in the full energy peak for the γ-ray that exhibits the exact energy of the sum peak. This is known as the 'summing in' effect (Bri_14). An example can be shown for ^{214}Bi (Fig. 2.21). The sum of the two cascade γ-rays, namely 1120 and 609 keV, coincides with the emission of the γ-ray at 1730 keV and therefore, the sum peak will be displayed together with the full energy peak of 1730 keV in the spectrum.

Opposed to pile-up, TCS effects occur within the same nuclei exhibiting a cascade decay scheme and do not depend on the activity of the source. On the contrary, it always occurs when cascade radionuclides are present in the sample. The occurrence of TCS depends on the properties of the source (density, composition, size) when voluminous samples are involved, the measurement setup and the properties of each particular radionuclide (decay scheme properties). In more detail, concerning the detector-source geometry (measurement setup) and the nuclides present in the source, TCS effects are controlled by the branching ratio of the γ- or X-rays, the angular correlation that may exist between them, the emission probability of each γ-ray, and above all, the solid angle subtended by the detector and the sample, as well as, the type of the detector and more

particularly the material of the detector window (more prominent with a carbon fiber window). TCS effects are drastically reduced when the source is placed far from the detector window and are negligible for detector-source distances larger than approximately 10 cm.

TCS effects play an important role in environmental samples measurements since the majority of the naturally occurring radionuclides exhibit a complicated cascade decay scheme. Moreover, the measurements are usually held in touch geometry between the detector and the source, in order to reduce the time necessary to acquire adequate statistics. Unfortunately this detection geometry maximizes TCS effects (Deb_79; Deb_88). Although in laboratory measurements, the samples could be placed in far distances, this would be accomplished at a severe expense of the acquisition time and thus is usually avoided. Moreover, TCS effects strongly affect the performance of *in situ* measurements in the aquatic environment in touch geometries.

The increase or decrease in the full energy peak counts leads to erroneous results in the activity concentrations. To obtain the correct activity concentrations for a cascade radionuclide, a correction must be applied to the full energy peaks for the γ-rays of the corresponding radionuclide. An experimental way to eliminate TCS effects is to use, for the detection efficiency calibration of natural or artificial radioactivity peak yields, a calibrated source of the same radionuclide, having the same radioactivity (which can be found within IAEA reference materials). TCS effects influence the same way both the count-rates of the peaks of the efficiency calibration measurements and the ones of the peaks of the sample to be investigated. Therefore, when the latter are converted into activity units by means of the efficiency calibration coefficients obtained from the former, the results are automatically corrected for TCS effects.

In cases where calibrated sources with the exact physical properties are absent, correction factors for TCS effects need to be determined and included in the activity concentration calculations. Different techniques have been widely applied to account for TCS corrections and can be found in the literature. These techniques involve experimental calculations (Qui_95), derivation of analytical expressions (Nov_07; Kor_92), semi-empirical calculations (Yüc_10; Fel_00; Fel_02), or the implementation of general-purpose Monte Carlo codes (Bri_14; Dec_96; Zhu_08). Often, combinations of the available techniques have been utilized, mostly based on semi-empirical calculations combined with Monte Carlo codes (Lépy_12; Vid_11; Lépy_07; Sima_96,01; Piton_00). The aforementioned technique offered the possibility of developing software programs that

provide TCS corrections for a variety of detector crystal types, detector sizes and shielding material, as well as, for different samples properties for a wide list of radionuclides. There are several developed software programs including either commercially available or home products (IAEA_02). One of these programs, the EFFTRAN code (Vid_05), is implemented in the present work to estimate the TCS factors for the efficiency calculations, as well as the activity concentrations concerning the laboratory measurements. The TCS effects regarding *in situ* measurements are treated using the Monte Carlo codes MCNP-CP and FLUKA. The principles of MC simulations, as well as the characteristics and differences of the two MC codes are discussed in the next chapter.

2.4.4. Detection efficiency influence by sediment properties

It has been seen that seawater presents rather homogenous physical characteristics (density, chemical composition), whereas this is not the case for the physical properties of marine sediment samples, whose density, texture, porosity and chemical composition can greatly vary. As a direct consequence, the detection efficiency values would also vary according to the different characteristics (Ra_99) especially for the large voluminous samples (typically > 14 cm^3) used in laboratory γ-ray spectrometry. For this reason, a standard sample pre-treatment procedure has been established according to IAEA guidelines (IAEA_03). In brief, this procedure includes drying, sieving and pulverizing the sediment samples prior to the final measurement, in order to obtain a more uniform distribution concerning the bulk density, water content (which is totally extract), pore space and grain sizes. Nevertheless, the differences in the chemical composition and especially in the sample's dry density imply deviations in the efficiency for every sample. Therefore a correction factor related to the differences in density and composition should be calculated and applied to the final calculation of the activity concentrations. There are several developed software programs based on efficiency transfer calculations able to provide accurate efficiency calculations for different sample sizes and properties. Among them, there are both commercially available programs, such as GESPECOR (Semk_15) and ANGLE™ (Bell_12), or publicly available codes such as DETEFF (Díaz_08) and EFFTRAN (Vid_05). The software developed by Vidmar et al. (2005), which can also account for TCS effects, was utilized in the present work to correct the efficiency values both for TCS effects and for differences between the sediment samples and calibrated

sources properties, according to each sample physical characteristics. Moreover it was implemented to correct the activity concentration results, as discussed in the previous section.

The differences in the physical characteristics of the marine sediments can greatly affect the photopeak efficiency of the detectors used for *in situ* measurements on the seabed. In such measurements the differences in the attenuation of photons are even more pronounced due to the larger volumes involved. Moreover, the presence of water within the sediment matrix (water-saturated) in the real environment is a significant parameter contributing to the diversity of sediment physical properties. The influence of sediment physical properties to the detector photopeak efficiency is thoroughly discussed in chapter V.

2.4.5. Data quantification

The most commonly applied technique in laboratory γ-ray spectrometry for the derivation of the activity concentrations requires the analysis of the photopeaks present in the pulse-height spectra of the measured sample and of a background-level measurement performed under the same conditions, to account for the ambient background radiation (cosmic rays, building material, detector shielding effects, Rn in air, unidentified sources). The activity concentrations A (Bq/kg) in sediment samples are derived by calculating the specific activity (the activity per unit mass of the sample), using the following formula:

$$\boldsymbol{A = \frac{N_s - N_b}{I_\gamma \cdot \varepsilon' \cdot T \cdot C_f \cdot M}} \tag{2.9}$$

where:

N_s : the counts detected under the net peak area (after the subtraction of the Compton continuum background) of a photopeak in the acquired spectrum for the sediment sample

N_b : the counts detected under the net peak area (after the subtraction of the Compton continuum background) of the same photopeak in the spectrum of the background-level measurement, acquired in the same time interval and under the same conditions

ε': the measured photopeak efficiency ε, at the photopeak centroid energy, corrected for differences in the physical properties between the sample and calibration sources (relative

measurements), using a correction factor C_p, and corrected for TCS effects for the corresponding γ-ray, taking into account the physical characteristics of the sediment sample, using a correction factor C_{TCS}, (in case of emission in cascade mode)

$$\boldsymbol{\varepsilon' = \varepsilon \cdot C_p \cdot C_{TCS}} \tag{2.10}$$

$\boldsymbol{T}$: the acquisition life time in seconds

$\boldsymbol{M}$: the mass (kg) of the measured sample

$\boldsymbol{I_\gamma}$: the emission probability or the γ-ray forming the corresponding photopeak

$\boldsymbol{C_f}$: A product of several correction factors accounting for

$$\boldsymbol{C_f = C_1 \cdot C_2 \cdot C_3 \cdot C_4} \tag{2.11}$$

C_1, is the correction factor for the elapsed time from the sample collection to the start of the measurement (=1 except in cases of small half lives $T_{1/2}$)

C_2, is the correction factor for the nuclide decay during the measurement (=1 except in cases of small half lives $T_{1/2}$)

C_3, is the correction factor for random summing (=1 except in cases of high count-rates)

C_4, is the factor for TCS effects correction (=1 except in cases of γ-rays emitted in cascade)

2.5. Detection systems utilized in the present work

The γ-ray spectroscopy measurements on the seabed and in the seawater were carried out by deploying the *in situ* underwater γ-ray spectrometer KATERINA (Tsab_04; Tsab_08). Additional measurements by means of laboratory high-resolution spectrometry using different HPGe detectors have also been conducted. These measurements were performed on collected samples from the studied sites in order to derive the activity concentrations. The measurements were held on the laboratory facilities of the Hellenic Centre for Marine Research (Marine Environmental Radioactivity laboratory-MERL, Institute of Oceanography) and the Nuclear Physics Laboratory at the National Technical University of Athens (NTUA). The laboratory-based measurements were implemented for

the evaluation of the *in situ* data regarding the efficiency calibration results, as well as, the estimated activity concentrations in several different applications. The specifications of the utilized detection systems are described in the following sections, while details on the measurements and the corresponding results are thoroughly discussed in chapter 4 regarding the measurements in the seawater and in chapters 5 and 6 regarding the measurements in the seabed.

2.5.1. The underwater detection system KATERINA

The underwater γ-ray spectrometer KATERINA utilized in the present application for γ-ray measurements in the seawater column and on the seabed was developed at the Hellenic Centre for Marine Research (Tsab_04; Tsab_08). The system consists of a commercial 3″×3″ NaI(Tl) scintillation crystal, connected to a built-in photomultiplier tube, a preamplifier and a power supply for the detector operation (high voltage bias), together with the electronics for signal amplification, data acquisition and storage. A representation of the system is presented in Fig. 2.22.

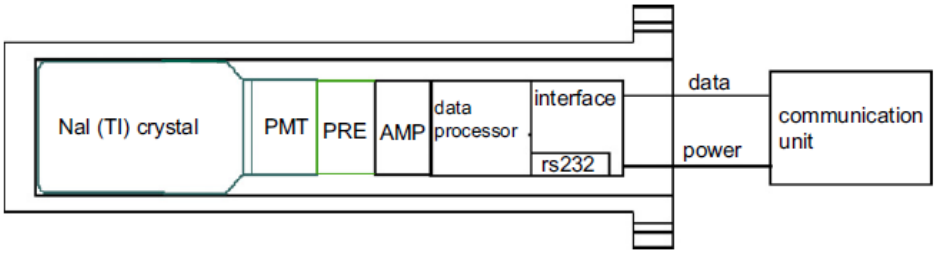

Fig. 2.22: The representation of the underwater γ-ray spectrometer KATERINA, including the detector and coupled electronic units (Tsab_08).

The output of the preamplifier is connected to a shaping amplifier, especially designed for underwater applications, where a low gross counting rate occurs (~10–40 cps). The output of the shaping amplifier is introduced to a Multi Channel Analyzer and the serial output is connected to a PC. The specifications of the system are depicted in Fig. 2.23, along with a photo of the system. The electronic modules were especially designed to fit inside the detector housing (85 x 550 mm). A special memory and microcontroller is incorporated in the system in order to be independent of any computer connection, allowing for measurements in autonomous or real-time mode.

The specifications of the detection system "KATERINA"

Sensor type	$3'' \times 3''$ NaI(Tl)
Energy range	Adjustable maximum and minimum energy of detection (with maximum value of 3000 keV)
ADC	Successive approximation 10 bit
High voltage	Internally controlled 100–1200 V
Spectroscopy	Adjustable 256, 512 or 1024 channels
Gain amplification, pole-zero cancellation, base-line restoration	Internally controlled and adjustable
Dead time	<0.5% in aquatic operation mode
Energy resolution (140.5 keV)	10%
Energy resolution (661.6 keV)	6.5%
Operating temperature	−5 °C to +50 °C
Consumption	1.2–1.4 W
Preset time	Gross γ and γ-spectrometry
Output	Time, date, cps, spectrum, dead time.
RS232 settings	Baud rate adjustable, parity "space", flow control "none"
Enclosure	Shape "Cylinder", material "Acetal"

Fig. 2.23: The underwater detection system KATERINA (Tsab_08).

A water-tight cylindrical enclosure (housing) has been designed, consisting of a low density (ρ=0.825g/cc) polymer, namely Acetal ($C_7H_{14}O_2$). The housing is used to protect the detector along with the electronics and was designed to offer continuous operation up to 400 m water depth. A different housing material is also available that offers secure operation up to a depth of 3000 m.

Some of the advantages of the detection system KATERINA, are the ability of autonomous operation for long-time periods (approximately for 4 months), the relatively low power consumption, the operational depth at sea (400m), the low-Z material used for the detector water-tight shielding, and the ability of installing the system on oceanographic buoys and seabed platforms. The system KATERINA is calibrated for radionuclide concentration measurements in the aquatic environment and has been successfully deployed in lakes, rivers and in the marine environment (Tsab_10, Tsab_11). The efficiency calibration for measurements in the water column was experimentally performed at the NTUA laboratory facility. The system was deployed in a calibration tank of 5.5 m^3 in capacity. The tank was filled with still water and a solution of diluted calibrated sources of ^{99m}Tc (photopeak at 142 keV), ^{137}Cs (photopeak at 662 keV) and ^{40}K (photopeak at 1460 keV) was added. At the bottom of the tank an electric pump was placed and operated before the measurements. The pump was used to circulate the water and therefore to ensure that

i.) the measurements be performed under homogeneous conditions

ii.) the sedimentation of the radionuclides in the bottom of the tank is avoided.

Additionally, an acid environment was created to limit the adhesion of the radionuclides in the tank walls by adding appropriate amounts of a nitric acid (HNO_3) solution. The experimental efficiency calibration was performed by deploying the detector in the middle of the tank to acquire spectra in different time intervals. More details concerning the experimental calibration can be found in Tsabaris et al., (Tsab_04), Bagatelas et al., (Bag_10) and Vlastou et al., (Vlast_06).

The efficiency calibration was subsequently extended in a wide range of γ-ray energies by performing Monte Carlo (MC) simulations using the GEANT4 code (Bag_10; Vlast_06). Initially, the simulation results were validated by comparison with the experimental photopeak efficiency data and subsequently several runs were performed over a wide range of γ-ray energies (200-3000 keV) with a step of 100 keV, to estimate the efficiency values in the γ-ray energy region suitable for environmental applications (150-3000 keV) using NaI(Tl) detectors. The MC estimated volumetric efficiency values (in units of m^3) along with the experimental values are depicted in Fig. 2.24, along with a schematic illustration of the experimental calibration measurement.

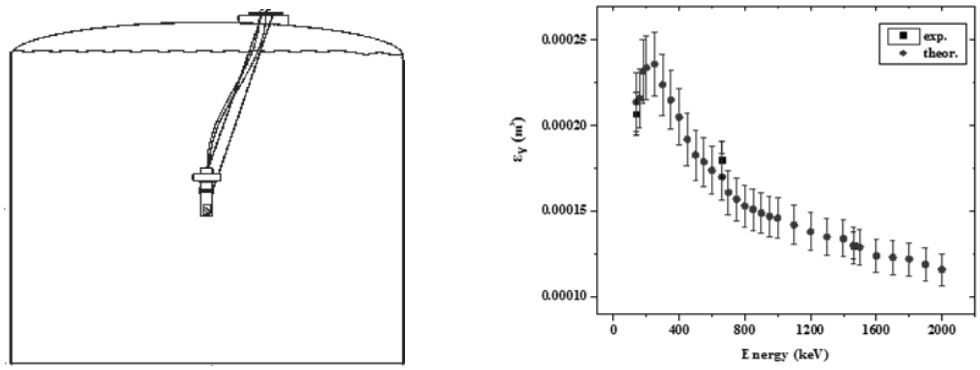

Fig. 2.24: Schematic of the experimental efficiency calibration (left) along with the corresponding experimental and simulation results (right) (Bag_10).

2.5.2. The HPGE system at the Hellenic Centre for Marine Research

The detection system at the HCMR facility consists of a HPGe detector connected to a liquid Nitrogen dewar of large dimensions (cooling system) along with the necessary

electronic units including

i) a high voltage bias supply for the detector operation at 4.8kV (TC950A, Tennelec)

ii) an amplifier unit for the signal amplification and shaping (2020, Canberra)

iii) a computerized MCA system (SpectechUC530) for the data acquisition and storage

iv) a PC connected to the MCA output equipped with an appropriate analysis software (Spectech driver).

The measurements are performed by a p-type coaxial High Purity Ge (HPGe) detector of 85mm in diameter x 64 mm in length, with an ultra-thin entrance window of carbon fiber foil (model GEM-FX8530P4), constructed by ORTEC®. The detector has a 50% nominal relative efficiency and a resolution of 2.1 keV at 1.33MeV (warranted value at 1.9 keV) along with a computerized MCA system for the data acquisition. In order to reduce the ambient gamma-ray background a lead shielding (58.5mm thick and 21mm height) is placed around the detector (Fig. 2.25).

Fig. 2.25: The HPGe detector (left) and the Pb shielding (right) at the facilities of the HCMR.

2.5.3. The facility at the National Technical University of Athens

The detection system at the NTUA facility consists of a HPGe detector connected to a compact liquid Nitrogen dewar (cooling system) along with the necessary electronic units including:

i) a high voltage bias supply for the detector operation at 3.5 kV (FAST ComTec, NHQ 205M)

ii) an amplifier unit for the signal amplification and shaping (627, Ortec)

iii) a computerized MCA system (Canberra Model 8715) for the data acquisition and storage

iv) a PC connected to the MCA output equipped with an appropriate analysis software (Genie2000, Canberra).

The measurements are performed by a p-type coaxial HPGe detector of 67mm in diameter x 67 mm in length with an entrance window of a 1mm thick Al foil (model GC5021) constructed by Canberra®. The detector has a 50% nominal relative efficiency and a resolution of 2.3 keV at 1.33MeV (warranted value at 2.1 keV) along with a computerized MCA system for the data acquisition. A key difference compared to the HPGe detector at HCMR is the use of Al for the detector window having a thickness of1 mm. This results in reduced photopeak efficiency values for low to medium γ-ray energies due to the high attenuation in the Al window which is a relatively high Z material. A detector shielding is again used to reduce the ambient gamma-ray background consisting of a horizontal cylinder of three different layers, an outer layer of Pb 50 mm thick, cadmium (Cd) layer of 2.5 mm, and a copper layer (Cu) of 2.5 mm. The cylinder is hollow inside and a hole of 16 cm in the front side allows for the positioning of the detector crystal inside the shielding, while performing the measurements. The detector and its shielding are depicted in Fig. 2.26. In Fig. 2.27 the background-level measurements acquired in the same time using the HPGe detector in the two different shielding systems are presented along with a measurement free of shielding. The efficiency calibration for the two utilized systems, Canberra GC5021 (NTUA) and ORTEC GEM-FX8530P4 (HCMR), for measurements on sediment samples is depicted in Fig. 2.28.

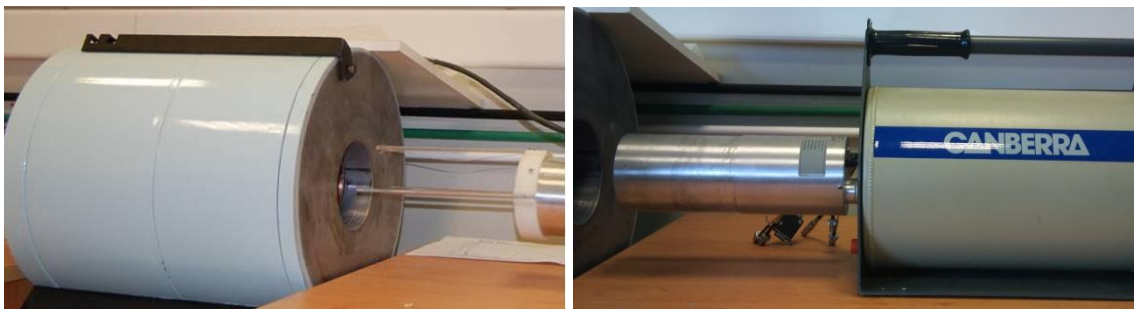

Fig. 2.26: The SEGe detector (right) and the Pb shielding (left) at the facilities of the Nuclear Physics Laboratory at the NTUA.

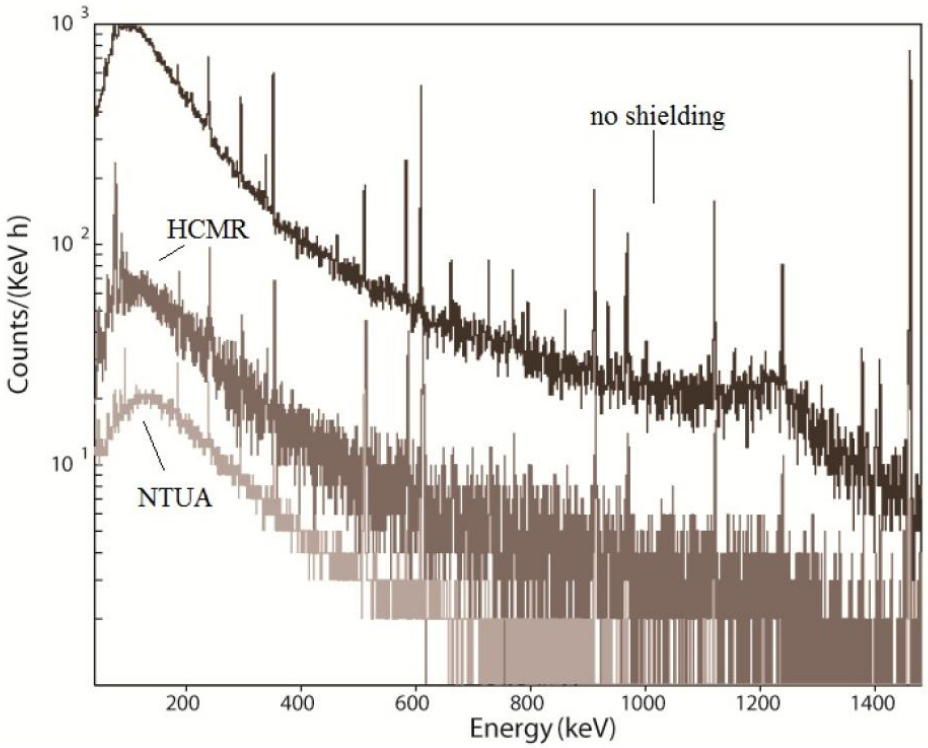

Fig. 2.27: Background-level measurements acquired in the same time using the two different shielding systems (at HCMR and NTUA) are presented along with a measurement without shielding (Elef_15).

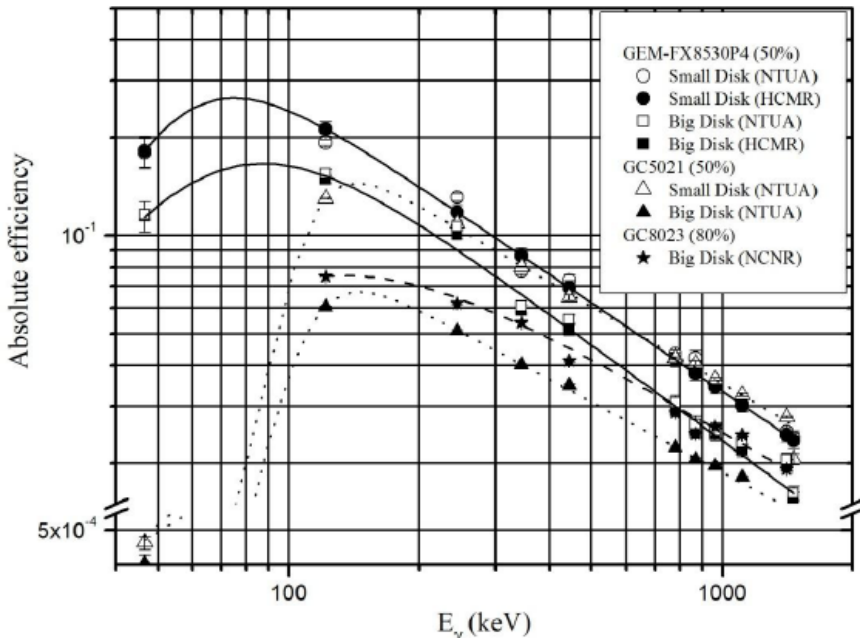

Fig. 2.28: Absolute efficiency calibration of the two stationary detectors at HCMR (GEM-FX8530P4) and NTUA (GC5021) for sediment samples measurements (Elef_15).

CHAPTER III:

Monte Carlo codes utilized in the framework of the thesis

3.1. Introduction

In this chapter a description of the Monte Carlo (MC) method and the MC codes utilized in this work is given, followed by the evaluation of these codes in specific applications.

The implementation of Monte Carlo (MC) codes started with the pioneer work of von Neumann, Ulam and Metropolis (Metro_49) and the development of high performance computers. Nowadays, the MC statistical method has become a powerful auxiliary tool for treating complex problems that are either difficult to solve analytically, or for which an alternative experimental treatment would be rather cost-inefficient, or impractical.

Monte Carlo simulation is a method that relies on random sampling and on probability statistics and utilizes random number generation algorithms, to imitate the propagation of complex systems and uses mathematical functions to estimate the desired quantities, through an iterative procedure. Concerning nuclear applications, the MC method is implemented for solving complex problems, involving particle transport and their interactions as they pass through matter. In such problems, a MC simulation probes a physical system by tracking the history of a single primary particle and all secondary generated particles, from their generation till they are fully absorbed (energy below threshold), using probability density functions to randomly determine the result of the interaction in each step of the particle track. The final simulation result is obtained by repeating the procedure for a large number of primary particles and is calculated from the average of all the generated particles.

As a consequence, the accuracy of the result highly depends on the number of the primary particles and is improved by increasing this number at the expense of computing time. Concerning the precision of the results, crucial systematic uncertainties may arise

reflecting missing or incorrect features in the MC modeling description. These include the poor reproduction of a) the underlying interaction physics, b) the details (geometry, physical properties) of the instruments and the surrounding environment modeling, c) the incident source (or background) particle distribution description (Kippen_04). Although there is a large list of available MC codes, the steps that need to be followed in order to carry out a reliable simulation are common and involve:

- Modeling the geometry of the system: All the information of the real environment that will affect the results should be described in detail, including the object dimensions, shape and the materials forming the real environment as well as the boundaries of the simulation geometry.
- Defining the particle generation (source), including the number of generated events, the particle type, size, direction, position, energy and intensity.
- Correctly describing the underlying particle interaction physics, by including all the processes involved in a specific problem according to the generated particles (primaries, secondaries).
- Specifying the information needed to be estimated (scoring).

The MC simulations are well established as a powerful tool in nuclear physics applications. Among the different applications, MC simulations have been extensively used in γ-ray spectrometry for detector characterization. MC simulations have been widely applied to reproduce experimental results even in complex geometries (Elef_13; Mauč_09; Askri_08; Róden_07; Hendr_02). In the present work the MCNP5, MCNP-CP and FLUKA codes were utilized for the photopeak efficiency estimation of the system KATERINA in the marine environment. In general the selection of the appropriate MC code relies on the purpose of a specific application, as each MC code provides different capabilities to the end users. A brief description of the characteristics and physics settings of the different codes is given in the following sections along with a comparison of the estimated results for specific test cases.

3.2. MC codes utilized in this work

3.2.1. The MCNP5 code

Among the available validated MC codes, the Monte Carlo N-particle transport code

(MCNP) code is a general purpose MC code able to perform a statistical simulation of the transport of neutrons, photons, and electrons separately or coupled (multi-type source) in an arbitrary three-dimensional geometry (X-5_03). The MCNP5 code is a user-friendly code and has been extensively used in γ-ray related environmental studies (Róden_07; Hendr_02; Cine_16), providing accurate results. The MCNP5 code contains different estimators (tallies) according to the studied quantity such as, surface current and flux, track length, point or ring detectors, particle heating, fission heating, pulse height estimators for energy or charge deposition, mesh tallies (spatial distribution of different tally results in a designated zone), and radiography tallies. For radiation applications the most commonly utilized estimators are the pulse height (F8 tally) and the energy deposition (F6 tally) ones. The simulated processes are based in evaluated data for energy ranges from 10-11 to 20 MeV for neutrons, with data up to 150 MeV for some nuclides, 1 keV to 1 GeV for electrons, and 1 keV to 100 GeV for photons.

Regarding the transport of photons, the code takes into account by default, incoherent (Compton) and coherent (Thomson) scattering, the possibility of multiple scattering, fluorescent emission after photoelectric absorption, absorption in electron-positron pair production with local emission of annihilation radiation, and bremsstrahlung emission. Electron/positron transport processes account for the angular deflection through multiple Coulomb scattering, the energy loss with optional straggling, and the production of secondary particles including K x-rays, knock-on (Møller scattering) and Auger electrons, bremsstrahlung and annihilation γ-rays from positron annihilation at rest (X-5_03). Photonuclear physics is also available but for a limited number of elements. Electron transport does not include the effects of external or self-induced electromagnetic fields. A disadvantage of the code is that it can generate only a single particle per event. This means that it cannot account for correlations among particles, such as TCS (True Coincidence Summing) effects. In problems that such effects become important, other MC codes should be utilized instead.

3.2.2. The MCNP-CP code

The MCNP-CP code is an upgraded version of the general purpose Monte-Carlo N-Particle transport code MCNP4c (Briesm_97) that was developed by Dr. Andrey Berlizov (Ber_06). It is a validated code which reproduces experimental data for various applications (Szent_13; Ber_10a; Zhu_08), including environmental ones (Jäder_15; Ber_10a; Ber_08).

In environmental γ-ray spectrometry applications TCS effects for cascade radionuclides are always present. Moreover, numerous radionuclides with complicated decay schemes contribute to the measurements and therefore an efficient simulation of all the corresponding emitted γ-rays is necessary. The great benefit of this upgraded version is its ability to incorporate in the simulations a source of correlated nuclear particles based on the Evaluated Nuclear Structure Data File (ENSDF) (Tuli_87). Using this code, the direct simulation of all the prominent emitted γ-rays (exhibiting an emission probability > 0.3%) along with the corresponding intensities for each radionuclide is achieved via a single command card (ZAM option, extension of the SDEF card), offering a considerable time and effort saving from having these values manually inserted by the user. Therefore, a source consisting of a particular radionuclide, can be accurately and efficiently reproduced, consisting of all the emitted γ-rays and taking into account the corresponding intensity probabilities for each γ-ray emission. Moreover, more than one photon per event can be generated and simultaneously transported in every step of the simulation and therefore offers the possibility to account for true coincidence-summing (TCS) effects using again a single card (Correlated Particle Source settings card CPS). Both of the aforementioned advantages are critical for environmental γ-ray spectrometry applications (measurements performed in contact geometries between a multi-nuclide source and the detector).

In addition to these advantages, there are several other improvements within this extended version of MCNP regarding both physics and scoring (tallies). The low energy photon transport physics (X-5_03) has been extended, based on the GEANT Low-Energy Compton Scattering package (Kippen_04), to account for the Doppler shift simulation of scattered photons and the detailed physics of Compton scattering in the low-energy regime, where bound electron effects become important. These features are controlled by two different cards, namely DEC511 and GLECS, respectively. Moreover, a versatile multi-cell coincidence/anticoincidence pulse height tally (extension of the F8 tally) was incorporated, which enables detection efficiency estimations in cases of complex detection systems, such as phoswich, cluster detectors, Compton suppression spectrometers, etc.

3.2.3. The FLUKA code

The FLUKA code (Batti_07; Ferra_05) is a general purpose Monte Carlo code able to simulate the interaction and transport of about 60 different particles including photons and electrons, neutrinos, muons and hadrons in arbitrary materials (Batti_15). It is a free,

open source code and its physical models are continuously upgraded and benchmarked against experimental data (Batti_15). For historical reasons, FLUKA is best known for applications involving hadronic and electromagnetic interactions (Batti_15; Fasso_03) and is particularly reliable in treating problems in the fields of radiotherapy and radiation protection (Fasso_03). However, it is a multi-purpose, multi-particle code that can be applied in many different fields (Fasso_03), from proton and electron accelerator shielding, to target design, calorimetry, activation, dosimetry, detector design, radiotherapy, Accelerator Driven Systems, cosmic rays or neutrino physics. Regarding electromagnetic interactions, the energy range covered using the FLUKA code is very wide, ranging between 1 PeV and 1 keV for photon and electron transport, while photonuclear reactions are implemented from threshold up to energies of about 20 TeV (Fasso_03).

The FLUKA code can easily handle problems involving very complex geometries due to the efficient structure of SimpleGeo (additional supplied algorithm) and the incorporated powerful Graphical User Interface (Flair). Flair (Vlach_09) is a user-friendly graphical interface for the FLUKA code providing an environment to the user with which one can control and to some extent automate the processes involved in all the stages of a simulation, including the creation of an input file, the debugging (by incorporating user written routines), the execution, the status monitoring, the data processing and the plot generation (Batti_15). The geometry specification structure is very similar to the MCNP code and in fact Flair is capable in importing and exporting in various file formats including the MCNP input format (Batti_15). Nevertheless, this option should be performed with caution, as differences in the material properties (default settings) from the required ones could be present. The simulation model (input file) has a similar structure as compared to MCNP, meaning that the commands/options are driven by simple data cards properly selected by the user. However, contrary to the MCNP code, in FLUKA the relevant physics (scoring, sources, thresholds) are fully user-specified and therefore special attention is required in order to fully include the correct underlying physics in a problem. Although, in general, the majority of the problems associated with simulations do not require programming by the user, the great benefit of the FLUKA code is the ability of efficiently (using Flair) incorporating in the simulation any user-defined routine.

Regarding the photon transport physics, a detailed transport of electrons, positrons and photons is considered, including the photoelectric effect and the secondary fluorescence and Auger production, the pair production with energy dependent angular distribution (while it additionally accounts for differences between electron and positron scattering), the

Rayleigh and Compton scattering including bound electrons effects (Compton profiles), while Thomson scattering is not taken into account. Moreover, two additional features of great importance for environmental applications are the ability (a) to account for TCS effects and (b) to create a source of correlated nuclear particles based on the ENSDF, as when using the MCNP-CP code.

FLUKA has not been widely implemented for environmental applications, although it offers several advantageous capabilities strengthening its utilization. The generation of all the emitted γ-rays along with the corresponding intensity probabilities of a specific radionuclide is performed automatically, by sampling all the involved emissions according to the decay scheme of a specific radionuclide, based on information obtained from the National Nuclear Data Center at Brookhaven National Laboratory (Evaluated Nuclear Structure Data File (ENSDF)) (Tuli_87). Another advantageous feature is that it can both generate and simulate multiple particles in a single event; therefore primary and secondary particles can be correlated. More specifically, for problems that involve γ-ray detection, TCS effects are thus taken into account. Another critical advantage is the ability of this code to easily incorporate a user-defined routine. This capability can be crucial when sources with complex geometry (e.g. representation of a soil or sediment source) or particle energy distributions are involved in the simulations.

3.3. MC code selection for different applications

The three presented general purpose MC codes exhibit differences both in the underlying physics incorporated in each one, as well as in the capabilities provided to the end users. Therefore a main objective was to perform an evaluation of the different codes capabilities and the obtained results, prior to the implementation of each one in a specific application. This study aimed at assisting to the selection of the most appropriate MC code with respect to the thesis purposes.

One factor affecting the activity concentration results is the presence of True Coincidence Summing (TCS) effects. The occurrence of TCS depends on the properties of the source (density, composition, size) when voluminous samples are involved, the measurement setup (including the detector geometry and materials as well as the measurement solid angle) and the decay scheme properties of each particular cascade radionuclide. These effects are always present when the source is placed close to the detector (distance < 10cm). In such cases, correction factors (CF) should be included in the

analysis; otherwise, if TCS effects are not taken into account, a systematic uncertainty may be introduced in the activity concentration, in cases where cascade radionuclides appear in the spectrum. Regarding *in situ* measurements in the marine environment, TCS effects are always present since the measurements are performed with the detector positioned in close contact with the source.

The evaluation of the significance of TCS effects concerning *in situ* measurements on the marine environment using the detection system KATERINA was performed via the MCNP-CP code. This was accomplished by performing two separate runs (by activating and de-activating the CPS card). The methodology details and the obtained results are presented in the following section 3.3.1. The MCNP-CP code is a reliable code in the field of γ-rays and the TCS results have been validated using experimental and theoretical data, by implementing other MC codes (e.g. GEANT). However, no data were available until recently in the literature (Andr_16b) concerning applications in the marine environment. For this reason an evaluation of the obtained results was performed with corresponding simulations using the FLUKA code. As no data are reported regarding the utilization of FLUKA for γ-ray applications in the marine environment, a comparison of the two codes was considered mandatory, before deciding, which is the most suitable one. The comparison results are presented in section 3.3.2. It is important to note here that comparisons between the MCNP5 code and its extended version MCNP-CP were not performed as the only major difference between them (for the specific applications) is the inclusion of TCS in the latter.

In the end of this Chapter a brief discussion is given on the final code selection utilized in the developed quantification methods for *in situ* measurements in the seawater column (presented in Chapter IV) and on the seabed (presented in Chapter V).

3.3.1. Evaluation of TCS effects using the MCNP-CP code

In order to estimate the TCS correction factors, for measurements with the system KATERINA both in the seawater and on the seabed, MC simulations were performed using the MCNP-CP code. The TCS correction factors were estimated considering two different cascade radionuclides as a source, namely ^{214}Bi and ^{208}Tl, which are prominent in the marine environment. Moreover, the detector and the surrounding materials characteristics (density, composition, size), were properly introduced in the simulations. In the following sections the simulation details and the obtained results are discussed.

3.3.1.1. Simulation setup

The MC model consisted of the detector, a spherical volume source surrounding the detector, where the primaries were generated and a spherical cell (object) larger than the source, representing the marine environment (seawater) and defining the geometrical boundaries of the problem (Fig. 3.1). Separate runs were performed for each radionuclide by automatically sampling all the emitted γ-rays using a spherical source.

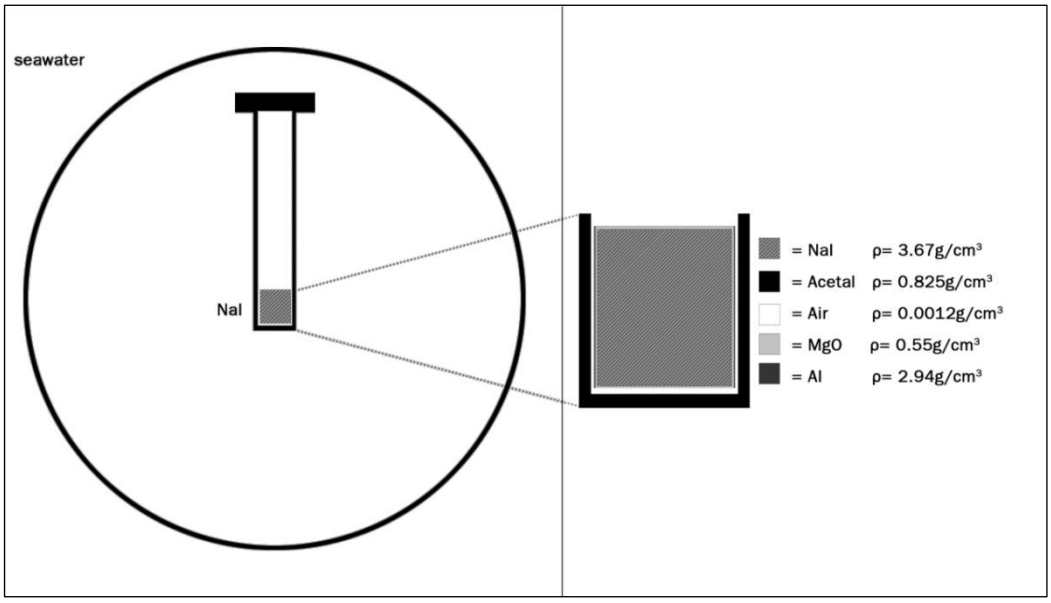

Fig. 3.1: The described MC geometry model used in the simulations including the detector, the source and all the utilized materials.

Additionally, different radii values were utilized for the source description in each run (each radionuclide), with respect to the emitted γ-ray with the highest energy for each radionuclide. The spherical shape of the source represents the maximum distance, from which a generated event in the seawater column can reach the detector and get recorded in the spectrum (Andr_15). The maximum distance (radius of the spherical source) was calculated using the total attenuation coefficients derived from the software XCOM (Berg_10) and the Beer-Lambert exponential attenuation law, assuming the condition that I ≥0.0001 Io. The described geometry model used in the simulations including the detector, the source and all the utilized materials is presented in Fig. 3.1 for the case of ^{208}Tl. The volumetric source is represented by a sphere surrounding the detector having a radius that is calculated using the software XCOM based on the emitted γ-ray which exhibits the maximum energy for each radionuclide.

Regarding the simulation setup for measurements on the seabed the utilized geometry is depicted in Fig. 3.2. In the selected geometry setup, the detector window is positioned in contact with the seabed. The volumetric source is represented by a hemisphere, as only the events arising from radionuclides that are present in the seabed are of interest. To a complete analogy to the measurements in the seawater column, the radius of the hemisphere regarding the measurements on the seabed is defined as the maximum distance, from which a generated event in the sediment can reach the detector and get recorded in the spectrum.

Again, different radii values were utilized for the source description, in a separate run for each radionuclide, with respect to the emitted γ-ray with the highest energy. The radius of the source (r_{eff}) each time was calculated using the total mass attenuation coefficients derived from the software XCOM and the exponential attenuation law, assuming the condition that $I \geq 0.0001$ Io.

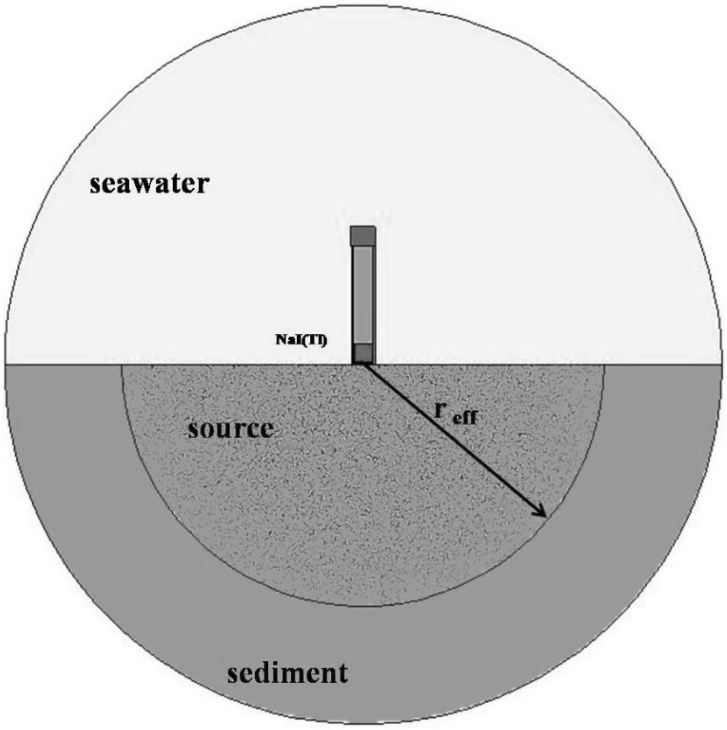

Fig. 3.2: The described MC geometry model used in the simulations including the detector, the source and the surrounding environment.

In order to calculate the correct mass attenuation coefficients a typical sediment composition consisting of Al_2O_3 (5.67%), SiO_2 (37.65%), P_2O_5 (0.04%), K_2O (0.24%), CaO (12.08%), TiO_2 (0.40%), Fe_2O_3 (8.18%), Na_2O (0.73%), MgO (5.86%), SO_3 (3.09%) and

MnO (0.07%) with a water content (H_2O) of 26% was introduced in the XCOM software. In the final radius calculation of the hemisphere using the exponential attenuation law, a sediment density of 2.1 g/cc was assumed. The same values for the density, composition and water content of the sediment material, were also utilized in the MC model description.

The utilized geometry setup, with the detector placed exactly on the seabed, was selected as the most commonly applied setup for *in situ* measurements on the seabed and moreover, using this configuration setup, the TCS effects are maximized (smallest distance between the detector and the source).

In order to estimate the TCS correction factors, the MCNP-CP code was executed twice for each simulation model, assuming a fully uncorrelated source in the first run, where TCS are not taken into account and a fully correlated source (inclusion of TCS according to the radionuclides decay scheme) in the second run. This was accomplished by changing the value of the first entry of the CPS card, from a negative to a positive number, in the physics description. In more detail, a total of eight runs were executed, of which a total of four runs (two for each radionuclide) were utilized to estimate the TCS correction factors (CF) for measurements in the seawater column and on the seabed, respectively, considering as sources the radionuclides ^{208}Tl and ^{214}Bi. Regarding the physics settings, the default values were used and the F8 pulse-height tally was utilized to derive the corresponding spectra for each run. The actual detector energy resolution was excluded from the simulations in order to detect the differences between the two runs for the same radionuclide. A different number of primaries were considered in each run, ranging from 1 to $6 \cdot 10^8$ particles. The MC statistical uncertainty was kept below 5% in the most intense γ-rays of the two radionuclides. The CF were estimated for all the emitted γ-rays of the corresponding radionuclides, as the ratio of the net counts (after the Compton continuum subtraction) detected in each photopeak, in the spectra obtained using a fully uncorrelated source, to the ones detected using a fully correlated source.

3.3.1.2. Results and Discussion

The simulated spectra for the case of a ^{208}Tl radioactive source for the configuration of the measurements on the seabed are depicted together in Fig. 3.3 as obtained using a fully uncorrelated source (uncor.) and by turning on the CPS card to take into account TCS effects (corr.). The estimated CF results for the most prominent peaks of ^{208}Tl and ^{214}Bi in the spectra are summarized in Tables 3.1 and 3.2 for the measurements in the seawater

column and on the seabed respectively. The CF (ratios) ranged from 1.05 to 1.16 for the prominent γ-rays of both radionuclides for the two measurement configurations. The largest CF values were found for the 583and 2614 keV γ-rays from the ^{208}Tl decay and for the 609 keV γ-ray from the^{214}Bi decay.

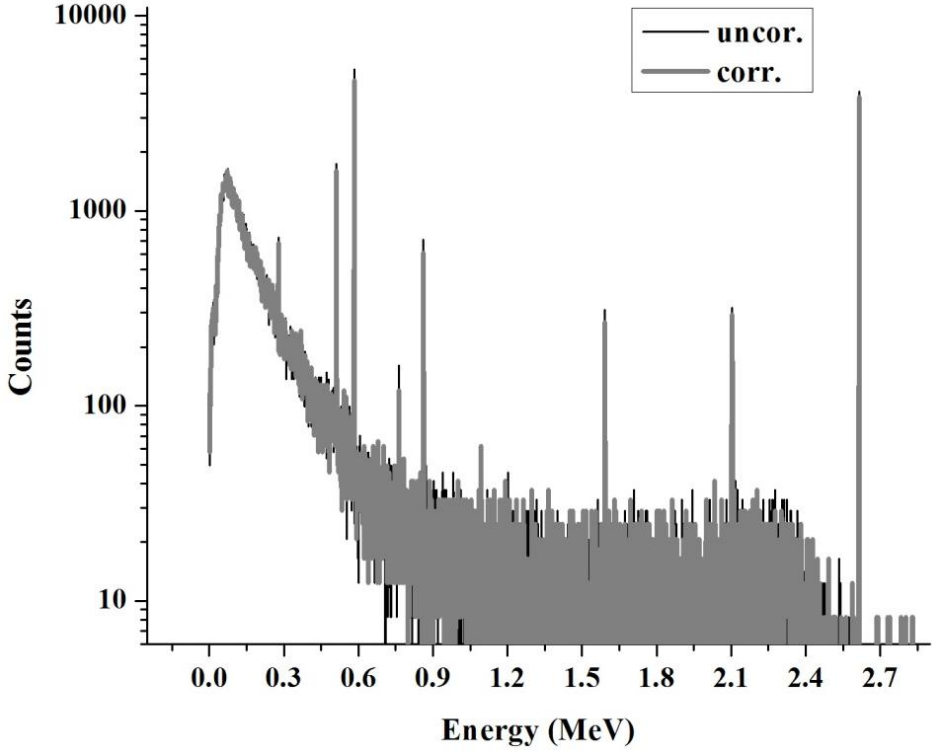

Fig. 3.3: The MC spectra obtained using the MCNP_CP code for a ^{208}Tl radioactive source and the configuration (MC model) for measurements on the seabed, assuming no correlations between the primaries (uncor.) and by enabling the simulation of TCS effects using a correlated source (corr.).

The estimated CF values (ranging from 4-16%) for both measurements on the seabed and in the seawater column, were found roughly comparable to the typical experimental measurements statistical uncertainty (~10%, depending on the acquisition time, specific site and γ-ray energy).

As a result, even if the TCS corrections are excluded from the activity concentration calculations, the obtained results would usually remain reliable within the total estimated statistical uncertainty (in cases of low counting rates). Nevertheless, a systematic error for cascade radionuclides occurs if the TCS effects are excluded from the MC simulations, biasing the corresponding estimated efficiency values.

Table 3.1: Correction factor (CF) values for the prominent γ-rays of the ^{214}Bi and ^{208}Tl radionuclides, estimated using the MCNP-CP code for measurements in the seawater column.

Source	Intensity %	γ-ray Energy (MeV)	Counts (uncor.)	Counts (corr.)	CF (ratio)	uncertainty %
^{208}Tl	6.31	0.277	813 (6)	736 (6)	1.10	8
	84.5	0.583	5845 (2)	5304 (2)	1.10	3
	12.42	0.860	720 (6)	690 (6)	1.04	8
	99.0	2.614	4367 (3)	3778 (3)	1.16	4
^{214}Bi	46.1	0.609	5655 (1.6)	5329 (1.3)	1.06	2
	15.1	1.120	1552 (3)	1465 (3)	1.06	4
	2.92	1.729	270 (7)	295 (6)	0.91	9
	15.4	1.765	1318 (3)	1415 (2)	0.94	4

Table 3.2: Correction factor (CF) values for the prominent γ-rays of the ^{214}Bi and ^{208}Tl radionuclides, estimated using the MCNP-CP code for measurements on the seabed.

Source	Intensity %	γ-ray Energy (MeV)	Counts (uncor.)	Counts (corr.)	CF (ratio)	uncertainty %
^{208}Tl	6.31	0.277	731(8)	685 (8)	1.07	10
	84.5	0.583	5326 (3)	4674 (3)	1.14	4
	12.42	0.860	710 (8)	611 (8)	1.16	11
	99.0	2.614	4084 (3)	3815 (3)	1.07	5
^{214}Bi	46.1	0.609	3584 (3)	3283 (3)	1.09	4
	15.1	1.120	1079 (5)	1016 (6)	1.06	8
	2.92	1.729	* -	-	-	-
	15.4	1.765	970 (6)	1038 (5)	0.93	8

**large MC statistical uncertainty below acceptance.*

Concerning the MC results for the case of measurements on the seabed, they only provide a measure of the CF values, as TCS effects depend on the source characteristics that can greatly vary in marine sediments. Nevertheless, the estimated CF resulted in

comparable values for both configuration measurements, as it can be seen from the comparison of the results presented in Tables 3.1 and 3.2, showing a relatively low dependence on the material (density, composition) change, for the two utilized materials (sediment, seawater).

3.3.2. FLUKA evaluation for photon transport in the marine environment

3.3.2.1. Test cases

The effect of TCS for cascade radionuclides was further studied for the detection system KATERINA and for the studied measurement in the seawater column using the MC code FLUKA. In more detail, these runs were performed to evaluate the code function/capabilities concerning a) the simulation of photon transport in seawater, b) the automatic generation of a radionuclide source based on ENSDF and c) the simulation of TCS effects. The results were compared with corresponding runs using the MCNP-CP code. In the simulations different sources were considered. Three different radionuclides were generated within the source, including the artificial ^{60}Co, although it is rarely detected in the marine environment, and the naturally occurring ^{208}Tl and ^{214}Bi. A separate MC run was executed for each radionuclide using both MC codes. These three radionuclides were selected due to the differences appearing in their decay schemes (from the simple cascade case of ^{60}Co, to the most complex case of ^{214}Bi). Moreover, ^{208}Tl and ^{214}Bi are naturally occurring radionuclides from the ^{232}Th and ^{238}U series, respectively, and are two prominent radionuclides present in the marine environment in concentrations that are detectable by an *in situ* γ-ray spectrometer.

3.3.2.2. Model description and Physics settings

The two codes (FLUKA, MCNP-CP) were implemented to estimate the pulse height spectra of the underwater γ-ray detection system KATERINA for measurements in the seawater. The detector resolution was again excluded in all the simulations, and a small bin width of 1 keV was selected instead, in order to ease and enhance the accuracy of the comparison results between the two codes.

The simulation setup for measurements in the seawater column is already discussed in section 3.3.1.1 and was kept the same (Fig. 3.1) also in these runs. Three different

radioactive sources were considered. Separate runs were performed for each radionuclide by automatically sampling all the emitted γ-rays using a spherical source of different radius with respect to the emitted γ-ray with the highest energy. The physics settings were carefully tuned in order to properly simulate the underlying physics, including in the simulations the relevant interaction processes for photon and electron transport. For this purpose, the FLUKA simulations were performed under the EM-CASCAde default, which allows for a detailed transport of electrons, positrons and photons. Additionally, in order to adjust the production and transport energy thresholds to the proper settings (1 keV for both photon and electrons), the EMFCUT cards were required, as well as the implementation of a DELTARAY card, for the delta rays production.

Regarding the utilized spherical volumetric source, a user-routine was developed and incorporated in the simulation, since this type of sampling is not available among the FLUKA default options. The developed user-routine for the correct sampling of the generated particles within the volume of the source was written in FORTRAN. The radionuclide sampling within the source, using the FLUKA code, was handled through the HI-PROPE card, in which the properties (mass and atomic number) of the primary heavy ion are defined. The simulation of the radioactive decay was controlled by the RADDECAY card in the semi-analog mode along with the accompanied SCORE and DCYSCORE cards. The final spectra were obtained by using an EVENTBIN scoring card to estimate the energy deposited in the detector for each event, and converting the results to spectra, using again a 1 keV binning.

In order to perform a valid comparison between the FLUKA code and the MCNP-CP code, all the MC run features, including the geometrical features, dimensions and material composition were kept exactly the same in both simulation codes. As mentioned above, this was efficiently managed through the FLUKA code graphical interface Flair, which is capable to import and export geometries in various file formats, including the MCNP input format. Nevertheless, the material properties should be examined with caution, since the FLUKA pre-defined materials could be different from the desired ones. The physics options provided to end-users were carefully tuned in order to perform a consistent comparison.

Concerning the MCNP-CP code physics settings, the transport energy cutoffs are by default set to 1 keV for both photons and electrons, allowing also for delta rays production. The direct simulation of all the prominent emitted γ-rays was achieved via a single command card (ZAM option, extension of the SDEF card) based again on the ENSDF. The

Correlated Particle Source card CPS (Ber_10b) was activated to account for TCS effects. The final spectra were obtained using a pulse-height estimator (F8 tally), which scores the number of detected counts per initial event, accompanied with an E8 card, in which again a 1 keV binning was applied.

The same seed number regarding the random number generator was utilized in both codes. The number of generated particles (primaries) was kept the same in both codes and ranged from 1 to $5 \cdot 10^8$ depending on the utilized radionuclide. These large numbers of generated particles were required in order to obtain sufficient statistics (i.e. uncertainty lower than 10%) in the prominent photopeaks of the simulated spectra.

3.3.2.3. Comparison, results and Discussion

A very important difference regarding the radioactive decay of naturally occurring radionuclides was observed between the two codes in the present work. In FLUKA, when the simulation of a radioactive source consisting of naturally occurring radionuclides within a radioactive series is requested, the radioactive decay simulation includes the production and transport of γ-rays from all the daughter nuclides of the series till a stable nuclide is reached. This is demonstrated in Fig. 3.4 panel a, for a ^{234}Pa source, where it can be seen that in the output of the EVENTBIN card, interactions of γ-rays not only from the ^{234}Pa decay, but also from other daughter nuclides of the series are recorded in the spectrum, in this case the photopeaks of ^{214}Pb, ^{214}Bi, ^{226}Ra decay can be observed, as opposed to the MCNP-CP code, which is strictly limited to γ-rays, following the beta decay of ^{234}Pa.

This is highly inconvenient for environmental applications, where disequilibria among parent and daughter radionuclides are present and therefore a separate treatment of each one is required. As a first approach, this defect was manually solved, in order to obtain the free-of-daughter spectrum in the case of ^{234}Pa, as described below. The procedure involved the following steps: Initially, separate simulations for the parent (total spectrum) and immediate daughter radionuclides (daughter radionuclide spectrum) were executed. Then, the probability distribution of the generated daughter radionuclides in the parent simulation was calculated by estimating the ratios of the detected counts in a photopeak of the total spectrum, to the detected counts of the same photopeak in the daughter radionuclide spectrum. Subsequently, a spectrum for the daughter radionuclide was created using the corresponding probability. The parent, free-of-daughter, radionuclide spectrum is then obtained by subtracting this spectrum from the total one. Although this is a

straightforward procedure, the required computing time to get a reliable result and the corresponding total uncertainty drastically increase. Moreover, the spectra subtraction may yield unphysical results in the Compton continuum region, in cases of low statistics.

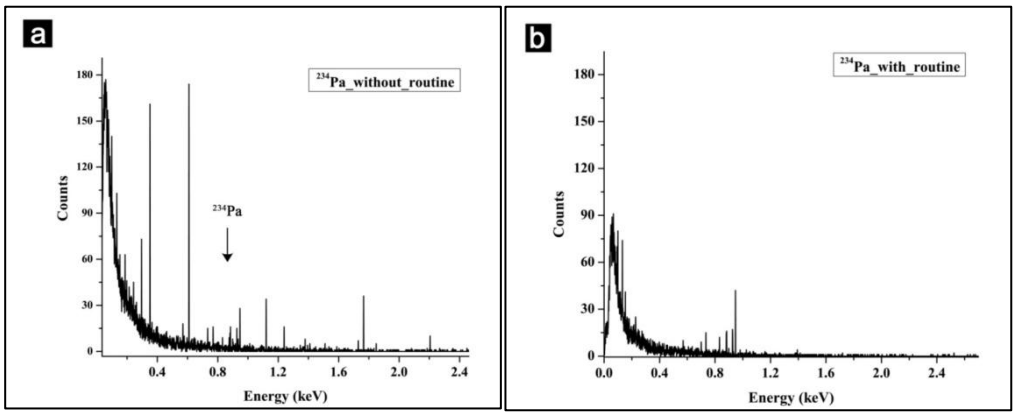

Fig. 3.4: Simulated spectrum of a ^{234}Pa source using the FLUKA code without using the developed routine (panel a) and after the activation of the developed routine (panel b).

Therefore a modified version of the user-routine usrmed was utilized which restricted the generation and transport into only first generation particles, meaning that the decay was successively stopped in the first daughter radionuclide (e.g. ^{234}U for a ^{234}Pa source), as in the MCNP-CP code. The result (MC spectrum) of the same run by activating the user-defined routine is depicted in Fig. 3.4 panel b, where it can be seen that γ-rays solely from the ^{234}Pa decay are recorded in the spectrum.

In FLUKA, when a radioactive decay is requested, all secondary particles/nuclei are transported carrying a time stamp (age), while a different "track number" is associated to each "new" particle. In the developed routine the simulation of only first generation particles was accomplished by checking the time stamp (associated track number) of each "new" particle and terminating the process when this number differed from the one associated with the primary particle. Moreover the generation and transport of the followed alpha or beta decay is excluded from the simulation using this routine, thus dramatically reducing the required computing time. This developed routine is readily available to the scientific community involved in environmental applications upon request.

In this work, the developed routine was utilized only for the simulation run with the ^{214}Bi source, while for the ^{208}Tl source it was not necessary, since the radioactive decay of this particular radionuclide leads directly to the stable ^{208}Pb. The simulated spectra using the two codes (FLUKA, MCNP-CP) are depicted together in Fig. 3.5, for ^{60}Co, ^{208}Tl and ^{214}Bi, in panel a-c, respectively. A satisfactory agreement was observed between the two

codes in all cases. Nevertheless, the differences between the results of the two codes appeared larger in the case of the ^{214}Bi source. This could be attributed to the inadequate MC statistics, as a lower number of primaries, namely $3 \cdot 10^8$, were utilized in these runs.

The evaluation of the FLUKA code in all cases was performed by calculating the ratio of the measured counts under the most intense photopeaks to the corresponding estimated results using the MCNP-CP code. The summary results are presented in Table 3.3, for ^{60}Co, ^{208}Tl and ^{214}Bi together. The uncertainty of the calculated ratio was determined by error propagation according to the MC statistics, denoted in the parenthesis next to the detected counts expressed in percentage.

A quite satisfactory agreement was observed from the comparison in all the involved runs, in the energy range from 0.3 to 2.6 MeV, yielding a maximum difference of 10% between the two codes (including uncertainty) regarding the photopeak regions of the prominent γ-rays (intensity probability > 6%) for all three radionuclides. The comparison regarding the low intensity probability emissions yielded ratios ranging from 0 to maximum 25% within uncertainty; however these higher values could be drastically improved by increasing the MC statistics (increase of the generated primaries number) – at the expense of computing time.

More particularly, concerning the ^{60}Co source a ratio of 1.0 and 0.96 was calculated for the two photopeaks, at 1173 and 1332 keV respectively, as demonstrated in Table 3.3. An excellent agreement was also observed for the ^{208}Tl source as well, regarding the comparison results in the most intense ($I_\gamma > 6\%$) photopeak regions. A reasonable agreement within uncertainty (a ratio of 0.92 ± 0.26) was observed also for the sum peak of the spectrum (peak at 2505.74 keV) where statistics was low. Regarding ^{214}Bi, a quite satisfactory agreement (differences < 15 %) was observed for the photopeak regions of the most prominent γ-rays, with the exception of the 1238 keV γ-ray, for which a ratio of 1.21 with an uncertainty of 9% was observed.

Overall, the code comparison yielded quite satisfactory results, and a similar behavior between the two MC codes regarding TCS effects was observed from the comparison of the recorded counts in the photopeaks formed from cascade emissions. The comparison was restricted for high intensity γ-rays only, due to the inadequate statistics of the MC results both for the sum peaks and for low intensity γ-rays. The results render the FLUKA code a valuable alternative for various applications, in which the study of the transport of low-energy single or cascade photons (below 3 MeV) is important (e.g. detector

physics, environmental applications). More importantly, the ability of incorporating user-defined routines in the simulations, especially in cases of problems exhibiting complicated source geometries (Askri_08), distinguishes FLUKA as a highly competitive MC code.

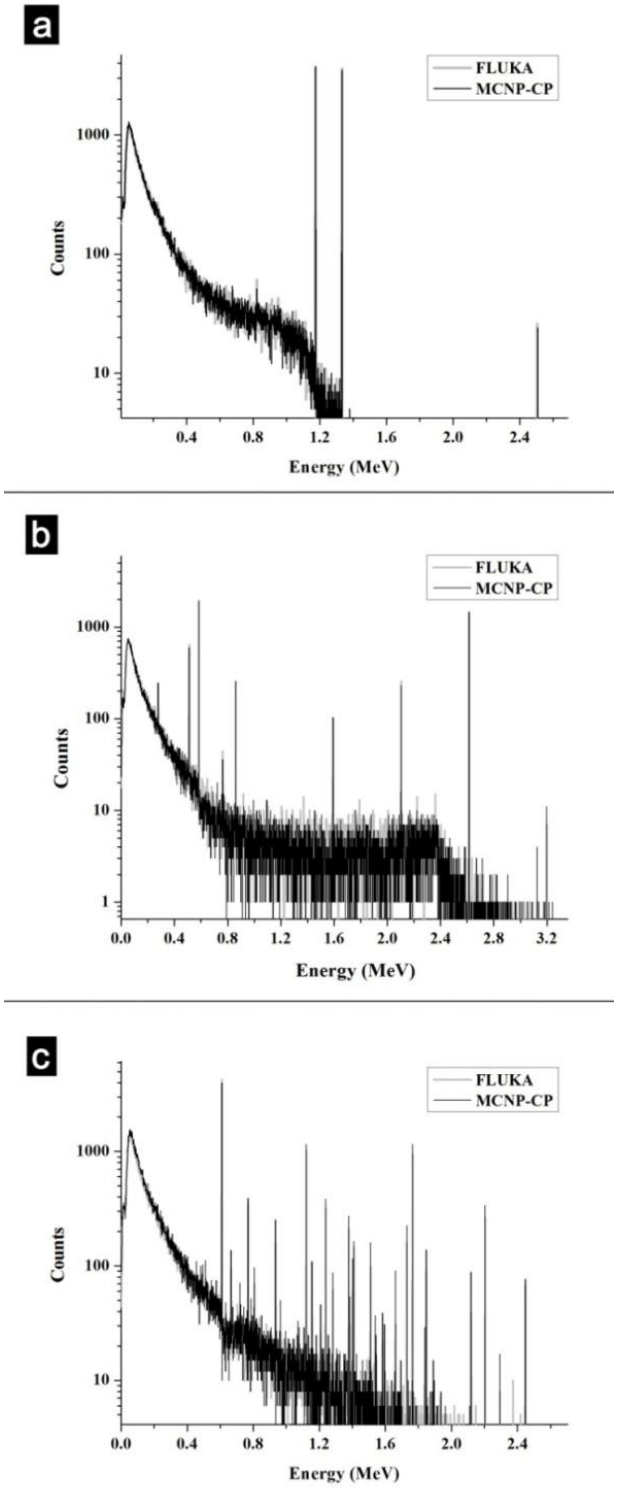

Fig. 3.5: The simulated spectra of the FLUKA and MCNP-CP codes for a spherical ^{60}Co. (panel a.), ^{208}Tl (panel b.) and ^{214}Bi (panel c.) radioactive source, respectively.

Table 3.3: Comparison results of the estimated detected counts under the most intense photopeaks for a ^{60}Co, ^{208}Tl and ^{214}Bi source using the MC codes (FLUKA, MCNP-CP) and the corresponding counts ratio.

Source	Energy keV	Intensity I_γ%	Counts FLUKA	Counts MCNP-CP	ratio	uncertainty
^{60}Co	1173.24	99.97	3744 (2)	3754 (2)	1.00	0.03
	1332.5	99.99	3638 (2)	3482 (2)	0.96	0.03
^{208}Tl	277.35	6.3	241 (7)	248 (6)	1.03	0.09
	510.77	22.6	644 (4)	600 (4)	0.93	0.05
	583.19	84.5	1963 (2)	1928 (2)	0.98	0.03
	763.13	1.8	44 (16)	36 (16)	0.82	0.18
	860.56	12.4	256 (6)	255 (6)	1.00	0.09
	2614.53	99.0	1434 (3)	1465 (3)	1.02	0.04
^{214}Bi	609.32	46.1	4243 (2)	3973 (2)	0.94	0.02
	768.36	4.94	337 (5)	390 (5)	1.16	0.06
	1120.29	15.1	1017 (3)	1155 (3)	1.14	0.05
	1238.11	5.79	317 (6)	384 (5)	1.21	0.09
	1764.49	15.4	916 (3)	882 (3)	0.96	0.04
	2204.21	5.08	255 (6)	233 (7)	0.91	0.06

To summarize, in this work, the effects of TCS in the detection efficiency for measurements both in the seawater column and on the seabed were evaluated for the prominent cascade radionuclides ^{208}Tl and ^{214}Bi, found in the marine environment. The results were evaluated by corresponding simulation runs using the MC code FLUKA, for measurements in the seawater. As a result, it is concluded that, the implementation of MC codes such as MCNP-CP and FLUKA which can incorporate the TCS effects is preferable over simpler ones, such as MCNP, when such effects become important. However, the decision of which is the most appropriate MC code for a specific application, depends exclusively on its purposes, and the inclusion of TCS effects should be selectively utilized, as it requires a drastic increase of the necessary computing time and is therefore rather inconvenient.

In the following Chapter (IV), a quantification methodology for *in situ* measurements in the seawater column is presented based on MC simulations, using the Full Spectrum Analysis technique. The simulated spectra for *in situ* measurements in the aquatic environment were reproduced using the MCNP-CP code taking into account TCS effects. On the contrary, in Chapter V, where a sensitivity study of the *in situ* detector efficiency for

measurements on the seabed detector with respect to alterations in the sediment physical properties and different configuration setups is performed, the MCNP5 code was utilized instead, in order to achieve reasonable computing times, since a large number of simulations was required in this case.

The observed satisfactory agreement between the two codes (MCNP-CP, FLUKA) lead to the consideration of the alternative utilization of the FLUKA code, in future applications regarding simulations for *in situ* measurements in the marine sediment. The advantageous capability, to incorporate user-defined routines, is deemed to provide a better representation of the geometry of the sediment source which can be rather complex as thoroughly described in Chapter V.

CHAPTER IV:

In situ spectrometry based on the Full Spectrum Analysis technique

4.1. Introduction

The development and the implementation of *in situ* systems for direct measurements in the environment continuously evolve, as *in situ* measurements constitute a cost-effective technique and the measurements are much faster compared to laboratory ones and more representative of the studied environment. The most widely applied approach for the analysis of the *in situ* spectra is to monitor broad spectral windows that include the photopeaks of the radionuclides of interest. Nevertheless, there are some crucial drawbacks related to this technique, as it exploits only limited spectral information (typically the analysis is performed in three selected energy windows) and the analysis is impeded by two factors: a) the existence of convoluted peaks within the windows and b) the uncertainty arising from the background counts removal. The most crucial drawback is the inability of the method to identify other radionuclides (Cac_12) that may contribute to the count rate in the corresponding window interval and are not taken into account in the analysis. As a consequence, this technique has been gradually substituted by more promising ones that rely on the Full Spectrum Analysis (FSA).

The FSA technique is based on producing separate standard spectra for the radionuclides of interest, either from different calibration measurements (Cac_12; Hendr_01), or by MC simulations (Graaf_11; Vlastou_06; Mauč_04), taking into account the exact geometry and features of the actual *in situ* measurement. The experimental spectrum (actual measurement) is represented by a linear combination of the standard spectra multiplied by arbitrary parameters that are fixed in appropriate values using χ^2 minimization. The optimal values of the unknown parameters are derived by fitting the simulated spectrum to the measured one, using different numerical methods to perform the minimization procedure and reach convergence. The corresponding activity concentration

values for each radionuclide are then calculated from these parameters. The benefits of the utilization of the FSA technique are (a) the decrease of the acquisition time required to reach sufficient accuracy (Hendr_01), (b) the exploitation of the full extent of the spectrum, that offers the possibility to quantify more radionuclides, to crosscheck the results from different peaks and to detect anomalies (e.g. identify the presence of other radionuclides that were not considered in the analysis) and c) the fast derivation of the activity concentration results, which can be crucial in cases where immediate actions need to be taken (e.g. nuclear accidents). During the last decade, techniques based on FSA have been widely implemented, for various *in situ* detection systems in different applications (Mahm_13; Cac_12; Graaf_11; Kovler_13; Mauč_04; Guil_01; Hendr_01; Minty_92).

In the present work, a method using the FSA technique has been developed, able to provide rapid estimations of activity concentrations for *in situ* measurements in the aquatic environment using the underwater detection system KATERINA. There are several differences of the developed methodology compared to other techniques used in the past which are: a) the production of the standard spectra using a MC code that takes into account TCS effects, b) the inclusion of all the prominent radionuclides (a total of 9 different radionuclides) from the ^{238}U and ^{232}Th series, whose activities are considered to be totally independent (absence of radioactive equilibrium) in the calculations and c) the progressive performance of the minimization procedure in steps (in selected energy windows covering the whole range of the experimental spectrum) to derive the optimal activity concentration results. The steps of the developed methodology and the evaluation of the obtained results are thoroughly discussed in this chapter. In more detail, the description of the simulations and the utilized routines to derive the standard spectra are presented in sections 4.2.1 to 4.2.3. The steps of the minimization procedure are given in detail in section 4.2.4, while the results of the application of the FSA technique are presented in section 4.3.

4.2. Methodology

4.2.1. MC simulations

The MC method is a powerful auxiliary tool suitable for simulations of particle transport, especially in complex-geometry, multi-layer problems and thus, it is widely implemented for detection efficiency calculations in various areas of applied nuclear and particle physics, as well as in FSA applications. In the present work the MCNP-CP code

was implemented for the reproduction of the required standard spectra (Jäder_15).

The MCNP-CP code was selected due to its ability to incorporate in the simulations a source of correlated nuclear particles based on the Evaluated Nuclear Structure Data File (ENSDF). Therefore, the MC spectrum for each radionuclide was accurately and efficiently reproduced, consisting of all the emitted γ-rays, taking into account the corresponding intensity probabilities and true coincidence-summing (TCS) effects. As numerous radionuclides with complicated decay schemes contribute to the *in situ* measurements in the marine environment, the utilization of the MCNP-CP code offered an efficient simulation tool, reducing the effort and time spent by the user.

The reproduction of the MC spectra was assessed using the pulse-height estimator, F8 tally (X-5_03), which gives the pulses per initial event recorded in an energy window selected by the user. A histogram over an energy window ranging from 0 keV to 3000 keV, with an 1 keV binning step, was generated. The small energy binning enhances the accuracy of the obtained results, although the necessary computing time to reduce the statistical error per bin increases. Nevertheless, it should be noted here that the generation of the MC histograms is carried out only once, for each radionuclide, since the simulation of the electronic setup and detector resolution effects is assessed via external algorithms as explained in section 4.2.2. The utilized initial events (histories) per run (MC execution) ranged between $1 \cdot 10^8$ to $8 \cdot 10^8$, in order to achieve a statistical uncertainty below 5% in the main photopeak regions (γ-rays with emission probability >1%), in the MC simulations for all the radionuclides. In order to eliminate any possible systematic uncertainty, the simulation modeling was carefully tuned to match the experimental conditions, by introducing in the simulations the exact geometry and the materials involved in the experimental measurement.

In more detail, the 'infinite' geometry of the measurement is represented in the simulation by an extended water source having the shape of a sphere (Andr_15; Zhang_15), as explained in Chapter 3. The effective radius (r_{eff}) of the sphere, in which the photons are generated, was calculated using the Beer-Lambert law (exponential attenuation law) and the derived total mass attenuation coefficients from the software X-COM (Berg_10) assuming a seawater density of ρ=1.026g/cc and a seawater composition of 87.15% O, 10.98% H, 0.7% Na and 1.1% Cl. Various effective radii were calculated at different γ-ray energies. However, since each radionuclide is simulated as a whole, taking into account all the emitted γ-rays, only one single effective volume had to be defined in each MC execution. The proper dimension of the sphere representing the source was calculated considering the

following argument. The volumetric detection efficiency (ε·V) is the product of the volume of the source (V) and the full-energy peak efficiency (ε), provided from the MC output (F8 tally).If the volume of the source is larger than the effective one but thenumber of generated events per units of volume (N/V) remains constant, the volumetric detection efficiency does not change within the estimated uncertainty. This has been confirmed elsewhere via different MC codes (Zhang_15; Bag_10) and also in this work for the case of ^{208}Tl at 583 keV. As shown in Fig. 4.1, the volumetric detection efficiency (ε·V) reaches a plateau around the effective radius (~ 128 cm) and remains constant even if the radius is further increased.

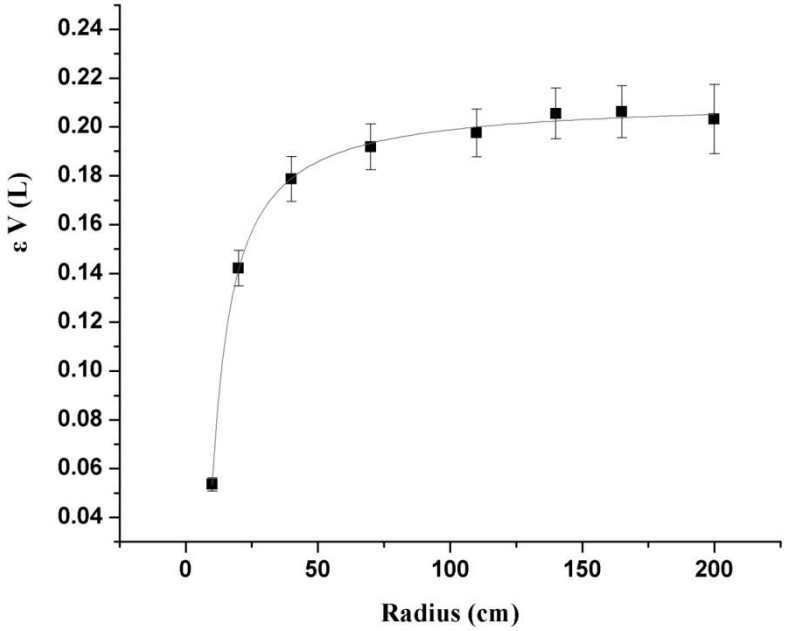

Fig. 4.1: Schematics of the effect of the source radius to the detection efficiency (ε·V) of photons from ^{208}Tl having an energy of 583keV.

This is a reasonable result, since, by definition, the photons generated outside the effective volume cannot reach the detector. Therefore, in each standard spectrum, the spherical volume representing the source (effective volume) was calculated with respect to the γ-ray with the highest energy. The simulated geometrical setup considering a ^{208}Tl source is shown in Fig. 4.2.

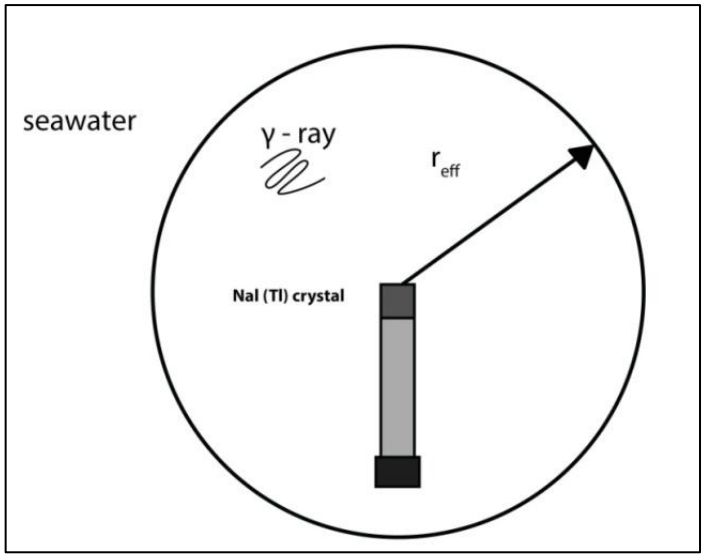

Fig. 4.2: Schematics of the measurement setup in the marine environment (Andr_15).

The naturally occurring radionuclides present in the marine environment, namely ^{208}Tl, ^{228}Ac, ^{212}Bi, ^{212}Pb (series of ^{232}Th), ^{214}Bi, ^{214}Pb, ^{234}Pa, ^{226}Ra, ^{222}Rn (series of ^{238}U) and ^{40}K were included in the simulation. Regarding the artificial radionuclide ^{137}Cs, the activity concentrations in the Mediterranean Sea (where the developed technique was applied) are below the system detection limits, however the simulation ('standard' spectrum) was also performed for this radionuclide, and can be utilized in the FSA calculations in cases where it is needed.

4.2.2. External algorithms for the energy and resolution calibration

In order to accurately reproduce the experimental spectrum, it is necessary that the detector energy resolution and the energy calibration are precisely introduced in the simulated ones. Both parameters are essential to the FSA calculations. The MCNP-CP code offers the possibility to include these parameters in the simulation. Nevertheless, the inclusion of these parameters in the MC input file would lead to inefficient and time consuming repetitions, since both the detector resolution and the behavior of the electronic components can vary from one measurement to the other.

The alternative, which was adopted in the present methodology, was to use external algorithms in order to introduce these quantities in the simulated spectra. Therefore, a Gaussian broadening was externally applied to the obtained MC histograms, using an appropriate exponential Gaussian broadening algorithm (see Appendix A). The detector

resolution can be determined either by using directly the experimental spectrum or by using standard reference sources. In this work, the energy resolution values were calculated from the experimental spectrum. The results were fitted by an arbitrary exponential function which was subsequently introduced in the algorithm to perform the Gaussian broadening.

Moreover, a second external algorithm was developed in order to introduce to the simulated spectra the experimental energy calibration. Therefore, using this algorithm (see Appendix B), the simulated spectra were reformed according to the experimental binning and energy calibration of the spectrum, namely the calibration constant (keV/channel) and the energy offset (keV), assuming a linear energy function. The algorithm can in principle incorporate the possibility of a non-linear rebinning of the MC spectra but the effect of such energy non-linearities in the experimental spectra were found to be negligible.

The calibration of the MC spectra is a crucial step to the overall FSA procedure and a necessary step before the minimization procedure, since both the experimental and the MC spectra are introduced as input (in counts per channels) in the MINUIT package. Precise calculations of the experimental energy calibration are mandatory in order to match the gain settings of the experimental spectrum, as gain mismatch can drastically affect the activity concentration results. The same also applies to the experimental energy resolution calibration, although miscalculations in the Gaussian broadening would mostly affect the fitting results and not the activity concentrations, as the χ^2 minimization is performed by comparing the counts in a selected channel integral containing the whole photopeak.

In Fig. 4.3 the steps of the described procedure are illustrated for the MC spectrum of the radionuclide ^{214}Bi. The normalized MC spectrum (after the multiplication with the effective volume and the acquisition time) assuming 1 Bq/L activity concentration is depicted in Fig. 4.3 panel a, along with the result of the implementation of the external convolution algorithm (Gaussian broadened spectrum), while the gain calibration procedure using the external rebinning algorithm is demonstrated in Fig. 4.3 panel b.

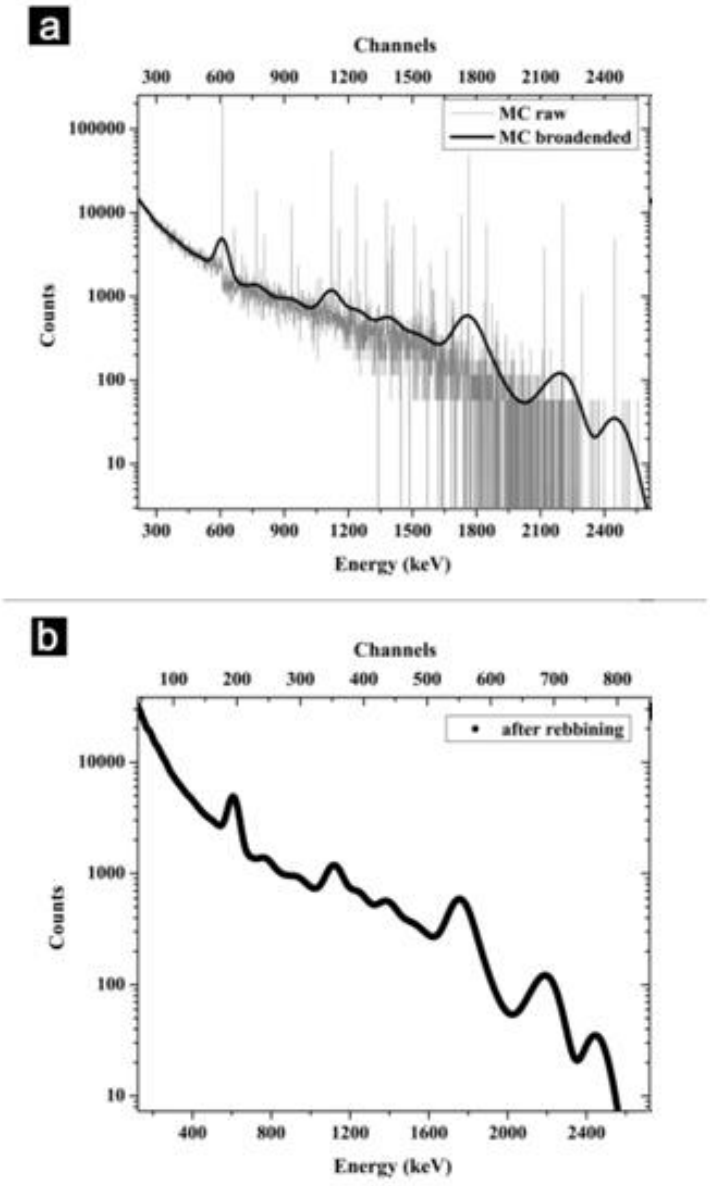

Fig. 4.3: Representation of the ^{214}Bi standard spectrum in all processing steps. The normalized MC spectrum, assuming 1Bq/L activity concentration, is depicted along with the corresponding spectrum after the implementation of the Gaussian broadening (MC broadened), in panel a, and after the rebinning procedure, in panel b.

4.2.3. Standard Spectra

The final spectra implemented to simulate the marine environment consist of 10 separate standard spectra from the ^{238}U and ^{232}Th series along with ^{40}K, assuming an initial 1Bq/L activity concentration. These spectra are presented in Fig. 4.4 panel a for the radionuclides of the ^{232}Th series along with ^{40}K and in Fig. 4.4 panel b for the

radionuclides of the ^{238}U series, assuming typical values for the electronic calibration (energy resolution and binning). The emitted γ-rays are reproduced according to the decay scheme for each radionuclide. In the case of ^{40}K, although only a single γ-ray at 1460.8 keV is emitted, additional features are present in the spectrum. These are artifacts attributed to low MC statistics in those areas. In Fig. 4.4 panel c, all the standard spectra (10 spectra) are presented together.

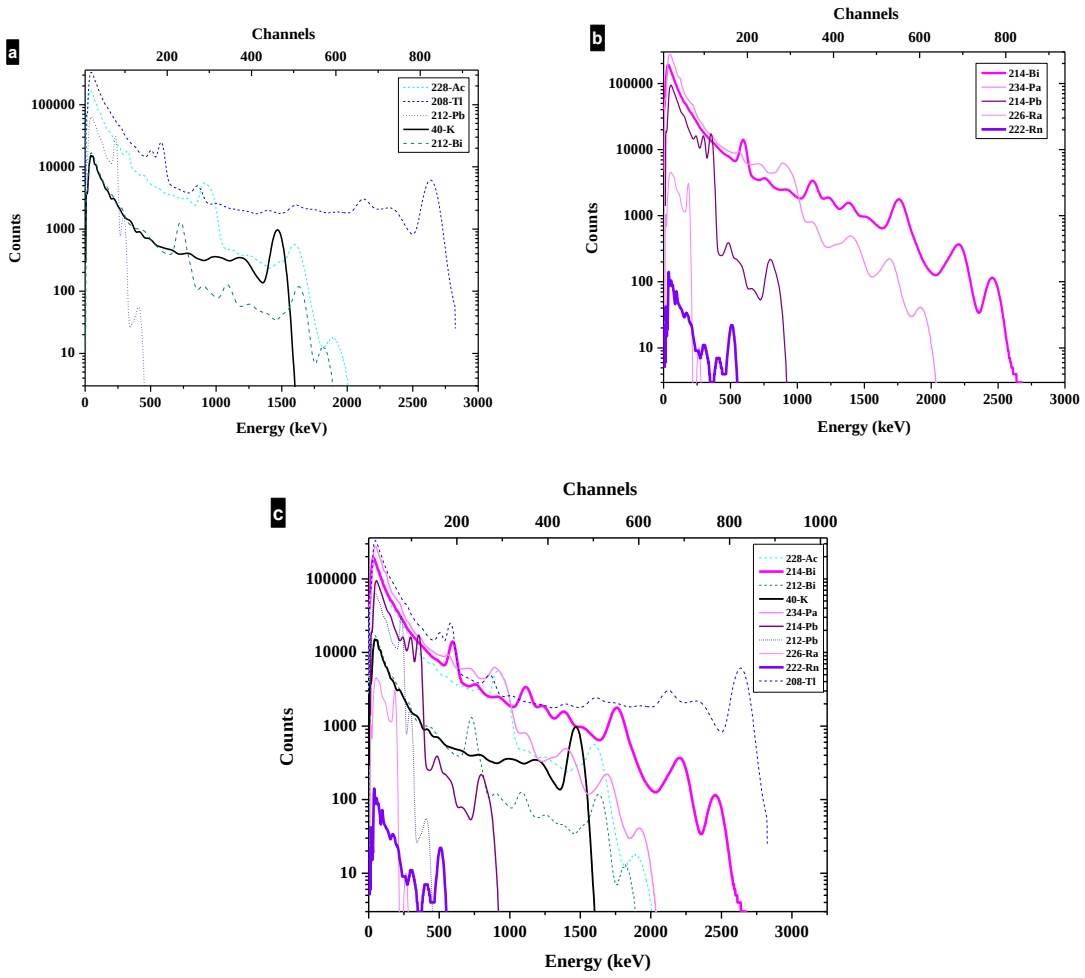

Fig. 4.4: Representation of the 10 standard spectra for the radionuclides ^{40}K and the ^{232}Th series (panel a) and the ^{238}U series (panel b), along with the total MC spectra (panel c) assuming equal 1Bq/L activity concentrations for all the radionuclides.

The appearance of convoluted peaks in practically every energy region (Fig. 4.4 panel c), is attributed to the inherent low resolution of the employed detector (NaI(Tl) crystal).More specifically, starting with the high energy part of the spectrum, the first peak

(at about 2600 keV) is a convolution of the ^{208}Tl (2614 keV with 99% intensity) and ^{214}Bi (2447.86 keV with 1.6% intensity) photopeaks, while the second one consists of the ^{208}Tl first escape peak (2103 keV), the ^{208}Tl Compton edge (2381 keV) and the ^{214}Bi photopeaks (most prominent one at 2204 keV with 5.1% intensity). Moving to the left (lower energy part) the complexity rises, as more radionuclides contribute to each peak formation. The peak present at 1760 keV is mostly attributed to the γ-rays of ^{214}Bi (at 1729 and 1765 keV) while a notable contribution arises to the left side from the ^{228}Ac photopeaks (1588 keV is the most prominent photopeak with 3.2% intensity) and from the ^{208}Tl second escape peak (1592 keV). Additional peaks with reduced contributions are the ^{234}Pa and ^{212}Bi ones, while several sum peaks could be hidden under the convoluted peaks due to the ^{214}Bi and ^{234}Pa complex cascade decay schemes (e.g. summation of the ^{214}Bi 609 and 1120 keV γ-rays). The ^{40}K photopeak (1461 keV), which is always present and usually predominant in spectra obtained in the seawater column, strongly interferes with the Compton edge of the 1764.5 γ-ray (1541 keV) and several ^{214}Bi photopeaks (most prominent at 1377 keV with 5.1% intensity) and much less with ^{234}Pa photopeaks (most prominent at 1394 keV with 2.1% intensity).The complexity in the medium energy part of the spectrum rises due to the presence of many γ-rays from various radionuclides, while the situation is much improved in the lower energy part of the spectrum where the photopeaks of ^{214}Pb (241, 295, 352 keV) and ^{212}Pb (239 keV) are well separated from contributions originating from other radionuclides.

The presented standard spectra were subsequently utilized in the FSA calculations through χ^2 minimization. A schematic diagram of all the steps involved in the presented FSA technique is illustrated in Fig. 4.5. The methodology procedure steps are summarized as follows: Separate MC runs are performed for the radionuclides of interest to estimate the pulse-height spectra of the detector KATERINA for measurements in the seawater column. The results are multiplied with the necessary constants to be converted to spectra in appropriate units (gammas/(Bq/L)/channel).The experimental calibration is applied to the MC spectra via external routines that are executed to automatically derive the final standard spectra using the calibration values (both energy and resolution) are provided by the user (operator). The gain calibrated, broadened and rebinned MC standard spectra (counts per channel) are introduced along with the experimental one in the MINUIT package. Then, the user-defined routine incorporated in the MINUIT package automatically performs a summation of the standard spectra by implementing a linear combination using different initial parameters α_j for each standard spectrum in order to derive the optimal values that

accurately fit the experimental spectrum using χ^2 minimization. A detailed description of the χ^2 minimization performance, which is utilized in order to derive the activity concentration values, is described in detail in the following section 4.2.4.

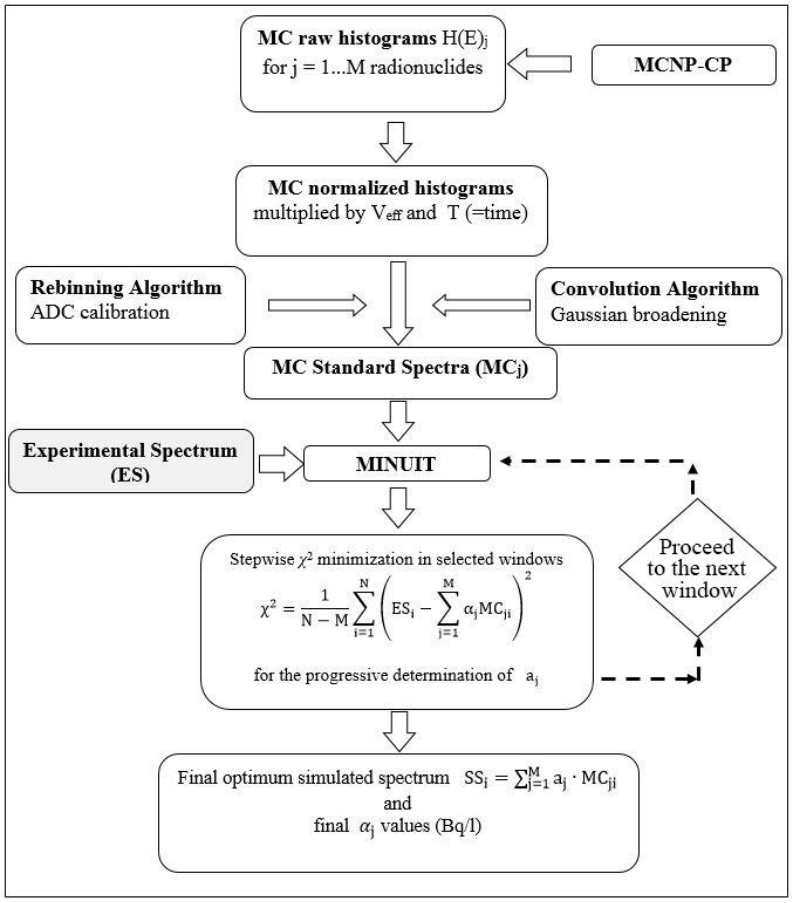

Fig. 4.5: Schematic of the steps involved in the adopted FSA technique from the MC simulations to the χ^2 minimization performance.

4.2.4. Activity concentration calculations using χ^2 minimization

The key aspect of the FSA technique is the implementation of the χ^2 minimization in order to derive the optimal activity concentration values (unknown parameters α_j) for the experimental measurement. The estimation of the unknown parameters is accomplished by minimizing the difference between the simulated and the experimental data, with the former being represented by a collective function $F(\alpha_j)$, where α_j are the unknown normalization factors (James_94; James_75). Among the different minimization algorithms, the MINUIT package (developed at CERN by the CN/ASD Group, 1993), utilized in this work, is designed to handle any function F(X) offering the possibility to incorporate user-defined subroutines and has been successfully implemented in a great variety of different

applications in the past.

A user-defined routine was developed and incorporated in the MINUIT package, to perform the minimization procedure and determine the optimal values of the unknown parameters α_j, which are in fact the activity concentrations. The developed routine performs a summation of the standard spectra (gain calibrated, broadened and rebinned MC spectra) by implementing a linear combination using different initial scaling factors (α_j parameters) for each standard spectrum. Each factor αj, represents the activity concentration (in units of Bq/L) for the specific radionuclide. These unknown parameters α_j are determined through χ^2 minimization, to accurately fit the experimental spectrum. The optimal α_j values are obtained when the χ^2 value is minimized and the best fit to the experimental spectrum is obtained. The minimization was performed according to the following reduced chi-square (χ^2) equation (James_04):

$$\chi^2 = \frac{1}{N-M}\sum_{i=1}^{N}\left(ES_i - \sum_{j=1}^{M}\alpha_j MC_{ji}\right)^2$$

Where:

i= the channel (up to N, usually equal to 1024 for standard NaI(Tl) scintillators)

M= the total number of standard radionuclide spectra (from j=1 to 10 in the present case)

ES_i= the measured experimental yield (counts) in channel i

α_j=the activity concentration of each individual radionuclide, in units of Bq/L

MC_{ji}= the yield of the final gain calibrated, broadened and rebinned MC spectrum of radionuclide j in channel i, in units of counts/(Bq/L).

Since the measurements are performed in the seawater column, well below the sea surface, no 'background' spectrum or any other additional external contribution need to be subtracted. The contribution of the cosmic radiation to the Compton continuum in the experimental spectra is negligible, since the cosmic radiation is drastically decreased when the detector is placed at several meters below the sea surface (Bag_10; Andr_15). Moreover, the intrinsic radiation of the detection system (crystal, enclosure) is also negligible (Tsab_10). In fact, NaI(Tl) is one of the cleanest scintillators (Quar_13), exhibiting small amounts (< 0.5 ppm) of K in the crystal. This concentration contributes to the Compton continuum in the whole spectrum till 1.35 keV but the estimated count rate is extremely low (~ 10^{-3} counts/sec/channel) as compared to the counting rate measured in the marine environment.

The minimization is performed in specific channel regions of the experimental spectrum (windows) in steps using an iterative procedure. The number (regions)of the channels is selected by the user, according to the features of the experimental spectrum, including all the prominent peaks. The minimization procedure starts from the high energy part of the spectrum and is completed when the last peak (that is, the peak with the lowest energy in the spectrum) is fitted. By starting from the high energy region (low count rates) the minimization procedure is focusing in these low statistics areas and is thus forced to converge; thus the precision of the results regarding their physical interpretation is strengthened. Additionally, in the high energy part region the presence of convoluted peaks is limited, allowing for more reliable results. The χ^2 minimization, in each step, is performed by calculating and comparing integrals in the selected channel regions (windows). In each selected channel region, the optimal activity concentration results of the corresponding radionuclides contributing to the existing peaks are fixed.

The minimization procedure and the selected windows are schematically shown in Fig. 4.6, where the standard MC generated spectra for each radionuclide are given in typical activity concentration values found in the aquatic environment. The starting point (i.e. the first minimization window) lies in the high energy region of the spectrum and is selected to be the energy interval under the first two peaks exhibiting the highest energy values (from approximately channel 650 to 990). The only radionuclides contributing to the formation of these peaks are ^{208}Tl and ^{214}Bi. By slightly changing the minimization window (3-4 channels) the best fit solution is obtained and therefore the activity concentrations for ^{208}Tl and ^{214}Bi, are fixed, allowing only for a slight variation around the obtained value (within ~5%) till the whole procedure converges. The remaining parameters (activity concentrations for the remaining radionuclides) are determined by repeating the same procedure after changing the minimization window, gradually moving towards the lower energy part regions. Therefore, the next minimization window is selected to be around the peak at 1460 keV (^{40}K photopeak), including the first two peaks on the right (^{228}Ac γ-ray at 1588 keV, 510 to 570 channels) and left (^{40}K Compton edge,^{214}Bi γ-ray at 1238 keV,410 to 440 channels and ^{234}Pa γ-ray, 420 to 450 channels).

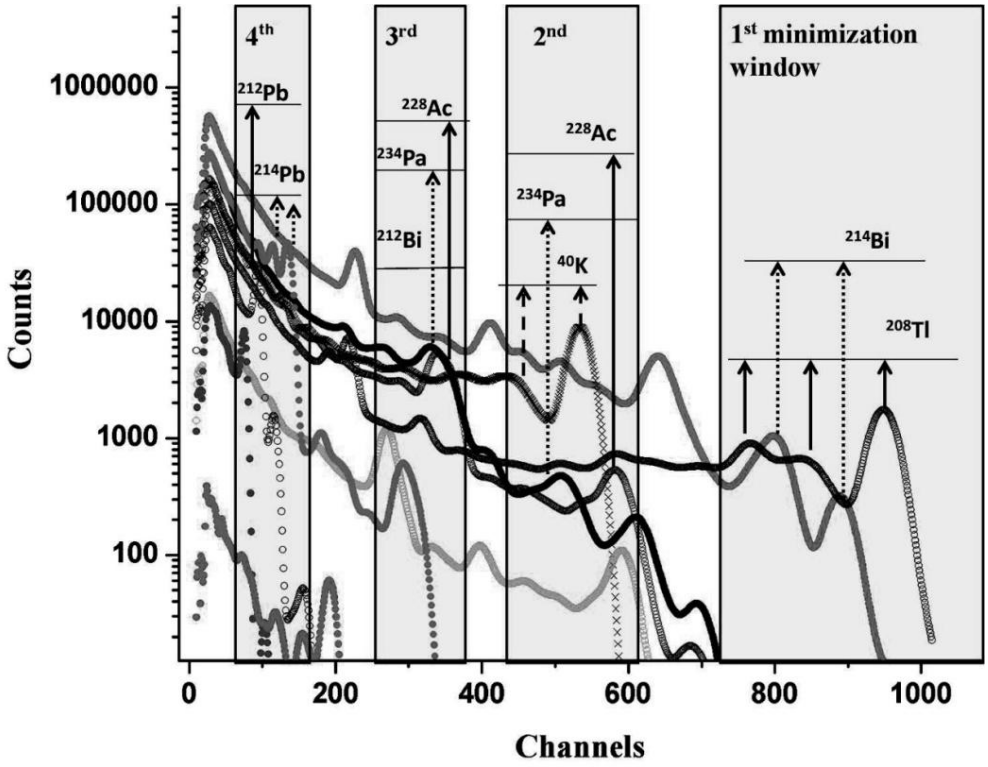

Fig. 4.6: Representation of the 10 standard spectra and the minimization windows assuming typical values for the activity concentrations of the radionuclides.

In the third minimization window (220 to 343 channels) the activity concentration of ^{212}Bi (220 to 260 channels), ^{234}Pa (251 to 328 channels, most prominent peak at 934 keV) and ^{228}Ac (271 to 343 channels) are fixed, since the contributions in the selected area originate from the γ-rays of the aforementioned radionuclides and others that are already fixed (^{40}K, ^{214}Bi, ^{208}Tl). In the last (4^{th}) minimization window, which includes the first three low-energy peaks in the spectrum (γ-rays from ^{214}Pb and ^{212}Pb), the parameters for ^{214}Pb and ^{212}Pb are fixed. Usually the photopeaks of ^{226}Ra (186 keV) and ^{222}Rn (511 keV) do not appear in the spectrum due to their low emission probabilities and high MDA values. In cases, however, where these peaks are evident in the experimental spectra, two additional minimization windows should be selected around the corresponding energy values.

The overall procedure is fast and the results are obtained in a few minutes, depending on the number of the α_j parameters and minimization windows. The activity concentration values are automatically printed in the screen in each step. The final output of the χ^2 minimization execution (apart from the printed activity concentration values) is the simulated spectrum with the activity concentrations incorporated therein.

In this work, the χ^2 minimization is handled by performing a biased chi-square minimization step by step in different selected windows and fixing the corresponding α_j

values (for the radionuclides that contribute to the peak) in each step. If one uses a single large minimization window (including all the spectral information), the minimization procedure would be mostly focused in the high count rate regions of the spectrum (low energy regions) and the convergence would be hindered by the high Compton continuum background interfering in these areas.

4.2.5. FSA uncertainty derivation

Concerning the reliability of the utilized FSA technique, both statistical and systematic uncertainties are taken into account. The statistical uncertainty is estimated by taking into account the photopeak counting statistics of the experimental spectrum and the statistical uncertainty of the MC results. The statistical error in experimental yields typically ranges from 6% to 20% depending on the activity concentrations, the acquisition time and the γ-ray energy, while, regarding the MC simulations the uncertainty was kept below 5% in the main photopeak regions for all the standard spectra. Thus the total statistical experimental uncertainty is mainly governed by the counting statistics.

The systematic uncertainty on the other hand may be attributed to the simulation modeling (geometry measurement, materials), the energy and resolution calibration and to the minimization process (selection of the minimization windows). The systematic uncertainty arising from the selection of the minimization windows was estimated to be considerably less than 10%, by changing the energy range of the selected windows. All the other contributions were considered to be negligible, since they were carefully tuned according to the experimental data. Nevertheless, the systematic uncertainty critically depends on the accurate determination of the energy (gain) calibration, while possible miscalculations in the Gaussian broadening (energy resolution calibration) would mostly affect the shape of the fitted spectrum and not the activity concentrations, since the minimization procedure is performed by count integration in the selected regions.

The accuracy of the results strongly depends on the number of the utilized parameters and the minimization windows. The usage of many parameters α_j, and the performance of the minimization in steps, in properly selected regions of the spectrum, by fixing in each step the activity values of the corresponding radionuclides, increases the number of the available equations to perform the minimization procedure and therefore the possibility of obtaining a unique, 'more physical' solution. Nevertheless, regardless the number of the utilized standard spectra (for different radionuclides), the FSA technique can

give reliable results only for the radionuclides that contribute to the formation of a peak in the experimental spectrum.

4.3. Application of the FSA technique and results

The FSA technique was initially applied to reproduce the data (experimental spectrum, activity concentration results) of the experimental detection efficiency calibration of the system KATERINA for measurements in the aquatic environment held at the water tank in NTUA. The details of the experimental calibration were given in section 2.5.1. In section 4.3.1 some technical aspects related to the experimental measurement are discussed along with the results of the FSA technique. After this first evaluation, the developed technique was subsequently applied in three different test cases, to reproduce experimental data obtained from the deployment of the *in situ* system KATERINA in the marine aquatic environment in different areas of the Mediterranean Sea, namely at Vasilikos port (Cyprus) (site1), Ierissos Gulf (Greece) (site 2) and Stoupa Bay (Greece) (site3). The different measurement setups (acquisition time, gain calibration) utilized in each deployment were properly introduced in the standard spectra. The discussed methodology was applied in all cases and the theoretical results were compared with the activity concentrations derived by analyzing the experimental spectra using the SPECTRW software (Kalf_16). An additional FSA performance test was conducted in site 3, assuming secular equilibrium between the radionuclides of the same series. For this particular test case, only three standard spectra were utilized, namely the standard spectra from ^{40}K, ^{238}U (summation of the standard spectra from the radionuclides ^{214}Bi, ^{214}Pb, ^{234}Pa, ^{226}Ra and ^{222}Rn) and ^{232}Th (summation of the standard spectra from the radionuclides ^{208}Tl, ^{228}Ac, ^{212}Bi and ^{212}Pb). The comparison of the spectra (theoretical, experimental) and the corresponding activity concentration results are presented in sections 4.3.2.1 to 4.3.2.3 for the sites 1 to 3, respectively.

4.3.1. Implementation of the FSA technique in the laboratory

The FSA technique was applied to reproduce the results of the experimental calibration of the KATERINA detection system (Tsab_12; Tsab_08) for measurements in the aquatic environment. The system KATERINA was deployed in a 5.5 m^3 water tank containing diluted sources of the radionuclides ^{40}K, ^{99m}Tc and ^{137}Cs having known activity concentrations (as shown in Table 4.1). Details on the experimental calibration procedure

can be found elsewhere in the literature (Tsab_08; Vlastou_06). To reproduce the calibration spectrum, the MCNP-CP code was implemented to simulate the three aforementioned radionuclides according to the exact existing experimental conditions. The three standard spectra (^{40}K, ^{99m}Tc and ^{137}Cs) were linearly combined to form the simulated spectrum. The theoretical activity concentrations were derived directly through χ^2 minimization, using the MINUIT package, by fitting the simulated spectrum to the experimental one. The experimental spectrum is depicted with the simulated one after the minimization procedure in Fig. 4.7a.

The activity concentrations derived via the FSA technique are compared with the nominal ones in Table 4.1. It is evident that the reproduction of the experimental spectrum is poor (Fig. 4.7a) and the comparison of the activity values exhibits large differences, up to 40% for the radionuclide ^{99m}Tc (Table 4.1). This is attributed to the ambient background radiation (cosmic radiation, building materials) as well as to background contributions from the water constituents of the tank, which are not subtracted from the experimental spectrum. Moreover, the observed discrepancies at the low energy peak (the case of ^{99m}Tc) are attributed to pile-up effects that were present due to the high activity concentration of the ^{99m}Tc calibration source. The pile-up contribution in the experimental spectrum was calculated to 10%.

Therefore, the χ^2 minimization was repeated, after the inclusion in the calculations of two additional standard spectra (total of five), for the radionuclides ^{214}Bi and ^{208}Tl, since the corresponding photopeaks of these radionuclides were evident in the experimental spectrum (peaks at 609, 2200 and 2600keV) yielding a significant contribution to the measurement. The contribution of other naturally occurring radionuclides was considered to be negligible (no other peaks were observed in the experimental spectrum).

The ‘corrected’ simulated spectrum is compared with the experimental one, as shown in Fig. 4.7b. The improvement in the results (Table 4.1, second run) is reflected also in the better quality fitting of the experimental spectrum. The differences between the nominal and the FSA activity values were found to be ~7%, 12% and 23% for the radionuclides ^{40}K, ^{137}Cs and ^{99m}Tc, respectively. The enhanced difference found only in the case of the radionuclide ^{99m}Tc can be exclusively attributed to artifacts in the experimental measurement pile-up due to the high count rate, which were not corrected, nor included in the simulation.

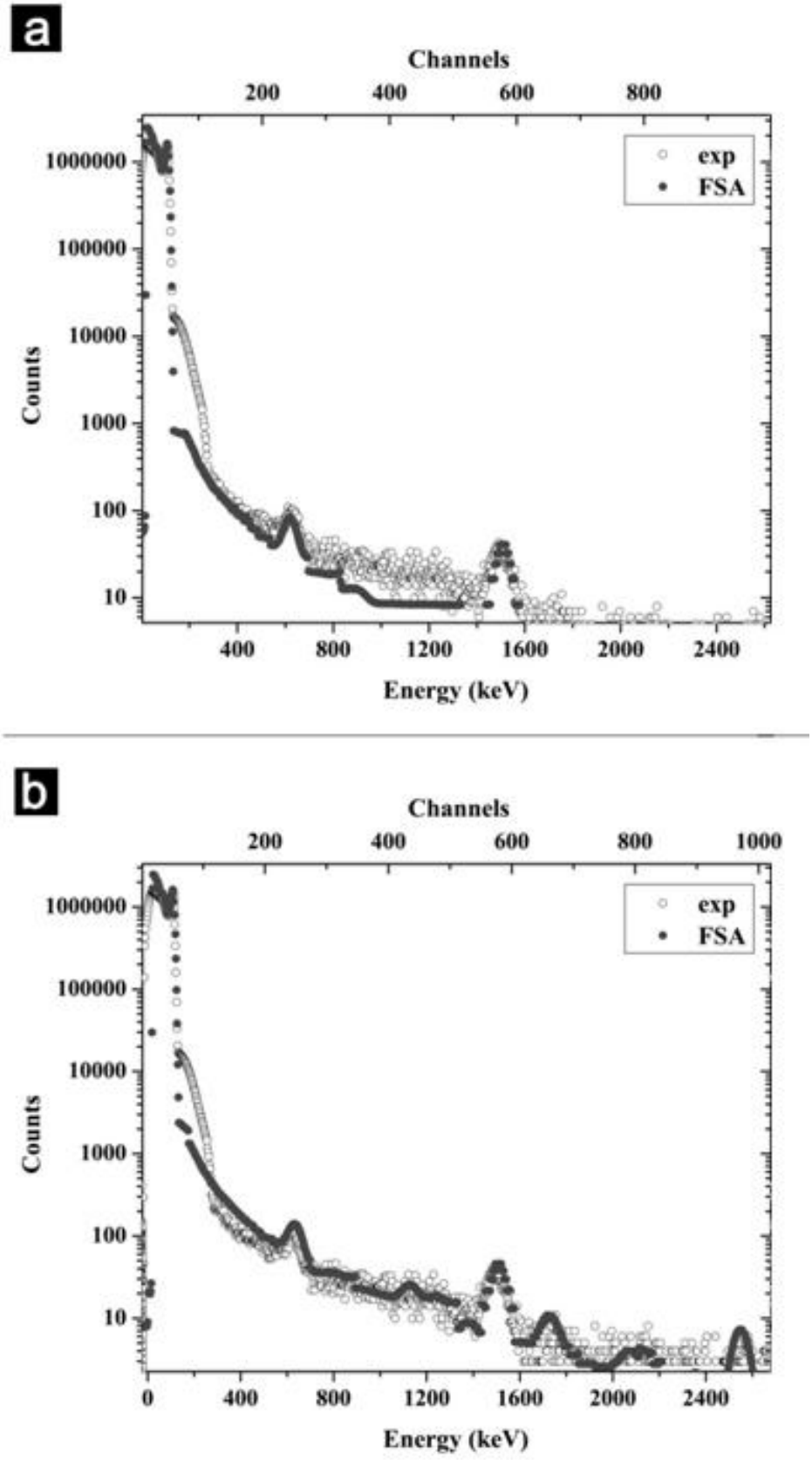

Fig. 4.7: Comparison between the simulated and experimental spectra of the water tank utilizing three standard spectra for the radionuclides ^{40}K, ^{137}Cs and ^{99m}Tc (panel a), and utilizing standard spectra for the radionuclides ^{40}K, ^{137}Cs, ^{99m}Tc, ^{214}Bi and ^{208}Tl (panel b).

An important result from this validation procedure was that the technique is highly sensitive to the complete representation of the simulated environment. A poor representation using a diminished number of standard spectra is directly reflected in the significant differences in the spectral features, both in the photopeak regions, but also in the Compton continuum (Fig. 4.7a). However, when standard spectra from all the radionuclides that contribute to the measurement are included in the calculations, the FSA results can accurately reproduce all the features of the experimental spectrum (Fig. 4.7b).

Table 4.1: Simulated and nominal activity concentration results (Bq/L) comparison for the calibration experiment using three (*first run*) and five (*second run*) standard spectra.

		First run		Second run	
Radionuclides	*Nominal values*	*FSA*	%	*FSA*	%
	(Bq/L)	(Bq/L)		(Bq/L)	
^{40}K	7.44	8.20	10	7.99	7
^{99m}Tc	4814	3900	23	3800	26
^{137}Cs	0.92	1.25	37	0.80	14
^{214}Bi	-	-	-	0.98	-
^{208}Tl	-	-	-	0.20	-

4.3.2. Implementation in the marine aquatic environment

4.3.2.1. Application in Vasilikos

The detection system KATERINA was deployed in Vasilikos port (coords. 33.29376N, 34.72321E) near a former fertilizer industry. The system was positioned well above the seabed and below the seawater surface and the experimental spectrum was obtained using a 17- hour acquisition time. Details for the area and the measurement setup are found at Androulakaki et al. (2015). The experimental spectrum was analyzed to determine the energy resolution (FWHM calibration), the energy calibration (gain setup) and the activity concentration values for ^{40}K and ^{214}Bi using the SPECTRW software. The activity concentration value for ^{40}K was determined by peak integration of the corresponding peak (at 1461 keV) after subtracting the counts attributed to the ^{214}Bi photopeaks. The experimental spectrum is compared to the theoretical one in Fig. 4.8.

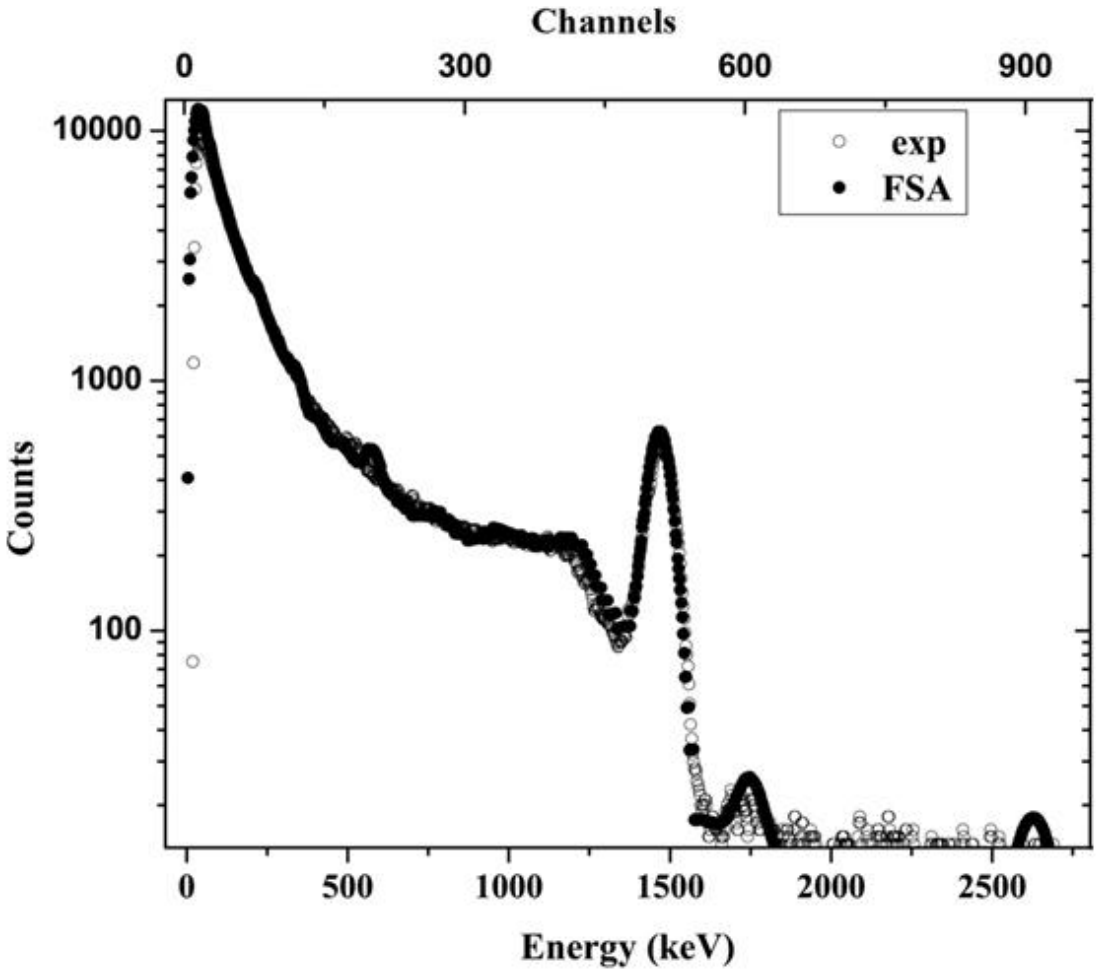

Fig. 4.8: Comparison between the simulated and experimental spectra for site1 (Vasilikos).

The reproduction of the Compton continuum and the peaks over the whole experimental spectrum is very satisfactory. The corresponding activity concentration values for the radionuclides ^{40}K and ^{214}Bi are compared with the experimental ones in Table 4.2 (site1). The relative differences from the experimental values for both radionuclides did not exceed 10%.

4.3.2.2. Application in Ierissos

The detection system KATERINA was deployed in the Ierissos port (cords. 40°23.900'N 023°53.102'E) which is located in Chalkidiki near an operating gold mining industry. The system was positioned well above the seabed and below the seawater surface and the experimental spectrum was obtained using a 9-hour acquisition time.

The experimental spectrum is presented along with the theoretical one in Fig. 4.9.

The reproduction of the peaks appearing in the experimental spectrum, along with the Compton continuum, is again satisfactory.

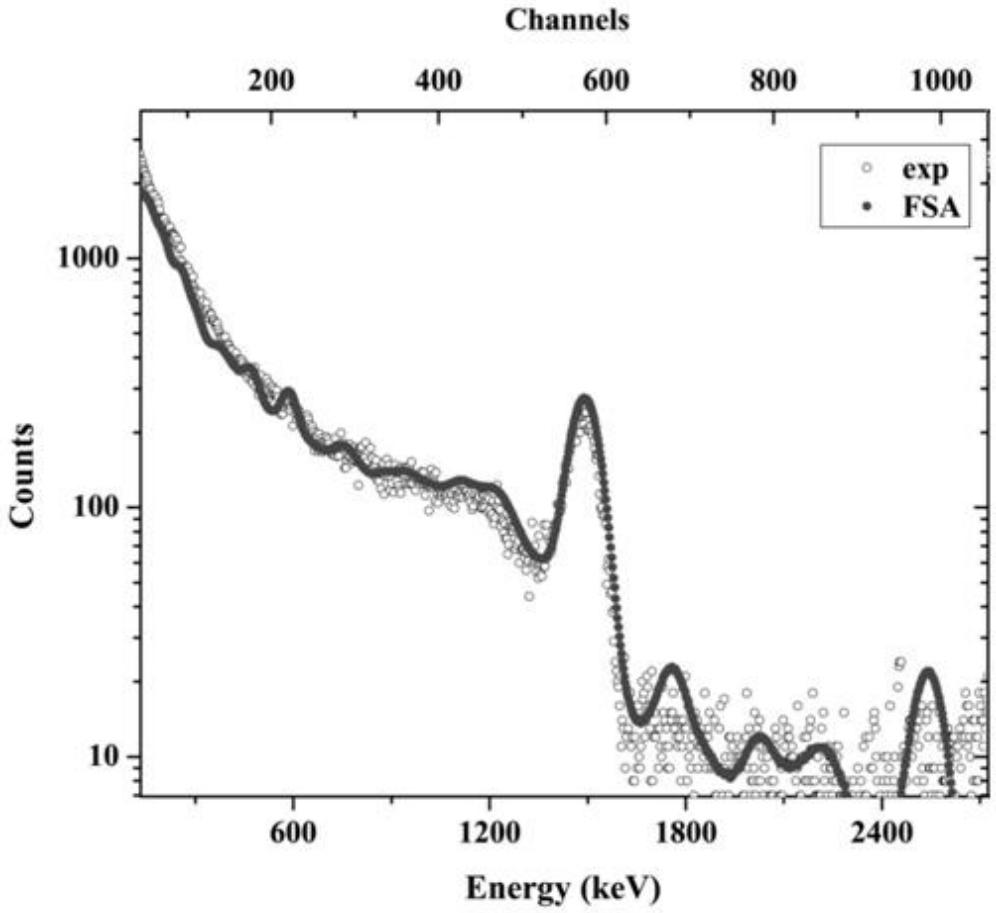

Fig. 4.9: Comparison between the simulated and experimental spectra for site2 (Ierissos).

The corresponding activity concentration values for the radionuclides ^{40}K and ^{214}Bi are compared with the experimental ones in Table 4.2 (site2). The relative differences from the experimental values for both radionuclides were found again to be around 10%.

Table 4.2: Simulated and experimental activity concentration results (Bq/L) for the two deployments, in Vasilikos port (site1) and in Ierissos Gulf (site2).

sites	1			2		
Nuclides	*In situ*	*FSA*	%	*In situ*	*FSA*	%
	(Bq/L)	(Bq/L)		(Bq/L)	(Bq/L)	
^{40}K	18.10 (6%)	16.80	8	15.06 (8%)	13.85	9
^{214}Bi	0.26 (21%)	0.24	8	0.34 (19%)	0.31	10

4.3.2.3. Application in Stoupa bay

The Kalogria Bay is located north of Stoupa town, in the southwest Peloponnesus (Messinia Prefecture) and the area is characterized by the presence of numerous minor Submarine Groundwater Diffusion (SGD) sources. The detection system KATERINA was deployed in the Kalogria Bay to acquire measurements in the water column in close touch with the SGD source, for several different periods, from July 2009 till May 2010. Details on the experimental setup are given in the literature (Tsab_12). The experimental activity concentration values were derived by analyzing the *in situ* data as discussed above. Moreover, in order to check that all the radionuclides present in this environment were included in the FSA analysis, high resolution measurements by means of a HPGe system were performed on collected water samples from the site. These measurements yielded similar values with the *in situ* ones (Elef_13). The selected experimental spectrum for the application of the FSA technique was obtained during an expedition on March 2010. The minimization procedure was executed twice, first by simulating only three standard 'series' spectra, namely ^{40}K, ^{238}U and ^{232}Th, assuming secular equilibrium between the radionuclides of the same series, followed by a second analytical FSA performance test using 10 standard spectra, as discussed above. The first run was performed in order to investigate the validity of the secular equilibrium assumption. The experimental spectrum is presented along with the simulated ones in Fig. 4.10a (in the case of three standard 'series' spectra assuming secular equilibrium) and Fig. 4.10b (in the case of 10 standard spectra).

The first run using the assumption of secular equilibrium among the radionuclides of the same series, failed to reproduce the experimental spectrum. This was expected, since the secular equilibrium is disturbed by the different solubility of the radionuclides in the water column. The differences between the two spectra are mostly attributed to the overestimation of the ^{234}Pa activity concentration (peak around channels 260-328) and ^{208}Tl as well as to the underestimation of ^{214}Bi. The effect in the corresponding estimated activity concentration values is significant, especially for ^{40}K (convoluted photopeak with ^{214}Bi, ^{234}Pa, ^{228}Ac) as shown in Table 4.3 (1st run). The activity concentrations in the second run were found to be in very good agreement with the experimental ones, as shown in Table 4.3 (2nd run).

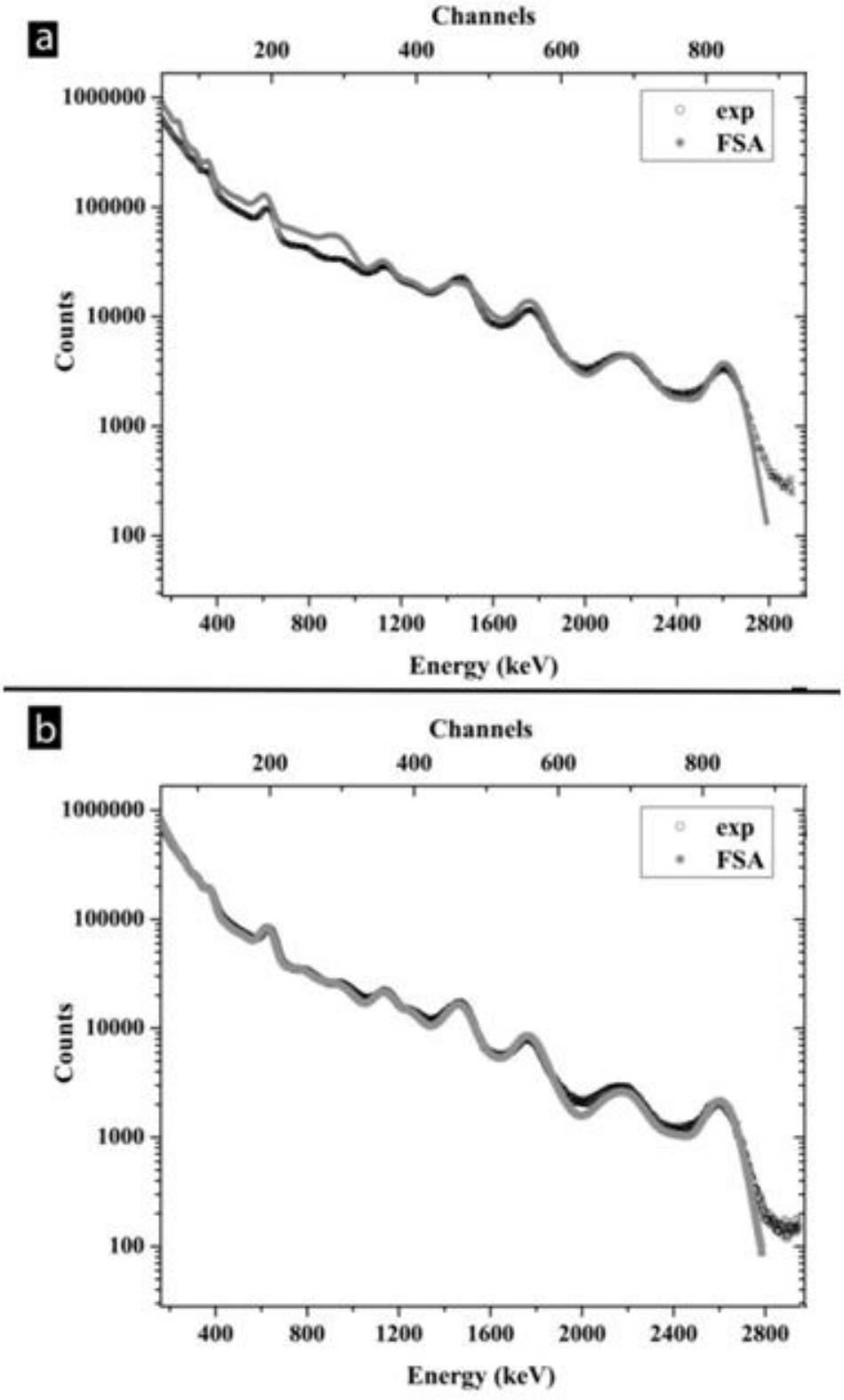

Fig. 4.10: Comparison between the simulated and experimental spectra for site3 (Stoupa Bay) using only three standard spectra for ^{40}K, ^{232}Th and ^{238}U assuming secular equilibrium (4.10 panel a) and using all 10 standard spectra (4.10 panel b).

Table 4.3: Simulated (FSA), and experimental (*in situ*), activity concentration results (Bq/L) in Stoupa Bay (site3) using only three parameters considering secular equilibrium (1st run) among the radionuclides of the same series and using 10 independent parameters (2nd run).

		1st run		2nd run	
Radionuclides	*In situ*	*FSA*	%	*FSA*	%
	(Bq/L)	(Bq/L)		(Bq/L)	
^{40}K	6.40 (6%)	10.38	62	7.02	10
^{214}Pb	3.27 (9%)	3.35	2	3.39	4
^{214}Bi	4.20 (5%)	3.35	20	4.30	2
^{208}Tl	0.30 (13%)	0.35	18	0.32	7
^{228}Ac	1.05 (10%)	1.06	1	1.20	14

4.4. Discussion

The developed FSA technique for *in situ* quantitative measurements in the marine environment provides accurate results reducing the necessary time to perform the analysis and it is sensitive to detect and identify anomalies that could be related to unexpected radionuclides, since the analysis comprises all the features of the spectrum. More importantly, there are several features in the experimental spectrum (escape peaks, Compton edges, sum peaks) that often interfere with the photopeaks, due to the low detector resolution. When the spectrum is treated merely by window or peak analysis, these features cannot be quantified and experimentally subtracted, thus the analysis leads to a decrease in the accuracy of the obtained results. On the contrary, in the FSA technique these features are by definition included in the analysis and are properly taken into account automatically in order to estimate the activity results.

The satisfactory reproduction, of the experimental data renders the MCNP-CP code appropriate to be utilized in diverse environmental applications. The main advantages of the MCNP-CP code are the automatic consideration of the true coincidence summing effects, which become important in contact geometries, and the direct simulation of all the prominent emitted γ-rays along with the corresponding intensities for each radionuclide.

An interesting result from the FSA application in the marine environment was the inadequacy to reproduce the experimental data when the *a priori* assumption of a secular equilibrium existence between the radionuclides of the same series was applied (case study site3). As demonstrated, this assumption can greatly affect the quality of the different features in the theoretical spectra as well as the activity concentration results and thus it should be avoided for marine environment applications.

The adopted methodology offers the possibility of rapid activity concentration calculations in any aquatic environment using detection systems based on NaI(Tl) crystals and could be easily readjusted to include different types of detectors (e.g. BGO, $CeBr_3$, HPGe). Moreover, it can be applied for various geometries and different environments (seabed, soils), provided that accurate standard spectra exist for the geometry and/or materials under study. Therefore, as a next step the FSA technique will be subsequently implemented for seabed applications. The great obstacle in applying the FSA technique for *in situ* measurements on the seabed is that the detection efficiency is influenced by alterations of the sediment physical characteristics. These characteristics (density, porosity, composition) can greatly vary, and thus the FSA derived activity concentrations would be subject to severe systematic errors, unless the sediment properties are properly introduced in the simulations. Nevertheless, the performance of simulations for the reproduction of pulse-height spectra, including all the possible values of the aforementioned characteristics would require enormous computation time, rendering the technique highly inefficient. Therefore, as a first step, a sensitivity study of the influence of the detection efficiency to the sediment physical properties was performed, via Monte Carlo simulations, using the simpler, standard MCNP5 code. Separate runs were performed using monoenergetic volumetric sources covering the γ-ray energy range of interest (150-2600 keV), while typical ranges of the aforementioned sediment physical characteristics values (as discussed in Chapter II) were considered in the simulations. This extensive study allowed the establishment of well-defined relations between the sediment properties and the detection efficiency. The details of the simulations are presented in Chapter V along with the obtained results. Moreover, an alternative methodology based on peak analysis is presented for the activity concentration estimations regarding *in situ* measurements on the seabed.

CHAPTER V:

Implementation of the system KATERINA for measurements on the seabed

5.1. Introduction

Laboratory-based activity measurements using the γ-ray spectroscopy method are widely performed on marine sediment samples for many decades now. The activity concentration results are exploited in several different applications such as a) site characterization of contaminated areas, b) studies of geothermal and oceanographic phenomena (radio-tracing techniques), and c) their utilization (as input parameters)in dispersion models for the radionuclide accumulation and dose-rate estimations. The performance of such measurements requires time-consuming sea trials and special equipment for the samples collection. Additionally, the measurement itself is rather time-consuming and moreover, a sample pretreatment and storage precede each measurement.

The implementation of an *in situ* method instead has clear advantages as it provides the possibility to obtain large scale data in reduced time intervals and the results are obtained within few hours. As a consequence, the interest for such measurements increases. Pioneer works regarding *in situ* measurements in the marine sediment have been performed by different groups (Pov_96; Osv_01; Jones_01; Thorn_13a,b; Graaf_11; Maučec_04; Ocone_04) and this technique has been practiced for several years now. Nevertheless, there are still issues affecting the accuracy of the results associated both with the adopted analysis techniques (window method) and with parameters related directly to the *in situ* measurements. The two major issues regarding the application of the *in situ* technique for measurements in the marine sediment are the influence to the detection efficiency of the sediment physical properties alterations and the existence of inhomogeneous depth profiles regarding the radionuclide concentrations within the seabed.

In this chapter, a developed methodology for *in situ* γ-ray spectroscopy measurements is presented and the results obtained from the test deployments of the system

KATERINA in four different sites, are discussed. The efficiency calibration was performed via MC simulations over a wide energy range covering the whole spectrum, thus allowing the simultaneous detection of the most prominent radionuclides found in the marine environment. The methodology involves a detailed study of the parameters affecting the detection efficiency related to differences in the physical characteristics of sediments and in the geometrical characteristics of the measurement. Moreover, the effect of the background contribution from radionuclides present in the seawater column to the measurement on the seabed is also discussed in detail, considering different setups. An alternative post-survey experimental calibration is also discussed. The experimental calibration was performed in each studied site and was utilized for the evaluation of the Monte Carlo (MC) results. Therefore the MC results were evaluated by experimental corresponding measurements in environments exhibiting different sediment properties.

In more detail, in section 5.2 the adopted measuring setup is described (section 5.2.2) along with the data manipulation to extract the activity concentrations (section 5.2.3). For the quantification of the radionuclides, the efficiency calibration of the detection system is required (section 5.2.2). In this work the efficiency calibration was performed via MC simulations. A major problem associated with *in situ* measurements on the seabed is the influence of the detection efficiency to sediment properties alterations, and thus in section 5.3 a sensitivity study of the parameters affecting the detection efficiency is performed again via MC simulations. This theoretical study includes both geometrical parameters, considering different setups, and alterations in the sediment physical properties. Moreover, in the end of this section the effect of inhomogeneous vertical activity concentration profiles is assessed and discussed. The aim of this study was to provide a measure of the effect of different inhomogeneous depth profiles, to the measurements (detection efficiency) and in this way to test the limits of the applicability of the adopted methodology. The evaluation of the MC results is conducted by corresponding experimental measurements performed directly on the field in four different environments (section 5.4). The adopted methodology for the experimental detection efficiency calibration is presented in section 5.4.1. The details of the experimental measurements, including the *in situ* system deployments and the conducted supplementary laboratory analysis are given in sections 5.4.2.1 and 5.4.2.2-3 respectively, along with the results of the evaluation of the MC simulations, which are presented in section 5.4.2.4.

5.2. Methodology for *in situ* measurements on the seabed

5.2.1. Measurement setup and fieldwork

In order to perform activity measurements on the seabed, the detector has to be placed in close contact with the seabed ('touch' geometry), as even for small distances above the sediment surface the counting rate dramatically drops, due to the strong attenuation of γ-rays in the seawater. At the other extreme, an alternative positioning would be to cover part of the detector with the sediment material in a way that the detector crystal is completely immersed in the seabed. This would lead to a high increase of the counting rate, however this option was not implemented as it presents several technical difficulties. The initial drawback was the positioning the detector inside the seabed. More importantly, it is difficult to keep a fixed distance between the sediment surface and the detector's window in each deployment that is required in order to avoid solid angle corrections in the efficiency calculations. Moreover, this setup poses the risk of injuring the detector in case of deploying the system in a rough (rocky) seabed. Consequently, the 'touch' geometry described above was chosen as the most appropriate setup for *in situ* measurements on the seabed. The system is placed in the center of a platform with a cylindrical base along with the battery supply, as shown Fig. 5.1 panel (a).

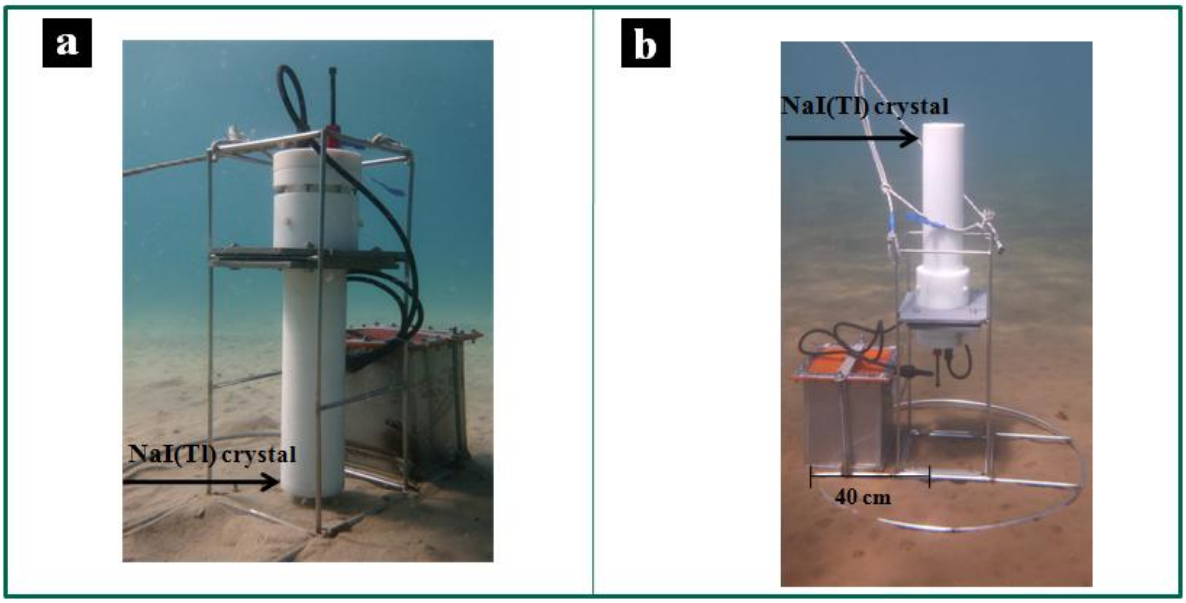

Fig. 5.1: Photo of the deployment for *in situ* measurements on the seabed (panel a) and in the seawater column (panel b).

By using this configuration setup, the detection system is placed perpendicular to the seabed surface. Additionally, this configuration also ensures only small deviations from orthogonality that may be present (in cases of inclined or soft seabed), as the base (circular shape of 40cm radius) is placed parallel to the seabed. The distance between the detector window and the sediment surface is fixed and measured prior to the measurements and when possible, it is additionally measured by a diver during the deployment. Using this setup a wide range of different distances ranging from 0 to 60 cm can be utilized. This is important as different configurations may be required pending on the application. In this work, only small distances (up to 6.5 cm) from the seabed surface were utilized.

Naturally, when the detector positioned inside the seawater in close contact with the seabed, events originating from radionuclides present both in the seawater and the sediment are recorded in the spectrum. These events are γ-ray transitions emitted from the radionuclides present in the sediment layer lying beneath the detector and also in the seawater volume surrounding the detector (Fig. 5.2 (a)).

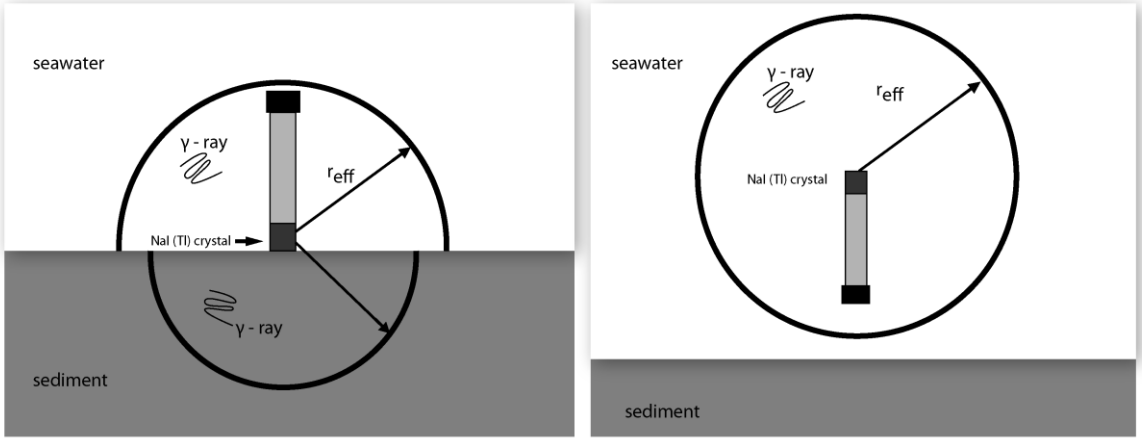

Fig. 5.2: Illustration of the configuration setup for the *in situ* measurements on the seabed (left) and in the seawater column (right), including the detector, the surrounding environment and the effective radii (r_{eff}) in both measurements, defined as the maximum distance from which events can get recorded.

As a result, an additional measurement in the seawater column (Fig 5.1 panel (b)) is required with the detector positioned well above the seabed, in order to subtract from the foreground spectrum (deployment on the seabed), the contribution of the radionuclides present in the seawater(background measurement). The distance of the detector crystal from the seabed surface, for this measurement, should ideally exceed 1.8 m, so that the system

records events exclusively attributed to radionuclides present in the seawater. At this distance, events from the decay of the radionuclides present in the seabed cannot reach the detector, as the effective radius of the recorded γ-ray with the highest energy (2614 keV from ^{208}Tl) in the seawater is 160 cm. Nevertheless, in shallow waters (3 m depth), a distance of about 1 m is considered instead. As the detector length is 60cm, using this setup the distance of the crystal from the seabed surface rises to 1.6 m, ensuring a negligible contribution to the spectrum of detected events arising from radionuclides present in the seabed. For the same reason, the detector crystal should be placed at a distance at least of 160 cm below the seawater surface to discard events arising from the decay of radionuclides present in the atmosphere. From the above discussion it is clear that one of the main tasks was to select a practical setup for *in situ* measurements both in the seawater column and on the seabed. In the proposed configuration, the only setup modification, for the seawater measurement, is the detector's orientation which is mechanically adjusted (without stopping the detector operation), resulting in a rapid and practical transition between the two measurements.

Following the deployment of the detection system in close contact with the seabed, the minimum acquisition time necessary to achieve enough statistics (~10%) in the full spectrum, is approximately 3 h (depending on the application) regarding the measurement on the seabed (Andr_15). However, when possible, using a longer acquisition time better statistics could be obtained. In practice the acquisition time depends on the time available during the research cruise and on the specific site. Concerning the measurement in the seawater column, the acquisition time should be notably prolonged to achieve adequate statistics for the radionuclides quantification, since the concentrations in the seawater are significantly lower compared to those found in the marine sediment. Nevertheless, for seabed characterization applications (sediment mapping) a single measurement in the seawater column using the same acquisition time of the measurements on the seabed suffices, except for environments with strong re-suspension phenomena, currents or the presence of SGD (Submarine Groundwater Discharge). In such cases more spectra should be acquired in the seawater column in the sites affected by the aforementioned phenomena.

Apart from the *in situ* measurements, the collection of sediment samples from the deployment sites is additionally required (see section 5.2.2). Due to the influence of the detector efficiency on the sediment (source) physical characteristics (density, water content, chemical composition), as thoroughly described in section 5.3, these values are required in order to perform accurate activity concentration measurements on the seabed using the

proposed *in situ* method.

5.2.2. MC simulations for the efficiency derivation

In order to extract the activity concentrations, an efficiency calibration of the detector for *in situ* measurements on the seabed is mandatory. In this work, the MCNP5 code was exclusively utilized to study the influence of the sediment properties (wet density, water content, composition) and measurement geometry to the detection efficiency. The utilized MC code constitutes a reliable tool that can accurately reproduce experimental data even in complex geometries and has been utilized for efficiency estimations in a great variety of environmental applications (Elef_13; Mauč_09; Róden_07; Hendr_02). In this section, the details of the simulation setup (geometry, estimators, materials), along with the necessary quantities that are inserted as input parameters in the simulation are discussed. The simulation results are presented in sections 5.3 and 5.4.2.

The performed simulations present similarities with those discussed in section 4.2.1 (Chapter IV) for the *in situ* measurements in the seawater, but there also exist some distinct differences regarding the photon tracking settings and the shape of the source in which the primary photons are generated.

For this application separate runs were performed considering monoenergetic γ-rays in the energy range of interest, from 238 to 2614 keV. This option offered the possibility to drastically reduce the computing time, as explained below. In order to estimate the detection efficiency, one has to estimate only the counts recorded under the photopeak per initial event, and when monoenergetic sources are used, the counts under this region are clear from any type of contributions (e.g. Compton Continuum from γ-rays of higher energy). Therefore, a narrow energy window around the primary photon energy was selected, in which the pulses per initial event were recorded using the F8 tally, instead of producing a large histogram over the whole energy range (200 -2600 keV). This way the computing time to achieve sufficient statistics reduces from hundreds of hours to several minutes or hours pending mostly on the energy of the simulated photons.

The characteristics of the detector MC model (geometry, materials) were presented in section 4.2.1 and are not further discussed here. For the proper simulation of the photon transport through the materials in the specified problem, the measurement geometry details and the sediment matrix properties, including the sediment wet density, the water content and the chemical composition, are required. These values could be rapidly obtained by

shipboard methods or via laboratory measurements on collected sediment samples. The same quantities are also required for the effective volume calculation (a maximum distance from which they can reach the detector and get recorded) as the effective radius varies with the γ-ray energy, and additionally highly depends on the media through which the photons are transported (density, Z_{eff}). When these values (sediment properties, measurement geometrical characteristics) are altered the solid angle of the measurement (via the effective volume) also changes, as described below.

When the detector is placed exactly on the seabed the effective volume takes the form of a hemisphere following the analysis presented in section 4.2.1. The effective radius is calculated using the Beer-Lambert law assuming a ratio Io/I=10000, after the appropriate modification of the sediment matrix composition according to the values of the sediment water content (water saturated sediment). When the detector is placed a few cm (distances larger than 1cm) above the seabed, photons travel in two different media (sediment and water) before reaching the detector. The presence of two different media causes the distortion of the spherical symmetry of the measurement (Askri_08). The effective volume is calculated from the effective radius, which in such cases has a strong dependence on the geometry setup. The effective radius, $\boldsymbol{r_i(z_i, E)}$, represents the maximum lateral distance from which γ-rays can reach the detector with respect to the sediment depth $\boldsymbol{z_i}$, and is given as a function of the distance $\boldsymbol{h}$ of the detector above the seabed, the sediment depth ($\boldsymbol{z_i}$), the maximum depth $\boldsymbol{d}$ (Eq. 5.3) and the total linear attenuation coefficients of each γ–ray in the media (seawater, sediment), as shown in Eq.5.1:

$$\boldsymbol{r_i(z_i, E)} = \sqrt{\left(\frac{\mu_1(E)}{\mu_2(E)} \cdot \boldsymbol{h} + \boldsymbol{d}\right)^2 \cdot \left(\frac{(h - z_i)}{\frac{\mu_1(E)}{\mu_2(E)} h - z_i}\right)^2 - (\boldsymbol{h} - \boldsymbol{z_i})^2} \tag{5.1}$$

The maximum depth d, is calculated using the Beer-Lambert law assuming a ratio Io/I=10000, taking into account the mass-weighted coefficients of the solid and fluid constituents (Bodw_94), as shown in Eq. 5.2 and 5.3.

$$\boldsymbol{I = I_0 \cdot e^{-\sum_i(\mu_i \cdot z_i)}} \quad \textit{, i=1 (water), 2 (sediment)} \tag{5.2}$$

$$\boldsymbol{z_{max}(E) = \frac{ln(10000) - \mu_1(E) \cdot h}{\mu_2(E)} = d} \tag{5.3}$$

The total mass attenuation coefficients of each γ–ray (determined from the web database NIST X-COM (Berg_10) are converted to total linear attenuation coefficients (μ_1(E), μ_2(E)), for the specific sediment properties, namely the wet density and the sediment matrix chemical composition (modified according to the water content value). A representation of the calculated effective volume for a distance, ***h***, of 2.5 cm above the seabed is given in Fig. 5.3, considering two different sediment wet densities, namely 1.4 and 1.9 g/cc.

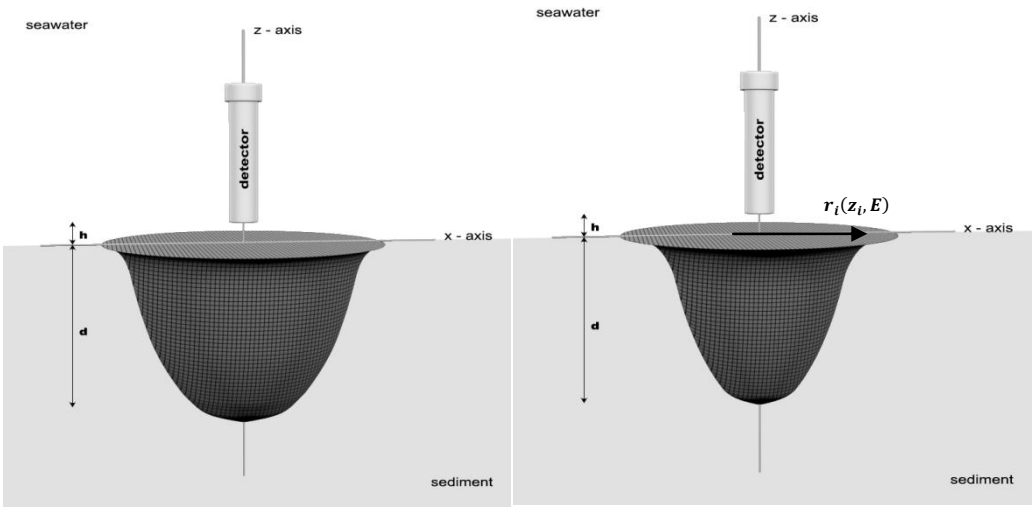

Fig. 5.3: Schematic diagram of the simulation model for the measurements on the seabed for a 2.5 cm distance (*h*) between the detector window and the seabed surface assuming a wet density of 1.4g/cc (panel a) and 1.9 g/cc (panel b).

These analytical expressions were taken into account in the utilized optimized geometry for the effective volume in the MC simulations. As a first approximation, photons were generated in a volume of a truncated cone, large enough to enclose the actual geometry (Fig. 5.4 panel (a)). Subsequently, the actual volume was subdivided into parallel horizontal planes set in equal distances and the boundaries of each box (vertical planes) slightly overlapped for the actual geometry in each subdivision, forming this way a finite number of parallel cylinders (Fig. 5.4 panel (b)) which provided a more close resemblance to the actual geometry.

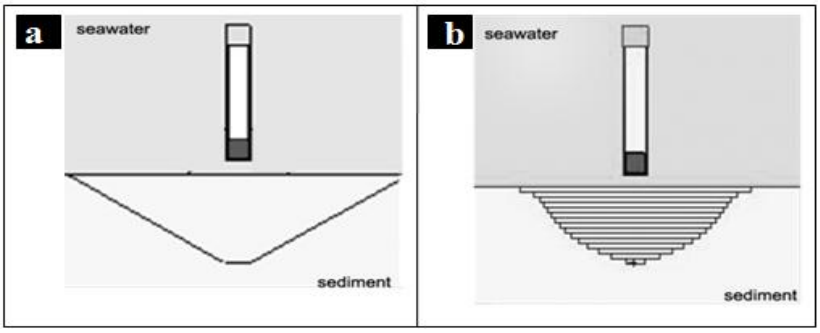

Fig. 5.4: Schematic diagram of the simulation models for the seabed measurements using a truncated cone (panel a) and finite parallel cylinders (panel b) to describe the effective volume (sediment source).

The differences in the obtained efficiency results between the two geometrical approaches did not exceed 10%, and thus, the simplified geometry (truncated cones) which also leads to a less complex input file, was selected for the corresponding simulations.

5.2.3. Activity concentration derivation

As explained in section 5.2.1 the *in situ* system is deployed in a specific site to acquire two spectra, one on the seabed and one in the seawater column (background spectrum). Subsequently, the background spectrum is properly subtracted from the seabed spectrum to remove the contribution ($\boldsymbol{Cont._w}$) of the detected γ-rays emitted from radionuclides present in the seawater, during the measurement. The seawater contribution can be easily calculated when the detector is placed exactly on the seabed (touch geometry). The subtraction of the counting rate attributed to events generated in the seawater column, is given in Eq. 5.4 in the simple case where the detector is laid perpendicularly relative to the seabed and exactly on the seabed surface:

$$\boldsymbol{Netcps_s = Ncps_s - {}^1/_2 \cdot Ncps_w}$$

$$\boldsymbol{Cont._w = {}^1/_2 \cdot Ncps_w} \quad (5.4)$$

where $\boldsymbol{Ncps_s}$, is the net counting rate (after the subtraction of the Compton continuum contribution) in the selected peak in the spectrum acquired on the seabed, $\boldsymbol{Ncps_w}$, is the corresponding net counting rate of the spectrum acquired of the seawater column, and

$\boldsymbol{Netcps_s}$, refers to the net counting rate (clear of contributions attributed to the Compton continuum and to radionuclides in the seawater column) of a peak present in the spectrum acquired on the seabed. The geometric factor $\mathbf{1}/_{\mathbf{2}}$ corresponds to the solid angle ratio of the two different setup configurations during the deployments on the seabed and in the seawater (Fig. 5.2), for the detection of the radionuclides present in the seawater column. Although during the measurement in the seawater column events are recorded from a sphere surrounding the detector, while during the deployment on the seabed only half of this volume participates in the measurement, differences between the two hemispheres are not expected, since radionuclide homogeneity in the seawater is preserved (except in extreme cases of dynamic environments, eg. strong currents, SGD, radioactive gass emissions at submarine faults, mud volcanoes, pockmarks etc) and moreover the attenuation in the detector's low-Z shielding is negligible, except for low-energy γ-rays.

When the detector is placed even a few cm above the seabed, the contribution of events generated in the seawater column rises and the above formula is no longer valid, on the contrary, the exact calculations become rather complex. The contribution of the events attributed to radionuclides present in the seawater column increases, since an additional seawater layer contributes to the measurement on the seabed. This enhanced contribution, clearly depends on the distance of the detector position from the seabed, but also depends on the photon γ-ray energy.

MC simulations (MCNP5 code) were again utilized to estimate the water contribution in these cases, although analytical expressions are also available (Boson_06) and could be implemented instead. Separate simulations were performed to estimate the rise of the seawater contribution with respect to a detector distance of 2 and 6 cm above the seabed surface. The pulse-height estimator was used (f8 tally), to estimate the detection efficiency and the results were then converted to detected counts. To ensure the consistency of the results regarding the different volumes involved in the simulation runs, the ratio N/V, namely, the generated events N over the effective volume V, was kept constant at a fixed value, by changing the number of generated events N in each run according to the effective volume values. The statistical uncertainties were kept below 10% for all the simulation runs.

To simulate the enhanced contribution of the radionuclides present in the seawater during the deployment on the seabed, a volume source of a hemisphere was utilized in the simulation runs consisting of seawater, as shown in (Fig. 5.5 panel (a)). The volume source

was separated in two parts using a plane, thus the photons were generated in the first series of runs in the upper source layer (Fig. 5.5 panel (b)), which was a slice of 6 cm and 2 cm followed by a second series of runs in which the photons were generated in the whole effective volume (Fig. 5.5 panel (a)). The different radius of the hemisphere was calculated with respect to the energy of the emittedγ-ray from the total linear attenuation coefficient for seawater (density=1.026 g/cm^3) using the X-COM database, as described in section 2.1 and separate runs were performed for each γ-ray energy, in the range from 351 keV to 2614 keV. The contribution of the events generated in the upper layer (**cont.$_{u.l.}$%**) is calculated as the ratio of the counts detected in the first few cm of the hemispheric water source to the total counts detected from the whole volume (considering an hemispheric water source) that contributed to the measurement on the seabed. To check the accuracy of the results a third series of runs was executed where the photons were generated in the lower volume part (Fig. 5.5 panel (c)).

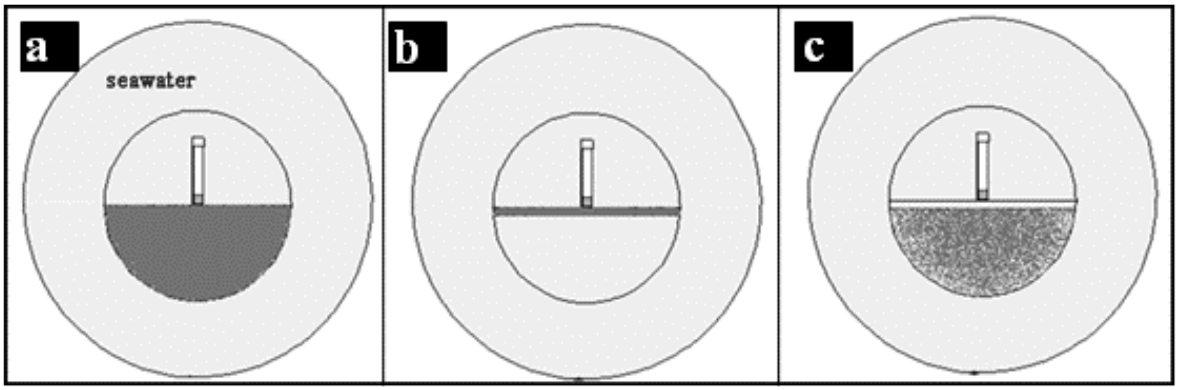

Fig. 5.5: Schematics of the MC models for the water contribution estimations, assuming the events are generated in the whole effective volume with a shape of a hemisphere (panel a), in the first few cm (2 cm in the first run and 6 cm in the second) and finally c. in the lower volume part below the first few centimeters (panel c).

The runs were checked for consistency by summing the detected events in the upper and lower volume parts and comparing with the counts recorded in the runs where the photons were generated in the whole effective volume. The obtained values of the detected events in both cases were found to be in agreement within the statistical uncertainty. The results are summarized in Table 5.1 (**cont.$_{u.l.}$%**), for two studied different distances, namely 6 cm and 2 cm. The results showed that the ratios (contribution of the upper layer) varied from 66% to 38% and from 30% to 18% for a distance of 6 cm and 2 cm, respectively and the

variation was reduced with increasing γ-ray energies, as expected. The data are fitted by an exponential equation (Fig. 5.6) to expand the results over a broad range of γ-ray energies.

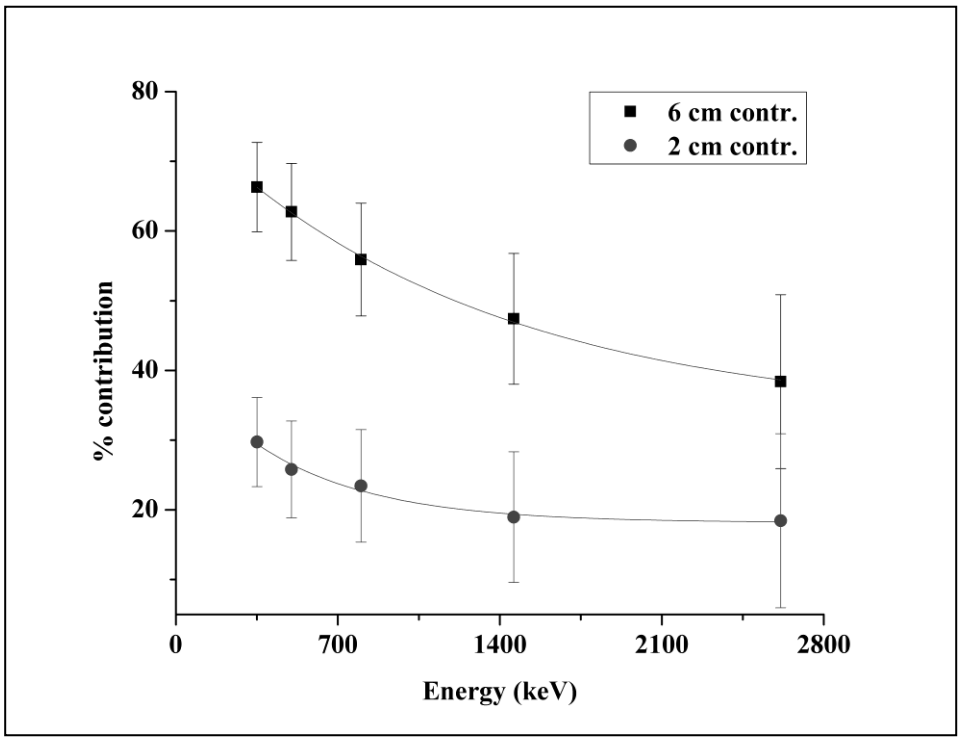

Fig. 5.6: Contribution ($\boldsymbol{cont._{u.l.}}$ %) of the events generated in the seawater, in cases where the detector is placed few cm above the seabed (namely at distances of 2 and 6 cm).

Table 5.1: MC simulation results for the contribution of different water layers ($cont._{u.l.}$), calculated as the ratio of the detected counts in the upper water layer to the whole volume (hemisphere), for different γ-ray energies.

Energy (keV)	upper layer (u. l.) of 6 cm	upper layer (u. l.) of 2 cm
	$cont._{u.l.}$%	**$cont._{u.l.}$%**
351	66	30
500	63	26
800	56	23
1460	47	19
2614	38	18

Therefore it was demonstrated that, when the detector is positioned even at small distances above the seabed, Eq. 5.4 is altered due to the enhanced contribution from the seawater, $\boldsymbol{Cont._w'}$. The correction in the net counting rate, $\boldsymbol{Netcps_s}$ is performed as follows (Eq. 5.5 and Eq. 5.6):

$$\boldsymbol{Netcps_s} = \boldsymbol{Ncps_s} - \left(\boldsymbol{1/2} \cdot \boldsymbol{Ncps_w}\right) - \boldsymbol{cont._{u.l.}} \cdot \left(\boldsymbol{1/2} \cdot \boldsymbol{Ncps_w}\right) \quad (5.5)$$

$$\boldsymbol{Cont._w'} = \left(\boldsymbol{1/2} \cdot \boldsymbol{Ncps_w}\right) - \boldsymbol{cont._{u.l.}} \cdot \left(\boldsymbol{1/2} \cdot \boldsymbol{Ncps_w}\right) \quad (5.6)$$

and combining with Eq. 5.4 the final result is obtained (Eq. 5.7):

$$\boldsymbol{Netcps_s} = \boldsymbol{Ncps_s} - \boldsymbol{Cont._w} - \boldsymbol{cont._{u.l.}} \cdot \boldsymbol{Cont._w} \quad (5.7)$$

After the proper subtraction of the ambient background contribution, the derivation of the activity concentrations is straightforward for all the radionuclides evident in the spectrum acquired on the seabed, as the detection efficiency is derived as a function of energy. The activity concentrations $\boldsymbol{A}$ are deduced by calculating the net counting rate of the observed peaks in the sediment spectrum, $\boldsymbol{Netcps_s}$, covering the full spectral range, as shown in the following Eq. 5.8:

$$\boldsymbol{A} = \frac{\boldsymbol{Netcps_s}}{\boldsymbol{I_\gamma} \cdot \boldsymbol{\varepsilon_V}} \quad (5.8)$$

where $\boldsymbol{I_\gamma}$ is the γ-ray emission probability of the studied γ-ray calculated from the decay scheme of the corresponding radionuclide and $\boldsymbol{\varepsilon_V}$, is the full energy peak efficiency for the measurement on the seabed estimated via MC simulations (MCNP5), over a wide energy range (from 238 to 2614 keV), taking into account the physical characteristics of the sediment matrix and the geometry details of the measurement setup in the specific application. The importance of the effect of these values to the detection efficiency is thoroughly described in the following section 5.3.

The accuracy of these measurements is governed by the statistical uncertainty of the MC simulations (below 10%) and the counting rate (ranging from 3-15% for acquisition times of about 3h) depending on the energy and the activity concentrations in the studied

area. Systematic uncertainties may arise both from inaccuracies related to the measurement setup and to the sediment properties, as the MC setup relies on these values. These uncertainties can be eliminated if an accurate determination of distance and the orthogonal positioning of the detector are ensured. The effect of all these factors on the detection efficiency is thoroughly described in the following section 5.3.

5.3. Sensitivity study of the detection efficiency

An extensive theoretical study was performed via MC simulations, to systematically examine the influence of the detector efficiency to alterations in the sediment physical properties (composition, wet density, water content, inhomogeneous radionuclide distributions) and measurement setup (distance from the seabed, inclined seabed), considering different scenarios. The methodology described in section 5.2.2 was utilized to derive the efficiency estimations in each case.

The main objective of these MC simulations was to determine the contribution of each parameter to the efficiency alterations and therefore its significance. Therefore all the aforementioned parameters were initially examined independently, by changing the values of each studied parameter, while at the same time keeping all the other parameters in fixed values.

5.3.1. Effect of sediment physical properties

The first studied parameter aimed at detecting possible alterations of the estimated efficiency values attributed to the presence of differences in the composition of the sediment matrices. It is known that the major sediment matrix element concentrations greatly vary depending on the sediment origin (terrigenous, biogenous, magmatic origin, etc.). In order to study the effect of differences in the chemical composition of the sediment matrix to the detection efficiency, three different sediment matrices (sed 1, sed 2, sed 3) were considered. A fixed number of typical compounds found in marine sediments were utilized and the fractional abundances (wt. %) of the four most prominent compounds changed each time, namely Si, Fe, Al and Ca oxides, as shown in Table 5.2. The differences concerning the calculated effective atomic number, Z_{eff}, referred here as the weighted Z according to the atomic weight of each constituent and the fractional abundance of each compound ranged from 11.7 (sed 1) to 15.2 (sed3), respectively. The selected matrices are

based on data found in the literature (Andr_15; Bass_14; Zaab_14), although the fractional abundances of each compound, are normalized according to the water content values (0.15). The different matrices were inserted in the code, while the other sediment parameters were kept fixed during the simulations (water content of 0.15, with 2.1 g/cc wet density).

Table 5.2: Sediment matrices (based on data found in the literature) utilized in the detection efficiency sensitivity study.

	Major elements (wt. %)											**w.c. (%)**
	Al_2O_3	**SiO_2**	**P_2O_5**	**K_2O**	**CaO**	**TiO_2**	**Fe_2O_3**	**Na_2O**	**MgO**	**SO_3**	**MnO**	**H_2O**
sed 1	2.6	55.3	0.1	0.6	8.5	0.3	8.4	1.2	2.6	5.1	0.5	15.0
sed 2	8.5	14.5	0.1	2.4	34.0	0.3	17.0	1.2	2.6	4.0	0.5	15.0
sed 3	8.5	8.5	0.1	2.6	26.4	0.8	31.5	1.2	2.6	1.7	1.2	15.0
sed 4	6.5	43.2	0.04	0.3	13.9	0.5	9.4	0.8	6.7	3.5	0.1	15.0

The runs were performed in ‘touch’ geometry (0 cm distance between the detector and the seabed), in order to derive the maximum differences that could be observed, as it was considered that, when the distance between the seabed and the detector rises the differences would be smeared out. The differences of the effective atomic number Z_{eff} mostly affected the lower energy part. The higher difference was observed between the matrices sed1 and sed3 and exhibited a value of 30% (at 238 keV), which dropped with increasing energy to less than 5% (at 1460 keV). Nevertheless, in extreme cases (sediments with a high Fe, Ti, or Mn content) the differences of the effective atomic number Z_{eff} and thus the differences in the detection efficiency could be enhanced even for the high energy part region.

The influence of the detection efficiency to the sediment pore size alterations, regarded as alterations in the water content of the sediment matrix, was studied as in the next step. Three different water content values were considered, covering the range from 10% to 50%. The runs were performed in ‘touch’ geometry and as before, all the other sediment parameters were kept constant, using a typical wet density of 1.9 g/cc and the chemical composition given at Table 5.2 (sed 1). The estimated efficiency results considering different water content values, namely 0.1, 0.25 and 0.5 are presented in Fig. 5.7. The maximum relative differences were found to be 8% between the values 0.1 and 0.5 and could be attributed to the variations of the calculated sediment effective atomic number Z_{eff} caused by the addition of water (low Z material). The variations of the sediment water content can be considered as an extreme case of sediment composition variation, since a very light element (hydrogen) is added to the sediment matrix. The only quantity that actually changes in MC simulations is the fractional abundance of the sediment constituents

with respect to the water content values (fractional abundance of the H_2O compound). The results showed that the whole energy part is affected, but in different ways, due to the differences in the photon interactions with respect to the Z_{eff} of the material and each γ-ray energy (Bhand_93).

The effect of the alterations of the water content values to the detection efficiency seems to be tolerable (below 8%), although the differences depend on the texture of the sediment matrix that greatly varies in different environments. Therefore, the differences in the sediment composition would be insignificant, at least for the medium (500-1200 keV) and high parts of the energy region (1200-2600 keV), and comparable to the experimental (counting rate) uncertainties.

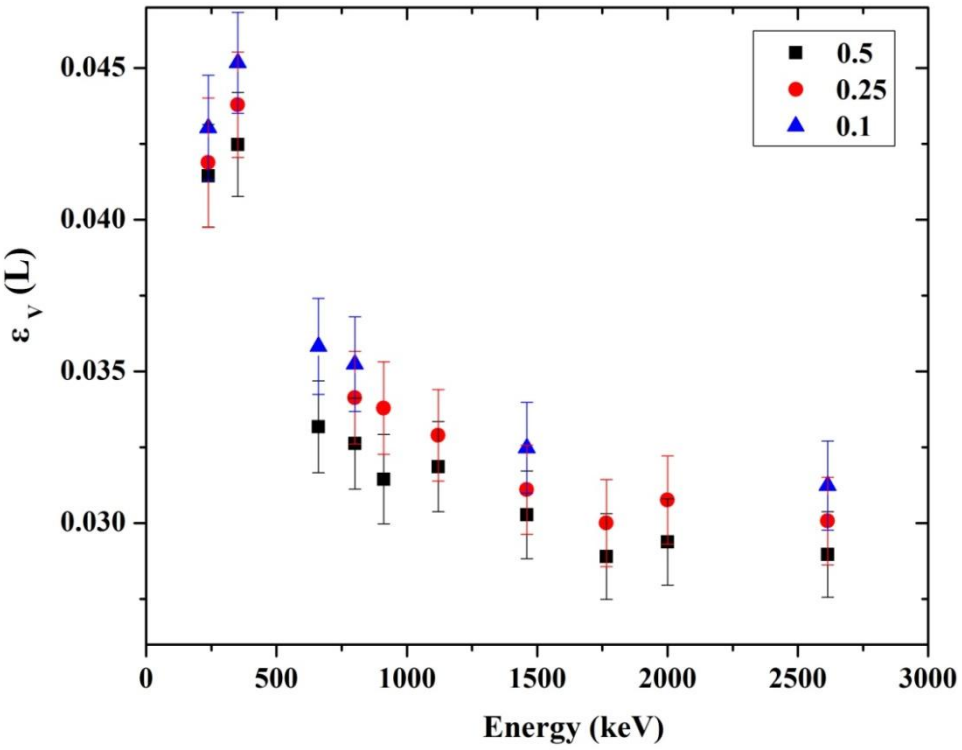

Fig. 5.7: MC results concerning the sensitivity of the detection efficiency, ε_v, to different sediment water content values, namely 0.1, 0.25 and 0.5.

The influence of the sediment wet density was examined for a wide range of the values found in sediments, namely from 1.1 g/cc to 2.6 g/cc. The water content was fixed at 0.26 in all the involved simulations and the chemical composition of the sediment matrix, sed 4 (Table 5.2), was utilized. The simulations were performed again in 'touch' geometry. The results are shown in Fig. 5.8. A constant decrease of the efficiency values was observed,

over the whole energy range, as the sediment wet density value increased, which matched, within uncertainties (below 5%), the exact ratio of the wet density values.

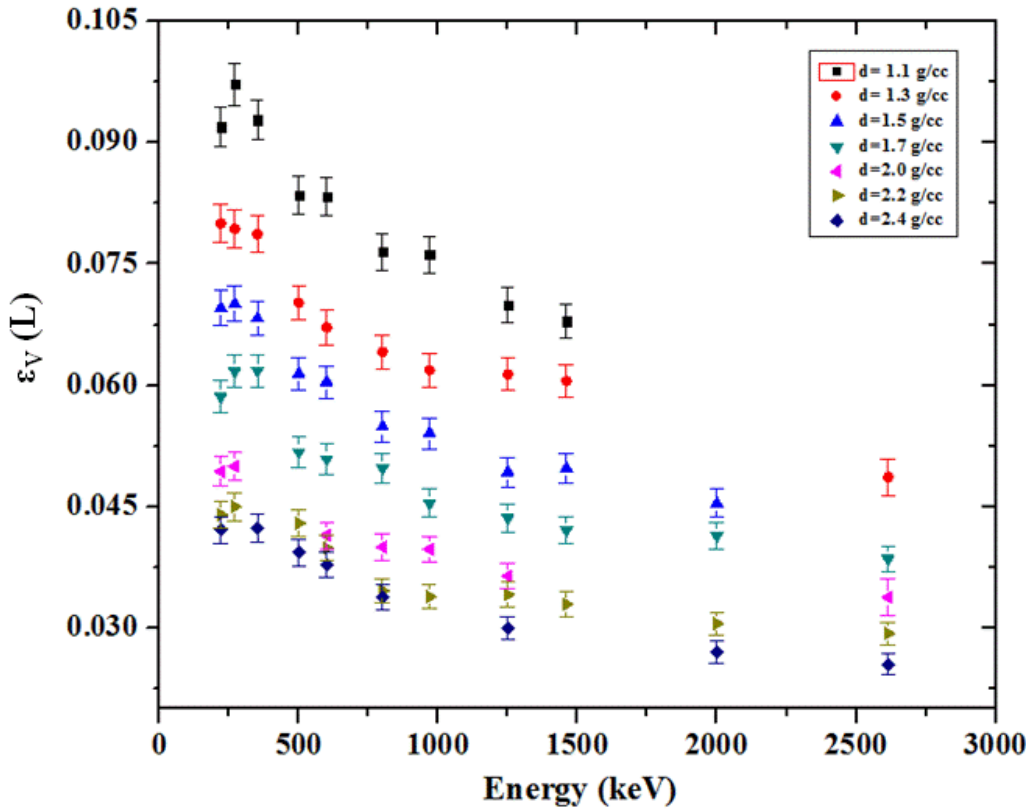

Fig. 5.8: MC results concerning the sensitivity of the detection efficiency, $\boldsymbol{\varepsilon_V}$ (in units of L), to different wet density values, ranging from 1.1 g/cc to 2.4 g/cc.

Similar simulations were repeated for wet density values of 1.4 g/cc and 1.9g/cc assuming the detector was positioned at a distance of 2 cm above the seabed. For these runs a constant water content value of 0.2 was considered along with the sediment matrix (sed 1) described in Table 5.2. The efficiency results for the two sediment matrices exhibiting different wet density values are presented in Fig. 5. 9.

An approximately constant decrease (a factor of ~1.4) of the efficiency values, over the whole energy range, as the sediment wet density value increased, which again approximated the exact ratio of the density values. This observation renders this parameter invariant of the distance of the detector from the seabed. The importance of this result lies in the fact that the wet density is an easy to handle parameter, since the efficiency values can be directly derived from one density value to another, just by multiplying with the ratio of the two values.

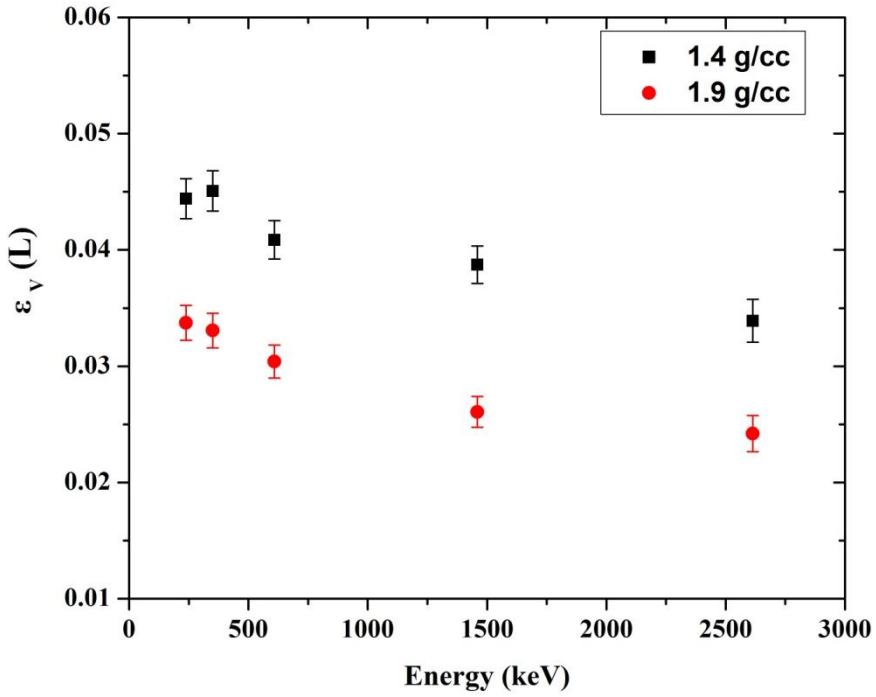

Fig. 5.9: MC results concerning the sensitivity of the detection efficiency, ε_v, (in units of L), to 2 different wet density values, namely 1.4 g/cc and 1.9 g/cc.

5.3.2. Effect of the measurement setup geometrical properties

Two different scenarios were considered regarding the geometrical properties of the setup for measurements on the seabed. The parameters examined were a) the effect in the detection efficiency when the distance between the detector window and the sediment surface rises and b) the effect when the detector is placed at varying angles with respect to the seabed surface. The simulations were performed assuming a specific sediment matrix (sed1) of 1.9 g/cc wet density and 0.2 water content. The influence of the detection efficiency to the detector position above the seabed was studied separately for 4 different distances namely, 0.5 cm, 2.5 cm, 4.5 cm and 6 cm above the seabed. The results are depicted in Fig. 5.10, in the energy range from 238 to 2614 keV.

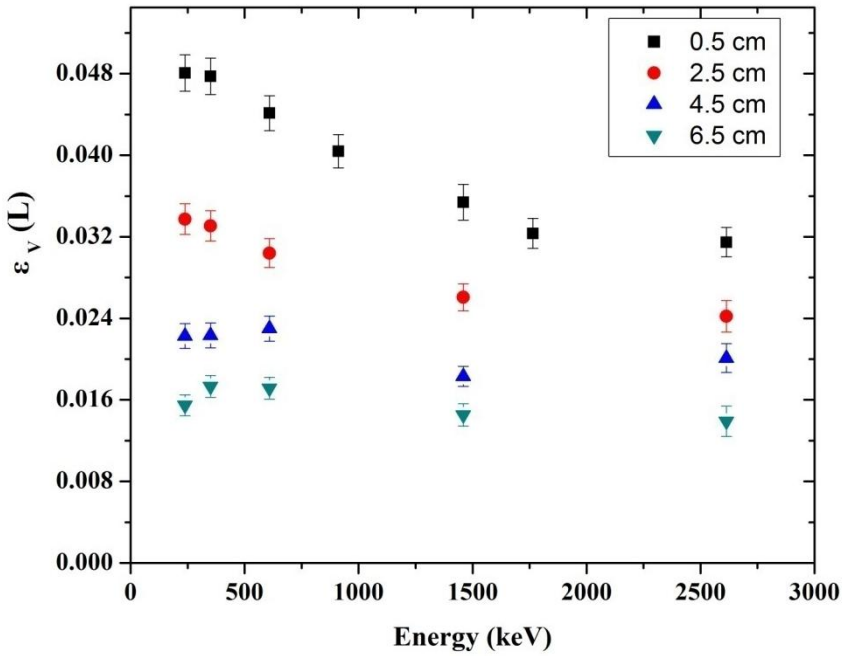

Fig. 5.10: MC results showing the sensitivity of the detection efficiency, ε_v (in units of L), to different distances (in units of cm) of the detector position above the seabed.

The efficiency values drastically drop, over the whole energy range, as the distance of the detector from the seabed rises, as the photons are attenuated in the intermediate seawater layer. In more detail, the efficiency values drop by a factor of 1.4 (238 keV) to 1.3 (2614 keV) when the distance changes from 0.5 cm to 2.5 cm and from 4.5 cm to 6 cm above the seabed and a higher decrease is observed, by a factor of 1.5 (238 keV) to 1.2 (2614 keV) when the distance increases from 2.5 cm to 4.5 cm above the seabed. The greatest differences were observed, as expected, between the estimated values at 0.5 cm and 6 cm. The higher calculated difference was a factor of 3.1 (238 keV), decreasing to a value of 2.2 (2614 keV) for the corresponding efficiency values.

These particular setups, in which the detector is positioned a few cm above the seabed are preferable in cases of an unknown seabed morphology (e.g. rocky seabed), to protect the whole measuring system from damage as well as to diminish the solid angle differences in cases of a non-parallel positioning of the system with respect to the sediment surface.This is the most crucial parameter affecting the detection efficiency, and thus, during an experiment, precise measurements of the distance between the detector and the seabed are required in order to obtain accurate and reliable results.

In the second scenario, MC runs were additionally performed considering deviations from the orthogonal positioning of the detector with respect to the seabed. Although the

distance between the sediment-water interface and the detector window is fixed prior to the measurement, in cases of an inclined orientation of the detector relative to the seafloor the efficiency values might slightly change, due to the change in the measurement solid angle. The MC results showed that the effect to the detection efficiency by placing the detector in up to 5 degrees with respect to the seabed was small, for over the whole studied energy range (Fig. 5.11).

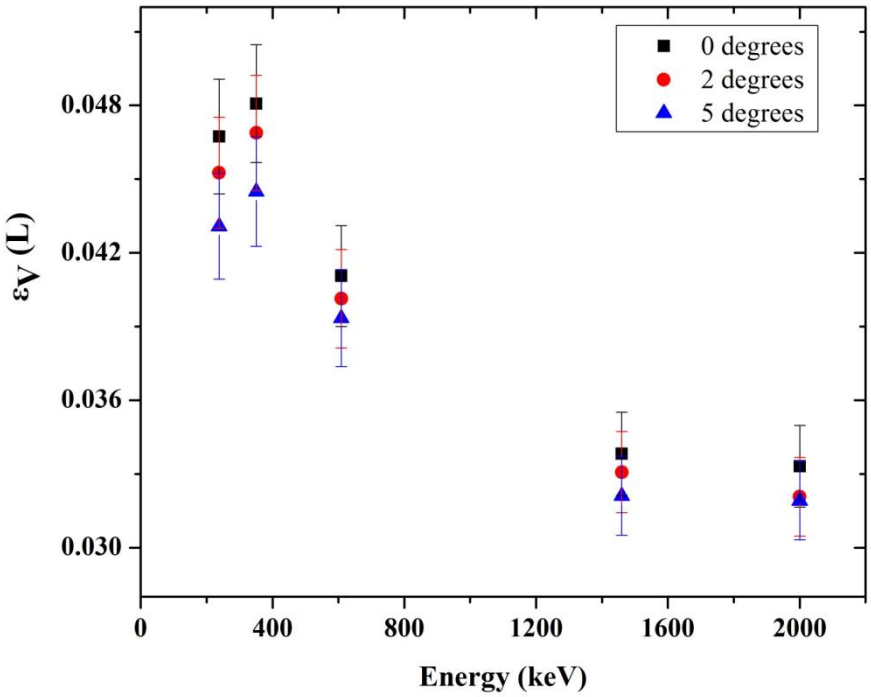

Fig. 5.11: MC results showing the sensitivity of the detection efficiency, ε_v (in units of L), to the deviation of the detector position from orthogonality (for 2 and 5 degrees) with respect to the seabed surface.

The observed differences were found lower than 10% for 2 or 5 degrees, while in the extreme case of an inclination by 10 degrees, differences up to 16% (for the γ-ray energy at 352 keV) were observed, although this last scenario is considered highly unlikely to occur.

5.3.3. Effect of inhomogeneous vertical profiles

In all the aforementioned calculations a homogeneous source within the effective volume in which the γ-rays are generated was considered. Nevertheless, in real environments inhomogeneous depth profiles regarding the activity concentrations have

been reported. In such cases the detection efficiency would be affected, since the detector records events arriving from large depths up to approximately 2 m (depending on the γ-ray energy, the sediment properties and the geometrical setup). The effect of the detection efficiency in cases of inhomogeneous activity-depth profiles is studied considering three different scenarios. In all the runs, the effective volume was separated in slices of 10cm. In each slice a different number of primaries (Norm. N/V (L^{-1})) were generated, with respect to the volume of each slice, in order to simulate the inhomogeneous profiles. In the first scenario a linear regression (linear_d) with depth is assumed, (Fig. 5.12 panel b). In the second scenario an exponential decrease (exp_d) is considered and in the third case an exponential growth (exp_i) is considered instead. The differences of the detection efficiency in cases of inhomogeneous profiles are summarized in Fig. 5.12.

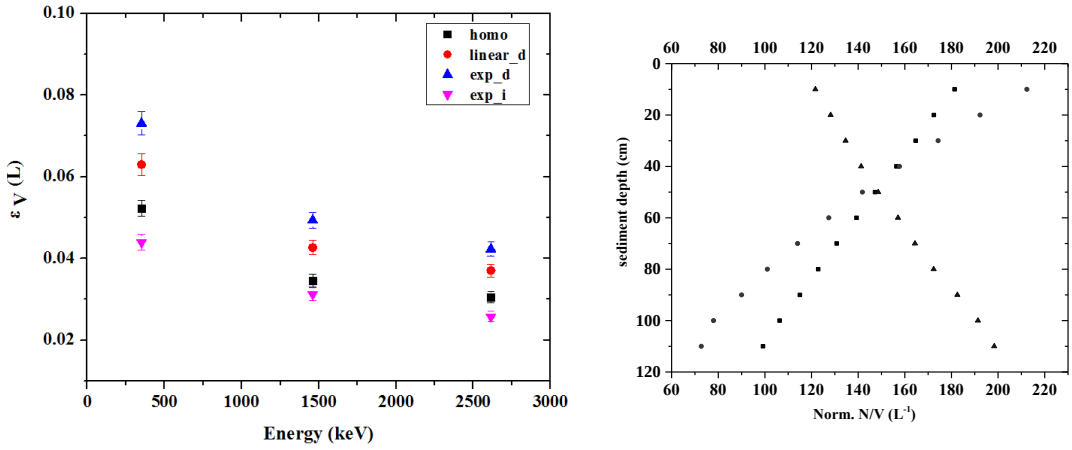

Fig. 5.12: MC results (left) of the detection efficiency, ε_v, (in units of L), in cases of inhomogeneous radionuclide profiles within the seabed (right).

The maximum differences (ratio) were found for the vertical decrease (exp_d). The efficiency results are given in Table 5.3 along with the values of the maximum observed differences that were calculated as the ratios of the estimated efficiency values of the depth profile, exp_d, to the ones with inhomogeneous distributions (homo), in the energy range 351 keV to 2614 keV. An additional simulation was performed assuming an inhomogeneous vertical profile regarding the sediment wet density (linear decrease from 2.0 g/cc to 1.7 g/cc). In this case the observed differences over the whole energy range (351-2614 keV) were negligible and within the estimated MC statistical uncertainties (8%).

Table 5.3: MC estimated efficiency results in different cases of inhomogeneous vertical profiles within the seabed.

	linear_d	exp_d	exp_i	homo	
Energy (keV)		**Detection efficiency**		ε_v **(L)**	**ratio**
351	0.0630(4)	0.0731(4)	0.0439(4)	0.0523(4)	1.40 ±0.07
1460	0.0174(4)	0.0201(4)	0.0127(4)	0.0345 (5)	1.43 ±0.08
2614	0.0370(4)	0.0423(4)	0.0257 (5)	0.0306(5)	1.38±0.09

5.3.4. MC based efficiency calibration for different sediment matrices

Regarding the influence of the sediment physical parameters to the detection efficiency the sediment wet density seems to be the major contributor to the observed variations in the detector efficiency, and to a lesser extend the water content, while differences in the composition of the sediment matrix affect mostly the low energy part. The wet density and porosity values are correlated in the real environment, as described in section 2.2.1 (Chapter II). To incorporate this correlation in the MC derived efficiency results, additional simulations were performed taking into account the dependence of the sediment wet density to the porosity.

Although the water content and the wet density values are strongly correlated, the utilized linear equations to fit the data (Hamil_70) exhibit large variations in different environments (sampling sites),as found in the literature (Komi_11; Hamil_70; Nafe_57).The reason is that both the constant values vary, from 1.0-1.04 g/cc for the seawater density and typically from 2.1-2.9 g/cc for the mean grain density although higher and lower grain density values have also been reported in different studies (Komi_11; Gealy_07; Hamil_70; Nafe_57). This means that sediment matrices exhibiting similar wet density values may exhibit very different porosity values. To demonstrate this, in Fig. 5.13 the wet density is given with respect to the different porosity values calculated using Eq. 2.3 and assuming different grain density values ranging from 1.7 to 3.16 g/cc.

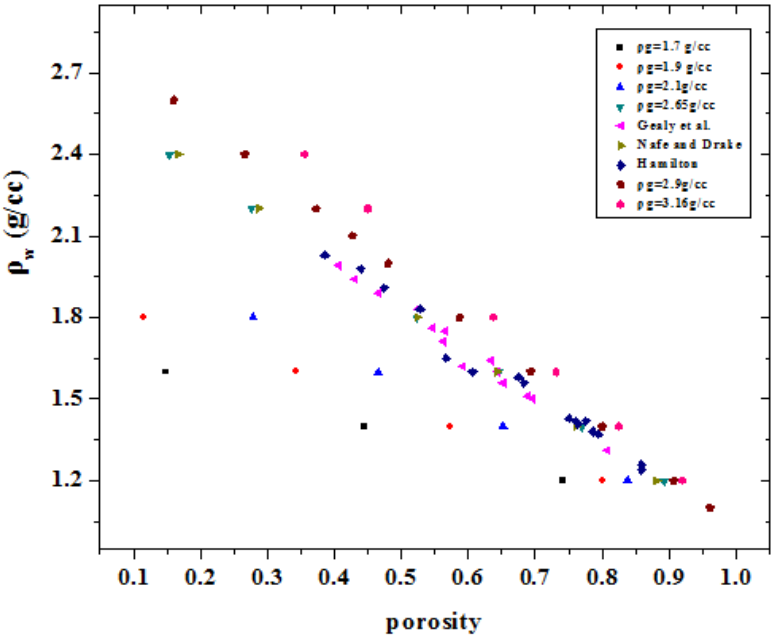

Fig. 5.13: Linear dependence of the sediment wet density (ρ_w) to porosities, with respect to different grain density values (ρ_g =1.7 -3.16 g/cc)).

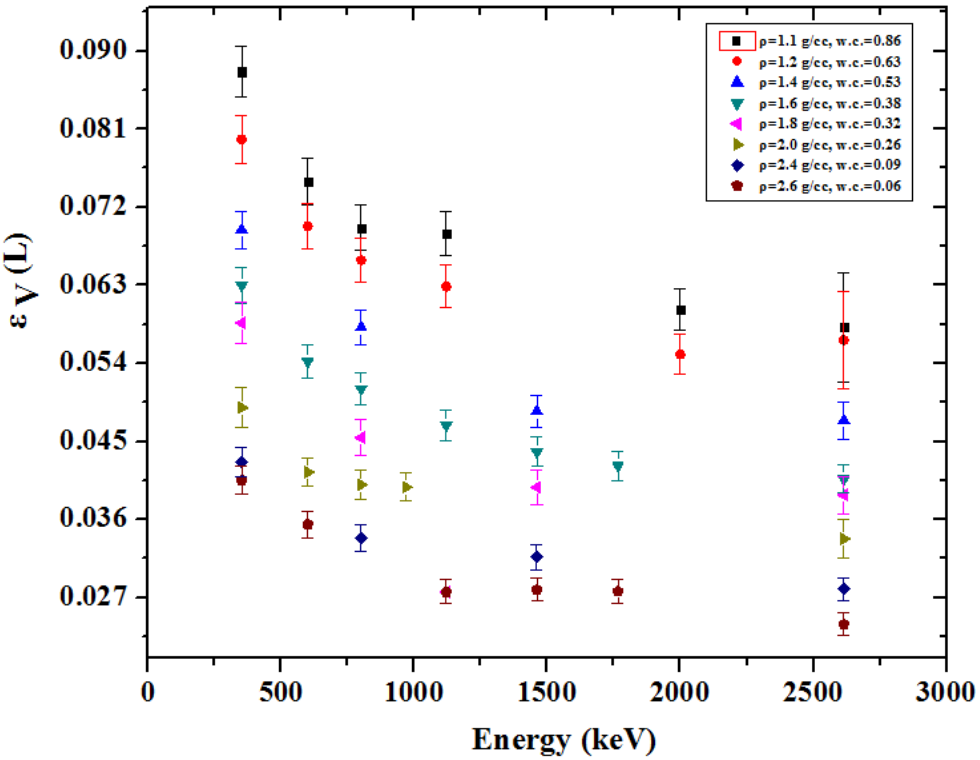

Fig. 5.14: MC results concerning the detection efficiency, ε_v, (in L), for correlated wet density (ρ) and water content (w.c.) values found in marine sediments.

Using this data, the mean porosity values (using typical grain density (ρ_g) ranges

from 2.1-2.9 g/cc) with respect to the corresponding wet densities were calculated, converted to water content values and subsequently inserted in the MC simulations that were performed for wet density values ranging from 1.1 to 2.6 g/cc, covering in this way the typical values found in marine sediments (although in extreme cases wet densities with values below 1 g/cc can be found). The simulations were performed assuming the detector is placed exactly on the seabed ('touch' geometry). The same sediment composition (sed 4) was utilized in all the simulations however the fractional abundances were altered in each run, according to the water content value. The estimated efficiency results, ε_V, along with the (%) statistical uncertainty of the simulations are given in Fig. 5.14 in the energy range of interest, namely from 351 to 2600 keV.

Table 5.4: MC efficiency results considering different coupled density and water content values.

Energy (keV)	MC **detection efficiency** ε_V **(L)**							
	ρ= 1.1g/cc w.c.= 0.86	***ρ= 1.2g/cc w.c.= 0.63***	***ρ= 1.4g/cc w.c.= 0.53***	***ρ= 1.6g/cc w.c.= 0.38***	***ρ= 1.8g/cc w.c.= 0.32***	***ρ= 2.0g/cc w.c.= 0.26***	***ρ= 2.4g/cc w.c.= 0.09***	***ρ= 2.6g/cc w.c.= 0.06***
351	0.0876 (3)	0.0798 (3)	0.0694 (2)	0.0630 (2)	0.0587 (2)	0.0489 (2)	0.0426 (2)	0.0405 (2)
600	0.0750 (3)	0.0698 (3)	-	0.0542 (2)	-	0.0415(2)	-	0.0355 (2)
800	0.0696 (3)	-	0.0581(2)	0.0511(2)	0.0454 (2)	0.0400 (2)	0.0339 (2)	-
1120	0.0690 (3)	0.0659 (3)	-	0.0469 (2)	0.0277(2)	-	-	-
969	-	-	-	-	-	0.0397 (2)	-	-
1460.8	-	0.0629 (3)	0.0485 (2)	0.0438 (2)	0.0397(2)	-	0.0317 (2)	0.0277 (2)
1765	0.0602 (3)	-	-	0.0422 (2)	-	-	-	0.0279 (2)
2000	0.0582 (3)	0.0551 (3)	-	0.0407 (2)	-	-	-	0.0277 (2)
2614	-	0.0567 (3)	0.0474 (2)	0.0407 (2)	0.0388 (2)	0.0338 (2)	0.0280 (2)	0.0239 (2)

The results of the wet density, the porosity and the calculated water content values that were incorporated in the simulations are given in Table 5.4 along with the efficiency results. The obtained results are similar with those obtained in section 5.3.2 (Fig. 5.8). These results can be used to extract the activity concentrations (from γ-rays emitted in the energy range from 600 to 2614 keV) using the developed methodology, in any marine environment as they cover a wide range of the actual values found in marine sediments. The proposed *in situ* methodology requires the prior determination of the aforementioned parameters and the accuracy of the activity concentrations relies on the precision of these measured values (water content, wet density). In order to obtain accurate results for radionuclides detected in the low-energy part region (below 400 keV) the sediment matrix

composition should also be determined; if not however, the results are still expected to be valid with a systematic uncertainty not exceeding 40%.

5.4. Experimental evaluation of the MC results

5.4.1. Experimental efficiency calibration methodology

In the adopted approach a post-survey experimental calculation of the detection (full energy peak) efficiency was performed using both the field data (*in situ* acquired spectra) and complementary laboratory activity concentration measurements on sediment samples collected from the deployment sites. The experimental detection efficiency values were derived in the energy range 300 to 2614 keV by analyzing the prominent peaks in the *in situ* spectra using Eq. 5.9:

$$\boldsymbol{\varepsilon_V} = \frac{\boldsymbol{Netcps_s}^{\boldsymbol{E,i}}}{\boldsymbol{I_\gamma}^{\boldsymbol{E,i}} \cdot \boldsymbol{A_{ref}}^{\boldsymbol{i}}} \tag{5.9}$$

where $\boldsymbol{\varepsilon_V}$(given in units of L), is the full energy peak efficiency for the seabed measurement setup at a specific γ-ray energy, $\boldsymbol{Netcps_s}^{\boldsymbol{E,i}}$ (given in units of s^{-1}) is the counting rate calculated using Eq. 5.4 at the peak of the corresponding γ-ray energy ($\boldsymbol{E}$), Iγ is the corresponding γ-ray emission probability (number of emitted γ-rays of the specific energy per decay) given from the decay scheme of the radionuclide $\boldsymbol{i}$, and $\boldsymbol{A_{ref}}$ (given in units of Bq/L), is the activity concentration of the corresponding radionuclide $\boldsymbol{i}$. The quantity, $\boldsymbol{Netcps_s}^{\boldsymbol{E,i}}$**,** refers to the net counting rate of a peak **(**clear of contributions attributed to the Compton continuum and to radionuclides in the seawater column**)** present in the spectrum acquired on the seabed. As a result, by performing a peak analysis in the acquired spectra covering the full spectral range, the photopeak efficiency was deduced as a function of energy. The only unknown values in Eq. 5.9 were the activity concentrations of the radionuclides present on the seabed ($\boldsymbol{A_{ref}}$).

These values were determined by complementary measurements in the laboratory, by means of a high resolution system (HPGe detector) on the collected sediment samples. The results are implemented in the efficiency calculations as reference values, $\boldsymbol{A_{ref}}$. The collected samples were transported to the laboratory where they were further processed, as

the samples should closely match the physical and the geometry properties of the reference materials used to calibrate the detector, such as the sample holder diameter, height, chemical composition and density (IAEA_10a) and stored prior the measurement (progeny ingrowth). In order to enhance as much as possible the homogeneity among the samples (reduced grain sizes and density (dry) values close to 1 g/cc), as large differences could affect the detector efficiency, the samples were oven-dried, and additionally grinded (final grain sizes ranging from 0-2mm) prior to the measurement. Nevertheless in cases of large differentiations among the sediment samples, concerning their density and composition, appropriate corrections were applied using the software EFFTRAN (Vid_05). Details on the setup and the results of the laboratory measurements are given in section 5.4.2.3.

Although the activity concentrations present in the initial (untreated) sediment samples are preserved during this process the density values of the final sediment sample is highly reduced (due to the removal of water). Therefore, the radionuclides present in the initial sediment sample are concentrated in a considerable smaller mass and additionally the sediment characteristics (density, water content) differ between the two measurements (lab, *in situ*). To exclude the differences in the samples density (wet, dry) in the final activity concentrations, $\boldsymbol{A_{ref}}$, the results are derived in units of Bq/L by dividing the calculated activity concentrations (derived in units of Bq) with the volume of the sample holder (capacity of 0.0654 L). In this way, the effect of the sediment density (reflecting the mass differences) between the two measurements to the activity concentration results is eliminated, while the results can be converted to units of Bq/kg (wet weight) by multiplying with the wet density. Therefore, the activity concentrations derived in the laboratory were calculated in units of Bq/L, by dividing the calculated count rates with the sediment sample holder volume (0.0654 L). As a result, the experimental efficiency values are derived in units of volume (L) and the comparison with the corresponding MC data is straightforward. Moreover, a direct comparison with the activity concentrations found in the seawater column can be performed as both values are given in Bq/L.

The aforementioned Eq. 5.9 is valid when only a single radionuclide contributes to the peak formation and was thus utilized for the analysis of the peaks at 2614 keV (^{208}Tl γ-ray with 99% intensity) and at 1764.5 keV (convolution of ^{214}Bi γ-rays at 1730 with and at 1764.5 with intensities 5% and 15%). However, due to the moderate resolution of the detection system (NaI(Tl)), many peaks appearing in the acquired spectra consist of multiple overlapping photopeaks attributed to different radionuclides (Fig. 5.16). At the

present study, overlapping photopeaks are found at the energies of 351 keV (^{214}Pb and ^{228}Ac photopeaks), 609 keV (^{214}Bi ^{137}Cs and ^{208}Tl photopeaks), 940 keV (^{228}Ac and ^{214}Bi photopeaks) and 1460 keV (^{40}K and ^{214}Bi photopeaks). These peaks cannot be analyzed directly or de-convoluted. This means that the net recorded counts in specific regions (peaks) in the spectrum are a summation of events related to the decay of different radionuclides. Thus, for these cases, an appropriate modification in Eq. 5.9 is required in order to achieve accurate efficiency calculation values as described below for the peak at 1460 keV. A similar analysis is followed in all the calculations where convoluted photopeaks appear.

In order to derive the efficiency value at 1460 keV, taking into account that events from both the radionuclides ^{214}Bi and ^{40}K contribute to this peak, while the contribution of ^{40}K is most prominent, Eq. 5.9 is reformed to Eq. 5.10 by substituting the corresponding values:

$$\boldsymbol{\varepsilon_V} = \frac{\boldsymbol{Netcps_s}}{\boldsymbol{{I_\gamma}^{E,i}.\,{A_{ref}}^i}} = \frac{\boldsymbol{Ncps_{s|40K} - Cont._w}}{\boldsymbol{{I_\gamma}^{1460,40K}.A_{ref|40K}}} \tag{5.10}$$

$$\boldsymbol{Ncps_{s|40K} = Ncps_s - Ncps_{s|214Bi}} \tag{5.11}$$

The quantity $\boldsymbol{Ncps_{s|40K}}$, represents the net counting rate of the full energy peak (photopeak) of the ^{40}K decay. This quantity is equal to the difference of the count rate attributed to ^{214}Bi γ-rays (energies between 1377 – 1583 keV, total intensity of 11.6%) from the quantity $\boldsymbol{Ncps_s}$, which is the total net counting rate measured at the 1460 keV peak, as shown in Eq.5.11. By substituting, the obtained result is shown in Eq. 5.12:

$$\boldsymbol{\varepsilon_V} = \frac{\boldsymbol{Ncps_s - Ncps_{s|214Bi} - Cont._w}}{\boldsymbol{{I_\gamma}'.A_{ref|40K}}} \tag{5.12}$$

The quantity, $\boldsymbol{Ncps_{s|214Bi}}$, represents the counting rate attributed to the full energy peak of ^{214}Bi. Although this quantity is unknown, following the same approach, and assuming the same $\boldsymbol{\varepsilon_v}$ value in the specified energy range (1377-1583 keV) the desired quantity $\boldsymbol{\varepsilon_V}$ at the energy 1460 keV could be also calculated exploiting the ^{214}Bi photopeaks, using Eq. 5.13:

$$\boldsymbol{\varepsilon_V} = \frac{\boldsymbol{Netcps_s}}{\boldsymbol{I_\gamma{}^i \cdot A_{ref}{}^i}} = \frac{\boldsymbol{Ncps_{s|214Bi} - Cont._w}}{\boldsymbol{I_\gamma{}'' \cdot A_{ref|214Bi}}} \quad (5.13)$$

$$\boldsymbol{Ncps_{s|214Bi} = \varepsilon_V \cdot I''_\gamma \cdot A_{ref|214Bi} + Cont._w} \quad (5.14)$$

By substituting the derived quantity of Eq. 5.14 in Eq. 5.12 the final result is obtained (Eq. 5.16):

$$\boldsymbol{\varepsilon_V} = \frac{\boldsymbol{Ncps_{s|214Bi} + Ncps_{s|214Bi} - Cont._w}}{\boldsymbol{I_\gamma{}^{E,i} \cdot A_{ref}{}^i}} \quad (5.15)$$

$$\boldsymbol{\varepsilon_V} = \frac{\boldsymbol{Netcps_s}}{\boldsymbol{I_\gamma{}' \cdot A_{ref|40K} + I_\gamma{}'' \cdot A_{ref|214Bi}}} \quad (5.16)$$

where $\boldsymbol{A_{ref|40K}}$, $\boldsymbol{A_{ref|214Bi}}$ are the activity concentrations for the involved radionuclides, which are determined on the processed sediment samples in the laboratory. This final equation, in which all the quantities can be calculated, is invariant to the number of radionuclides contributing to the peak and can be generalized for n radionuclides as follows:

$$\boldsymbol{\varepsilon_V} = \frac{\boldsymbol{Netcps_s}}{\boldsymbol{\sum I_\gamma{}^i \cdot A_{ref}{}^i}} \quad (5.17)$$

5.4.2. Application in four test cases

In situ γ-ray measurements on the seabed were performed by deploying the system KATERINA in four different areas, in order to experimentally determine the detection efficiency with respect to the variations of the measurement conditions (different setup, seabed geomorphology) and compare with the corresponding theoretical (MC) results. In addition to the differences of the seabed geomorphology, inhomogeneous radionuclide vertical distributions were found in site 3, while in a different case (site 4), ground water discharges (SGD) through the seabed (diffusive source) were also present. Such environments are widely studied as SGD constitute an important factor in the sustainable management of coastal fresh water aquifers and a significant pathway for material transfer

between the land and the sea. The implementation of the described methodology in the specific site aimed at testing the applicability limits of the adopted technique in dynamic environments (SGD presence), as such environments are widely studied. In all the studied sites the system was deployed to acquire two spectra, on the seabed and in the seawater in the same location. These spectra were obtained in order to be utilized in the post-survey efficiency calibration. For this purpose sediment samples were also collected at the end of the measurements from the same sites using the grabbing technique in sites 2 and 4, or sediment corers in sites 1 and 3, respectively.

5.4.2.1. Fieldwork results

In situ measurements were performed in different regions of the Mediterranean and the Black Sea in order to conduct an experimental calibration of the detection system KATERINA for measurements on the seabed. The studied sites are depicted in Fig. 5.15. This section starts with a brief description of each studied area, followed by a detailed description of the measurements that were performed on the field in each case along with the obtained results.

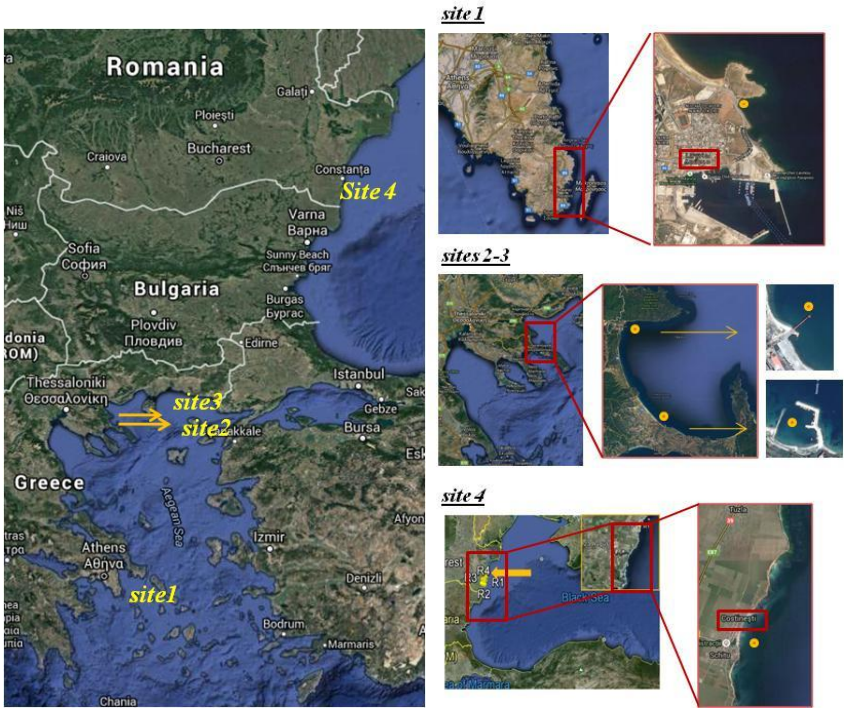

Fig. 5.15: Position of the four deployments of the detection system KATERINA.

The first measurement was carried out at Thorikos bay (site1, 37°71'94.19"N, 24°06'32.00"E), near Lavrion port (Greece). This area is of particular interest as intense

mining activities have been conducted in the past, exploiting silver and lead from carbonate or sulphide ores, for more than 2700 years. The field work included the deployment of the detector to acquire measurements on the seabed and in the seawater column (background measurement) on the same spot. The acquisition times for the measurement on the seabed and in the seawater were ~17 h (61517 s) and (somewhat prolonged to ensure good statistics) ~20 h (70750 s), respectively. For the first measurement the detector was placed 2 cm above the seabed. This distance was selected, so that the NaI(Tl) crystal lay in close contact with the sediment (Fig. 5.1 (a)), while for the measurement in the seawater (Fig. 5.1 (b)) the system was placed well above the seabed (distance between the crystal and the water-sediment interface >1.5 m), to eliminate any contribution to the spectrum from radionuclides present in the sediment. The seawater depth in this site was 4.5 m. The acquired spectra normalized in time are depicted in Fig. 5.16.

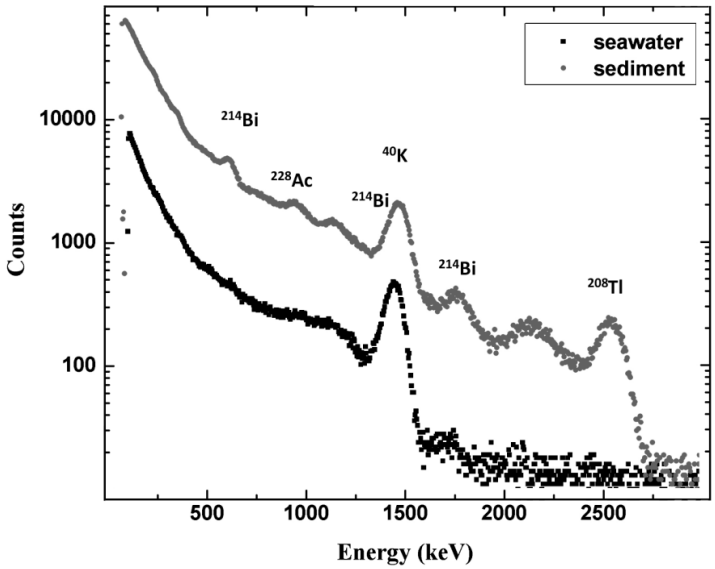

Fig. 5.16: The acquired spectra, normalized in time (61517 sec), of the *in situ* measurements at Lavrion region (site 1).

Following the in situ measurements, a sediment core (maximum depth of 60 cm) was collected from the position of the deployments (site 1), to derive the activity concentrations by supplementary γ-ray spectroscopy in the laboratory and use the results for the experimental efficiency calibration. A similar operation plan was followed in all the studied sites.

A second experimental calibration was conducted in a selected site (site 2, 40°23.900'N, 23°53.102'E) in the port of Ierissos which is located in Chalkidiki Peninsula, northern Greece (Fig. 5.17). Ierissos is a densely populated area and a touristic attraction

during summer months. For this measurement the system was placed ~3 cm above the seabed. The seawater depth in the site was 4m. The acquisition time was ~2 h (7200 s) and ~12 h (33197 s), for the measurements on the seabed and in the seawater, respectively. The two acquired spectra are presented together in Fig. 5.17 normalized to the same acquisition time. Additionally a sediment sample (of 6.5 cm maximum depth) was collected from the deployment site after the end of the measurement.

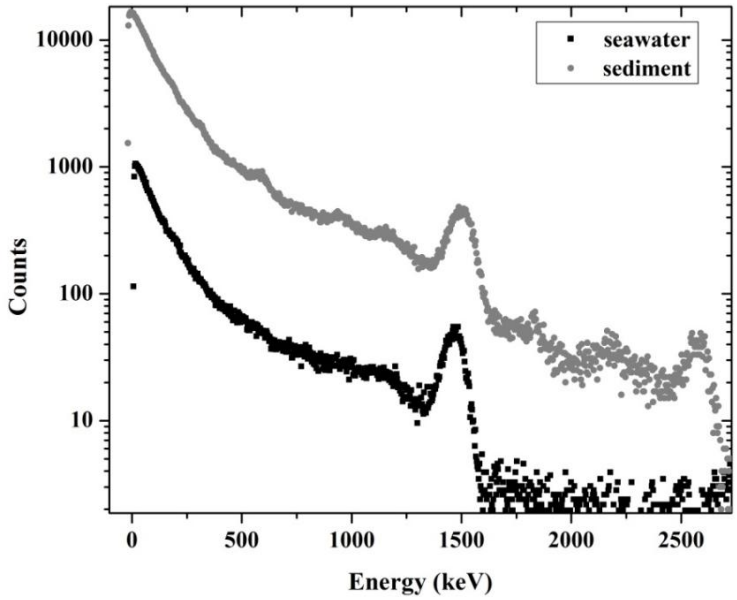

Fig. 5.17: The acquired spectra, normalized in time (7200 sec), of the *in situ* measurements at Ierissos region (site 2).

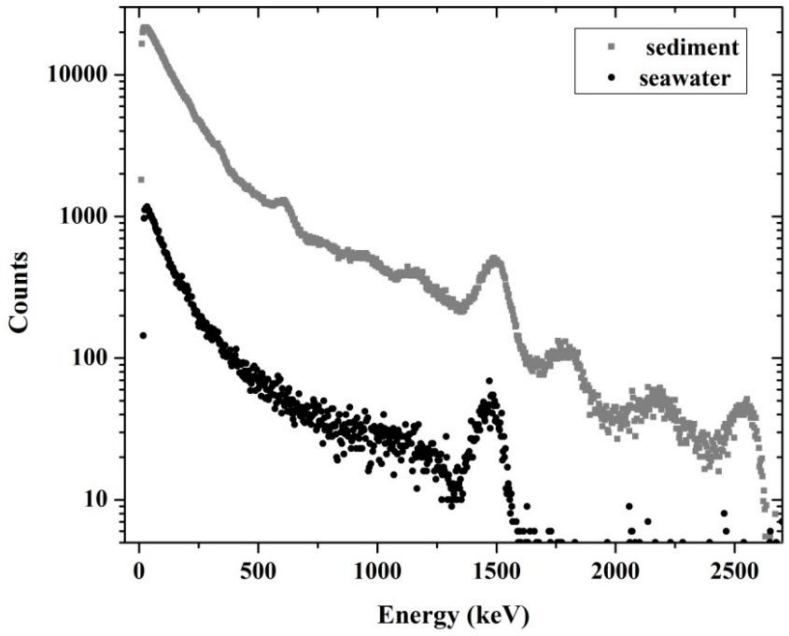

Fig. 5.18: The acquired spectra, normalized in time (6587 sec), of the *in situ* measurements at Stratoni region (site 3).

At a distance of 13 km from the port of Ierissos, an operating gold mining industry (Stratoni area) is located. A site near the shore and close to the load-pier area of the industry (site 3, 40°30.930'N 023°49.870'E) was selected to perform an additional experimental calibration. In the third calibration point (site 3) an acquisition time of ~3 h (10800 s) and ~1 h (6587 s) was utilized for the measurements on the seabed and in the seawater, respectively. The same geometrical setup was utilized while the water depth in this site was ~10 m. The normalized in time spectra are depicted together in Fig. 5.18. Following the *in situ* measurements, two sediment cores (maximum depth of 60 cm) were collected from the position of the deployments.

The fourth deployment was held at Costinesti (site 4, 43°56'44.46"N, 28°38'4.73"E), a closed bay located on the Black Sea shore near the Mangalia port (Romania).The acquisition time were ~16 h (57585 s) and ~20 h (72125 s) for the measurement on the seabed and in the seawater, respectively. The normalized in time spectra are depicted together in Fig. 5.19.

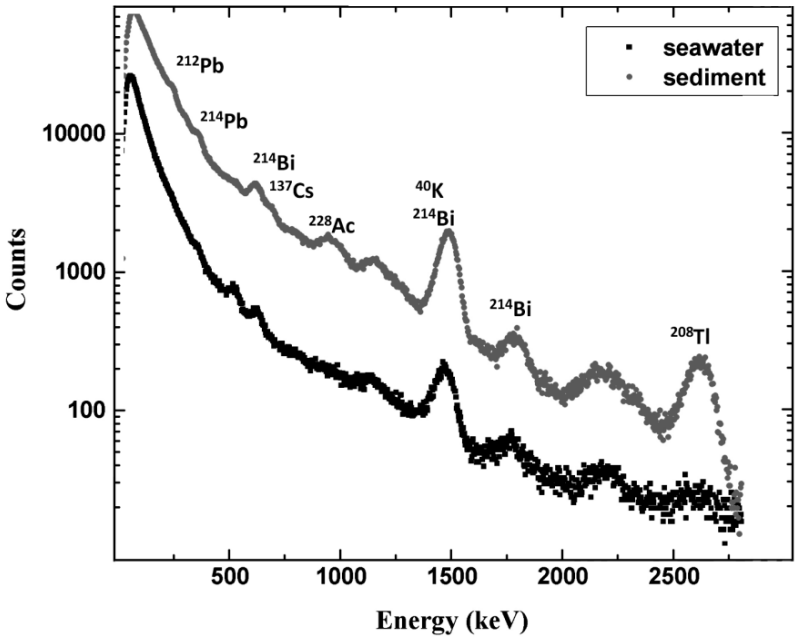

Fig. 5.19: The acquired spectra, normalized in time (57585sec), of the *in situ* measurements at Costinesti region (site 4).

An observed difference compared to the other sites, was the appearance of peaks attributed to ^{222}Rn progenies (^{214}Bi peaks at 609 keV, 1764.5 keV and 2200 keV) in the spectrum acquired in the seawater column. Regarding the spectrum acquired on the seabed, intense peaks were observed attributed to radionuclides of the ^{238}U (^{214}Pb at 351 keV and

^{214}Bi at 609, 1120, 1765, 2200 keV) series and ^{232}Th series (^{212}Pb at 238 keV, ^{228}Ac at 911 and 968 keV, ^{208}Tl at 2614 keV) as well as to the artificial radionuclide ^{137}Cs (661.67 keV peak), which was not observed in the other areas of study (Mediterranean Sea). For the measurement on the seabed the detector was placed at ~6 cm above the sediment. For the measurement in the seawater column the system was placed at ~1.2 m above the seabed. The seawater depth in this site was approximately 2 m. In the end, of the *in situ* measurements, a sediment sample (collected from a 15 cm deep sediment layer) was again collected using a grabber, from the deployment site 4, to be analysed in the laboratory.

The software SPECTRW (Kalf_2016) was utilized for the analysis of all the acquired spectra (*in situ*, laboratory). A screenshot of the utilized software is presented in Fig. 5.20. The analysis was performed as described in section 5.2.3.

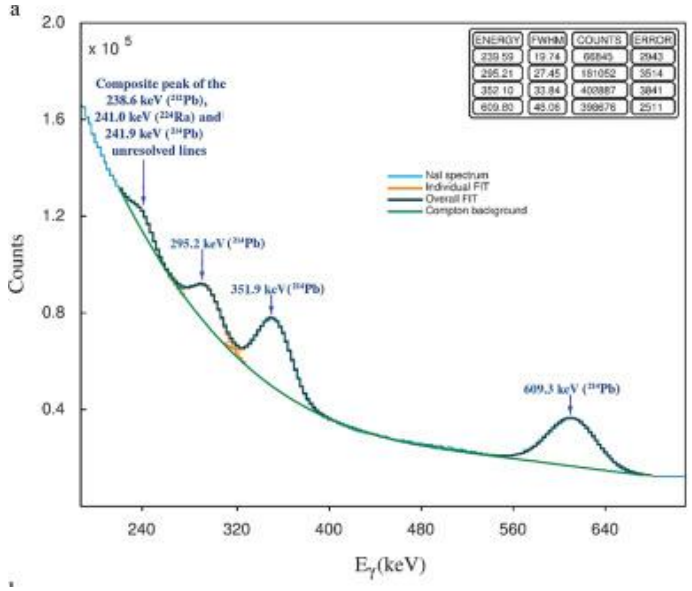

Fig. 5.20: The SPECTRW software implemented for the spectra (*in situ*, laboratory) analysis (Kalf_2016).

The results of the analysis, including the calculated counting rates of the intense peaks appearing in the acquired spectra on the seabed ($\boldsymbol{Ncps_i}$) and in the seawater column ($\boldsymbol{Ncps_i}$) for all the studied sites (1-4) along with the radionuclides contributing to each peak are summarized in Table 5.5. Additionally, the total % contribution of the background measurement (radionuclides present in the seawater) to the spectra acquired on the seabed, $\boldsymbol{R_{w/s}}$, is calculated as the ratio of the total counting rate $\boldsymbol{Cont._w'}$, contributing to the measurement on the seabed, to the total net counting rate $\boldsymbol{Ncps_s}$, in all the analysed peaks. The results are presented in Table 5.5, and are calculated in percentage (%) according to Eq. 5.18:

$$R_{w/s} = \frac{Cont._w{}'}{Ncps_s} \quad (5.18)$$

Table 5.5: Analysis results of the *in situ* spectra using the SPECTRW software.

Sites	1			2			3			4		
Energy	$Ncps_s$	$Ncps_w$	$R_{w/s}$	$Ncps_s$	$Ncps_w$	$R_{w/s}$	$Ncps_s$	$Ncps_w$	$R_{w/s}$	$Ncps_s$	$Ncps_w$	$R_{w/s}$
(keV)	(s^{-1})	(s^{-1})	%	(s^{-1})	(s^{-1})	%	(s^{-1})	(s^{-1})	%	(s^{-1})		%
238	0.30 (10)	-	-	-	-	-	-	-	-	0.37 (6)	-	-
351	0.23 (7)	-	-	0.43 (10)	-	-	1.11(7)	0.04 (32)	1	0.23 (6)	0.054(13)	12
609	0.38 (5)	-	-	0.46 (8)	-	-	1.30 (5)	-	-	0.36 (4)	0.044(10)	6
911	0.11 (5)	0.005 (6)	3	* 0.32 (9)	-	-	* 0.36 (13)	-	-	0.16 (5)	0.005(16)	1
968	0.06 (4)	0.003 (3)	3	-	-	-	-	-	-	0.10 (8)	0.002(15)	1
1120	0.11 (6)	-	-	-	-	-	-	-	-	0.11 (6)	0.028(10)	13
1461	0.78 (3)	0.259 (3)	17	0.11 (1)	0.23 (3)	7	2.10 (1)	0.27 (11)	1	0.80 (3)	0.102(3)	6
1765	0.11 (8)	0.031 (5)	14	0.15 (7)	0.008 (14)	5	0.40 (5)	-	-	0.09 (4)	0.032(5)	17
2614	0.12 (3)	0.013 (3)	6	0.43 (5)	-	-	0.23 (3)	-	-	0.15 (3)	0.013(3)	4

* Calculated assuming a total intensity of 0.416 for the two 228Ac photopeaks at 911 and 969 keV.

5.4.2.2. Determination of physical properties

The water content and the wet/dry density were determined by mass and volume calculations (Flemm_00). In more detail the wet density was calculated using the measured water content and dry density of the samples and moreover it was additionally calculated (by mass and volume measurements) immediately after the collection, when possible. To derive the sediment water content the water mass was calculated by weighting the sediment sample before and after oven-drying (for at least for 48h). The major component analysis (Al, Ca, Fe, K, Mg, Na, P, Si, and Ti oxides) was performed by the specialized HCMR staff using the X-Ray Fluorescence (XRF) technique, on a Phillips PW-2400 wavelength dispersive X-Ray spectrometer, calibrated for marine sediment fused beads (Karag_05).

Table 5.6: Measured sediment properties for all the studied sites (1-4), including the major element analysis results, dry/wet density (ρ_d, ρ_w) and the water content (w.c.) values.

				Major elements (wt. %)										
	w.c. %	ρ_w g/cc	ρ_d g/cc	Al_2O_3	SiO_2	P_2O_5	K_2O	CaO	TiO_2	Fe_2O_3	Na_2O	MgO	SO_3	MnO
site 1*	0.26	1.88 (4)	1.57 (4)	3.49	28.34	0.1	0.69	19.91	0.3	14.55	1.12	1.96	11.34	0.78
site 2	0.21	2.2 (3)	1.74 (3)	9.68	65.04	0.09	2.16	8.65	0.28	1.01	2.89	1.25	0.07	0.04
site 3*	0.35	1.71 (5)	1.26 (3)	10.78	48.31	0.16	2.93	9.96	0.35	13.39	1.88	3.52	7.73	0.98
site 4	0.6	1.78 (6)	1.12 (3)	12.17	60.83	0.23	2.11	5.86	0.83	4.38	1.69	1.97	0.82	0.06

The major element analysis results given in percentage (wt. %) are summarized in Table 5.6 for all the studied sites (1-4) along with the dry/wet density (ρ_d,ρ_w) and the water content (w.c.) values. Concerning the major element analysis, the values accompanied with *, are referring to the calculated mean values in the two collected sediment cores at sites 1 (26 samples, maximum depth of 60 cm) and 3 (27 samples, maximum depth of 27 cm), while the detailed results for each sample from the specific sites 1 and 3 are given in Appendix C and D, respectively. This data was incorporated in the simulations after the appropriate modifications regarding the major element results, in order to include the measured water content values.

The obtained results for the core collected at Lavrion area (site 1), showed a rich in Fe_2O_3 sediment (mean value of 15%). The SiO_2 values ranged from 25% to 34% and relatively high CaO values were also observed ranging from 15% to 30%, while MnO values ranged from 0.1% to 1.2%. The results are comparable with values found in literature (Baz_11). Concerning the other studied sediment properties, the sediment mean water content (w.c.) was calculated at 0.26 resulting in a wet sediment density of 1.88 g/cc (calculated from the measured w.c. and dry density) and the grain separation measurement (dry sieving) which was performed in separately collected sediment samples in the same area, showed a sediment mostly consisting of sand (70-90%).

The obtained results for the sediment sample collected at Ierissos immediately after the deployment, showed a SiO_2value of 65% and lower CaO and Fe_2O_3values of 8.65% and 1.01%, respectively. The MnO calculated value of 0.04% was the lowest observed value in all the studied sites. A higher wet density of 2.2 g/cc and lower w.c. of 0.21 were calculated in the collected sediment sample. In the sediment core collected from the site of the deployment point near the load-pied of the mine at Stratoni (site 3), the calculated values ranged from 36% to 46%, 8% to 13% and from 7% to 14% for SiO_2, Fe_2O_3 and CaO respectively. The MnO calculated values ranged from 0.5% to 1.4%. Regarding Al_2O_3, TiO_2 and K_2O_5concentrations, similar values were found in both sites.

In the area of Costinesti (site 4), the results showed a marine sediment consisting mostly of SiO_2 (60.8%), of Al_2O_3 (12.2%), and to a lesser extend of CaO (5.8%) and Fe_2O_3 (4.4%), while higher values of TiO2 (0.8%) and MnO (0.06%) were observed. These results are comparable with values found in soils in the same area (Tugu_16). Concerning the other studied sediment properties, the obtained results showed a well-sorted sediment material (97% of the sediment mass exhibited grain sizes < 63 μm) exhibiting a wet density of 1.78 g/cc and a high water content (60%).

5.4.2.3. Laboratory activity concentration results

The utilized detection systems were already calibrated for environmental sediment/soil samples. The detection efficiency of the utilized HPGe detectors for sediment analyses was determined using four reference sources containing the radionuclides $^{152/154}$Eu, ^{40}K, ^{210}Pb and ^{238}U series progenies (Elef_15; Tsab_11; Tsab_07). The first utilized reference material consisted of a diluted liquid radioactive source of $^{152/154}$Eu (emitted γ-rays in the energy range 121-1408 keV) with a known activity concentration, dripped into an inert material (talcum powder), homogenized and enclosed in the same sample holder used for the sediment samples. The second source was a grinded KCl source (^{40}K abundance of 0.0117% in natural K) constructed in the laboratory, while the ^{210}Pb source was constructed from a sediment reference source (IAEA-385) in the framework of an inter-calibration exercise among different gamma-spectroscopy laboratories (IAEA_05b; Elef_15). These two sources were utilized in order to determine the efficiency value at the energy of 1460.8 keV and 45 keV, respectively. The last utilized reference source constituted a NORM source and was constructed from a rock sample (tectonized/reprocessed organic-rich phosphatized limestone), collected at the region of Perivleptos in Epirus (NW Greece). This reference source was utilized in order to determine the efficiency at 1764.5 keV (emitted γ-ray from ^{214}Bi with 15% intensity). The sample was grinded and enclosed in the sediments sample holder. In this case silicone was used to ensure an airtight enclosure in order to rule out ^{222}Rn losses. The ^{238}U activity concentration was determined with high accuracy by utilizing different methods (Tzif_14) and the secular equilibrium among the progenies of ^{238}U was preserved. The calibration procedure was periodically repeated to ensure that the detection efficiency was not affected from possible random instabilities of the detection system and the utilized electronic units.

Due to differences among the calibrated sources regarding their physical properties (density, chemical composition), the efficiency transfer software EFFTRAN was implemented to correct the efficiency values that were experimentally calculated using peak integration (SPECTRW software) and Eq. 2.9. The differences in the chemical composition and density between the calibrated sources and the sediment samples were also incorporated in the calculations. Therefore the final results of the detection efficiency were derived in the energy range from 121 keV to 1765 keV and were normalized to the measured density (dry density after pulverization) of the studied sediment samples. Moreover the software EFFTRAN was utilized to correct the results for TCS effects that

were present in the spectra acquired by measuring both the calibrated sources ($^{152/154}$Eu) and the sediment samples, especially as the latter were placed in close contact with the detector window.

The measurement acquisition time was set to 24 h per sample and additionally ambient background measurements were performed every 3 days. The counting rate of the background measurement was subtracted from the foreground measurement in order to determine the activity concentrations of the radionuclides present in the sediment samples. In Fig. 5.21 two typical acquired spectra (foreground and background) are depicted together (acq. time 86400 s). The measurements were performed for a total number of 41 samples. The collected sediment core in Lavrion (site 1), was divided into 26 samples using a 2cm slice, while only 21 samples were measured. In Ierissos (site2) and Costinesti regions, a single sediment sample was collected from the deployment sites. Both sediment cores exhibited compression during the collection (a higher compression degree was present in the core selected from site 3, as the sediment consisted mostly from silt material), resulting in a smaller sediment core size. The following analysis did not include corrections for this compression. The collected sediment cores (2) in Stratoni (site 3), were divided into a total of 27 samples, each using a 1 cm slice (the sediment samples of the two cores were jointed together).

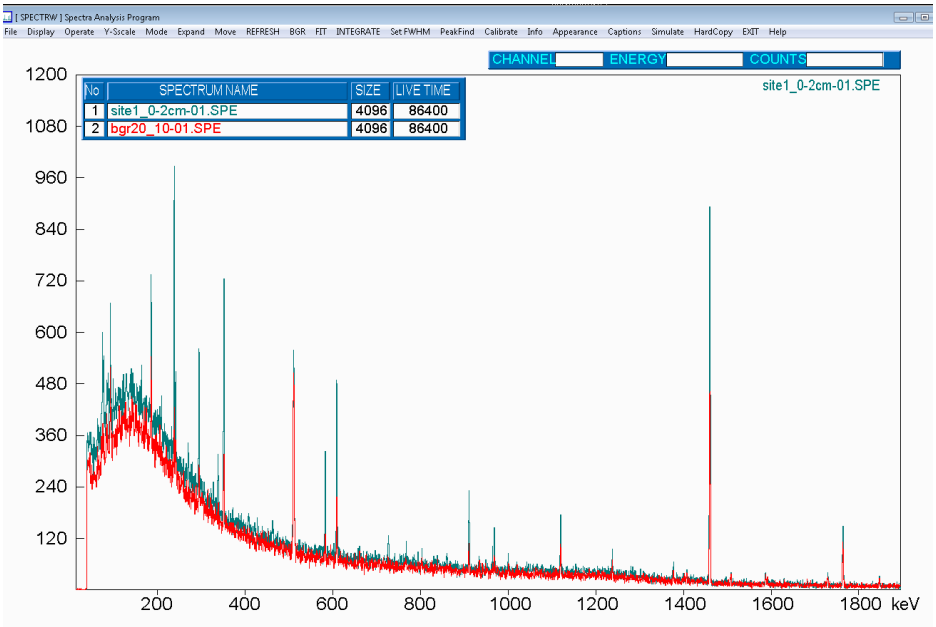

Fig. 5.21: Two typical acquired spectra (foreground and background) using the stationary HPGe detector (model GC5021).

The two collected cores (one from each site) are depicted together in Fig. 5.22 along with a picture of the dried sediment samples.The obtained results of the activity concentration measurements in units of Bq/kg (dry weight) on the collected samples from sites 2 and 4, are given in Table 5.7, for the naturally occurring radionuclides, that were also analyzed with the *in situ* method, and for the artificial ^{137}Cs. The depth profiles for ^{214}Bi (^{238}U series), ^{208}Tl (^{232}Th) and ^{40}K in Bq/kg (dry weight) for all the measured samples (2 cm slices), are presented in Fig. 5.23 for site 1. The results are grouped per radioactive series, as small differences were observed among the different radionuclides of the same series.

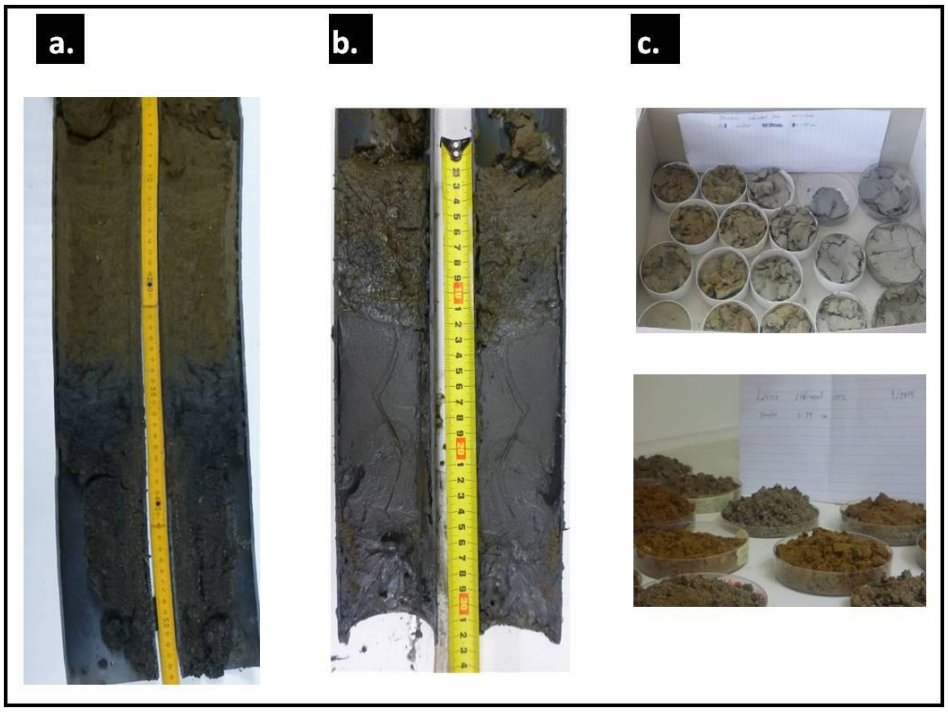

Fig. 5.22: The two collected cores from sites 1 (panel a) and 3 (panel b) along with a photo of the oven-dried sediment samples from the cores (panel c).

Regarding the second sediment core collected at the Stratoni region inhomogeneous depth profiles were observed for all the detected radionuclides. The depth profiles in Bq/kg (dry weight) for all the samples, are given in Fig. 5.24 for site 3, for ^{214}Bi, ^{208}Tl, ^{40}K and ^{137}Cs. In the same figure the depth profiles of the calculated wet density (using the dry density and the water content values) and the dry density of the grinded samples are given. Enhanced values were observed for the ^{238}U series radionuclides, ranging from 60 to 100 Bq/kg. The ^{232}Th series radionuclides ranged from 20 to 32 Bq/kg. The ^{40}K activity concentration values ranged from 500 to 680 Bq/kg. The depth profile of ^{137}Cs (observed

peaks at 5.5 and 12.5 cm) gave a sedimentation rate of 2.19 $g \cdot y^{-1}$, which is in excellent agreement with the values found in literature (Peris_89).

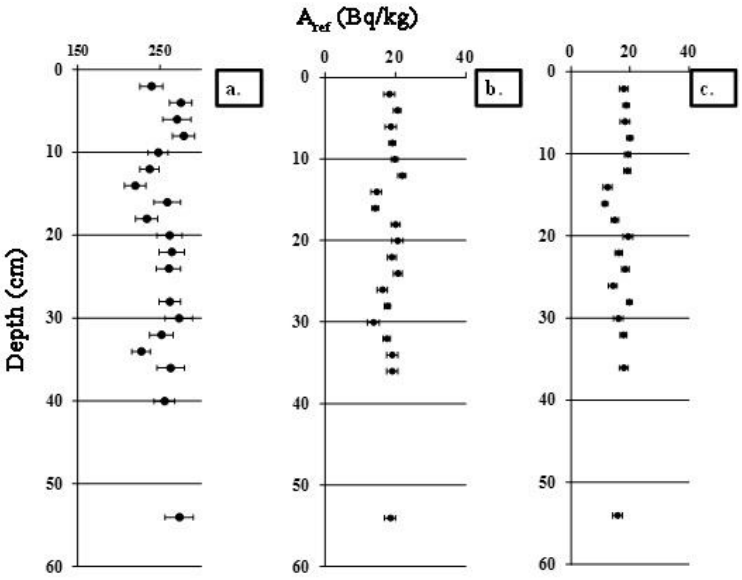

Fig. 5.23: Activity concentration vertical profiles, for ^{40}K (panel a) and the two natural series ^{238}U (panel b), ^{232}Th (panel c), for site 1 (Lavrion area) (Andr_16a).

Table 5.7: Laboratory results of the activity concentrations from sediment samples collected at the deployment sites 2 (Ierissos region) and 4 (Costinesti region).

Sites		**Site 2**			**Site 4**	
Series		Activity concentration measurements A_{ref} (dry weight)				
		Energy (keV)	A_{ref}(Bq/kg)	± %	A_{ref}(Bq/kg)	± %
^{238}U	^{210}Pb *	46.5	-	-	60	20
	^{214}Bi	1764.5	18	10	22	7
	^{214}Pb	351.9	19	6	21	6
^{232}Th	^{228}Ac	911.2	15	9	39	8
	^{208}Tl	583.2	15	8	34	5
	^{212}Bi	727.3	20	18	33	21
	^{212}Pb	238.6	19	6	40	6
-	^{40}K	1460.8	509	5	561	6
-	^{137}Cs	661.7	0.62	26	24	6

* *detector model (Ortec GEM-FX8530P4)*

The measured activity concentrations (Bq/kg dry weight) in all sites, were found below/within the world average reference values (UNSC_00) indicating a negligible radiological impact to the environment. The higher (approximately 2 orders of magnitude) activity concentration value regarding the radionuclide ^{137}Cs at site 4 (Costinesti) can be justified from the location of this site (Black Sea).

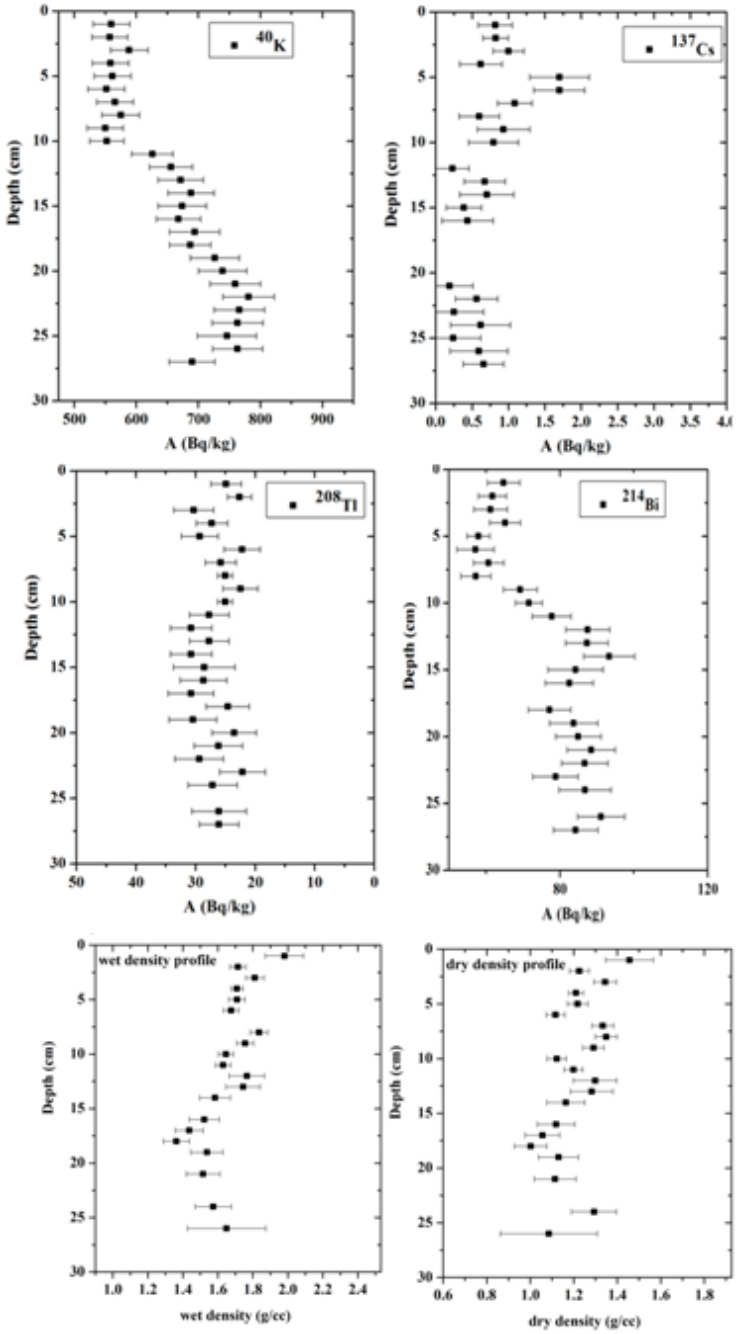

Fig. 5.24: Activity concentration vertical profiles, for ^{14}Bi, ^{208}Tl, ^{40}K and ^{137}Cs, for site 3 (Stratoni), along with the depth profiles of the calculated wet density (using the dry density and the water content values) and the dry density of the grinded samples.

5.4.2.4. Efficiency calibration comparison results

MC estimations for the efficiency values in the real test cases were subsequently performed, in order to compare with the corresponding experimental results. In order to perform a valid comparison, all the crucial parameters that affect the detection efficiency should be explicitly included in the simulation. For this purpose, the experimentally determined sediment properties namely the wet density, the water content and the composition (major elements analysis)were properly inserted in the simulations along with the exact geometrical properties of the deployment setup. The methodology presented in section 2.1 was followed, in all the simulation runs, and the MC efficiency values were derived, for all the test cases, over a broad γ-ray energy range from 238 keV to 2614 keV. The final MC model for the configuration setup (site 1 to 4) consisted of the detector model, the photon generator volume source and the surrounding environment.

The comparison between the experimentally and the theoretically derived efficiency values in the energy range from 351 keV to 2614 keV are presented in Figs. 5.25 to Fig. 5.28 for the measurements at Lavrion (site1), Ierissos port (site 2), Stratoni (site 3) and Costinesti (site 4), respectively.

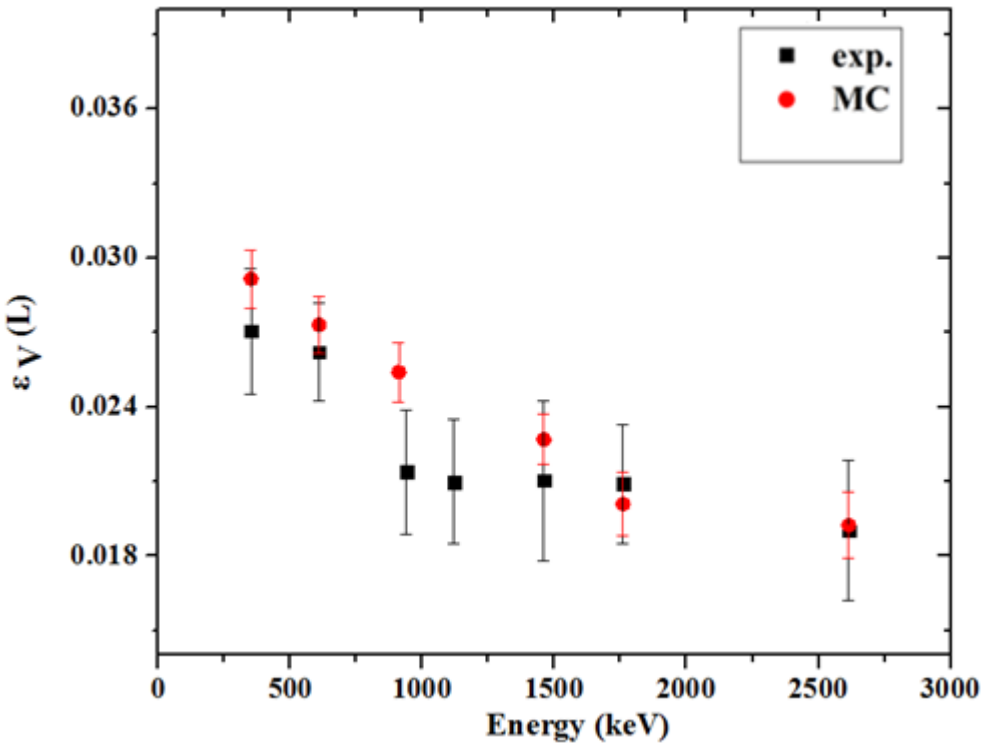

Fig. 5.25: Comparison between the experimental (exp.) and the MC values, of the detection efficiency (ε_V (L)) for site 1.

The MC results obtained implementing these complex geometries were found to be in satisfactory agreement with the experimentally derived efficiency values for the measurements at Lavrion (site 1), as shown in Fig. 5. 25. The relative differences did not exceed 8% in all the obtained results, except for the 911 keV peak where the relative difference was found to be ~12%. An excellent agreement, within uncertainties, was also observed in site 2. The efficiency comparison results for site 2 (Ierissos) are presented in Fig. 5. 26.

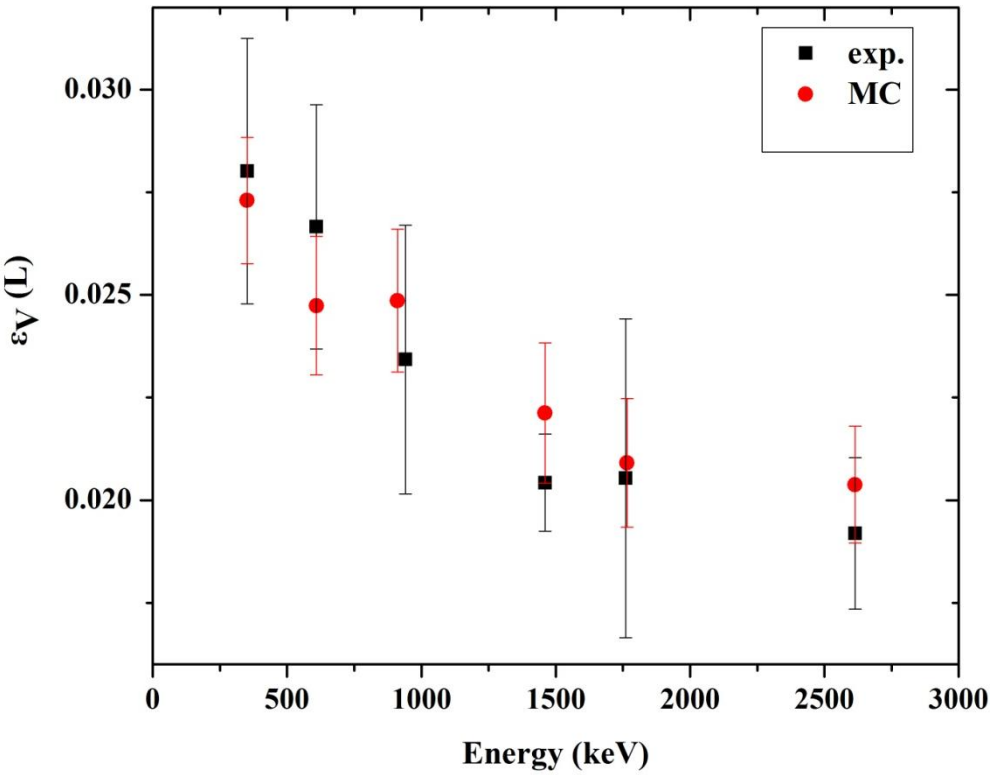

Fig. 5.26: Comparison between the experimental (exp.) and the MC values, of the detection efficiency (ε_V(L)) for site 2 (Ierissos).

The calculated relative differences ranged from 2 to 6 %. In the analysis of the data obtained in site 3 (Stratoni), both the experimental and the MC efficiency values were derived under the assumption of homogeneous vertical profiles within the seabed. The comparison results are presented in Fig. 5.27.

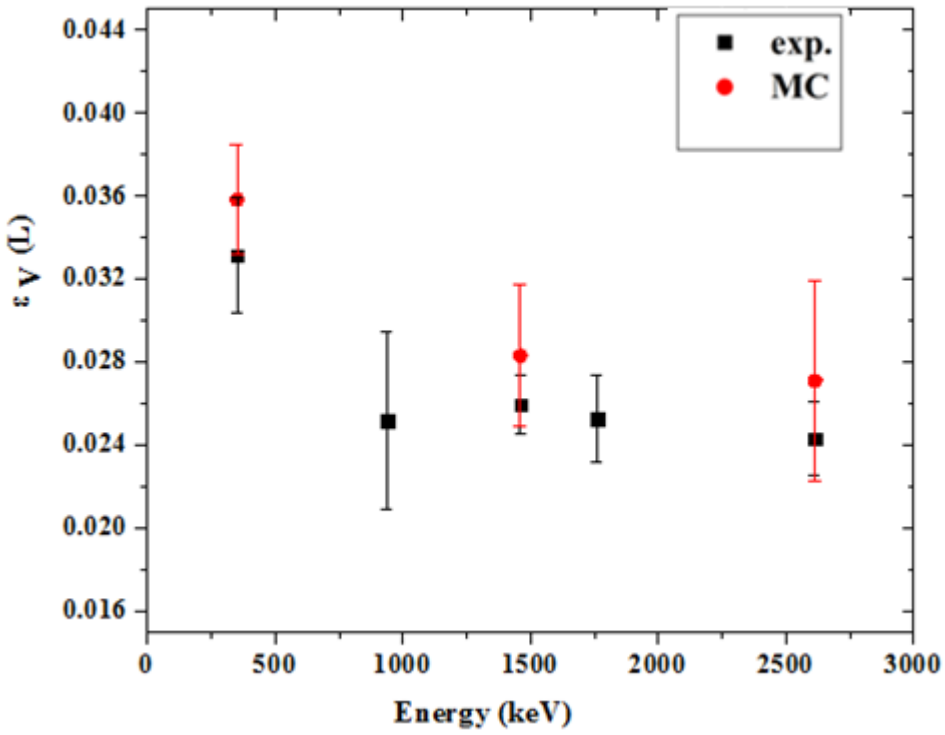

Fig. 5.27: Comparison between the experimental (exp.) and the MC values, of the detection efficiency (ε_V(L)) for site 3 (Stratoni).

The calculated relative differences were found 8%, 5%, 9% and 11% for the peaks appearing in the spectrum at the energies 351 keV, 609 keV, 1460 keV and 2614 keV, respectively. The calculated relative differences were in satisfactory agreement within the calculated uncertainties. The MC statistical uncertainty of these runs was ~ 10%.

Regarding the deployment in the dynamic environment of Costinesti (site 4), a satisfactory agreement, within uncertainties, was observed for the analyzed peaks of ^{232}Th series and the radionuclide ^{40}K (Fig. 5.28). In more detail, the relative differences between the theoretical and the experimental efficiency values at 238 keV (^{212}Pb peak with a total intensity of 43.5%), 338 keV (^{228}Ac peak with a total intensity of 14.36%), 911 keV (^{228}Ac peak with 26.6% intensity) and 968 keV (^{228}Ac peak with 16.23% intensity) and 2614 keV (^{208}Tl peak with 0.3564% intensity) were found to be 9% (238 keV), 10% (338, 911) and 4% (2614 keV), respectively.

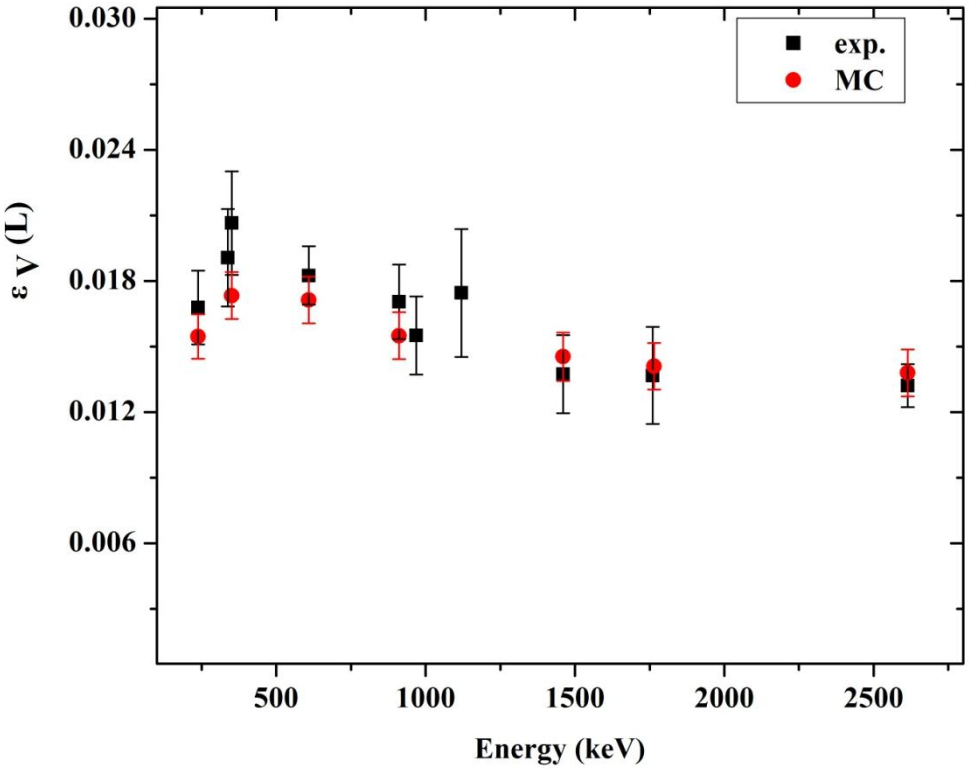

Fig. 5.28: Comparison between the experimental (exp.) and the MC values, of the detection efficiency for site 4 (Costinesti region).

Higher relative differences were observed for the analyzed peaks of ^{222}Rn progenies in the low and medium energy part regions. More specifically, the relative differences were calculated to be 19%, 7%, and 15%, for the corresponding peaks at 351 keV (^{214}Pb peak with 37.1% intensity), 609 keV (^{214}Bi peak with 46.1% intensity) and 1120 keV (^{214}Bi peak with a total intensity of 23%), respectively. The origin of these higher observed differences should be attributed to the presence of groundwater diffusion through the seabed, in the area. Since the groundwater is rich in ^{222}Rn (Burn_06), an essential contribution, mostly affecting the lower part energy region, is present in the spectrum acquired on the seabed due to the decay of ^{222}Rn and its progenies. This contribution was absent during the laboratory measurements, due to ^{222}Rn escape. Since ^{222}Rn is an inert gas, it is very difficult to capture it and accurately measure it, thus it considered to be underestimated in the laboratory measurement. Therefore, in cases of dynamic environments the experimental efficiency calibration should in fact be avoided as the *in situ* measurements lead to more representative results (^{222}Rn losses in the laboratory). SGD environments have been widely studied (Tsab_12; Burn_06; Pov_06a,b) as submarine ground water discharges constitute an important factor in the sustainable management of coastal fresh water aquifers and a

significant pathway for material transfer between the land and the sea. The MC simulation results will be further evaluated by future deployments in similar environments (SGD presence).

To summarize, a methodology able to provide accurate concentration results in different environments was developed. The accuracy of the activity concentrations applying the proposed methodology depends primarily on the accurate determination of the sediments characteristics, since the MC estimated efficiency is the key tool for the application of the proposed approach. The major contribution to the detection efficiency alterations with respect to the sediment properties is the sediment wet density. An effect of less significance may also arise from alterations in the sediment porosity values, while alterations in the sediment chemical composition could be considered negligible, at least for the medium and high parts of the energy region (500-1460 keV). Regarding the vertical distributions of the activity concentrations, it was shown that the lack of knowledge of the actual profiles in a studied environment prior to the measurement could introduce significant systematic uncertainties in the results (a maximum systematic uncertainty of 40% was estimated for the studied scenarios). Regarding the measurement setup, a drastic decrease in the efficiency was observed by increasing this distance (a factor of 3 for a distance of 6 cm above the seabed), while the MC results, assuming inclined seabed, showed that the efficiency values were not significantly affected. Moreover, the theoretical investigation showed that the seawater contribution significantly increases when the system is positioned a few cm above the seabed.

The MC simulations evaluation was achieved by deploying the detector KATERINA, for *in situ* measurements on the seabed, in different environments (Black and Mediterranean Seas). The comparison results between the two methods (MC, experimental), showed a satisfactory agreement with the corresponding laboratory measurements, in the energy range from 351 to 2614 keV, even in the case of inhomogeneous distributed activity concentrations profiles. Moreover the application in site 4 (case of dynamic environment) demonstrated the superior quality of the MC derived efficiency values, as the ^{222}Rn losses associated with the laboratory measurements affected the experimental calibration results.

CHAPTER VI:

Conclusions and future perspectives

The main objective of this thesis was to study several technical aspects related to direct measurements in the marine environment, using the *in situ* γ-ray spectrometry method, and provide solutions that could enhance the reliability of the results, allowing thus the expansion of the *in situ* method in a broad field of applications. A new methodology was developed, regarding the quantification of the *in situ* data for measurements in the seawater column and on the seabed. Therefore, the main core of the thesis was divided into two subsections, consisting of the adopted methodology for the quantitative analysis of *in situ* measurements acquired in the seawater column (Chapter IV), and on the seabed (Chapter V).

Although nowadays the necessity for *in situ* measurements in the seawater column has grown (nuclear accidents, progressive development of modeling), and as a result, the utilization of this method increases, still in the majority of applications, the quantification methodologies rely on the window analysis technique. This selection poses difficulties which are directly related to the moderate resolution of the utilized applications (NaI, BGO crystals). In several cases HPGe detectors are implemented instead, however, only small operation times can be achieved due to the necessity of cooling, limiting thus, till now, the field of applications.

In situ measurements on the seawater column

Regarding *in situ* measurements in the seawater, a quantification methodology based on the Full Spectrum Analysis (FSA) technique was developed, utilizing (a) the MINUIT package for the χ^2 minimization performance and (b) MC simulations (MCNP-CP code) to derive the theoretical standard spectra. The proposed FSA methodology allows for rapid activity concentration derivations (within a few minutes) of high accuracy, as all the features of the spectrum, including True Coincidence Summing (TCS) effects, are incorporated in the data analysis, which is moreover performed almost automatically. Several modifications were considered in the developed approach for the marine environment, as compared to standard FSA techniques utilized by different groups:

- The methodology proposes a progressive χ^2 minimization performance in order to strengthen the accuracy of the obtained results.
- The minimization is performed using a number of ten (10) different standard spectra discarding any *a priori* assumption of the existence of radioactive equilibrium among the radionuclides of the same series.
- The production of the standard spectra using the MCNP-CP code, offered the capability to simulate a radionuclide source as a whole, drastically reducing thus, the necessary time to construct the MC setup, and moreover this code automatically takes into account TCS effects.

The advantages of the proposed methodology compared to the commonly applied techniques (window, peak analysis) are summarized below:

- It offers the possibility of rapid activity concentration calculations (convergence within a few minutes), in any aquatic environment using detection systems based on NaI(Tl) crystals
- It is sensitive to detect and identify anomalies that could be related to unexpected radionuclides, since the analysis comprises all the features of the spectrum.
- It can provide Minimum Detectable Activity values (when the radionuclide under study cannot be identified by a peak in the spectrum), related to different acquisition periods, as well as different salinity (related to ^{40}K activity concentrations) values.
- The methodology is invariant under the geometry and the materials involved and thus, could be easily readjusted to include different types of detectors (e.g. BGO, $CeBr_3$, and HPGe) and different environments (seabed, soils).

The presented FSA methodology was evaluated using both experimental and corresponding MC data utilizing the code FLUKA, and subsequently was applied in real field measurements, yielding satisfactory agreement in all cases. An interesting result of this work, regarding the FLUKA code, was the modification of a user routine in order to account for the observed disequilibrium among the series radionuclides in the marine environment. The new, modified routine 'usrmed' is available to the scientific community upon request. The FLUKA code proved a valuable alternative for environmental applications, due to the advantageous characteristics, which are (a) the capability to

incorporate user-defined routines, (b) the time gain, in terms of the MC model design, utilizing the user-friendly graphical interface, from which all the steps of the simulation (MC model construction, geometry debugging, MC runs execution) can be efficiently controlled, and (c) FLUKA code is a freely distributed code for scientific and academic purposes.

The beneficial characteristics of the FSA technique compared to the conventional utilized techniques (window or peak analysis covering the whole spectrum) can be exploited in a great variety for applications:

- In cases of long-time monitoring applications in which large data sets are obtained, this methodology provides a reliable and rapid tool to handle the data, as the data analysis is performed automatically and in a systematic way.
- In SGD characterization applications, in which the radionuclides under study appear in overlapping peaks in the spectrum, this method is expected to enhance the accuracy of the obtained results, regarding the identification of the radionuclides and their activity concentrations.
- The proposed FSA methodology will be further tested in short and long-term applications for the identification and temporal study of dynamic environments (SGD, pockmarks, cold seeps, mud volcanoes, faults).

In situ measurements on the seabed

Regarding *in situ* measurements on the seabed, the quantification process depends on the sediment characteristics (which may greatly vary even in the same study area). In the framework of this thesis, key parameters that affect the detection efficiency were studied. The analysis for the efficiency calibration was based exclusively on MC simulations taking into account the specific sediment physical properties (chemical composition, water saturated density, water content) and different geometry setups.

The developed methodology allows for the detection of multiple radionuclides and the simultaneous determination of their activity concentrations, using the full spectral range. The proposed methodology for *in situ* measurements on the seabed using the detection system KATERINA, provides a cost-effective solution eliminating the requirements for sampling expeditions and laboratory-based analytical work. The results of this work, render the *in situ* method preferable for a great variety of applications in the marine environment, including (a) large scale radiological characterization of

uncontaminated areas, (b) temporal studies in dynamic environments (e.g. mud volcanoes, SGDs) by operating the detection system in a continuous mode, as well as (c) hot spot investigations (buried radioactive sources on the seabed, wastes at the seabed, contaminated areas etc).

In more detail, the main conclusions of the thesis concerning *in situ* γ-ray spectrometry on the seabed are summarized below:

- The detection efficiency of the *in situ* KATERINA γ-ray spectrometer was deduced for measurements in marine sediments. The major contribution to the detection efficiency alterations, with respect to the sediment physical properties, was originating from the sediment wet density alterations. The efficiency was much less affected by alterations in the sediment porosity values. These values (wet density, water content) can be rapidly obtained on board avoiding thus the time-consuming laboratory work. As a result, the activity concentration results using the *in situ* method can be obtained in a drastically reduced time, as an acquisition period of 2-3 h usually suffices to obtain adequate statistics.
- Regarding inhomogeneous activity concentration vertical profiles, a more systematic study is required.
- The proposed optimum setup selection:

a) Ensures the knowledge of the exact distance of the detector window from the seabed surface prior to the measurement.

b) Provides a practical transition between the two measurements in the seawater column and on the marine sediment. The increase of the seawater contribution to the measurement, when the system is positioned even a few cm above the seabed, and the accompanied loss in counting rate, indicates the preferential position of the detector at a maximum distance of 1 cm above the seabed surface.

Regarding the marine environment, the *in situ* method is a valuable tool to a variety of applications related to radiological hazards, and the utilization of this method may provide large databases regarding different environmental studies, including:

- Dose rate assessments and radionuclides dispersion modeling.
- Geological exploration (mud volcanoes, faults, cold seeps, pockmarks) through the quantification of the radioactive gas emissions.

- The establishment of a baseline reference related to the environmental characterization due to pre-operational, operational and post-operational periods at industrial areas.
- The characterization of waste containers and waste emissions released to the marine environment. The *in situ* method is the only solution when immediate response is required while it also ensures minimum doses to the scientific staff.

The proposed MC methodology regarding *in situ* measurements on the seabed, can be expanded to include the determination of the activity concentrations in cases of recent depositions (e.g. ^{137}Cs fallout), as the presented methodology is currently valid under the assumption of homogeneously distributed radionuclide concentrations. Moreover, both developed methodologies can be applied for different detection systems (e.g. $CeBr_3$ crystals), increasing thus even further the applicability of the *in situ* method, since such crystals exhibit a highly improved energy resolution.

The beneficial characteristics of the presented FSA technique will be exploited also for *in situ* measurements on the seabed, using the presented methodology, in combination with extensive MC simulations. For this purpose the FLUKA code will be implemented to simulate the exact geometry of the sediment source (via user-defined routines), in order to properly modify the standard spectra according to the measurement details (sediment properties, geometry setup). The expansion of the FSA technique, also for measurements on the seabed, is expected to further increase the accuracy of the results and as a consequence to broaden the existing field of applications.

APPENDICES:

Appendix A

Gaussian Broadening Algorithm developed for FSA calculations

```
C     PROGRAM CONVOLUTION
      REAL*8 A(3050),C(3050),M(3050),W,D,F,S,G
      REAL*8 B(3050)
      CHARACTER*50 FROSO,MIKE
       D=0.
       F=0.
          S=0.
      WRITE(*,*)'PLEASE GIVE ME THE NAME OF THE INPUT FILE'
      READ(*,2)MIKE
      WRITE(*,*)'PLEASE GIVE ME THE NAME OF THE OUTPUT FILE'
      READ(*,2)FROSO
  2   FORMAT(A50)
      OPEN(10,FILE=MIKE,STATUS='OLD')
      DO 20, I=1,2800
      READ(10,*) A(I),B(I)
  20  END DO
      CLOSE(10)
      DO 30, I=1,3050
      C(I)=0.
  30  END DO
      DO 40, I=1,2800
      W=-0.021+0.0862*SQRT(A(I)-0.0765*A(I)**2)
      S=0.60056120439322*W
c     W=SQRT(A(I)*3.29-239.5)
      IF(S.GT.0.001)THEN
      D=D+B(I)
      DO 50, K=1,2800
      C(K)=C(K)+B(I)*(1/(S*1.7724538509)*EXP(-((A(K)-A(I))**2/S**
2)))
  50  END DO
      ENDIF
  40  END DO
      DO 70, J=1,2800
          F=F+C(J)
  70  END DO
      OPEN(11,FILE=FROSO,STATUS='UNKNOWN')
      DO 60, L=1,2800
       M(L)=C(L)*D/F
          G=G+M(L)
      WRITE(11,*) A(L),M(L),B(L)
  60  END DO
      WRITE(11,*) D,G
c     Kleinoume to arxeio eksodou kai teleiwnoume to programma!
      CLOSE(11)
      END
```

Appendix B

Rebinning Algorithm developed for FSA calculations

```
C       PROGRAM FOR HISTOGRAM REBINNING GENERAL ROUTINE
        REAL*8 EXPER,MCNP,ENERGEIA,O,P,MODULO1
        INTEGER DIV,L,CHANNEL,N,ORIO
        REAL*8 MODULO,FULL,SUMMY(2100),SUMM(2100),NEWOLOK
        REAL*8 ENERGY(3000),BINCON(3000),BINTHEO(3000)
        REAL*8 BINMCNP,BINEXP,BINOFF,EN(3000),OLOKLIR
        REAL*8 YIELD(2100),NEWOLOK1
        CHARACTER*50 FILENAM1,FILENAM2
        WRITE(*,*)'PLEASE GIVE ME THE NAME OF THE INPUT FILE'
        READ(*,2)FILENAM1
        WRITE(*,*)'PLEASE GIVE ME THE NAME FOR THE OUTPUT REBINNED
FILE'
        READ(*,2)FILENAM2
 2      FORMAT(A50)
        WRITE(*,*)'NOW I WANT THE keV/ch EXPERIMENTAL PARAMETER'
 12     READ(*,*)BINEXP
         IF(BINEXP.LE.0.OR.BINEXP.LT.1.)THEN
         WRITE(*,*)'THAT IS CRAP...TRY AGAIN!'
         GOTO 12
         ENDIF
        WRITE(*,*)'...AND THE OFFSET PLEASE (IN keV)'
        READ(*,*)BINOFF
C        EDW DIABAZEI TO ARXEIO EISODOY...
C        YPOLOGIZEI KAI TO OLOKLHRWMA AYTOY
        OPEN(UNIT=25, FILE=FILENAM1, STATUS='OLD')
        DO I=1,2800
        READ(25,*)ENERGY(I),BINCON(I),BINTHEO(I)
        EN(I)=ENERGY(I)*1000
        OLOKLIR=OLOKLIR+BINCON(I)
 25     END DO
        WRITE(*,*)'TO OLOKLHRWMA TOY ARXIKOY FASMATOS
EINAI:',OLOKLIR
        CLOSE(25)
        BINMCNP=EN(2)-EN(1)
        DIV=0
        NEWOLOK=0.
        FULL=0.
        MODULO=0.
        REST=0.
        EXPER=BINEXP/BINMCNP
        MCNP=BINMCNP
        DO 47, I=1,2100
          SUMM(I)=0.
          SUMMY(I)=0.
          YIELD(I)=0.
 47     ENDDO
        CHANNEL=2800/EXPER+1
         IF(CHANNEL.GT.1000)THEN
          ORIO=2047
          ELSE
```

```
        ORIO=1023
       ENDIF
      OPEN(UNIT=35,FILE=FILENAM2,STATUS='UNKNOWN')
      DO 55, K=1,CHANNEL
       DIV=INT(K*EXPER)
       FULL=K*EXPER
       MODULO=FULL-DIV
       DO 45, I=1,DIV
       SUMM(K)=SUMM(K)+BINCON(I)
45     END DO
      SUMM(K)=SUMM(K)+MODULO*BINCON(1+DIV)
      DIV1=INT((K+1)*EXPER)
      FULL1=(K+1)*EXPER
      MODULO1=FULL1-DIV1
       DO 46, I=1,DIV1
       SUMMY(K)=SUMMY(K)+BINCON(I)
46     END DO
       SUMMY(K)=SUMMY(K)+MODULO1*BINCON(1+DIV1)
       IF(K.EQ.1)THEN
        YIELD(K)=SUMM(K)
       ENDIF
       YIELD(K)=SUMMY(K)-SUMM(K)
      NEWOLOK=NEWOLOK+YIELD(K)
55    ENDDO
      DIV=INT(EXPER)
      FULL=EXPER
      MODULO1=FULL-DIV
      DO 86, K=1,CHANNEL
       ENERGEIA=K*BINEXP+BINOFF
       N=INT(BINOFF/BINEXP)
       O=BINOFF/BINEXP
       P=ABS(O-N)
        IF(MODULO1.LE.0.5.AND.P.LE.0.5)THEN
         WRITE(35,*)K,ENERGEIA,YIELD(K+N-1)
        ENDIF
        IF(N.GT.0.AND.P.GT.0.5)THEN
         WRITE(35,*)K,ENERGEIA,YIELD(K+N-1)
        ENDIF
         IF(N.LE.0.AND.P.GT.0.5)THEN
         WRITE(35,*)K,ENERGEIA,YIELD(K+N-2)
        ENDIF
86    ENDDO
      DO 65, K=CHANNEL+1,ORIO
      ENERGEIA=K*BINEXP+BINOFF
      N=INT(BINOFF/BINEXP)
      O=BINOFF/BINEXP
       P=ABS(O-N)
```

```
          IF(P.LE.0.5)THEN
           WRITE(35,*)K,ENERGEIA,YIELD(K+N-1)
          ENDIF
          IF(N.GT.0.AND.P.GT.0.5)THEN
           WRITE(35,*)K,ENERGEIA,YIELD(K+N-1)
          ENDIF
           IF(N.LE.0.AND.P.GT.0.5)THEN
           WRITE(35,*)K,ENERGEIA,YIELD(K+N-2)
          ENDIF
65      ENDDO
        CLOSE(35)
        WRITE(*,*)'TO NEO OLOKLHRWMA EINAI',NEWOLOK
        STOP
        END
```

Appendix C

Major Element Analysis Results on the core selected at Lavrion

(*site 1*, 37°71'94.19"N, 24°06'32.00"E)

Depth	L.O.I	Al2O3	SiO2	P2O5	K2O	CaO	TiO2	Fe2O3	Na2O	MgO	SO3	MnO
cm	(%)	(%)	(%)	(%)	(%)	(%)	(%)	(%)	(%)	(%)	(%)	(%)
1	8.62	8.1	44.8	0.18	2.25	9.5	0.36	10.7	2.20	2.97	9.0	1.37
3	8.86	7.9	45.8	0.16	2.19	10.4	0.36	10.0	2.03	3.01	7.9	1.36
4	11.33	7.8	44.8	0.17	2.17	10.5	0.35	10.6	1.90	3.02	5.9	1.29
5	10.05	7.7	45.0	0.17	2.17	9.9	0.37	10.6	1.70	2.96	8.0	1.26
6	9.87	7.8	45.4	0.18	2.19	9.6	0.36	10.8	1.63	2.97	7.9	1.26
7	19.90	6.1	35.6	0.13	1.72	7.5	0.28	8.2	1.23	2.30	15.8	1.01
8	11.61	8.0	45.1	0.16	2.19	9.6	0.34	10.4	1.40	3.04	7.0	1.20
9	8.75	8.1	44.8	0.17	2.24	9.4	0.36	10.5	2.77	2.98	8.0	1.22
10	11.00	8.0	43.6	0.16	2.23	8.8	0.33	12.0	2.11	2.93	7.7	0.96
11	14.18	8.9	41.7	0.14	2.48	8.8	0.31	12.2	1.98	3.07	5.2	0.83
12	15.44	9.7	40.4	0.14	2.60	8.7	0.29	12.2	1.78	3.19	4.0	0.75
13	16.51	9.9	39.3	0.13	2.63	8.7	0.29	12.4	1.73	3.28	4.2	0.71
14	16.71	9.5	39.9	0.13	2.60	8.9	0.30	12.4	1.66	3.22	4.0	0.73
15	13.89	9.7	38.9	0.13	2.58	8.8	0.29	12.3	1.30	3.25	8.0	0.70
16	15.64	9.7	38.8	0.13	2.62	8.9	0.28	12.6	1.38	3.32	5.8	0.67
17	17.02	10.0	38.5	0.12	2.68	8.1	0.27	12.5	1.23	3.22	5.6	0.57
18	16.45	10.1	40.1	0.12	2.74	7.8	0.27	12.2	1.48	3.06	5.0	0.57
19	16.23	10.3	39.8	0.12	2.78	7.7	0.27	11.3	1.47	3.04	6.0	0.55
20	14.27	10.3	39.4	0.12	2.75	8.1	0.27	12.6	1.35	3.17	7.0	0.60
21	15.38	10.5	40.1	0.13	2.84	7.5	0.27	12.5	1.24	2.99	5.9	0.58
22	15.48	10.8	41.0	0.13	2.90	7.4	0.27	12.1	1.37	3.01	4.5	0.56
23	13.72	10.8	41.4	0.12	2.87	7.5	0.27	12.1	1.28	2.99	6.5	0.54
24	15.05	10.9	41.9	0.13	2.93	7.4	0.27	11.8	1.59	2.94	4.3	0.54
25	13.42	10.3	42.1	0.12	2.77	7.7	0.28	11.5	1.18	2.92	7.0	0.65
26	13.83	11.0	41.7	0.13	2.96	7.4	0.28	11.5	1.50	2.95	6.1	0.54

Appendix D

Major Element Analysis Results on the core selected at Stratoni

(***site 3,*** **40°30.930'N 023°49.870'E**)

Depth	L.O.I	Al2O3	SiO2	P2O5	K2O	CaO	TiO2	Fe2O3	Na2O	MgO	SO3	MnO
cm	(%)	(%)	(%)	(%)	(%)	(%)	(%)	(%)	(%)	(%)	(%)	(%)
1	14.04	3.6	27.9	0.11	0.71	17.1	0.32	18.0	1.03	2.01	13.5	1.03
3	15.38	3.7	28.5	0.11	0.74	17.1	0.32	18.2	1.83	2.01	10.3	1.12
5	13.30	3.4	25.7	0.11	0.64	15.7	0.31	21.2	0.77	2.09	14.6	1.16
7	13.87	3.5	26.7	0.10	0.68	17.2	0.32	18.9	0.77	2.01	14.6	1.05
9	14.28	3.4	25.9	0.11	0.67	17.3	0.31	19.4	0.99	2.02	14.6	1.07
11	11.86	3.6	27.0	0.11	0.68	17.1	0.32	18.8	0.87	2.02	16.5	1.04
13	11.32	3.6	27.1	0.11	0.66	16.9	0.32	18.8	0.85	2.11	16.6	1.03
15	13.04	3.4	27.7	0.12	0.69	16.7	0.32	18.7	0.90	1.99	15.1	1.07
17	14.38	3.5	26.4	0.12	0.68	15.8	0.32	20.8	1.43	2.09	13.3	1.17
19	14.07	3.5	26.8	0.12	0.69	16.1	0.32	19.8	1.27	2.03	12.5	1.09
21	13.70	3.5	27.1	0.11	0.70	16.5	0.32	19.0	1.31	2.01	14.5	1.06
23	14.20	3.7	27.8	0.10	0.70	17.1	0.31	17.9	0.80	2.03	14.0	1.02
25	14.00	3.6	27.5	0.11	0.67	16.5	0.31	19.0	0.85	2.03	13.8	1.08
27	13.84	3.3	26.0	0.11	0.66	17.1	0.29	19.0	0.78	2.02	15.0	1.04
29	14.32	3.9	26.4	0.11	0.70	17.0	0.28	18.8	0.72	2.06	14.6	1.05
31	14.64	4.3	25.2	0.11	0.75	17.1	0.30	18.2	1.08	2.12	15.0	0.95
33	15.76	3.8	30.0	0.09	0.75	19.4	0.28	13.0	1.18	1.91	12.5	0.66
35	17.27	4.1	30.7	0.09	0.72	19.6	0.28	10.7	1.14	1.86	12.5	0.48
37	20.38	3.7	34.2	0.08	0.76	22.8	0.31	7.1	1.08	1.80	6.8	0.29
39	22.49	3.7	33.9	0.07	0.76	28.0	0.31	6.7	1.35	2.00	0.2	0.28
41	25.09	3.1	30.9	0.07	0.69	26.3	0.27	5.4	1.65	1.82	3.9	0.22
43	24.31	2.8	29.9	0.06	0.63	28.4	0.26	4.2	1.11	1.71	6.3	0.16
45	27.11	2.7	28.3	0.05	0.62	29.2	0.26	3.5	1.64	1.79	4.4	0.11
47	25.18	3.1	29.5	0.06	0.68	27.7	0.29	5.0	1.33	1.79	4.7	0.20
49	25.67	2.9	31.4	0.06	0.66	28.1	0.27	3.7	1.24	1.74	3.8	0.12
51	27.23	3.49	28.34	0.10	0.69	19.91	0.30	14.55	1.12	1.96	11.34	0.78

REFERENCES

Aak_95 Aakenes, U.R., 1995. Radioactivity monitored from moored oceanographic buoys. Chem. Ecol.10, 61–69.

Abril_92 Abril, J.M., Garcia-Leon, M., Garcia-Tenorio, R., Sanchez, C.I., 1992. Dating of Marine Sediments by an Incomplete Mixing Model, J. Environ. Radioact., 15, 135-151.

Ahre_95 Ahrens T. J., 1995. Global Earth Physics: A Handbook of Physical Constants (AGU Reference Shelf 1), Washington D.C.: American Geophysical Union.

Allys_94 Allyson, J.D. 1994. Environmental gamma-ray spectrometry: simulation of absolute calibration of in-situ and airborne spectrometers for natural and anthropogenic sources. PhD dissertation, University of Glasgow, Faculty of Science.

Allys_98 Allyson J.D., Sanderson D.C.W., 1998. Monte Carlo simulation of environmental airborne gamma-spectrometry, J. Environ. Radioact., 38, 3, 259-282.

Andr_15 Androulakaki E.G., Tsabaris C., Eleftheriou G., Kokkoris M., Patiris D. L., Vlastou R,. 2015. Seabed radioactivity based on in situ measurements and Monte Carlo simulations, Appl. Radiat. Isot., 101, 83-92.

Andr_16a Androulakaki E.G., Tsabaris C., Eleftheriou G., Kokkoris M., Patiris D.L., Pappa F.K., Vlastou R., 2016. Efficiency calibration for in situ γ-ray measurements on the seabed using Monte Carlo simulations: Application in two different marine environments, *in press*.

Andr_16b Androulakaki E.G., Kokkoris M., Tsabaris C., Eleftheriou G., Patiris D.L., Pappa F.K., Vlastou R., 2016. In situ γ-ray spectrometry in the marine environment using full spectrum analysis for natural radionuclides, Appl. Radiat. Isot., 114, 76-86.

ANSI_91 ANSI standard 1991. Gamma Ray Attenuation Coefficient and Buildup Factors for Engineering Materials. ANSI/ANS-6.4.3, 1991.

Anst_74 Anstey R.L., Chase T.L., 1974. Environments through time. Burgess Publishing Company, Burgess, Minneapolis, Minn.

Arrhe_51 Arrhenius G, Kjellberg G., Libby W.F., 1951. Age determination of Pacific chalk ooze by radiocarbon and titanium content: Tellus, 3, 222-229.

Askri_08 Askri B., Manai K., Trabelsi A., and Baccari B., 2008. Optimized geometry to calculate dose rate conversion coefficient for external exposure to photons. Radiat. Prot.Dosim., 128, 279-288.

Bag_10 Bagatelas C., Tsabaris C., Kokkoris M., Papadopoulos C.T., Vlastou R., 2010. Determination of marine gamma activity and study of the minimum detectable activity (MDA) in 4pi geometry based on Monte Carlo simulation. Environ. Monit. Assess., 165, 159-168.

Bah_07 Bahari I., Mohsen N., Abdullah P., 2007. Radioactivity and radiological risk associated with effluent sediment containing technologically enhanced naturally occurring radioactive materials in amang (tin tailings) processing industry, J. Environ. Radioact., 95, 161-170.

Bass_14 Bassey C., Eminue O., 2014. Preliminary evaluation of major and trace elements content of Cretaceous Palaeogene Formation of the Sokoto Basin, Northwestern Nigeria, NAFTA, 65,1, 69-76.

Bate_10 Bateman H. 1910. The solution of a system of differential equations occurring in the theory of radioactive transformations, Proc. Cambridge Phil., Sot. 15, 423.

Batti_07 Battistoni G., Muraro S., Sala P.R., Cerutti F., Ferrari A., Roesler S., Fassò A., Ranft J.,2007. Proceedings of the Hadronic Shower Simulation Workshop 2006, Fermilab 6--8 September 2006, M.Albrow, R. Raja eds., AIP Conference Proceeding 896, 31-49.

Batti_15 Battistoni, G., et al., 2015. Overview of the FLUKA code, Ann. Nucl. Energy, 82, 10-18.

Beck_72 Beck, H.L., De Campo J., Gogolak, C., 1972. In-Situ Ge(Li) and NaI(Tl) Gamma-Ray Spectrometry. HASL-258, United States Atomic Energy Commission Health and Safety (TID-4500), p. 75.

Beks_00 Beks J.P., 2000. Storage and distribution of plutonium, ^{241}Am, ^{137}Cs and $^{210}Pb_{xs}$ in North Sea sediments. Cont. Shelf Res., 20, 1941-1964.

Bell_12 Bell S.J., Judge S.M., Regan P.H., 2012. An investigation of HPGe gamma efficiency calibration software (ANGLE V.3) for applications in nuclear decommissioning, Appl. Radiat. Isot., 70, 12, 2737-2741.

Benk_00 Benke R.R, Kearfott K.J, 2000. Accounting for ^{222}Rn loss during oven drying for the immediate laboratory gamma-ray spectroscopy of collected soil samples, Appl. Radiat. Isot., 52, 2, 271-287.

Ber_06 Berlizov, A.N., 2006. MCNP-CP a correlated particle radiation source extension of a general purpose Monte Carlo N particle transport code, In: Semkov TM, Pommé S, Jerome SM (eds) ACS symposium series 945, American Chemical Society, Washington DC, 183–194.

Ber_08 Berlizov, A.N., Solovyena, S.L., 2008. A Dynamic Library for calculating true-coincidence summing correction factors, J. Radioanal. Nucl. Chem., 276, 663-668.

Ber_10a Berlizov, A.N., Mayer, K., 2010. Fast and accurate approach to γ-spectrum modeling: A validation study with a shielded/unshielded voluminous uranium sample, Appl. Radiat. and Isot., 68, 1822-1831
.

Ber_10b Berlizov, A. N., 2010. A correlated particle source extension of a general purpose Monte Carlo N-Particle transport code, MCNP-CP Upgrade Patch Version 3.2, manual, (*Personal communication*).

Ber_87 Berger M.J., Hubbell J.H., 1987. "XCOM: Photon Cross Sections on a Personal Computer," NBSIR 87-3597, National Bureau of Standards (former name of NIST), Gaithersburg, MD.

Berg_10 Berger M. J., Hubbell J. H., Seltzer S.M., Chang J., Coursey J.S., Sukumar R., Zucker D.S., Olsen K., 2010. XCOM: Photon Cross Section Database, (version 1.5). Online Available: http://physics.nist.gov/xcom.

Bhand_93 Bhandal G. S., Singh K., 1993. Study of the Mass Attenuation Coefficients and Effective Atomic Numbers in Some Multielement Materials, Appl. Radiat. And Isot., 44, 929-939.

Blum_97a Blum, P., Rabaute, A., Gaudon, P., and Allan, J.F., 1997. Analysis of natural gamma-ray spectra obtained from sediment cores with the shipboard scintillation detector of the Ocean Drilling Program: example from Leg 156. In Shipley, T.H., Ogawa, Y., Blum, P., and Bahr, J.M. (Eds.), Proc. ODP, Sci. Results, 156: College Station, TX (Ocean Drilling Program), 183–195.

Blum_97b Blum, P., 1997. Physical properties handbook. ODP Tech. Note, 26. doi:10.2973/odp.tn.26.1997.

Bodw_94 Bodwadkar, S.V., and Reis, J.C., 1994. Porosity measurements of core samples using gamma-ray attenuation. Nucl. Geophys., 8, 61–78.

Bol_95 Bolívar J.P., García-Tenorio R., García-León M., 1995. Fluxes and distribution of natural radionuclides in the production and use of fertilizers, Appl. Radiat. Isot., 46, 717-718.

Bor_14 Boryło A., Skwarzec B., 2014. Activity disequilibrium between ^{234}U and ^{238}U isotopes in natural Environment, J. Radioanal. Nucl. Chem., 300, 719–727.

Boson_06 Boson J., Lidström K., Nylén T., Agren G., Johansson L., 2006. In situ gamma-ray spectrometry for environmental monitoring: A semi empirical calibration method, Radiat. Prot. Dosim., 121, 310-316.

Boson_08 Boson J., 2008. Improving accuracy of *in situ* gamma-ray spectrometry. Department of Radiation Sciences, Radiation Physics Umeå University, Sweden.

Bourd_03 Bourdon B., Turner S., Henderson G.M., Lundstrom C.C., 2003. Introduction to U-series geochemistry, In: Rev. Mineral. Geochem., 52, 1, 1-21.

Breit_06 Breitzke M., 2006. Physical properties of Marine Sediments, Marine Geochemistry, 27-71.

Bri_14 Britton R., Burnett J. L., Davies A.V., Regan P.H., 2014. Characterisation of cascade summing effects in gamma spectroscopy using Monte Carlo simulations, J. Radioanal. Nucl. Chem., 299, 447-452.

Briesm_97 Briemeister J. F., 1997. MCNP-general Monte Carlo N-particle transport Code. Los Alamos National Laboratory Report, 1997, LA-12625-M.

Brö_04 Bröcker, M., Bieling, D., Hacker, B., Gans, P., 2004. High-Si phengite records the time of greenschist facies overprinting: implications for models suggesting mega-detachments in the Aegean Sea, J. Metamorph. Geol. 22, 427–442.

Brö_05 Bröcker, M., Franz, M., Franz, L., 2005. The base of the Cycladic blueschist unit on Tinos Island (Greece) re-visited: field relationships, phengite chemistry and Rb–Sr geochronology, Neues Jahrb. Mineral. Abh. 181 (1), 81–93.

Brö_93 Bröcker M., Kreuzer H., Matthews A., Okrusch M., 1993. 40Ar/39Ar and oxygen isotope studies of polymetamorphism from Tinos Island, Cycladic blueschist belt. J. Metamorph. Geol. 11, 223–240.

Bryant_81 Bryant W. R., Bennett R., and Katherman C, 1981. Shear strength, consolidation, porosity, and permeability of marine sediments. In Emiliani, C. (Ed.), New York (Wiley), 7, 1555-1616.

Bues_90 Buesseler K.O., Livingston H.D., Honjo S., Hay B.J., Konuk T., Kempe S., 1990. Scavenging and particle deposition in the southwestern Black Sea evidence from Chernobyl radiotracers, Deep Sea Res., 37, 3, 413-430.

Bues_92 Buesseler K.O., Bacon M.P., Cochran J.K., Livingston H.D., 1992. Carbon and nitrogen export during the JGOFS North Atlantic Bloom experiment estimated from ^{234}Th: ^{238}U disequilibria, Deep Sea Res. Part 1 Oceanogr. Res. Pap., 39, 7–8, 1115-1137.

Burn_03 Burnett W.C., Dulaiova H., 2003. Estimating the dynamics of groundwater input into the coastal zone via continuous radon-222 measurements, J. Environ. Radioact., 69, 1–2, 21-35.

Burn_06 Burnett W.C., et al., 2006. Quantifying submarine groundwater discharge in the coastal zone via multiple methods, Sc. Total Environ., 367, 498-543.

Cac_12 Caciolli A., et al., 2012. A new FSA approach for in situ γ ray spectroscopy, Sc. Total Environ., 414, 639-645.

Cai_12 Cai P., Shi X., Moore W.S., Dai M., 2012. Measurement of ^{224}Ra:^{228}Th disequilibrium in coastal sediments using a delayed coincidence counter, Marine Chemistry, 138–139, 1-6.

Canber_10 CANBERRA, 2010. Basic Counting Systems, © 2010 Canberra Industries, Inc.

Canber_14 CANBERRA, 2014. Nuclear Measurement Solutions for Safety, Security and the Environment, Gamma and X-Ray Detection, © 2014 Canberra Industries, Inc.

Casan_14 Casanovas R., Morant J.J., Salvadó M., 2014. Development and calibration of a real-time airborne radioactivity monitor using direct gamma-ray spectrometry with two scintillation detectors, Appl. Radiat. Isot., 89, 102-108.

Casas_04 Casas D., Lee H., Ercilla G., Kayen R., Estrada F., Alonso B., Baraza J., Chiocci F., 2004. Physical and geotechnical properties and assessment of sediment stability on the continental slope and basin of the Bransfield Basin (Antarctica Peninsula), Mar. Georesources Geotechnol., 22, 4, 253-278.

Casas_06 Casas D., Ercilla G., Lykousis V., Ioakim C.; Perissoratis C., 2006. Physical properties and their relationship to sedimentary processes and texture in sediments from mud volcanoes in the Anaximander Mountains (Eastern Mediterranean), Sci. Mar., Spain, 70/4, 643 – 650.

Chab_08 Chabaux F., Bourdon B., Riotte J., 2008. Chapter 3, U-Series Geochemistry in Weathering Profiles, River Waters and Lakes, In: S. Krishnaswami and J. Kirk Cochran, Editor(s), Radioactivity in the Environment, Elsevier, 2008, 13, p. 49-104.

Char_08 Charette M.A., Moore W.S., Burnett W.C., 2008. Chapter 5, Uranium- and Thorium-Series Nuclides as Tracers of Submarine Groundwater Discharge, In: S. Krishnaswami and J. Kirk Cochran, Editor(s), Radioactivity in the Environment, Elsevier, 2008, 13, p. 155-191.

Chop_13 Choppin G., Liljenzin J.-O., Rydberg J., Ekberg C., 2013. Chapter 18, Uses of Radioactive Tracers, In Radiochemistry and Nuclear Chemistry (Fourth Edition), Academic Press, Oxford, 2013, Pages 545-593.

Cine_16 Cinelli G., Tositti L., Mostacci D., Baré J., 2016. Calibration with MCNP of NaI detector for the determination of natural radioactivity levels in the field, J. Environ. Radioact., 155–156, 31-37.

Coc_05 Cochran J.K., Masqué P., 2005. Chapter 1, Natural radionuclides applied to coastal zone processes, In: Hugh D. Livingston, Eds., Radioactivity in the Environment, 6, 1-21.

Coc_08 Cochran J.K., and Kadko D.C., 2008. Uranium- and Thorium-Series Radionuclides in Marine Groundwaters, Radioactivity in the Environment, Volume 13, Chapter 10, p. 345-382.

Coc_92 Cochran J.K., 1992. The oceanic chemistry of the uranium and thorium series Nuclides. In: Ivanovich, M., Harmon, R.S. (Eds.), Uranium-series Disequilibrium: Applications in Earth Marine and Environmental Sciences. Oxford Science Publications, United Kingdom, p. 382–391.

Coc_84 Cochran J. K., 1984. The estuarine as a filter. Proceedings of the Seventh Biennial InternationalEstuarine Research Conference, Virginia Beach, Virginia, October 23-26, 1983. Academic Press Inc. London LTD.

Coc_86 Cochran J.K., Carey A.E., Sholkovitz E. R, Surprenant L. D., 1986. The geochemistry of uranium and thorium in coastal marine sediments and sediment pore waters, Geochim. Cosmochim. Acta, 50, 5, 663-680.

Coop_01 Cooper L.W., Hong G.H., Beasley T.M., J.M. Grebmeier J.M., 2001. Iodine-129 Concentrations in Marginal

Seas of the North Pacific and Pacific-influenced Waters of the Arctic Ocean, Mar. Poll. Bull., 42, 12, 1347-1356.

Cruz_13 Cruz A.P.S., Barbosa C.F., Ayres-Neto A., Albuquerque A.L.S., 2013. Physical and geochemical properties of centennial marine sediments of the continental shelf of southeast Brazil, Geochimica Brasiliensis 27, 1, 1-12.

Das_06 Das N.K., Choudhury H., Bhandari R.K., Ghose D., Sen P., Sinha B., Continuous monitoring of ^{222}Rn and its progeny at a remote station for seismic hazard surveillance, Radiat. Meas., 41, 5, 634-637.

Davi_76 Davis T.A., Gorsline D.S., 1976. Oceanic sediments and sedimentary properties, Chemical Oceanography, Eds., Riley J.P., Chester R., Orlando: Fla., Academic press, 1976.

Deb_79 Debertin, K. and Schotzig, U., 1979. Coincidence summing corrections in Ge(Li) spectrometry at low source-to-detector distances, Nucl. Instrum. Methods A, 158, 471-477.

Deb_88 Debertin, K., Helmer, R.G., 1988. Gamma X-ray spectrometry with semiconductors detectors. North Holland, Amsterdam.

Dec_96 Decombaz M., Laedermann J.-P., 1996. Efficiency determination of a 4π γ-detector by numerical simulation, Nucl. Instrum. Methods A 369, 375-379.

Del_14 Delfanti R., Özsoy E., Kaberi H., Schirone A., Salvi S., Conte F., Tsabaris C., Papucci C., 2014. Evolution and fluxes of ^{137}Cs in the Black Sea/Turkish Straits System/North Aegean Sea, J. Mar. Systems, 135, 117-123.

Díaz_08 Díaz N. C., M. Vargas J., 2008. DETEFF: An improved Monte Carlo computer program for evaluating the efficiency in coaxial gamma-ray detectors, Nucl. Instrum. Methods A, 586, 2, 204-210.

Eber_08 Eberth J., Simpson J., 2008. From Ge(Li) detectors to gamma-ray tracking arrays –50 years of gamma spectroscopy with germanium detectors. Progress in Particle and Nuclear Physics, 60, 283–337.

Elef_13 Eleftheriou G., Tsabaris C., Androulakaki E.G., Patiris D. L., Kokkoris M., Kalfas, R. Vlastou et al., C.A., 2013. Radioactivity measurements in the aquatic environment using in-situ and laboratory gamma-ray spectrometry, Appl. Rad. Isot., 82, 268-278.

Elef_15 Ελευθερίου, Γ., 2015. Χωροχρονική διασπορά ραδιονουκλιδίων στο υδάτινο περιβάλλον. Διδακτορική Διατριβή, Εθνικό Μετσόβιο Πολυτεχνείο, Αθήνα.

Encyc_16 Flemming D.W., Delafontaine M.T., 2016. Encyclopedia of Earth Sciences Series, Encyclopedia of Estuaries, Ed. Kennish M. J., Rutgers University New Brunswick, New Jersey, USA, Springer 2016, p.419-423.

Engel_08 Engelbrecht R., Schwaiger M., 2008. State of the art of standard methods used for environmental radioactivity monitoring, Appl. Radiat. Isot., 66, 1604– 1610.

Engel_12 Engelbrecht R., 2012. Chapter 10, Environmental Radioactivity Monitoring, In Handbook of Radioactivity Analysis (Third Edition), edited by Michael F. L'Annunziata, Academic Press, Amsterdam, 2012, 695-726.

Evans_55 Evans R.D., 1955. The Atomic Nucleus, McGraw Hill Book Co, New York.

Fasso_03 Fassò A., et al., 2003. The FLUKA code: Present applications and future developments Computing in High Energy and Nuclear Physics 2003 Conference (CHEP2003), La Jolla, CA, USA, March 24-28, 2003.

Fel_00 De Felice P., Angelini P., Fazio A., Biagini R., 2000. Fast procedures for coincidence-summing correction in γ-ray spectrometry, Appl. Radiat. Isot., 52, 745-752.

Fel_02 De Felice P., Angelini P., Fazio A., Capogni M., 2002. A national Campaign for Coincidence-Summing Correction in γ-Ray spectrometry, Appl. Radiat. Isot. 56, 117-123.

Feng_12 Feng T.C., Jia M.Y., Feng Y.J., 2012. Method-sensitivity of in-situ γ spectrometry to determine the depth-distribution of anthropogenic radionuclides in soil, Nucl. Instrum. Methods A, 661, 26-30.

Ferra_05 Ferrari, A., et al., 2005. FLUKA: a multi-particle transport code, CERN-2005-10, INFN/TC 05/11, SLAC-R-773.

Flem_00 Flemming B.W., Delafontaine M.T., 2000. Mass physical properties of muddy intertidal sediments: some applications, misapplications and non-applications, Cont. Shelf Res., 20, 10–11, 1179-1197.

Finck_76 Finck R.R., Lidén, K.; Persson, R.B.R., 1976. In situ measurements of environmental gamma radiation by the use of a Ge(Li)-spectrometer, Nucl. Instrum. Methods, 135, 3, p. 559-567.

Folk_54 Folk, R.L., 1954. The distinction between grain size and mineral composition in sedimentary rock nomenclature, J. Geol. 62, 344-359.

Fortin_13 Fortin D., Francus P., Gebhardt A. C., Hahn A., Kliem P., Pronovost A. L., Roychowdhury R., Labrie J., St-Onge G., 2013. Destructive and non-destructive density determination: method comparison and evaluation from the Laguna Potrok Aike sedimentary record, Quat. Sci. Rev., 71, 147-153.

Garc_12 García P.F., M.A. Ferro García, M. Azahra, 2012. 7Be behaviour in the atmosphere of the city of Granada January 2005 to December 2009, Atmos. Environ., 47, 84-91.

Gealy_07 Gealy, E.L., Saturated Bulk Density, Grain Density and Porosity of Sediment Cores from the Western Equatorial Pacific: Leg 7, Glomar Challenger, Reports of the Deep Sea Drilling Project, VI, 2007, 1081-1104. doi:10.2973/dsdp.proc.7.124.1971.

Gilm_08 Gilmore, R.G., 2008. Practical Gamma Ray Spectrometry (2nd Ed.), J. Wiley and Sons,Warrington.

Gonz_12 González J. C., Díaz N. C., Vargas M. J., 2012. Application of the Monte Carlo code DETEFF to efficiency calibrations for in situ gamma-ray spectrometry, Appl. Radiat. Isot., 70, 868-87.

Graaf _07 Van der Graaf E.R., Koomans R.L., Limburg J., deVries K., 2007. In situ radiometric mapping as a proxy of sediment contamination: assessment of the underlying geochemical and physical principles, Appl. Radiat. Isot., 65, 619–633.

Graaf_11 van der Graaf E.R., Limburg J., Koomans R.L., Tijs M., 2011. Monte Carlo based calibration of scintillation detectors for laboratory and in situ gamma ray measurements, J. Environ. Radioact., 102, 3, 270-282.

Grab_11 Grabowski R.C., Droppo I.G., Wharton G., 2011. Erodibility of cohesive sediment: The importance of sediment properties, Earth-Sci. Rev., 105, 3–4, 101-120.

Groot _09 De Groot A.V., van der Graaf E.R., DeMeijer R.J., Maučec M., 2009. Sensitivity of in-situ g-ray spectra to soil density and water content, Nucl. Instrum. Methods, 600,519–523.

Guil_01 Guillot L. 2001. Extraction of full absorption peaks in airborne gamma-spectrometry by filtering techniques coupled with a study of the derivatives. Comparison with the window method, J. Environ. Radioact., 53, 381-18.

Gust_98 Gustafsson Ö., Buesseler K.O., Geyer W.R., Moran S.B., Gschwend P.M., 1998. An assessment of the relative importance of horizontal and vertical transport of particle-reactive chemicals in the coastal ocean, Cont. Shelf Res., 18, 7, 805-829.

Hamil_70 Hamilton E.L., 1970. Sound velocity and related properties of marine sediments, J. Geophys. Res.,75, 1970, 4423-4446.

Hamil_74 Hamilton, E. L., 1974. Prediction of deep-sea sediment properties: state of the art. In Inderbitzen, A. L. (Ed.), Deep-Sea Sediments: Physical and Mechanical Properties: New York (Plenum), 1-43.

Hamil_94 Hamilton T.F., Ballestra S., Baxter M.S., Gastaud J., Osvath I., Parsi P., Povinec P.P., Scott E.M., 1994. Radiometric investigations of Kara Sea sediments and preliminary radiological assessment related to dumping of radioactive wastes in the Arctic Seas, J. Environ. Radioact., 25, 1–2, 113-134.

Harms_99 Harms, I.H., Povinec, P.P. 1999. The outflow of radionuclides from Novaya Zemlya Bays—modelling and monitoring strategies, Sci. Total Environ. 237/238, 193–201.

Harms_03 Harms I. H., Karcher M. J., Burchard H., 2003. Chapter 3, Modelling radioactivity in the marine environment: The application of hydrodynamic circulation models for simulating oceanic dispersion of radioactivity, In: E. Marian Scott, Editor(s), Radioactivity in the Environment, 4, 55-85.

He_97 He Q., Walling D.E., 1997. The distribution of fallout ^{137}Cs and ^{210}Pb in undisturbed and cultivated soils, Appl. Radiat. Isot., 48, 677-690.

Heat_95 Heaton B., Lambley J., 1995. TENORM in the oil, gas and mineral mining industry, Appl. Radiat. Isot., 46, 577-581.

Hend_03 Henderson G.M., Anderson R.F., 2003. The U-series toolbox for paleoceanography, Rev. Mineral. Geochem., 52, 1, 493-531.

Hendr_01 Hendriks P.H.G.M., Limburg J., de Meijer R.J., 2001. Full-spectrum analysis of natural γ-ray spectra, J. Environ. Radioact., 53, 3, 365-380.

Hendr_02 Hendriks P.H.G.M, Maučec M, de Meijer R.J, 2002. MCNP modelling of scintillation-detector γ-ray spectra from natural radionuclides, Appl. Radiat. Isot., 57, 449-457.

Hurd_77 Hurd D. C., and Theyer F., 1977. Changes in the physical and chemical properties of biogenic silica from the central equatorial Pacific: Part II. Refractive index, density, and water content of acid-cleaned samples. Am. J. Sci., 277, 1168–1202.

IAEA_02 International Atomic Energy Agency, 2002. Specialized software utilities for gamma ray spectrometry, IAEA-TECDOC-1275, Vienna, 2002.

IAEA_03 International Atomic Energy Agency, 2003. Collection and Preparation of Bottom Sediment Samples for Analysis of Radionuclides and Trace Elements, TECDOC-1360.

IAEA_04 International Atomic Energy Agency, 2004. Radiotracer Application in Industry -A Guidebook. Technical Report Series, 423.

IAEA_05a International Atomic Energy Agency, 2005. Worldwide marine radioactivity studies (WOMARS) Radionuclide levels in oceans and seas. TECDOC-1429.

IAEA_05b International Atomic Energy Agency, 2005. International Atomic Energy Agency, Marine Environmental Assessment of the Mediterranean Sea. Methodological guidelines. TC RER/7/003 2005-2010, IAEA,Vienna.

IAEA_10a International Atomic Energy Agency, 2010. Analytical Methodology for the Determination of Radium Isotopes in Environmental Samples, IAEA Analytical Quality in Nuclear Applications No. IAEA/AQ/19, Vienna.

IAEA_10b International Atomic Energy Agency, 2010. In-situ Methods for Characterization of Contaminated Sites, IAEA, Technical Meeting 38924, Vienna.

IAEA_91 International Atomic Energy Agency, 1991. Inventory of radioactive material entering the marine environment: Sea disposal of radioactive waste. TECDOC-588.

IAEA_99 International Atomic Energy Agency, 1999. Proceedings of a symposium held in Monaco, 5-9 October 1998.

Ivan_94 Ivanovich M., 1994. Uranium Series Disequilibrium: Concepts and Applications, Radiochimica Acta 64, 81-94.

Jacob_09 Jacobs W., Eelkema M., Limburg H., and Winterwerp J. C., 2009. A new radiometric instrument for in situ measurements of physical sediment properties, Mar. Freshwater Res., 60, 727–736.

Jäder_15 Jäderström J., Mueller W.F., Attrashkevich V., Adekola A.S., 2015. True coincidence summing correction and mathematical efficiency modeling of a well detector, Nucl. Instrum. Methods A, 784, 264-268.

James_04 James, F., 2004. MINUIT Tutorial, Function Minimization, (Reprinted from the Proceedings of the) 1972 CERN Computing and Data Processing School, Pertisau, Austria, 10–24 September 1972.

James_75 James F., and Roos M., 1975. Minuit-A system for function minimization and analysis of the parameter errors and correlations. Comput. Phys. Commun. 10, 343-367.

James_94 James F., 1994. MINUIT Function Minimization and Error Analysis: Reference Manual Version 94.1. CERN-D506.

Jones_01 Jones D.G., 2001. Development and application of marine gamma-ray measurements: a review, J. Environ. Radiact. 53, 313–333.

Kalf_16 Kalfas C.A., Axiotis M., Tsabaris C., 2016. SPECTRW: A software package for nuclear and atomic spectroscopy, Nucl. Instrum. Methods A, 830, 265-274.

Karag_05 Karageorgis A.P., Kaberi H., Price N.B., Muir G.K.P., Pates J.M., Lykousis V., 2005. Chemical composition of short sediment cores from Thermaikos Gulf (Eastern Mediterranean): Sediment accumulation rates, trawling and winnowing effects, Cont. Shelf Res., 25, 2456–2475.

Karst_07 Karsten L., Boguslaw M., Jens W., 2007. Availability of radium isotopes and heavy metals from scales and tailings of Polish hard coal mining, J. Environ. Radioact. 94, 137-150.

Kauf_81 Kaufman, A., Li, Y.-H., Turekian, K. K., 1981. The removal rates of ^{234}Th and ^{228}Th from waters of the NewYork Bight, Earth Planet. Sc. Lett., 54, 385-392.

Kippen_04 Kippen R.M., 2004. The GEANT low energy Compton scattering (GLECS) package for use in simulating advanced Compton telescopes. New Astronomy Reviews 48, 221–225.

Kn_00 Knoll, G.F., 2000. Radiation Detection and Measurement. Wiley, New York.

Kob_99 Kobayashi Y., Takahashi R., Shima S., Katagiri M., & Takahashi K., 1999. Development of a submersible Ge gamma-ray detector system. In Marine pollution. Proceedings of a symposium held in Monaco, IAEA-TECDOC-1094, p. 501-503. International Atomic Energy Agency, Vienna.

Koc_58 Koczy, F.F., 1958. Natural radium as a tracer in the ocean, In Proceedings of the 2nd International Conference of Peaceful Uses of Atomic Energy, p. 351-357, Geneva.

Koc_62 Koczy, F.F., Szabo B.J., 1962. Renewal time of bottom water in the Pacific and Indean Oceans, Journal of the Oceanographical Society of Japan, 20th anniversary volume, 590-599.

Komi_11 Kominz M. A., Patterson K., Odette D., 2011. Lithology dependence of porosity in slope and deep marine sediments, J. Sediment. Res., 81, 730–742.

Koom_01 Koomans R.L., de Meijer R.J., Venema L.B., 2001. Cross-Shore graded sediment transport: Grain size and density effects, Coastal Engineering Proceedings, 26, Proceedings of 26th Conference on Coastal Engineering, Copenhagen, Denmark, 1998.

Kor_92 Korum M., Martincic R., 1992. Coincidence summing in gamma and X-ray Spectrometry. Nucl. Instrum. Methods A, 325, 478-484.

Korun_91 Korun M., Martinčič R., Pucelj B., 1991. In-situ measurements of the radioactive fallout deposit, Nucl. Instrum. Methods A, 300, 611-615.

Korun_94 Korun M., Likar A., Lipoglavšek M., Martinčič R., Pucelj B., 1994. In-situ measurement of Cs distribution in the soil, Nucl. Instrum. Methods B, 93, 485-491.

Kovler_13 Kovler K., Prilutskiy Z., Antropov S., Antropova N., Bozhko V., Alfassi Z.B., Lavi N., 2013. Can scintillation detectors with low spectral resolution accurately determine radionuclides content of building materials, Appl. Radiat. Isot., 77, 76–83.

Krish_08 Krishnaswami S., Cochran J.K., 2008. Chapter 1, Introduction, In: S. Krishnaswami and J. Kirk Cochran, Editor(s), Radioactivity in the Environment, Elsevier, 2008, Volume 13, p. 1-10.

Lal_99 Lal D., 1999. An overview of five decades of studies of cosmic ray produced nuclides in oceans, Sci. Total Environ., 237–238, 3-13.

Landa_04 Landa E. R., 2004. Uranium mill tailings: nuclear waste and natural laboratory for geochemical and radioecological investigations, J. Environ. Radioact., 77, 1-27.

Landa_07 Landa E. R., 2007. Naturally occurring radionuclides from industrial sources: characteristics and fate in the environment, In: George Shaw, Editor(s), Radioactivity in the Environment, 10, 211-237.

Lépy_07 Lépy, M.C., 2007. Total efficiency calibration for coincidence-summing corrections, Nucl. Instrum. Methods A, 579, 1, 284-287.

Lépy_12 Lépy, M.C., et al., 2012. Intercomparison of methods for coincidence summing corrections in gamma-ray spectrometry—part II (volume sources), Appl. Radiat. Isot., 70, 2112-2118.

Libby_49 Libby W.F., Anderson E.C. and Arnold J.R. 1949. Age determination by radiocarbon content: World-Wide assay of natural radiocarbon, Science, 109, 227-228.

Lin_14 Lin W., Ma H., Chen L., Zeng Z., He J., Zeng S., 2014. Decay/ingrowth uncertainty correction of $^{210}Po/^{210}Pb$ in seawater, J. Environ. Radioact., 137, 22-30.

Lind_10 Lindahl P., Lee S.H., Worsfold P., Keith-Roach M., 2010. Plutonium isotopes as tracers for ocean processes: A review, Mar. Environ. Res., 69, 73–84.

Loeff_99 van der Loeff R., Moore, W.S., 1999. Chapter 13, Determination of natural radioactive tracers. In: Grasshoff, K., Ehrardt, M., Kremling, K. ŽEds.., Methods of Seawater Analysis. Verlag Chemie, Weinheim.

Loeff_01 van der Loeff R., 2001. Uranium-thorium Decay Series In The Oceans Overview, Encyclopedia of Ocean Sciences, J. Steele, S. Thorpe and K. Turekian, eds. Academic Press, p. 3135-3145/

Loz_12 Lozano R.L., Hernández-Ceballos M.A., San Miguel E.G., Adame J.A., Bolívar J.P., 2012. Meteorological factors influencing the 7Be and 210Pb concentrations in surface air from the southwestern Iberian Peninsula, Atmos. Environ., 63, 168-178.

Luo _00 Luo S. D., Ku T. L., Roback R., Murrell M., McLing T. L., 2000. In-situ radionuclide transport and preferential groundwater flows at INELL (Idaho): Decay-series disequilibrium studies. Geochimica et Cosmochimica Acta, 64, 867–881.

Luo_14 Luo X., Jiao J.J., Moore W.S., Lee C.M., 2014. Submarine groundwater discharge estimation in an urbanized embayment in Hong Kong via short-lived radium isotopes and its implication of nutrient loadings and primary production, Mar. Poll. Bull., 82, 144–154.

Mab_13 Mabit L., Meusburger K., Fulajtar E., Alewell C., 2013. The usefulness of ^{137}Cs as a tracer for soil erosion assessment: A critical reply to Parsons and Foster (2011), Earth-Sci. Rev., 127, 300-307.

Mab_14 Mabit L., Benmansour M., Abril J.M., Walling D.E., Meusburger K., Iurian A.R., Bernard C., Tarján S., Owens P.N., Blake W.H., Alewell C., 2014. Fallout ^{210}Pb as a soil and sediment tracer in catchment sediment budget investigations: A review, Earth-Sci. Rev., 138, 335-351.

Mahm_13 Mahmood H.S., Hoogmoed W.B., van Hentel E.J., 2013. Proximal Gamma-Ray Spectroscopy to Predict Soil Properties Using Windows and Full-Spectrum Anlysis Methods, Sensors 13,16263-16280.

Mar_10 Marion C., Dufois F., Arnaud M., Vella C., 2010. In situ record of sedimentary processes near the Rhône River mouth during winter events (Gulf of Lions, Mediterranean Sea), Cont. Shelf Res., 30, 1095–1107.

Mas_06 Mas J.L., San Miguel E.G., Bolívar J.P., Vaca F., Pérez-Moreno J.P., 2006. An assay on the effect of preliminary restoration tasks applied to a large TENORM wastes disposal in the south-west of Spain, Sci. Total Environ., 364, 1–3, 55-66.

Mauč_04 Maučec M., de Meijer R.J., Rigollet C., Hendriks P.H.G.M., Jones D.G., 2004. Detection of radioactive particles offshore by γ-ray spectrometry Part I: Monte Carlo assessment of detection depth limits, Nucl. Instrum. Methods, 525, 593-609.

Mauč_09 Maučec M., Hendriks P.H.G.M., Limburg J., de Meijer R.J., 2009. Determination of correction factors for borehole natural gamma-ray measurements by Monte Carlo simulations. Nucl. Instrum. Methods A, 609, 194-204.

Meij_02 De Meijer R.J., Limburg J., Venema L.B., 2002. Natural radioactivity in monitoring waste disposals. Phys. Scr., 97, 139–147.

Metro_49 Metropolis N., and Ulam S., 1949. The Monte Carlo Method, J. Am. Statist. Assoc., 44, 247, 335-341.

Miller_82 Miller J. M., Thomas B. W., Roberts P. D., and Creamer S. C., 1982. Measurement of Marine Radionuclide Distribution Using a Towed Sea-bed Spectrometer. Mar. Pollut. Bull., 13, 315-319.

Minty_92 Minty BRS, 1992. Airborne gamma-ray spectrometric background estimation using full spectrum analysis, Geophysics, 57, 279.

Miró_12 Miró C., Baeza A., Madruga M.J., Periañez R., 2012. Caesium-137 and Strontium-90 temporal series in the Tagus River: experimental results and a modelling study, J. Environ. Radioact., 113, 21-31.

Nab_16 Nabhani K. A., Khan F., Yang M., 2016. Technologically Enhanced Naturally Occurring Radioactive Materials in oil and gas production: A silent killer, Process Saf. Environ. Protection, 99, 237-247.

Nafe_57 Nafe J. E., Drake C. L., 1957. Variation with depth in shallow and deep water marine sediments of porosity, density, and the velocities of compressional and shear waves, Geophysics, 22, 1957, 523.

Noakes_99 Noakes J.E., Noakes S.E., Dvoracek D.K., Culp R.A., Bush P.B., 1999. Rapid coastal survey of anthropogenic radionuclides, metals, and organic compounds in surficial marine sediments, Sci. Total Environ., 237–238, 449-458.

Nov_07 Novkovic D., Kandic A., Đuraševic M., Vukanac I., Miloševic Z., Nadderd L., 2007. Coincidence summing of X- and -rays in -ray spectrometry, Nucl. Instrum Methods A, 578, 207–217.

Now_98 Nowotny R. XMuDat: Photon attenuation data on PC. IAEA-NDS-195. International Atomic Energy Agency, Vienna, Austria. 1998. Available from: http://th www.mds.iaea.or.at /reports/mds-195.htm.

Nu_15 Nuttin L., Maccali J., Hillaire-Marcel C., 2015. U, Th and Pa insights into sedimentological and paleoceanographic changes off Hudson Strait (Labrador Sea) during the last ~37 ka with special attention to methodological issues, Quat. Sci. Rev., 115, 39-49.

Ocone_04 Ocone R., Kostezh A., Kurinenko V., Tyshchenko A., Derkach G., Leone P., 2004. Substrate characterization

for underwater gamma spectrometry: tank measurement results utilizing efficiencies calculated via Monte-Carlo code, Appl. Radiat. Isot., 61, 2–3, 129-132.

Oku_07 Okunade A.A., 2007. Parameters and computer software for the evaluation of mass attenuation and mass energy-absorption coefficients for body tissues and substitutes. Journal of Medical Physics / Association of Medical Physicists of India, 32, 3, 124–132.

Osv_01 Osvath I., Povinec P.P., 2001. Seabed γ-ray spectrometry: applications at IAEA-MEL, J. Environ.Radioact., 53, 335-349.

Osv_05 Osvath I., Povinec P.P., Livingston H.D., Ryan T.P., Mulsow S., Comanducci J.F., 2005. Monitoring of radioactivity in NW Irish Sea water using a stationary underwater gamma-ray spectrometer with satellite data transmission. J. Radioanal. Nucl. Chem. 263, 437–440.

Osv_99 Osvath I., Povinec P., Huynh-Ngoc L., Comanducci J.-F., 1999. Underwater gamma surveys of Mururoa and Fangataufa lagoons, Sci. Total Environ., 237–238, 277-286.

Pap_13 Papucci C., Delfanti R., 1999. ^{137}Cs distribution in the eastern Mediterranean Sea: recent changes and future trends, Sci. Total Environ., 237–238, 30, 67-75.

Peate_05 Peate, D.W., Hawkesworth C.J., 2005. U series disequilibria: Insights into mantle melting and the timescales of magma differentiation, Rev. Geophys., 43, RG1003, doi:10.1029/2004RG000154.

Peris_89 Perissoratis C., Mitropoulos D., 1989. Late Quaternary evolution of the northern Aegean shelf, Quaternary Research, 32, 1, 36-50.

Piton_00 Piton F., Lépy M.-C., Bé M.-M., Plagnard J., 2000. Efficiency transfer and coincidence summing corrections for γ-ray spectrometry, Appl. Radiat. Isot., 52, 791-795.

Pittman_91 Pittman E.D., Larese R.E., 1991. Compaction of lithic sands: experimental results and applications, Am. Assoc. Pet. Geol. Bull., 75, 1279–1299.

Plank_98 Plank T., Langmuir C. H., 1998. The chemical composition of subducting sediment and its consequences for the crust and mantle. Chem. Geol., 145, 325–394.

Plast_10 Plastino W., et al., 2010. Uranium groundwater anomalies and L'Aquila earthquake, 6th April 2009 (Italy), J. Environ. Radioact., 101, 1, 45-50.

Porc_03 Porcelli D., Swarzenski P. W., 2003. The behavior of U- and Th-series nuclides in groundwater.In: Uranium-Series Geochemistry (Eds B. Bourdon, G. M. Henderson, C. C. Lundstrom and S. P. Turner). Rev. Mineral. Geochem., 52, 317–361.

Porc_08 Porcelli D., 2008. Chapter 4, Investigating Groundwater Processes Using U- and Th-Series Nuclides, In: S. Krishnaswami and J. K. Cochran, Editor(s), Radioactivity in the Environment, Elsevier, 2008, 13, p. 105-153.

Pov_01 Povinec P.P., La Rosa J.J., Lee S.H., Mulsow S., Osvath I.,Wyse E. 2001. Recent developments in radiometric and mass spectrometry methods for marine radioactivity measurements. J. Radioanal. Nucl. Chem. 248, 713–718.

Pov_05 Povinec P.P., 2005. Chapter 8, Developments in analytical technologies for marine radionuclide studies, In: Hugh D. Livingston, Editor(s), Radioactivity in the Environment, 6, 237-294.

Pov_06a Povinec P.P., Levy-Palomo I., Comanducci J.-F., de Oliveira J., Oregioni B., Privitera A.M.G., 2006. Submarine groundwater discharge investigations in Sicilian and Brazilian coastal waters using an underwater gamma-ray spectrometer, In: P.P. Povinec and J.A. Sanchez-Cabeza, Editor(s), Radioactivity in the Environment, 8, 373-381.

Pov_06b Povinec P.P., Comanducci J.F., Levy-Palomo I., Oregioni B., 2006. Monitoring of submarine groundwater discharge along the Donnalucata coast in the south eastern Sicily using underwater gamma-ray spectrometry, Cont. Shelf Res., 26, 874–884.

Pov_08 Povinec P.P., Osvath I., Comanducci J.-F., 2008. Underwater gamma-ray spectrometry, In: Pavel P. Povinec, Editor(s), Radioactivity in the Environment, Elsevier, 2008, 11, 449-479.

Pov_10 Povinec P.P., Lee S.H., Liong L., Kwong W., Oregioni B., Jull A.J.T., Kieser W.E., Morgenstern U., Top Z., 2010. Tritium, radiocarbon, ^{90}Sr and ^{129}I in the Pacific and Indian Oceans, Nucl. Instrum. Methods B, 268, 1214-1218.

Pov_12 Povinec P.P., Eriksson M., Scholten J., Betti M., 2012. Chapter 12, Marine Radioactivity Analysis, In

Handbook of Radioactivity Analysis (Third Edition), edited by Michael F. L'Annunziata,, Academic Press, Amsterdam, 2012, p. 769-832.

Pov_96 Povinec P.P., Osvath I., Baxter M.S., 1996. Underwater gamma-spectrometry with HPGe and NaI(Tl) detectors, Appl. Radiat. Isot., 47, 1127-1133.

Pov_97 Povinec, P.P., Osvath, I., Baxter, M.S., Harms, I., Huynh-Ngoc, L., LiongWee Kwong, L., Pettersson, H.B.L., 1997. IAEA-MEL's contribution to the investigation of Kara Sea radioactivity and radiological assessment. Mar. Pollut. Bull. 35, 235–241.

Prell_91 Prell, W. J., Niitsuma, N., et al., 1991, Proceedings of the Ocean Drilling Program, Scientific Results, Proc. ODP, Sci. Results, 117: College Station, TX (Ocean Drilling Program).

Pusch_73 Pusch, R., 1973. Influence of organic matter on the geotechnical properties of clays. Natl. Swedish Bldg. Res., 11.

Put_04 Van Put, P., Debauche A., DeLellis C., Adam V., 2004. Performance level of an autonomous system of continuous monitoring of radioactivity in seawater, J. Environ. Radioact., 72, 177–186.

Quar_13 Quarati F.G.A., Dorenbos P., van der Biezen J., Owens A., Selle M., Parthier L., Schotanus P., 2013. Scintillation and detection characteristics of high-sensitivity $CeBr_3$ gamma-ray spectrometers, Nucl. Instrum. Methods A, 729, 596–604.

Qui_95 Quintana B., Fernandez F., 1995. An empirical method to determine coincidence-summing corrections in gamma spectrometry, Appl. Radiat. Isot., 46, 961-964.

Quigley_02 Quigley, M.S., Santschi P., Hung C.-C., Guo L., Honeyman B.D., 2002. Importance of acid polysaccharides for ^{234}Th complexation to marine organic matter. Limnol. Oceanogr., 47, 367–377.

Ra_99 Ramos-Lerate I., Barrera M., Ligero R. A., Casas-Ruiz M., 1999. A New Method for Gamma-efficiency Calibration of Voluminal Samples in Cylindrical Geometry. J. Environ. Rad., 38, 47-57.

Reime_82 Reimers, C. E., 1982. Organic matter in anoxic sediments off central Peru: relations of porosity, microbial decomposition and deformation properties. Mar. Geol., 46, 175-197.

Róden_07 Ródenas J., Gallardo S., Ballester S., Primault V., Ortiz J., 2007. Application of the Monte Carlo method to the analysis of measurement geometries for the calibration of a HPGe detector in an environmental radioactivity laboratory. Nucl. Instrum. Methods B, 263,144–148.

Rouni_01 Rouni P.K., Petropoulos N.P., Anagnostakis M.J., Hinis E.P., Simopoulos S.E., 2001. Radioenvironmental survey of the Megalopolis lignite field basin, Sci. Total Environ., 272, 261-272.

Sal_95 Salomons, W., 1995. Environmental impact of metals derived from mining activities: Processes, predictions, prevention, J. Geochem. Explor. 52, 5-23.

Sant_02 Santos R.N., Marques L.S., 2002. Study of the radioactive disequilibrium of the volcanic rocks from the Trindade Island (Brazil), An. Acad. Bras. Ciênc., 74, 548-549.

Sant_08 Santos I.R., Burnett W.C., Godoy J.M., 2008. Radionuclides as tracers of coastal processes in Brazil: Review, synthesis, and perspectives, J. Braz. Oceanogr., 56, 2,115-131.

Sants_80 Santschi P. H., Adler D., Amdurer M., Li Y.-H., Bell J. J., 1980. Thorium isotopes as analogues for "particle-reactive" pollutants in coastal marine environments, Earth Planet. Sc. Lett., 47, 3, 327-335.

Sants_89 Santschi P.H., Honeyman B.D., 1989. Radionuclides in aquatic environments, Int. J. Radiat. Appl. Instrum. C Radiat. Phys. Chem., 34, 2, 213-240.

Sart_11 Sartini L., Simeone F., Pani P., Bue N., Marinaro G., Grubich A., Lobko A., Etiope G., Capone A., Favali P., Gasparoni F., Bruni F., 2011. GEMS: Underwater spectrometer for long-term radioactivity measurements, Nucl. Instrum. Methods A, 626–627, S145-S147.

Scherer_87 Scherer, M., 1987. Parameters influencing porosity in sandstones: a model for sandstone porosity prediction, Am. Assoc. Pet. Geol. Bull., 71, 485–491.

Schlo_91 Schlosser P., Bullister J.L., Bayer R., 1991. Studies of deep water formation and circulation in the Weddell Sea using natural and anthropogenic tracers, Mar. Chem., 35, 1–4, 97-122.

Schul_04 Schuller D., Kadko D., Smith C. R., 2004. Use of $^{210}Pb/^{226}Ra$ disequilibria in the dating of deep-sea whale

falls, Earth Planet. Sci. Lett., 218, 3–4, 277-289.

Semk_15 Semkow T.M., et al., 2015. Calibration of Ge gamma-ray spectrometers for complex sample geometries and matrices, Nucl. Instrum. Methods A, 799, 105-113.

Shep_54 Shepard, F.P., 1954, Nomenclature based on sand-silt-clay ratios: Journal of Sedimentary Petrology, 24, 151-158.

Sima_01 Sima O., Arnold D., Dovlete C., 2001. GESPECOR: A versatile tool in gamma ray spectrometry, J Radioanal Nucl Chem, 248, 359-364.

Sima_96 Sima O., Arnold D., 1996. Self-attenuation and coincidence-summing corrections calculated by Monte Carlo simulations for gamma-spectrometric measurements with well-type germanium detectors, Appl. Radiat. Isot., 47, 889-893.

Singh_14 Singh V.P., Badiger N.M., 2014. Comprehensive study on energy absorption buildup factors and exposure buildup factors for photon energy 0.015 to 15 MeV up to 40 mfp penetration depth for gel dosimeters, Radiat. Phys. Chem., 103, 234-242.

Smith_97 Smith J.T., Appleby P.G., Hilton J., Richardson N., 1997. Inventories and fluxes of ^{210}Pb, ^{137}Cs and ^{241}Am determined from the soils of three small catchments in Cumbria, UK. J. Environ. Radioact., 37, 127-142.

Sokolov_99 Sokolov A.D., Danengirsh S.G., Popov S.V., Pchelintsev A.B., Gostilo V.V., Druzhinin A.A., Maksimov M.Y., Lebedev N.M., Shapovalov V. I., 1999. A deep-water gamma-ray spectrometer on the basis of a high-purity germanium detector, Instrum. Exp. Tech., 42, 563-568.

Ste_08 Stewart R.H., 2008. Introduction To Physical Oceanography, Department of Oceanography, Texas A & M University.

Stein_14 Steinhauser G., Brandl A., Johnson T. E., Comparison of the Chernobyl and Fukushima nuclear accidents: A review of the environmental impacts, Sci. Total Environ., 800-817, 470–471.

Stirl_09 Stirling C.H., Andersen M.B., 2009. Uranium-series dating of fossil coral reefs: Extending the sea-level record beyond the last glacial cycle, Earth Planet. Sci. Lett., 284, 269-283.

Swarz_03 Swarzenski, P.W., Porcelli, D., Andersson, P.S., Smoak, J.M., 2003. The behavior of U- and Th-series nuclides in the estuarine environment, Rev. Mineral. Geochem. 52, 577–606.

Szent_13 Szentmiklósi, L., Kis, Z., Belgya, T., Berlizov, A.N., 2013. On the design and installation of a Compton-suppressed HPGe spectrometer at the Budapest neutron-induced prompt gamma spectroscopy (NIPS) facility, J. Radioanal.l Nucl. Chem., 298, 3, 1605-1611.

Tall_11 Talley, L.D. Pickard G.L., Emery W. J., Swift J. H., 2011. Chapter 3, Physical Properties of Seawater, In Descriptive Physical Oceanography (Sixth Edition), Academic Press, Boston, p. 29-65.

Tayl_13 Taylor A., Blake W.H., Smith H.G., Mabit L., Keith-Roach M.J., 2013. Assumptions and challenges in the use of fallout beryllium-7 as a soil and sediment tracer in river basins, Earth-Sci. Rev., 126, 85-95.

Ten_14 Tenzer R. and Gladkikh V., 2014. Assessment of Density Variations of Marine Sediments with Ocean and Sediment Depths. The Scientific World Journal. doi:10.1155/2014/823296.

Thorn_13a Thornton B., Ohnishi S., Ura T., Odano N., Fujita T., 2013. Continuous measurement of Radionuclide distribution off Fukushima using a towed sea-bed gamma ray spectrometer, Deep-Sea Res. Pt. I, 79, 10-19.

Thorn_13b Thornton B., et al., 2013b. Distribution of local 137Cs anomalies on the seafloor near the Fukushima Dai-ichi Nuclear Power Plant, Mar. Poll. Bull., 74, 344-350.

Truj_14 Trujillo A.P., Thurman H.V., 2014. Chapter 4, Essentials of Oceanography (11th edition), Pearson Education ©.

Tsab_04 Tsabaris, C. and Thanos, I., 2004. An underwater sensing system for monitoring radioactivity in the marine environment, Mediterr. Mar. Sci. 5, 5-12.

Tsab_05 Tsabaris C., and Ballas D., 2005. On line gamma-ray spectrometry, Appl. Radiat. Isot., 62, 82-89.

Tsab_07 Tsabaris, C., Eleftheriou, G., Kapsimalis, V., Anagnostou, C., Vlastou, R., Durmishi, C., Kedhi, M., Kalfas, C.A., 2007. Radioactivity levels of recent sediments in the Butrint Lagoon and the adjacent coast of Albania, Appl. Radiat. Isot., 65,445-453.

Tsab_08 Tsabaris C., Bagatelas C., Dakladas Th., Papadopoulos C.T., Vlastou R., Chronis G.T., 2008. An autonomous in situ detection system for radioactivity measurements in the marine environment, Appl. Rad. Isot., 66, 1419-1426.

Tsab_10 Tsabaris C., Scholten J., Karageorgis A. P., Comanducci J.-F., Georgopoulos D., Liong Wee Kwong L., Patiris D. L., Papathanassiou E., 2010. Underwater in situ measurements of radionuclides in selected submarine groundwater springs, Mediterranean Sea, Radiat. Prot. Dosimetry, 142, 273-28.

Tsab_11 Tsabaris C., Prospathopoulos A., 2001. Automated quantitative analysis of in-situ NaI measured spectra in the marine environment using a wavelet-based smoothing technique, Appl. Radiat. Isot., 69, 10, 1546-1553.

Tsab_12 Tsabaris C., Patiris D. L., Karageorgis A. P., Eleftheriou G., Papadopoulos V. P., Georgopoulos D., Papathanassiou E., Povinec P. P., 2012. In-situ radionuclide characterization of a submarine groundwater discharge site at Kalogria Bay, Stoupa, Greece, J. Environ. Radiact., 108, 50-59.

Tsab_14 Tsabaris C., Zervakis V., Kaberi H., Delfanti R., Georgopoulos D., Lampropoulou M., Kalfas C.A., 2014. ^{137}Cs vertical distribution at the deep basins of the North and Central Aegean Sea, Greece, Journal of Environmental Radioactivity, 132, 47-56.

Tsab_15 Tsabaris C., Patiris D.L., Fillis-Tsirakis E., Kapsimalis V., Pilakouta M., Pappa F.K., Vlastou R., 2015. Vertical distribution of ^{137}Cs activity concentration in marine sediments at Amvrakikos Gulf, western of Greece, J. Environ. Radioact., 144, 1-8.

Tugu_16 Tugulan, L. C. et al., 2016. On the geochemistry of the Late Quaternary loess deposits of Dobrogea (Romania), Quaternary International, 399, 100-110.

Tuli_87 Tuli J.K., 1987. Evaluated Nuclear Structure Data File. A Manual for Preparation of Data Sets. Brookhaven National Laboratory, BNL-NCS-51655-Rev.87.

Tyler_08 Tyler A. N., 2008. In situ and airborne gamma-ray spectrometry, In: Pavel P. Povinec, Editor(s), Radioactivity in the Environment, Elsevier, 11, 407-448.

Tyler_94 Tyler A.N., 1994. Environmental influences on gamma ray spectrometry. PhD dissertation, University of Glasgow, Faculty of Science.

Tyler_96 Tyler N., Sanderson D. C. W., Scott E. M. and Allyson J. D., 1996. Accounting for Spatial Variability and Fields of View in Environmental Gamma Ray Spectrometry, J. Environ. Rad. 33, 213-235.

Tyler_99 Tyler, A.N. 1999. Monitoring anthropogenic radioactivity in salt marsh environments through *in situ* gamma ray spectrometry, J. Environ. Radioact., 45 (3), 235–252.

Tzif_14 Tzifas, I.Tr., Godelitsas, A., Magganas, A., Androulakaki, E., Eleftheriou, G., Mertzimekis, T.J., Perraki, M., 2014. Uranium-bearing phosphatized limestones of NW Greece, J. Geochem. Explor., 143, 62-73.

UNSC_00 UNSCEAR, 2000. Sources and Effects of Ionizing Radiation, United Nations Scientific Committee on the Effects of Atomic Radiation. Report to General Assembly with Scientific Annexes, United Nations, New York.

Ve_01 Venema L.B. and de Meijer R.J., 2001. Natural radionuclides as tracers of the dispersal of dredge spoil dumped at sea, J. Environ. Radiact., 55, 221-239.

Vid_05 Vidmar, T., 2005. EFFTRAN— a Monte Carlo efficiency transfer code for gamma-ray spectrometry, Nucl. Instrum. Methods A, 550, 603-608.

Vid_11 Vidmar, T., Kanisch, G., Vidmar, G., 2011. Calculation of true coincidence summing corrections for extended sources with EFFTRAN, Appl. Radiat. Isot. 69, 908-911.

Viss_16 Visser A., Moran J.E., Hillegonds D., Singleton M.J., Kulongoski J.T., Belitz K., Esser B.K., 2016. Geostatistical analysis of tritium, groundwater age and other noble gas derived parameters in California, Water Res., 91, 314-330.

Vlach_09 Vlachoudis V., 2009. Flair: A powerful but user friendly graphical interface for FLUKA, American Nuclear Society - International Conference on Mathematics, Computational Methods and Reactor Physics, 2, 790-800.

Vlast_06 Vlastou R., Ntziou I.Th., Kokkoris M., Papadopoulos C.T. and Tsabaris C., 2006. Monte Carlo simulation of g-ray spectra from natural radionuclides recorded by a NaI detector in the marine environment, Appl. Radiat. Isot., 64, 116–123.

Weber_97 Weber M.E., Niessen F., Kuhn G., Wiedicke M., 1997. Calibration and application of marine sedimentary physical properties using a multi-sensor core logger, Mar. Geol. 136, 3, 151-172.

Wedek_99 Wedekind Ch., Schilling G., Grüttmüller M., Becker K., 1999. Gamma-radiation monitoring network at sea, Appl. Radiat. Isot., 50, 733-741.

X-5_03 X-5 Monte Carlo Team, 2003. MCNP5 – A General Monte Carlo N-Particle Transport Code, Version 5. LA-UR-03-198, LA-CP-03-0245, Los Alamos National Laboratory, 24. Available upon request at: https://laws.lanl.gov/vhosts/mcnp.lanl.gov/mcnp5.shtml.

Yam_12 Yamada M., Zheng J., 2012. ^{239}Pu and ^{240}Pu inventories and ^{240}Pu/^{239}Pu atom ratios in the equatorial Pacific Ocean water column, Sci. Total Environ., 430, 20-27.

Yiou_94 Yiou F., Raisbeck G.M., Zhou Z.Q., Kilius L.R., 1994. ^{129}I from nuclear fuel reprocessing; potential as an oceanographic tracer, Nucl. Instrum. Methods, 92, 1–4, 436-439.

Yüc_10 Yücel H., Solmaz A.N., Köse E., Bor D., 2010. A semi-empirical method for calculation of true coincidence corrections for the case of a close-in detection in γ-ray spectrometry, J. Radioanal. Nucl. Chem., 283, 305–312.

Zaab_14 Zaaboub N., Oueslati W., Helali M. A., Abdeljaouad S., Huertas F.J., Galindo A.L., 2014. Trace elements in different marine sediment fractions of the Gulf of Tunis (Central Mediterranean Sea), Chem. Spec. Bioavailab., 26, 1, 1-12.

Zhang_15 Zhang Y., Li C., Liu D., Zhang Y., Liu Y.,2015. Monte Carlo simulation of a NaI(Tl) detector for in situ radioactivity measurements in the marine environment, Appl. Radiat. Isot., 98, 44-48.

Zhu_08 Zhu H., Venkataraman R., Menaa N., Croft S., Berlizov A., 2008. Validation of gamma-ray true coincidence summing effects modeled by the Monte Carlo code MCNP-CP, J. Radioanal. Nucl. Chem., 278, 359-363.